Lattice-Boltzmann and lattice-gas simulations of binary immiscible and ternary amphiphilic fluids in two and three dimensions

Nélido González Segredo

Tesis doctoral
Departament de Física, Facultat de Ciències
Universitat Autònoma de Barcelona

dirigida por el Prof. Peter V. Coveney
University College London

2004

UAB

Director de tesis / Thesis supervisor:
Prof. Peter V. Coveney, catedrático de fisicoquímica
Christopher Ingold Laboratories, University College London
20 Gordon Street, London WC1H 0AJ, Reino Unido

Tutor:
Dr. Juan Camacho Castro, profesor titular de física
Departament de Física, Universitat Autònoma de Barcelona
08193 Bellaterra, España

Esta tesis cumple con los requisitos estipulados por los artículos 66 a 69 de la *Normativa de Doctorat* de la Universitat Autònoma de Barcelona, y por tanto se atiene al formato "Compendi de Publicacions".

This dissertation and the results presented therein are due to my own work under the supervision of my thesis supervisor, unless explicitly specified.

Acknowledgments

I WISH TO EXPRESS MY GRATITUDE to a number of people for their help and support at different stages during the development of this work: thesis supervisor Prof. Peter V. Coveney for his insight, and encouragement, and for providing access to state-of-the-art computational infrastructure; friends Maziar Nekovee, Antonio Padilla, Jordi Mompart, Rafael Hidalgo, Eva Rodríguez Zurita, Luz Marina Cairós, Cristina Zurita, Joan Peralta, Stephen Stackhouse, Simba Matondo, Anastasia Pavlidou, Jens Harting, David Benoit, and Jorge Stella. I also wish to thank Jonathan Chin, Dr. Peter J. Love and Dr. Ignacio Pagonabarraga for useful discussions, and Dr. Keir Novik, Dr. Simon Clifford and remaining CCS members for helpful technical assistance.

The lattice-Boltzmann FORTRAN90 code employed for this thesis (`LB3D`) was originally implemented by Jonathan Chin from a serial version provided by Dr. Hudong Chen. A number of people have contributed to debugging, extending and optimising `LB3D` in the past four years, from whose work my research has benefitted; my contribution in it has been the implementation of the pressure tensor measurement routines and various initial conditions routines. The serial lattice-gas C code employed for this thesis were originally implemented by Dirk Hellweg; the long-range routines were ported by myself from this onto a new serial version by Brian Gregor. The resulting code was parallelised by Dr. Martyn Foster. Most of the programs and scripting tools needed to postprocess simulation data were developed by myself in C, PERL and IDL.

I am indebted to Prof. David Jou, Prof. José Casas-Vázquez and Dr. Juan Camacho at the Universitat Autònoma de Barcelona, Spain, for their support in this endeavour, and Celia Martínez Melón for her assistance on the (lengthy) final administrative procedures before the *viva voce* examination. I also wish to thank Prof. Daan Frenkel for allowing me to finish off the edition of the thesis during the first weeks of a postdoctoral position at his group.

The development of this work was partly funded by a *Formación del Personal investigador* scholarship (FP95-78678168) from the Spanish Ministry of Science and Technology.

The infrastructure needed for numerical work presented in this thesis was financially supported by a number of institutions: (1) the UK Engineering and Physical Sciences

Research Council under grants GR/M56234 and RealityGrid GR/R67699 through access to Cray T3E-1200E, SGI Origin2000 and SGI Origin3800 supercomputers at Computer Services for Academic Research (CSAR), Manchester University, UK; (2) the Center for Computational Science, Boston University, USA, through a collaborative project to access their several SGI Origin2000 platforms; (3) the European Commission MINOS programme through a personal grant to gain access to Cray T3E-1200E and SGI Origin3800 supercomputers at the *Consorzio Interuniversitario per il Calcolo Automatico dell'Italia Nord Orientale* (CINECA); (4) the Higher Education Funding Council for England (HEFCE), through a 16-node SGI Onyx2 graphical supercomputer granted to the Centre for Computational Science, Chemistry Department, University College London, UK.

A mi familia:
Domingo, Feliciano, Lala, Mercedes, Nélido y Rodolfo.

Contents

Chapter 1

Introduction

Science may be described as the art of systematic over-simplification
—the art of discerning what we may with advantage omit.

Karl Popper

Fluids are part of our daily lives. Furthermore, they comprise two (possibly three) states of matter, and are ubiquitous: the ratio of solid to fluid matter in the observable universe is negligible. Moreover, if the solid state is defined as that in which atoms' positions are fixed, when averaged over sufficiently long times, and the fluid state as that in which they are not, then, in full rigour, only crystals are solids. Amorphous matter is characterised by an order parameter lacking not only the discrete translational symmetry found in crystals, but also, for fixed temperature and pressure, a state of global equilibrium. Interestingly, there are systems, microscopically considered as fluids according to the definition just given, that, however, present discrete translational invariance at larger length scales, i.e., mass density shows a crystalline structure when it is probed at length scales which are large enough to contain a statistically meaningful number of atoms, typically in the 10 nm—1 μm range. These systems have features reminiscent of solids if the word 'atoms' in the definition above is replaced by 'cells', a cell being a spatial sampling window large enough to allow the observation of statistical trends of the underlying microscopic fields, i.e., of a *mesoscopic* size. Matter showing these features is amenable to re-classification: in fact, it was baptised as *the liquid crystalline state*.

Early theoretical studies of fluids were exclusively based on *the continuum hypothesis*.

By 1830, the Navier-Stokes equations had become the equations of fluid motion *par excellence*, a prime example of a model for nonequilibrium phenomena decades ahead of a rigorous formulation of either kinetic theory or Gibbsian equilibrium statistical mechanics. It was not before the end of the 1930s that statistical mechanics had matured enough to be able to provide consistent mesoscopic condensed matter theories accounting for fluctuations and phase transitions. It was in 1932 that Onsager solved the two-dimensional Lenz-Ising model exactly, modelling a phase transition; in 1935 Landau published his phenomenological mean-field treatment of phase transitions; in 1940, Fowler & Guggenheim extended the *quasi-chemical* method of liquid solutions to take into account long-range interactions; in 1955, Noll proved that by taking appropriate phase averages, any molecular system modelled by statistical mechanics can be shown to satisfy exactly the equivalent field equation for a continuous material; in 1957 Alder & Wainwright computationally discovered a phase transition in a gas of hard spheres. Computer simulation was employed as a necessary tool in solving models of matter which incorporate microscopic information. Examples of these are kinetic models, mainly used for the calculation of transport properties of simple gases and their mixtures, and Ising-like, Monte Carlo and molecular dynamics models, used to study phase transitions, correlation functions and transport properties of liquids [1, 2, 3].

The advent of scaling theories in modelling polymer solutions [4] made it possible to tackle fluid systems of a more complex nature than the ones investigated hitherto; the distinction between 'simple' and 'complex' fluids came into existence for the first time. Also called 'soft matter' following P.-G. de Gennes, complex fluids encompass a range of systems whose common, defining feature is the presence of a mesoscopic length scale which necessarily plays a key role in determining their properties. At a first glance, features such as a multi-species composition or molecular self-assembly might also be considered as alternative definitions of a complex fluid. However, there are counter-examples to this: fluid mixtures do not necessarily present a mesoscopic length scale determining their properties, and, regarding the second feature, systems such as colloidal suspensions of particles of fixed molecular weight do not show self-assembly. Complex fluids invariably show 'anomalous' properties, in the form of rheological, optical, electrical and magnetic responses which are *nonlinear*, i.e., they are not proportional to the external 'force' causing them. In all of these cases, it is the supramolecular scale of the fluid that allows the molecular responses to superpose and yield a 'strong', co-operative effect; its behaviour is determined by several length and time scales.

It is enough to mention some examples of complex fluids to recognise their immediate and overwhelming practical importance. In fact, micellised surfactants provide the basis for numerous industrial processes and cosmetic and detergent applications; polymers constitute the most important class of synthetic materials due to their ample range of

structural, optical and rheological properties; most biological and geological fluids (e.g. blood, cell cytoplasm and mud) are colloidal suspensions of some kind. Furthermore, biological cell membranes are made up of closed bilayers of phospholipids, of an amphiphilic nature; on a more fundamental level, proteins and DNA are biopolymers.

As we shall see briefly, they consist of a surfactant-like species dispersed in a fluid which in turn can have internal structure, e.g., an immiscible fluid. Despite the fact that, e.g., surfactant molecules can have a relatively small size compared with that of polymers and colloids, they can give rise to striking modifications of the macroscopic behaviour of the fluid in which they are dispersed due to the broad range of length and time scales spanned as a result of their self-assembly. For this reason, amphiphilic systems can be considered a paradigm class of complex fluids of low molecular weight. Since they are so, it is reasonable to regard them as ideal testbeds for models aiming to incorporate, in a bottom-up fashion, following a complexity paradigm, the simplest possible molecular detail into existing fluid flow solvers in the mesoscopic domain such as lattice gases, and related lattice-Boltzmann methods.

Our objective for the research presented in this thesis has been the validation of variants of the lattice-Boltzmann and lattice-gas mesoscopic models for fluid dynamics by investigating surface tension, phase segregation, self-assembly and shear-induced properties in two types of complex fluids, binary immiscible and ternary amphiphilic mixtures. Within the broad context of condensed matter, these methods are generically classified as mesoscopic since they deliberately retain only a reduced set of the microscopic degrees of freedom. This makes them gain several orders of magnitud more algorithmic efficiency than fully-microscopic methods—the job of the modeller is, then, to map out their physically relevant parameter space.

The research carried out in this PhD project generated a number of papers accepted and/or published in both peer-reviewed international journals and conference proceedings, and a further work in the form of a preprint of imminent submission by this thesis' submission date. Copies of these papers, except the ones indicated, are included in chapters 3 and 4. The papers of whose work reported therein and writing I am the main contributor are, in inverse chronological order, the following:

1. N. González-Segredo, J. Harting and P. V. Coveney, "Stress response and structural transitions in sheared gyroid and lamellar amphiphilic mesophases: lattice-Boltzmann simulations." (Preprint, Centre for Computational Science, 2004.) (Annexed on p. 95.)

2. N. González-Segredo and P. V. Coveney, "Coarsening dynamics of ternary amphiphilic fluids and the self-assembly of the gyroid and sponge mesophases: lattice-Boltzmann simulations." Phys. Rev. E, (in press, 2004). (Annexed on p. 73.)

3. N. González-Segredo and P. V. Coveney, "Self-assembly of the gyroid cubic mesophase: lattice-Boltzmann simulations." Europhys. Lett. **65**, 795 (2004). (Annexed on p. 65.)

4. N. González-Segredo, M. Nekovee and P. V. Coveney, "Three-dimensional lattice-Boltzmann simulations of critical spinodal decomposition in binary immiscible fluids," Phys. Rev. E **67**, 046304 (2003). (Annexed on p. 47.)

5. N. González-Segredo and M. Foster, "pLRME2D: A parallel implementation of a two-dimensional hydrodynamic lattice-gas model with long-range interactions," Proceedings of the Sixth European SGI/Cray MPP Workshop, Manchester, UK (2000). (Annexed on p. 107 and available online,
cf. URL: http://mrccs.man.ac.uk/mpp-workshop6/proc/gonzalez.htm .)

The papers of which I am not first author are:

6. P. J. Love, M. Nekovee, P. V. Coveney, J. Chin, N. González-Segredo, and J. M. R. Martin, "Simulations of amphiphilic fluids using mesoscale lattice-Boltzmann and lattice-gas methods," Comp. Phys. Commun. **153**(3), 340-358 (2003). (Not included in this thesis.)

7. M. Nekovee, J. Chin, N. González-Segredo, and P. V. Coveney, "A parallel lattice-Boltzmann method for large scale simulations of complex fluids," E. Ramos et al. (eds), Computational Fluid Dynamics, Proceedings of the Fourth UNAM Supercomputing Conference, Singapore (World Scientific, 2001). (Not included in this thesis.)

It is worth noting that a new line of research at the Centre for Computational Science (Christopher Ingold Labs, University College London), namely, the study of defect dynamics in gyroid cubic mesophases, sprouted from the study of amphiphilic self-assembly presented in this thesis [5]. The first landmark of this ongoing line of research has been the successful TeraGyroid project [6, 7], aimed at harnessing the power of remote high-performance compute and visualisation platforms and storage devices via grid-enabled computational steering tools to explore the parameter space of the amphiphilic lattice-Boltzmann model presented herewith.

This dissertation is structured as follows. The remainder of this Introduction presents the physical features of the systems subject of our investigation. Section 1.2 gives an account of existing models for the simulation of multiphase fluids. Starting from kinetic theory and molecular dynamics basics, we justify the need for, and give an exposition of, methods in the mesoscopic scale which are able to either (a) contract the overwhelming amount of molecular information available from the microscopic realm and reduce the computational burden associated to their description, or (b) incorporate particulate

features, since continuum approaches are insufficient in dealing with phenomena such as self-assembly. Section 1.2 finishes with a presentation of the role of computer simulations in the study of fluid and soft matter and of the burgeoning field of high-performance computing. I finalise the Introduction with a presentation of the research reported in this thesis. In Chapter 2 I give a summary of the results and discuss them. In Chapter 3 I include copies of the papers published and accepted for publication in peer-reviewed international journals. In Chapter 4 I substantially complement the previous chapter by including one preprint to be imminently submitted, and one paper published in the Proceedings of an international conference. In Chapter 5 I provide the final conclusions.

1.1 Amphiphilic fluids are complex fluids

What is a 'simple' fluid? Figure 1.1 is a typical pressure-temperature phase diagram for a noble gas, such as argon, and let us consider a sample of which containing a large number of atoms. At sufficiently high temperature and moderate pressures, the sample will be in its gas or vapour phase; upon gradual cooling, the gas will undergo condensation which, depending on the pressure, will proceed via coalescence of liquid droplets or solidification into crystalline flakes. This phase transition from vapour to denser states can also occur at fixed temperature by increasing the pressure. Distinctive states in this diagram are given by the triple point, where three phases share the same thermodynamic variables, and the critical point, beyond which the transition between vapour and liquid is no longer first-order: it does not require a latent heat and the specific volume does not go through a step discontinuity.

Phase diagrams such as the one just described are characteristic of what we call 'simple' substances. We can include water among these; despite the unusual properties that this ubiquitous liquid exhibits, its equilibrium phases are still vapour, liquid and crystalline solid, its transitions are first-order, and areas of phase coexistence are of zero measure. In addition, 'simple' fluids are Newtonian: the stress is well described as being proportional to the velocity-field gradient, or strain rate, the proportionality constant being, in general, a tensor which does not depend on the velocity or its gradients.

Complex fluids are invariably characterised by equilibrium phase diagrams of a different nature, see Fig. 1.2. Their phases can be numerous and greatly depend upon the particular system under consideration (polymeric, colloidal, amphiphilic, liquid crystalline); the following phases are examples: sponge (dispersed or bicontinuous microemulsions), lamellar, columnar (or tubular), cylindrical or elongated micellar, cubic (fcc, bcc, micellar cubic, bicontinuous), and liquid crystalline isotropic, columnar, and nematic and smectic, the latter two names derived from Greek for 'filament' and 'to slide', respectively. Complex fluids' phase diagrams can present regions of phase coexistence of the same dimension-

ality, n, of the phase diagram itself, instead of $n-1$ as it occurs in phase diagrams of simple substances. Complex fluids' non-equilibrium properties are, in addition, typically, non-linear.

The term *amphiphilic fluid* is broadly used to denote multiphase fluids in which at least one species is of a surfactant nature (from surface active agent, also called an amphiphile). The kind of amphiphilic fluid we shall deal with in this thesis is that consisting of a binary immiscible fluid in which an amphiphile has been dispersed. I shall use the terms 'amphiphile' and 'surfactant' interchangeably, although others may understand the latter as only man-made and refer to the former in a different or broader context.

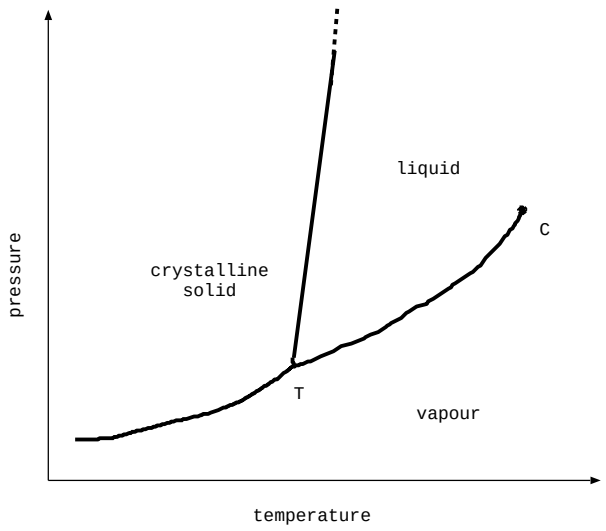

Figure 1.1: Phase diagram of a hypothetical 'simple' substance, showing the most common states of matter, first-order transitions between them and areas of phase coexistence of zero measure.

A surfactant molecule contains a polar headgroup attached to a hydrocarbon or aliphatic tail which, dispersed in a binary immiscible fluid mixture, such as oil and water, is driven towards and adsorbed at the interface between the two fluids. The selective chemical affinity between each part of the surfactant molecule and the components of the binary fluid is the mechanism responsible for such a taxis [9]. This is a process which is energetically favoured relative to their entropically beneficial dispersion in the bulk, provided that the amount of amphiphile is below the *critical micelle concentration*. Such a concentration is a threshold for the formation of globular clusters (colloidal aggregates) of amphiphilic molecules, bound together by the chemical affinity of their aliphatic chains and the repulsion from the ionic solvent; this is an activated process which can be favoured by certain changes in solution pH, and leads to sudden variations in interfacial tension once it starts, due to the fact that the micelle population eventually shoots off.

The interfacial tension of an immiscible fluid, or the surface tension of a liquid-vapour interface for a pure fluid, is a free energy per surface area in the sense of the amount of work needed to create a unit area; this is equivalent to the force per unit length associated to the (reversible) process of creating such a unit area. During the adsorption of amphiphile onto the interface, the temporal evolution of the interfacial tension depends upon the rate

and spatial distribution of the amphiphile adsorbed onto it. In a liquid-vapour mixture, interfacial tension is the result of intermolecular cohesion forces being different for the two phases, hence creating different molecular correlation lengths. In a binary immisicible fluid, intermolecular forces can predominantly be either cohesive or repulsive; either way, or both, this effectively creates a molecular selection mechanism which leads to molecular repulsion and, hence, phase segregation. The fact that the amphiphile has affinities for *both* of the phases or species leads to its interfacial adsorption, and, as soon as a statistically significant number has been locally adsorbed, to functioning as an *anchor* between the phases. The gradient of the order parameter, i.e., of the difference in compositions or densities, experiences a net local reduction due to the presence of a density of adsorbed surfactant, and hence so does the interfacial tension since it is proportional to such a gradient. This reduction makes the interface locally floppier and creates a local imbalance of lateral forces on the fluid layer defined between the interface and a depth into the bulk which will depend on the size of the surfactant molecule's head or tail and its correlation with the surrounding fluid. In other words, the fluid surrounding the interfacial region where surface tension has dropped will exert a force per unit length tangentially to the interface which will not be balanced by the forces from the region of lower surface tension. As a result, an unsteady and spatially nonuniform tangential shear stress will kick in, causing the interface to stretch, spreading the amphiphile monolayer and entraining the fluid below, deforming the interface. This kind of flow is generically called *Marangoni flow*.

The renowned property that amphiphiles lower the interfacial tension of a binary immiscible fluid (see, e.g., Ref. [10]) occurs for an equilibrated and homogeneous distribution of adsorbed amphiphile, which may well not be the general, nonequilibrium case. Local reduction of interfacial tension makes the interface locally floppier, causing the creation of interfacial surface. As more interfacial surface is created, so more amphiphile dispersed in the bulk can be accommodated on it. However, this mechanism is in competition with the Marangoni spreading flow, which causes the interfacial tension to increase to a value close to that for zero surfactant concentration. The actual fluid dynamics related to amphiphile adsorption is hence highly dependent on the particularities of the system, i.e., for example, densities, shear viscosities and chemical affinities.

Amphiphilic fluids are not only important in physical chemistry, structural biology, soft matter physics and materials science from a fundamental perspective, but their applications are also widespread. Detergents and mammalian respiration are two common examples in which surfactants are present. Living cell membranes are complex macromolecular assemblies comprised in large part by self-assembled phospholipids, of an amphiphilic nature [11]. Sponge mesophases are formed as a result of an amphiphile dispersion or melt at an appropriate composition, and enjoy numerous applications in medical research as well

as the pharmaceutical, cosmetic, food, and agro- and petrochemical industries [12, 13]. Lipidic, liquid crystalline mesophases, ubiquitous in biological systems, are also formed from amphiphilic dispersions or melts, and have important applications in membrane protein crystallisation, controlled drug release and biosensors [14, 15]. These phases are termed *mesophases* since their intrinsic internal length scales range between characteristic molecular and hydrodynamic (or macroscopic) ones [9, 10, 11].

Depending on temperature, pressure and fluid composition, the amphiphile can self-assemble and force the oil-water mixture into a wealth of equilibrium structures. The self-assembling process is dictated by the competing attraction-repulsion mechanisms present among the species. Lamellae and hexagonally-packed cylinders are examples of these mesophases, also referred to as L_α and H, respectively, with translational symmetry along one or two directions. Other examples are the sponge (L_3) mesophase and the micellar (Q^{223} or $Pm3n$, or Q^{227} or $Fd3m$), primitive ("P", Q^{229} or $Im3m$), diamond ("D", "F", Q^{224} or $Pn3m$) and gyroid ("G", Q^{230} or $Ia3d$) cubic mesophases, all of which lack translational symmetry [16]. Among all the aforementioned phases, only the sponge mesophase is devoid of long-range order and so cannot be classified as a liquid crystal: it is rather characterised by glassy features. Figure 1.3 shows a schematic depiction of some mesophases formed from a blend of two amphiphilic fluids. These mesophases are termed *lyotropic* since it is the mass fraction of the components that determines the transitions.

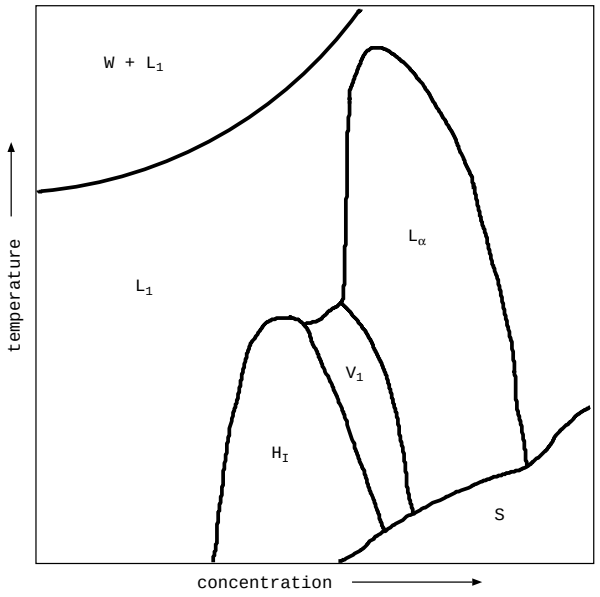

Figure 1.2: Phase diagram of a common nonionic surfactant, polyoxyethylene alkyl ether $C_{12}E_6$, where C_m is the hydrophobic, methylene or methyl chain, and E_n is the hydrophilic, oxyethylene chain. 'W' denotes the surfactant-containing water phase, 'L_2' denotes an inverse micellar phase, 'V_1' denotes a normal bicontinuous structure, and 'S' denotes a solid phase. Adapted from Hamley [8].

A sponge mesophase formed by the (amphiphilic) stabilisation of a binary immiscible fluid mixture is called a microemulsion. Since we shall be dealing with oil and water in equal proportions, we shall be concerned with bicontinuous microemulsions. A bicontinuous microemulsion is a structure consisting of two percolating, interpenetrating oil and

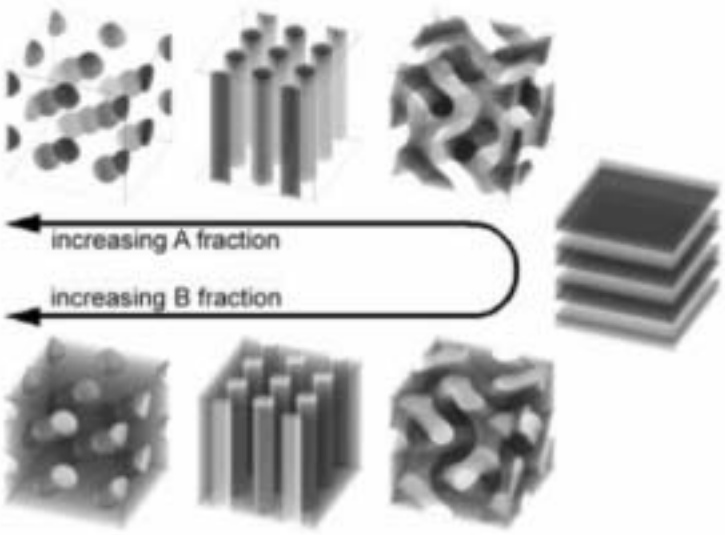

Figure 1.3: Schematic depiction of some mesophases formed from a blend of two amphiphilic fluids, A and B. In this example, the transition between the four renowned mesophases is lyotropic, i.e., driven by concentration. From left two right, the pictures correspond to the micellar, tubular, gyroid and lamellar mesophases.

water phases separated by a monolayer of surfactant molecules adsorbed at the interface. Oil and water are isotropically mixed, and ordering is short range. Sponge phases formed by the dispersion of amphiphile in a single phase solvent differ from microemulsions in that it is a surfactant bilayer which underlies the structure, and the regions it divides are occupied by the same fluid component. A gyroid phase is also a bicontinuous, interpenetrating structure; however, ordering is evidently long range, whence its classification as a liquid crystal. In the gyroid, the locus where most of the surfactant resides is a triply periodic minimal surface (TPMS) whose unit cell is of cubic symmetry. The surface has zero mean curvature, no two points on it are connected by a straight segment, and no reflexion symmetries are present. Isosurfaces of the gyroid phase for which oil and water are not at equal composition (minority phases) form mutually percolating, three-fold coordinated, regular lattices. Other examples of triply periodic surfaces of zero mean curvature arise in the P and D mesophases, the minority phase isosurfaces of which exhibit coordination numbers of six and four, respectively.

1.2 Modelling and simulation of multiphase fluids

Classically, the theoretical study of the non-equilibrium behaviour of fluids has been based on the solution of the Navier-Stokes equations [17]. These are equations for the balance of momentum and mass, which, for a compressible fluid and using an Eulerian system of

reference, have the form:

$$\partial_t \rho + \nabla \cdot (\rho \mathbf{u}) = 0\,, \tag{1.1}$$

$$\partial_t (\rho \mathbf{u}) + \nabla \cdot (\rho \mathbf{u}\mathbf{u} - \sigma) = \mathbf{F}\,, \tag{1.2}$$

$$\sigma = -p\mathsf{I} + \Pi \quad , \quad \Pi = 2\eta(\overset{\circ}{\nabla \mathbf{u}})^{\mathrm{s}} + \zeta(\nabla \cdot \mathbf{u})\mathsf{I} \tag{1.3}$$

where $\rho\mathbf{u}\mathbf{u} - \sigma$ is the momentum flux density tensor, σ is the stress tensor, p is the scalar or hydrostatic equilibrium pressure, $p = \frac{1}{3}\mathrm{tr}\sigma$, Π is the deviatoric, non-equilibrium or 'viscous' stress tensor, η is the dynamic shear viscosity, ζ is the bulk viscosity, the circle subtracts the trace, $\mathrm{tr}\nabla\mathbf{u} \equiv \nabla \cdot \mathbf{u}$, which is zero in an incompressible fluid, the "s" superscript denotes the symmetrisation $\frac{1}{2}(\mathsf{a} + \mathsf{a}^{\mathrm{T}})$, where a is a generic 2-tensor, I is the unit 2-tensor, and, finally, $\mathbf{F}$ is an external force. Setting aside the obvious effect of the external force, cf. Eq. (1.2), except when causing an initial perturbation, this Eulerian representation clearly shows the irreversible evolution of the system: the momentum density is locally increased at a rate set by $\nabla \cdot \sigma = -\nabla p + \eta\nabla^2\mathbf{u} + \zeta\nabla\nabla \cdot \mathbf{u}$, where we have assumed uniform viscosities. Alternatively, it is customary to find the last equations written in a Lagrangian representation; for an incompresible fluid, they appear as

$$\mathbf{D}_t \rho = -\rho \nabla \cdot \mathbf{u}\,, \tag{1.4}$$

$$\rho \mathbf{D}_t \mathbf{u} = -\nabla p + \eta \nabla^2 \mathbf{u} + \mathbf{F}\,, \tag{1.5}$$

$$\nabla \cdot \mathbf{u} = 0\,, \tag{1.6}$$

where $\mathbf{D}_t \equiv \partial_t + \mathbf{u} \cdot \nabla$ is the time derivative along the streamline.

The Navier-Stokes equations have been the paradigm equation of motion used by continuum fluid dynamicists for more than 150 years [18, 19]. Finding analytical solutions for them has drawn the attention of mathematicians seeking theorems of existence and uniqueness [20], and made significant contributions to the theory of non-linear equations.

The Navier-Stokes equations, however, remain an approximation to fluid motion, although this is frequently overlooked. From a kinetic-theoretic perspective, as we shall see in Section 1.2.1, they are derived at a restricted level of microscopic detail. In modelling multiphase flows, characterised by the presence of a moving boundary condition, much computational effort needs to be spent in tracking the evolution of the interface itself, although some recent progress has been made in this respect [21]. Indeed, the fact that the interface width is zero, i.e. diffusive effects are excluded, is a limitation in dealing with problems in which the fluid's length scales are comparable to such a width, such as in phase segregation, interfacial phenomena and flow in porous media.

1.2.1 Kinetic theory

Classical kinetic theory offers an alternative approach to the study of non-equilibrium fluid phenomena to continuum fluid dynamics. The time evolution of the system is described by

means of a single equation, the transport equation, whose only unknown, the distribution function, not only carries all the information on the spatial distribution of the fluid's molecular contituents, but also on their velocity distribution.

Kinetic theory is in turn an approximation to the full description of the system in terms of its microscopic, many-body, Newtonian dynamics. The BBGKY hierarchy [22, 23] for a system of N interacting molecules, equivalent to the Liouville equation for the (classical) motion of their N-particle probability distribution function in a $6N$ phase space, is an equation for the reduced, r-particle distribution, F_r, where $1 \leq\ r \leq\ N$, as a function of F_{r+1}. The reduced distribution F_r is defined as the integral of F_N over the phase space of the remaining $6(N-r)$ dynamic variables. The recursive character of the hierarchy is what holds up its equivalence to the fundamental, many-body, Liouville equation; for the hierarchy to be solved, it needs to be self-contained, i.e. it needs to be 'closed.'

Boltzmann equation

The closure of the BBGKY hierarchy is what defines the passing from a many-body theory to a kinetic or transport theory approach, which is done by defining F_{r+1} as a function of F_r in an *ad hoc* fashion. For most gases and liquids, and for practical reasons,the description is kept to its coarsest levels, namely $r = 1$ and 2. The closure at $r = 1$ is what is defined as the Boltzmann equation, which has the form

$$\partial_t f + \xi \cdot \nabla f + \frac{\mathbf{F}}{m} \cdot \nabla_\xi f = \iiint V(ff'|\tilde{f}\tilde{f}')\Big(ff' - \tilde{f}\tilde{f}'\Big)\ \mathrm{d}^3\xi' \mathrm{d}^3\tilde{\xi} \mathrm{d}^3\tilde{\xi}' \tag{1.7}$$

where $f = f(\mathbf{x}, \xi, t) \equiv F_1$, a prime means that the coordinates in question are those of the partner molecule in a binary collision whereas a tilde denotes pre-collisional coordinates, and $V(ff'|\tilde{f}\tilde{f}')$ is a scattering function, or probability of the transition from the ingoing distribution, $\tilde{f}\tilde{f}'$, to the outgoing distribution, ff'. This equation requires assumming the *Stosszahlansatz*, or molecular chaos assumption, i.e. the evolution of any one particle is sufficiently described by using single-particle distributions, and hence

$$F_2\ \equiv\ f\ f\,. \tag{1.8}$$

The *Stosszahlansatz*, Eq. (1.8), restricts the range of validity of the Boltzmann equation to what is known as the Boltzmann-Grad Limit (BGL) [24]. Effectively, the BGL is a prescription for the coarsest mean-field approximation that can be carried out on the equations of motion of the system.

Contraction of information

The Boltzmann equation is an integro-differential equation for the single-particle distribution function, f. This distribution, which lives on a 6-dimensional (position and velocity)

phase space, not only provides information on how probable it is for a molecule to be found around a given spatial position but also with what microscopic (or molecular) velocity; in other words, how populated such a microscopic velocity is at that position.

Continuum fluid dynamicists are, however, not concerned about the population of molecular velocities. Rather, they are ultimately interested in predicting macroscopic quantities such as the fluid velocity, stress and temperature fields. Even in regimes in which many-body quantum-mechanical effects [25] are negligible, such as for a broad range of temperatures and pressures in gases and liquids without chemical reactions, the uncertainty principle renders it impossible for experimental probes to fully explore microscopic information, which effectively becomes averaged out. This indicates the need to resort to averaging the minimally detailed information available at the microscopic level that a kinetic description provides in order to obtain one which can be directly related with experience.

This contraction of information is performed by integrating the transport equation over the whole subspace of microscopic velocities, in a similar fashion to the contraction of a subset of the Liouville equation's dynamic variables, leading to the BBGKY hierarchy. Since the macroscopic quantities of interest, such as mass and linear momentum density, stress (pressure tensor) and kinetic energy density are defined as moments of the distribution function with respect to the microscopic velocity ξ, by multiplying the transport equation by a polynomial of ξ and integrating over velocities, in what is called the Grad's moment method, leads to the macroscopic, hydrodynamical balance equations [26]. At this level, all reference to microscopic information has been lost. These equations, however, are not a closed set since they contain unknowns which are moments of higher order than those of the quantities being advected; in fact, they are related to the fluxes of the latter. These higher-order moments appear, in the Grad's method, as independent variables.

In theory, the determination of these higher-order variables poses no difficulty to the transport kineticist since a knowledge of the distribution function (solution of the transport equation) allows to determine directly and exactly all of its moments. A purely macroscopic approach, however, requires the closure of the set, i.e. the use of an *Ansatz*: the constitutive relations. Following such an approach, having obtained a non-closed set of balance equations by integrating the Boltzmann equation, the *Navier-Stokes* equations arise when the stress (second moment of f with respect to the excess or peculiar molecular velocity) is considered proportional to the strain rate; if the proportionality (transport) coefficient is independent of the latter, the fluid is termed Newtonian. In this scheme, the ideal hydrodynamic, or Euler, equations arise for an inviscid fluid, i.e. a fluid with zero shear viscosity. Newton's constitutive relation can be generalised to take into account viscoelastic effects by assuming a model for the dependence of the shear viscosity with the strain rate [27]. In order to close the energy balance equation, the heat flux needs to

be assumed proportional to the temperature gradient (Fourier's law), and its transport coefficient of proportionality (thermal conductivity) independent of it.

From the microscopic point of view, the Navier-Stokes-Fourier equations (Navier-Stokes equation along with the energy balance equation) are only an approximation and never exact, and they remain undetermined since the transport coefficients are unknown. In fact, in a microscopic approach, the balance equations are not needed in order to compute the evolution of the macroscopic variables. Instead, it is the Boltzmann equation which contains all the information required.

Naturally, the Boltzmann equation, as I have presented it so far, is limited to the BGL, which restricts the systems it can exactly model, for at least short times, to dilute and electrically neutral gases without internal structure so that collisions are binary and localised, and excluded-volume effects negligible. The BGL also precludes contributions to the energy from intermolecular force fields, since the latter are negligible; an alternative limit would need to be considered in order to include these effects.

Chapman-Enskog method

Even assuming the existence of solutions to the Boltzmann equation, it is, however, unrealistic to suppose that we would have fully detailed information of f at any instant, or, equivalently, the infinite set of its moments. In fact, Hilbert uniqueness theorem [22] states that "if f can be expanded in powers of some small parameter, then f is uniquely determined for times $t > 0$ by the values at $t = 0$ of its first five moments $\{\rho, \mathbf{u}, T\}$ only," i.e. by the mass density, baricentric or hydrodynamic velocity and temperature [22]. This small parameter can be identified with the Knudsen number, Kn, or ratio of a microscopic to a macroscopic length or time, and the solutions satisfying the assertion are called *normal solutions*. The macroscopic variables chosen are the only collisional invariants under binary collisions, the latter being the only ones allowed in the BGL. The Chapman-Enskog method [22, 23] is based on such an expansion of f in powers of Kn, and assumes that the system features a clear scale separation in which Kn is small. A zeroth-order expansion leads to the Euler equations for an inviscid fluid, whereas a first-order expansion yields the Navier-Stokes equations. The expressions for the stress and heat flux (second and contracted-third moments of f, respectively) used to obtain the Navier-Stokes-Fourier equations by closing the hydrodynamic balance equations emerge naturally from the method at second order of approximation. These expressions are linear relations between thermodynamic forces and fluxes, in the sense of the bilinear expression for the entropy production in local equilibrium thermodynamics [28], valid in a wide class of phenomena for small Kn numbers [27]. Most importantly, the Chapman-Enskog method gives expressions for the transport coefficients in terms of microscopic information.

Linear constitutive relations are, however, insufficient for high-frequency and high-

wavenumber phenomena, chemical reactions and viscoelastic behaviour. An improvement on this direction is meant to be given by the Chapman-Enskog method to second order, which leads to corrections to the first-order stress and heat flux (implicit in the Navier-Stokes-Fourier equations) in the form of first-order derivatives of the thermodynamic forces or products of two different of such forces. The closed set of equations obtained by using these corrected relations are called the Burnett equations, albeit still based on the Hilbert uniqueness theorem, i.e. leading to normal solutions.

Despite the fact that they are corrections to the Navier-Stokes equations, the Burnett equations have enjoyed considerably less success than the former, owing to a lack of knowledge of this type of partial differential equations, of the form of the boundary conditions needed to determine the higher-order derivatives in them, and of their validity in regimes where the first-order approximations cease to be valid [23].

Grad's moment method

In the search for a more general method of solution of the transport equation, including, in particular, solutions which are not normal (i.e. not well described by the hydrodynamic variables alone), Grad's method provided a suitable alternative [26]. Instead of expanding f in powers of a small parameter, leading to normal solutions, Grad's method expands it in terms of a basis of tensor Hermite polynomials of the microscopic velocity, the expansion coefficients being the moments of f with respect to the relevant polynomial. The advantage of this method rests on its generality: along with the hydrodynamic variables (ρ, $\mathbf{u}$ and T), it employs higher moments of f which are not collisional invariants, hence termed non-hydrodynamic, and whose balance equations can be derived. Also, the linear, or non-linear *ad hoc* forms for the constitutive equations hitherto mentioned are replaced in this approach by hyperbolic balance equations, and the idea is that using an increasing number of statistical moments of f provides for increasingly higher detail in the description, closer to that of the full transport equation. An expansion on the first thirteen moments, namely ρ, $\mathbf{u}$, T, $\{\sigma_{ij}\}$ and $\{q_i\}$, where the last two are the stress tensor and the heat flux, respectively, and $T \propto \mathrm{tr}\sigma/\rho$ is the temperature, leads to an important generalisation of the Navier-Stokes equations, which includes the balance equations for the fluxes $\{\sigma_{ij}\}$ and $\{q_i\}$. There have been attempts to use the Grad approximation at higher orders than the first thirteen moments, aimed at reproducing transport coefficients depending not only on the frequency, such as in the 13-moment approximation, but on the wavenumber too [29, 30]. Last but not least, Grad's moment method has been an inspiration for the formulation of thermodynamic theories of irreversible processes extending the number of state variables to include non-hydrodynamic, measurable fluxes [27]. Despite the apparent greater generality of Grad's method compared to Chapman and Enskog's, it nonetheless also has drawbacks, namely, the lack of an expansion parameter allowing

for control of the order of the approximation; moreover, transport coefficients obtained from the balance equations are less precise than those provided by a Chapman-Enskog procedure in the regimes where both are comparable [30].

Simplified Boltzmann models

In the foregoing paragraphs I have given a brief overview of the role of kinetic theory in fluid modelling. The Navier-Stokes equations are obtained from the Boltzmann equation at first order of approximation in the Chapman-Enskog method. This implies that the upper bound for the Knudsen number needs to be small enough, and certainly away from that of the transition regime between reversibility and irreversibility. On the other hand, the Boltzmann equation is valid only in the Boltzmann-Grad limit, i.e. for binary, localised collisions, which imposes a lower bound on the collision length and time scales, that is to say, on Kn. These two conditions restrict the range of applicability of the Boltzmann equation in reproducing Navier-Stokes flow.

Transport equations other than Boltzmann's are also available in order to deal with a broader range of systems [31]. An example is the Enskog equation, an extension of Boltzmann equation to dense gases with hard sphere's intermolecular potential [22, 23].

Finding analytical solutions to the full Boltzmann equation is a daunting task. For this reason, it is customary to adopt models for the collision term. Examples are the single relaxation time approximation (or Bhatnagar-Gross-Krook, BGK, model), multiple relaxation time models, Kac's, Carleman's and Broadwell's models [22]. Despite fact that these methods are simpler than the full Boltzmann equation, hence containing less information, their parameters provide a means of mapping their solutions to experimental data. In addition, in modelling phenomena at a given value of the Knudsen number, their algorithmic implementations are also more efficient.

In this thesis, one of the methods employed to model fluid dynamics is the lattice-Boltzmann (LB) method. This can be regarded as a discretisation of the Boltzmann equation, and hence it would be straightforward to think that such a method will inherit the properties of the latter, including the range of validity in Kn number. However, we shall see that, since the LB equation can also be derived from applying the *Stosszahlansatz* to a lattice gas, its validity is not particularly restricted to low densities [32].

The applications that we are concerned about in this thesis are binary immiscible and ternary amphiphilic fluids under creeping, slow flows. We are interested in their dynamics and the formation of structure, i.e., nonhomogeneities of the order parameter. The common denominator in these applications is the existence of different phases in the fluid. Kinetic theoretic methods to this end incorporate phase segregation in the form of repulsive pair potentials [33], which is the way it is incorporated in our LB model.

1.2.2 Mesoscopic models

Fluid dynamical methods in the mesoscopic scale came to light as a way to grasp the relevant thermohydrodynamical behaviour with as little computational effort as possible. This is achieved by evolving a microworld in which the usual vast number of molecular degrees of freedom and characterisation have been drastically reduced, based on the fact that, away enough from critical points, a fluid's macrostate is pretty much insensitive to many of its microscopic properties.

The mesoscopic scale comprises lengths and times which are intermediate between those of the atomistic and the macroscopic worlds. Since it can be defined by the size of a spatial or temporal probing window which is large enough so that statistical trends of the underlying microscopic fields can be extracted upon averaging, the actual size of the mesoscopic scale will depend on the system under scrutiny. Figure 1.4 shows how a scalar quantity measured on a hypothetical system will vary with the size of such a window increasing up to the hydrodynamic scale; different behaviours can be distinguished.

The upper limit of the mesoscale is, however, not set by the aforementioned definition. Depending on the number of statistical moments (of the distribution of the relevant observable) that we might pay attention to, we could obtain a description which is closer to one or the other limit in the scale. This vagueness in the definition of the mesoscale translates into a degree of freedom for the development of theoretical methods of analysis, which has led to a wealth of numerical approches for the study of complex fluids.

The aim of mesoscopic methods is to contract the amount of information needed for a fully atomistic description, aiming at grasping macroscopic behaviour which is insentitive to some of the microscopic details. Since (a) the methods are constrained by what it is experimentally observed, and (b), due to the contraction of information, in many cases it is necessary to introduce parameters in them in an *ad hoc* fashion, most of the methods fall in the category of phenomenological theories, as opposed to microscopic or *ab initio* methods.

There is a clear divide in the approaches taken by mesoscopic methods to date, based upon how close they are to the macroscopic limit to be modelled; I shall refer to them as *top-down* and *bottom-up* approaches. In connection with my mentioning of the number of statistical moments to use in probing the microdynamics, at the beginning of this section, phenomenological approaches ought to be based either on the idea that the microdynamics need to be gradually and explicitly replaced by thermohydrodynamic descriptions as we near the large-scale realm, or that the space of *ad hoc* parameters, introduced in order to coarse-grain microscopic interactions, needs to be mapped onto the large-scale phenomenology.

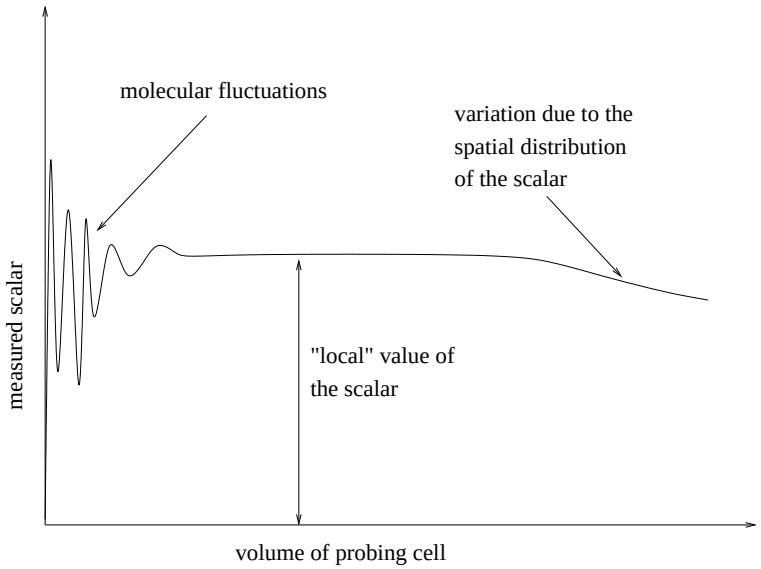

Figure 1.4: Variation of a scalar quantity measured on a hypothetical system by a probing cell of varying size. We assume that time and spatial variations have been smoothed out via averaging. The variation in the measured quantity with cell size is due to various mechanisms acting on different length scales: molecular interactions lead to considerable stochastic effects, and long-wavelength inhomogeneities lead to macroscale variations. In the middle is a 'mesoscale', well defined by a plateau in the plot. Adapted from Boon and Yip [2].

The Ginzburg-Landau theory and *model H*

Top-down approaches to multiphase fluid modelling assume the local equilibrium hypothesis and use a thermodynamic potential accounting for the phase transition between homogeneity and nonhomogeneity, which in a canonical ensemble is the Helmholtz free energy accounting for interfacial energetics and entropy. The method, known as the Ginzburg-Landau theory, is similar to the van der Waals' formulation of liquid-gas transitions [34], and the equilibrium properties of the fluid structure are obtained through numerical minimisation of the thermodynamic potential with relevant constraints. In the case of multiphase fluids where the inhomogeneities arise as a result of the self-assembly of amphiphilic molecules, such as in surfactant-containing fluids or co-polymer melts, the actual expression of the thermodynamic potential is computed from a mesoscopic model of such molecules under a mean-field approximation [35, 36]. As the reader might have realised, Ginzburg-Landau methods do not deserve the classification of mesoscopic since they are at the local thermodynamic level of description, that is to say, only the first-order statistical moments of the underlying microscopic observables are retained and studied at stationarity.

In order to model dynamics, such as phase segregation and self-assembly, the free energy is used to specify the chemical potential in a diffusion equation for the order pa-

rameter. Designed for regimes sufficiently far from criticality, i.e., where the correlation length and hence fluctuations are small, thermal effects are injected as a correction noise term into the diffusion equation. This noise term is what incorporates mesoscopic information in the system, albeit in an *ad hoc* fashion and not as a result of a renormalisation group, consistent coarse-graining procedure, as exemplified in Ref. [37]. The inclusion of hydrodynamics in phase-segregating fluids was carried out by Cahn and Hilliard [38] and termed *Model H* [39], which we present as follows. The model couples an *anti-diffusion* equation

$$\partial_t \phi + g\mathbf{u}\cdot\nabla\phi = M\nabla^2 \frac{\delta F}{\delta \phi} + \theta\,, \tag{1.9}$$

where $\phi = \phi(\mathbf{x}, t) \equiv \rho_{\mathrm{B}} - \rho_{\mathrm{A}}$ is the order parameter (difference between the components' densities), the functional derivative is the local chemical potential of the mixture, $\delta F/\delta\phi = \mu$, M is a phenomenological transport coefficient (the mobility), which serves to tune the interfacial tension, g is a coupling parameter, and θ is a Gaussian white noise source, correlated according to

$$\langle\theta\rangle = 0\,, \tag{1.10}$$

$$\langle\theta(\mathbf{x}, t)\theta(\mathbf{x}', t')\rangle \propto \delta(\mathbf{x}-\mathbf{x}')\delta(t-t')\,, \tag{1.11}$$

where the proportionality coefficient is a normalisation constant. In Eq. (1.9), F is the following free energy functional

$$F[\phi] = \int \mathrm{d}^d x \left\{ \frac{1}{2}(\nabla\phi)^2 + f(\phi) \right\}, \tag{1.12}$$

$$f(\phi) = a\phi^2 + b\phi^4\,. \tag{1.13}$$

Here, d is the space dimensionality, f is the local free energy density, and a and b are scalar functions of the temperature such that there is only one minimum ($\phi = 0$) above the critical temperature, T_{c}, and two symmetric minima ($\phi = \pm\phi_0$) below it; the order parameter becoming non-zero signals the symmetry breaking in the initial homogeneous phase, $\phi = 0$. Equation (1.9) models a purely diffusional phase segregation when $\mathbf{u} = 0$ and $M > 0$; in general, this equation is coupled to the Navier-Stokes momentum balance equation as follows

$$\rho \mathrm{D}_t \mathbf{u} = -\nabla p + \eta\nabla^2\mathbf{u} - \phi\nabla\frac{\delta F}{\delta\phi}\,, \tag{1.14}$$

where the last term of the right hand side accounts for a dissipative force proportional to the gradient of the chemical potential.

Lattice-gas models

The principle of similarity in fluid dynamics states that provided two fluids sharing the same Reynolds number, then, irrespectively of their microscopic differences, their flows

will behave identically. This justifies why wind or water tunnels may indifferently be used for testing low-Mach number flows. In fact, two fluids with quite different microscopic structures can have the same macroscopic behaviour because the form of the macroscopic equations is entirely governed by the microscopic conservation laws and symmetries. These observations, among others, led in 1986 to a novel simulation strategy for fluid dynamics, the lattice-gas automaton [40, 41], based on cellular automata. Cellular automata, first introduced by von Neumann [42], consist of a lattice, each site of which can have a finite number of states (usually coded by Boolean variables); the automaton evolves in discrete time steps, the sites being simultanously updated by a deterministic or nondeterministic rule, and typically, only a finite number of neighbours are involved in the updating of the states [32]. In addition to these features, lattice gases introduce particular constraints, such as mass and momentum conservation and the correct lattice symmetry, so as to recreate a fictitious discrete microworld approximation to that of continuum, 'real' molecular dynamics in a way that fluid dynamics is recovered in the macroscopic limit; in this sense, lattice gases are genuinely bottom-up, mesoscopic models.

The principle of similarity was not the only motivation in the development of lattice gases. It is known that numerical instabilities are a common cause for concern for most algorithms solving continuum fluid equations, especially at high Reynolds numbers. Aside from the intrinsic accuracy of the algorithm, precision is also a major contributing factor. In fact, since floating-point representations favour bits in the most significant places, the algorithm is rendered vulnerable to machine-dependent round-off noise [43].

Following Frisch et al. [32], I now give a general presentation of lattice gases and their hydrodynamics. Consider a D-dimensional regular, Bravais lattice $\mathcal{L}$ in $\mathbf{R}^D$ of finite extension L (eventually, we shall make $L \to \infty$). Assume that each node, $\mathbf{x}_*$, of such a lattice has a coordination number b, i.e., there are b 'velocity' vectors $\mathbf{c}_k$ of the same modulus c linking the node to its nearest neighbours, $\mathbf{x}_* + \mathbf{c}_k$. In addition, for any pair of links $\mathbf{c}_k$ and $\mathbf{c}_l$, there exists an element in the "crystallographic" group $\mathcal{G}$ of isometries which maps $\mathbf{c}_k$ into $\mathbf{c}_l$.

The automaton is constructed by associating to each node a b-bit state $N(\mathbf{x}_*) \equiv \{N_k(\mathbf{x}_*),\, k = 1, \ldots, b\}$, where each N_k is a Boolean variable. The evolution of the lattice, more precisely, the update of the Boolean field $N(.)$, is ruled by two steps, *collision* followed by *propagation*, also called *advection*. Propagation is defined by the spatial translation

$$N_k(\mathbf{x}_*) \leftarrow N_k(\mathbf{x}_* - \mathbf{c}_k)\,, \tag{1.15}$$

where periodical (i.e., wrap-around) boundary conditions are mostly used at the lattice edge, although others such as no-slip (bounce-back) or sliding periodic (Lees-Edwards') can also be implemented; eventually, the particular choice will be irrelevant for the properties of the bulk since hydrodynamics will emerge for $L \to \infty$. The collision step is the

simultaneous application at each node of nondeterministic transition rules from an in-state $\tilde{s} \equiv \{\tilde{s}_k,\, k = 1, \ldots, b\}$ to an out-state $s \equiv \{s_k,\, k = 1, \ldots, b\}$; $\tilde{s}$ and s are particular *assignments* that state $N(\mathbf{x}_*)$ can take on. Each transition is assigned a probability $A(s|\tilde{s}) \geq 0$, normalised to one $\Big(\sum_s A(s|\tilde{s}) = 1, \forall \tilde{s}\Big)$, and depending only on $\tilde{s}$ and s and not on the node. More conditions are imposed on the transition probabilities, namely

- Conservation laws: the only collections of b real numbers a_k such that

$$\sum_k (s_k - \tilde{s}_k) A(s|\tilde{s}) a_k = 0\,, \quad \forall \tilde{s}, s \tag{1.16}$$

  are linear combinations of unity and of the links' cartesian components $c_{k1}, \ldots, c_{kD}$, i.e., only particle number and linear momentum are conserved.

- Invariance under all isometries preserving the velocity set:

$$A\Big(g(s)|g(\tilde{s})\Big) = A(s|\tilde{s})\,, \quad \forall g \in \mathcal{G}\,, \quad \forall \tilde{s}, s\,. \tag{1.17}$$

- Semi-detailed balance:

$$\sum_{\tilde{s}} A(s|\tilde{s}) = 1\,, \quad \forall s\,. \tag{1.18}$$

Note that the stronger, *detailed balance* condition is $A(s|\tilde{s}) = A(\tilde{s}|s)$.

Specific forms of the transition probabilities can be given through examples of lattice-gas models, of which we shall give three. The Hardy-Pomeau-de Pazzis (or HPP) model uses a two-dimensional rectangular lattice, whence $b = 4$. In general, the Boolean representation of a state s is $(s_{b-1}2^{b-1}, \ldots, s_k 2^k, \ldots, s_1 2^1, s_0 2^0)$, where $s_k = 0$ or 1, and $k = 0, \ldots, b-1$ are velocity vectors' labels. In the HPP model, numbering the velocity vectors as non-negative integers (modulo 4) counterclockwise, the collision rules consist in exchanging, at each node, the four-bits states 1010 and 0101 and leaving all the other states unchanged. That is to say, head-on collisions, represented by occupied "input channels" $\{k, k+2\}$ lead to occupied "output channels" $\{k+1, k+3\}$; in brief, HPP simply rotates head-on collisions' incoming velocities by $\pi/2$, which conserves mass (number of particles) and momentum. The crucial property of the HPP lattice gas is the existence of *thermodynamic equilibria*, despite the fact that no ergodic theorem is known for it [43]. These equilibria are factorised over nodes and directions, independent of node position but dependent on direction, and have free *continuous* parameters (the ensemble-averaged mass and momentum). When density and momentum are varied slowly in space and time, emerging macrodynamical equations arise which differ from the Navier-Stokes equations owing to a lack of Galilean invariance and isotropy.

The Frisch-Hasslacher-Pomeau (or FHP) series of models are variants, still in two dimensions, of the HPP model, with a larger invariance group. The lattice is triangular,

hence $b = 6$. The larger group invariance is seen through the fact that head-on collisions are now degenerate: for in-state $\{k, k+3\}$ there are two out-states which conserve mass and momentum, $\{k+1, k+4\}$ and $\{k-1, k-4\}$. Systematically choosing one of the outcomes leads to a *chiral* lattice gas, of broken specular symmetry; a random choice will lead to a nondeterministic lattice gas. The actual random chain needs not be flat-distributed, and, as we shall see in the annexed paper on page 107, will certainly be node-dependent for multiphase models, in disagreement with the definition we put forward here.

The FHP collision rules, as they have been laid out so far, lead to invariants other than just mass and momentum. These so-called *spurious invariants* are the difference of particle numbers in any pair of opposite directions, occurring for head-on collisions. Unless they are removed from the microdynamics, the macrodynamical equations will differ drastically from the Navier-Stokes equations. One way to achieve this is to introduce triple collisions $\{k, k+2, k+4\} \mapsto \{k+1, k+3, k+5\}$. Another way to remove them is to add zero-velocity *rest particles* in binary collisions; at low densities, these remove spurious conservations more efficiently than triple collisions do. There are three versions of the FHP models, named FHP-I, FHP-II and FHP-III, depending on the increasing complexity of their collision rules, respectively. FHP-III contains rest and *spectator* particles, the latter being particles of non-zero velocity which are not affected upon collision.

Finally, as we shall see later, three-dimensional Bravais lattices do not have enough symmetry to guarantee macroscopic isotropy [43]; instead, isotropy is recovered when the underlying lattice is a four-dimensional, face-centred hypercube (FCHC), defined by vectors (x_1, x_2, x_3, x_4) such that their cartesian components are signed integers satisfying that $x_1 + x_2 + x_3 + x_4$ is even. From each node there are velocity vectors of length $c = \sqrt{2}$ linking to $b = 24$ nearest neighbours, two cartesian components of which differing by ± 1. The collision rules should conserve mass and four-momentum whilst avoiding spurious conservations; this can be achieved with just binary collisions, yet there are different strategies [32, 44]. Non-deterministic rules are needed to ensure that the collisions and the lattice have the same invariance group. Three-dimensional fluids are modelled using a projection of the FCHC model called the *pseudo-four-dimensional* or *projected FCHC model*. This is defined as a spatial three-dimensional cubic lattice with an underlying four-dimensional velocity lattice. The way the velocity lattice is embedded into the spatial lattice is by breaking the isotropy of the latter during the advection step: particles with a non-zero fourth component of the velocity, $c_{k4} = \pm 1$, are only allowed to advect to nearest-neighbouring nodes, one lattice unit apart, whereas particles with a null fourth component, $c_{k4} = 0$ are only allowed to advect to the next-nearest nodes, $\sqrt{2}$ lattice units apart. Nodes which are $\sqrt{3}$ lattice units apart do not intervene in advection. This prescription then allows for up to two particles to simultaneously advect to nearest-neighbour sites, whereas there is an exclusion principle for those travelling to the next-nearest sites: there can be

only one. Collision rules are identical to those for the FCHC model, preserving mass and four-momentum. A common notation referring to the spatial dimension, d, of the lattice and the number of velocities, q, on each node is DdQq.

So far we have specified the *microdynamics* of particular lattice-gas models in terms of their collision rules. It is however possible to give a compact representation of it in the form of an equation governing the node's population, $N(\mathbf{x}_*)$ [32]. For brevity's sake, we shall restrict ourselves to the HPP model; expressions for more complex collision rules such as those of the FHP and FCHC models are obtained in a similar fashion and involve many more factors and terms. It can be verified that the right-hand side of the following collision-advection equation is the out-state, expressed using Boolean operations on the in-state at node $\mathbf{x}_*$,

$$\begin{aligned} &N_k(\mathbf{x}_* + \mathbf{c}_k, t+1) = \\ &\Big(N_k \wedge \neg(N_k \wedge N_{k+2} \wedge \neg N_{k+1} \wedge \neg N_{k+3})\Big) \vee \Big(N_{k+1} \wedge N_{k+3} \wedge \neg N_k \wedge \neg N_{k+2}\Big) \end{aligned} \tag{1.19}$$

where the symbols $\wedge$, $\neg$ and $\vee$ stand for AND, NOT and OR, respectively. This equation can be re-arranged in the form $N_k(\mathbf{x}_* + \mathbf{c}_k, t+1) = N_k(\mathbf{x}_*, t) + \Delta_k(N)$, where the collision operator is a mapping of the type $\Delta_k : \ N(\mathbf{x}_*, t) \mapsto 0, \pm 1$. Since Boolean operations can be cast as base-10 operations, the HPP collision term can also be written as

$$\begin{aligned} &\Delta_k(N) = \\ &N_{k+1}N_{k+3}(1-N_k)(1-N_{k+2}) - N_kN_{k+2}(1-N_{k+1})(1-N_{k+3}) \end{aligned} \tag{1.20}$$

It is worth showing that the lattice-gas dynamics is the lattice equivalent of the Louville equation in phase space. For that, let us define the *collision operator* as $\mathcal{C} : N_k(\mathbf{x}_*) \mapsto N_k(\mathbf{x}_*) + \Delta_k(N_k(\mathbf{x}_*))$, the *streaming operator* as $\mathcal{S} : N_k(\mathbf{x}_*) \mapsto N_k(\mathbf{x}_* - \mathbf{c}_k)$, and their composition, $\mathcal{E} \equiv \mathcal{S} \circ \mathcal{C}$, as the automaton's evolution operator. Then we define the *phase space* Γ as the set of all possible assignments $s(.) \equiv \{s\}$ of the Boolean field $N(\mathbf{x}_*)$, at $\mathbf{x}_* \in \mathcal{L}$. We now consider at time $t_* = 0$ an *ensemble* of initial conditions, each endowed with a probability $P\Big(s(.), 0\Big) \geq 0$, such that $\sum_{s(.)\in\Gamma} P\Big(s(.), 0\Big) = 1$. Each element of such an ensemble evolves via the automaton's evolution operator $\mathcal{E}$, whence the time evolution of phase space Γ, i.e., the Liouville equation, can be written as the following equation for the conservation of probability

$$P\Big(s(.), t_* + 1\Big) = P\Big(\mathcal{E}^{-1}s(.), t_*\Big)\,. \tag{1.21}$$

Evidently, we are considering a deterministic automaton which allows for $\mathcal{E}$ to be invertible. An expression for Eq. (1.21) in terms of transition probabilities is readily obtainable for the nondeterministic case.

Keeping the analogy, we can now define a macroscopic quantity or *observable*, $q = q(\mathbf{x}_*, t_*)$, as the *mean value* of a microscopic quantity $Q\Big(s(.)\Big)$ as

$$\Big\langle Q\Big(s(.)\Big)\Big\rangle \equiv \sum_{s(.)\in\Gamma} P\Big(s(.), t_*\Big) Q\Big(s(.)\Big)\,. \tag{1.22}$$

For example, the *particle density*, $n_k(\mathbf{x}_*, t_*)$, which is a quantity evolved by coarse-grained, transport schemes (such as the LB method), specified at a certain point in position, velocity and time space, as we shall see, is defined by Eq. (1.22) with $Q \equiv N$,

$$\Big\langle N_k(\mathbf{x}_*, t_*)\Big\rangle \equiv n_k(\mathbf{x}_*, t_*) = N f_k(\mathbf{x}_*, t_*)\,, \tag{1.23}$$

where N is the total number of particles and f_k is a probability distribution function, not necessarily single-particle, in the new, reduced phase space $\{\mathbf{x}, \xi\}$. Macroscopic variables can be calculated by further averaging *à la* kinetic theory, i.e., as moments of the distribution function: for example, $\rho \equiv m\sum_k n_k$, $\mathbf{j} \equiv m\sum_k \mathbf{c}_k n_k$ and $m\sum_k(\mathbf{c}_k - \mathbf{u})(\mathbf{c}_k - \mathbf{u})n_k$, for the mass, momentum, and flux of momentum densities, respectively, where the latter includes the baricentric or peculiar velocity, $(\mathbf{c}_k - \mathbf{u})$, in terms of the mean or hydrodynamic velocity $\mathbf{u}$, defined through $\mathbf{j} = \rho\mathbf{u}$, and m is the particle mass.

The lattice-Boltzmann approximation

The LB method has an double origin: it is not only an approximation to the continuum Boltzmann equation, but also a coarse-grained lattice-gas microdynamics. In this introduction I shall only elaborate on the former following a derivation after Luo [45]. A derivation from the latter, the lattice-gas cellular automaton, is conceptually analogous to the derivation of the Boltzmann equation from the N-body Liouville equation, and is left at the reader's discretion [32, 46].

For the sake of generality, we consider the Enskog equation [23] as a starting point. The Enskog equation is an *ad hoc* extension of the Boltzmann equation to include the excluded-volume effect present in dense gases. The equation is restricted to identical hard spheres (henceforth of radius σ), which makes the chances of multiple simultaneous encounters negligible. Keeping the notation of Eq. (1.7) regarding pre- and post-collisional velocities, we consider the collision of two of such spheres with velocities ξ and ξ', respectively, being subjected to an external acceleration field $\mathbf{a}$. Letting $\hat{\mathbf{x}}$ be a unit vector pointing from the centre of the 'primed' to that of the 'unprimed' sphere at the instant of contact, and $\mathbf{c}$ be

the relative velocity $\xi' - \xi$, the Enskog equation in absence of external forcing reads

$$\begin{aligned} \mathrm{D}_t f = J[f]\,, \quad \mathrm{D}_t \equiv \partial_t + \xi \cdot \nabla\,, \\ J[f] \equiv \iint \mathrm{d}^2\Omega(\mathbf{c}\cdot\hat{\mathbf{x}})\mathrm{d}^3\xi' \Big\{ \chi(\mathbf{x}+\tfrac{1}{2}\sigma\hat{\mathbf{x}})\tilde{f}(\mathbf{x})\tilde{f}'(\mathbf{x}+\sigma\hat{\mathbf{x}}) \\ -\chi(\mathbf{x}-\tfrac{1}{2}\sigma\hat{\mathbf{x}})f(\mathbf{x})f'(\mathbf{x}-\sigma\hat{\mathbf{x}})\Big\}\,, \end{aligned} \tag{1.24}$$

where g is the radial distribution, and $\mathrm{d}^2\Omega(\mathbf{c}\cdot\hat{\mathbf{x}})$ is a solid angle which is a function of the projection of the relative velocity $\mathbf{c}$ onto the apse line $\hat{\mathbf{x}}$. For the point particles of the Boltzmann equation, such a projection is one; also, whilst the Boltzmann equation assumes the *Stosszahlansatz*, the Enskog equation utilises a different *Ansatz*: a non-zero correlation between the two colliding particles separated by vector $\mathbf{r}$, absorbed entirely by a radial correlation function g, i.e. $F_2(\mathbf{x},\xi,\mathbf{x}+\mathbf{r},\xi') = g(r)ff'$.

It can be shown [45] that the single relaxation time or BGK approximation (see Section 1.2.1) for Eq. (1.24), assuming the fluid to be isothermal and incompressible, is

$$\mathrm{D}_t f = -\frac{g}{\lambda}[f - f^{\mathrm{LM}}] + J'\,, \tag{1.25}$$

where λ is a scalar relaxation time and J' depends on the variables describing the volume exclusion effect, $J' \equiv -f^{\mathrm{LM}}\rho g(\xi-\mathbf{u})\cdot\nabla\ln(\rho^2 g)$; b is the second virial coefficient in the virial expansion of the equation of state. In addition, Eq. (1.25) includes the local Maxwell equilibrium distribution

$$f^{\mathrm{LM}} \equiv \rho(2\pi\Theta)^{-D/2}\exp\Big[-\frac{(\xi-\mathbf{u})^2}{2\Theta}\Big]\,, \tag{1.26}$$

where D is the spatial dimension, and ρ, $\mathbf{u}$ and $\Theta \equiv k_{\mathrm{B}}T/m$ are the mass density, mean velocity and specific thermal energy ($\Theta^{1/2}$ is the thermal velocity), respectively, where k_{B} is the Boltzmann constant and T is the kinetic temperature.

Following Luo [45], a formal solution of Eq. (1.25) can be obtained by integrating along a characteristic streamline ξ over a time interval δ_t,

$$\begin{aligned} f(\mathbf{x}+\xi\delta_t,\,\xi,\,t+\delta_t) &= e^{-\delta_t g/\lambda} f(\mathbf{x},\xi,t) \\ &+ \frac{g}{\lambda} e^{-\delta_t g/\lambda}\int_0^{\delta_t} \mathrm{d}t'\, e^{\delta_t' g/\lambda} f^{\mathrm{LM}}(\mathbf{x}+\xi t',\,\xi,\,t+t') \\ &+ e^{-\delta_t g/\lambda}\int_0^{\delta_t} \mathrm{d}t'\, e^{\delta_t' g/\lambda} J'(\mathbf{x}+\xi t',\,\xi,\,t+t')\,. \end{aligned} \tag{1.27}$$

Assuming that δ_t is small enough and that f^{LM} and f have sufficient smoothness in the kinetic phase space, terms of order $\mathcal{O}(\delta_t^2)$ or smaller can be neglected in the Taylor

expansions of the integrands of last equation. With these approximations, the following BGK-Enskog equation in continuous space and time is obtained [45, 47]

$$\begin{aligned} f(\mathbf{x}+\xi\delta_t,\,\xi,\,t+\delta_t) - f(\mathbf{x},\xi,t) &= -\frac{g}{\tau}[f(\mathbf{x},\xi,t) - f^{\mathrm{LM}}(\mathbf{x},\xi,t)] \\ &+ J'(\mathbf{x},\xi,t)\delta_t\,, \end{aligned} \tag{1.28}$$

where $\tau \equiv \lambda/\delta_t$ is a dimensionless relaxation time. The local Maxwellian Eq. (1.26) can be Taylor-expanded around $\xi = 0$; a good approximation for an isothermal fluid at low Mach number is a second-order expansion in $\mathbf{u}$ [47],

$$\begin{aligned} f^{\mathrm{LM}} \approx f^{(0)} &\equiv \rho\omega(\xi)\Big[1 + \frac{\xi\cdot\mathbf{u}}{\Theta} + \frac{(\xi\cdot\mathbf{u})^2}{2\Theta^2} - \frac{\mathbf{u}^2}{2\Theta}\Big]\,, \\ \omega(\xi) &\equiv (2\pi\Theta)^{-D/2}\exp\Big[\frac{-\xi^2}{2\Theta}\Big]\,. \end{aligned} \tag{1.29}$$

From this equation, the lattice-BGK approximation emerges from the correct discretisation of velocity space. 'Correct' here means choosing the basis of the discrete space such that not only the hydrodynamic variables but the higher moments of the distribution function are preserved *exactly*, i.e. the following quadrature is exact [47]

$$\int \mathrm{d}^3\xi\,\psi(\xi) f(\mathbf{x},\xi,t) = \sum_k W_k \psi(c_k) f(\mathbf{x},\mathbf{c}_k,t)\,, \tag{1.30}$$

where $\psi(\xi)$ is a polynomial of ξ and W_k is the relevant weight coefficient of the quadrature corresponding to microscopic discrete velocity $\mathbf{c}_k$. The existence of this quadrature means that, for example, the hydrodynamic moments can be written as $\rho \equiv mN\sum_k f_k = mN\sum_k f_k^{(0)}$ and $\rho\mathbf{u} \equiv mN\sum_k \mathbf{c}_k f_k = mN\sum_k \mathbf{c}_k f_k^{(0)}$, where $f_k = f_k(\mathbf{x},t) \equiv W_k f(\mathbf{x},\xi_k,t)$ and $f_k^{(0)} = f_k^{(0)}(\mathbf{x},t) \equiv W_k f^{(0)}(\mathbf{x},\xi_k,t)$, both of the same units of $f\mathrm{d}^3\xi$. m is the particle mass and N is the number of particles in the system. The actual values for the weights W_k can be obtained by evaluating the equilibrium expectation value $I \equiv \int \mathrm{d}^3\xi\,\psi(\xi) f^{(0)}$ for a particular discretisation of the velocity space. I is best calculated in polar coordinates, with the measure $\mathrm{d}^3\xi = \xi\mathrm{d}\xi\mathrm{d}\phi$ and the Sonine polynomial form $\psi(\xi) \equiv \psi_{\mathrm{m,n}}(\xi) \equiv \xi^{m+n}\cos^m\phi\sin^n\phi$. In particular, the 9-bit two-dimensional model adopts the following velocity discretisation

$$\mathbf{c}_k \equiv \begin{cases} (0,0) & \text{for } k = 0, \\ (\cos\phi_k, \sin\phi_k)c, \;\; \phi_k = (k-1)\pi/2 & \text{for } k = 1,\ldots,4 \\ (\cos\phi_k, \sin\phi_k)\sqrt{2}c, \;\; \phi_k = (k-5)\pi/2 + \pi/4 & \text{for } k = 5,\ldots,8 \end{cases} \tag{1.31}$$

where $c \equiv \delta_x/\delta_t$ is the "speed of light" and δ_x is the smallest lattice parameter. Note that for an ideal gas, since the equation of state is $p = \rho\Theta$, the specific thermal energy defines the speed of sound, $\Theta = c_{\mathrm{s}}^2$, and, for this model, $c = \sqrt{3}c_{\mathrm{s}}$. This model's lattice geometry leads to the following discretisation for the continuous low-Ma equilibrium, Eq. (1.29),

$$f_k^{(0)} = \rho w_k\Big[1 + \frac{3(\mathbf{c}_k\cdot\mathbf{u})}{c^2} + \frac{9(\mathbf{c}_k\cdot\mathbf{u})^2}{2c^4} - \frac{3\mathbf{u}^2}{2c^2}\Big] \tag{1.32}$$

which is exact only if

$$w_k \equiv \begin{cases} 4/9 & \text{for } k = 0, \\ 1/9 & \text{for } k = 1, \ldots, 4, \\ 1/36 & \text{for } k = 5, \ldots, 8, \end{cases} \tag{1.33}$$

and with the discretised volume-exclusion collision term, $J'_k \equiv -f^{(0)} b\rho g(\mathbf{c}_k - \mathbf{u}) \cdot \nabla \ln(\rho^2 g)$, to the lattice-BGK Enskog equation

$$f_k(\mathbf{x} + \mathbf{c}_k\delta_t,\, t + \delta_t) - f_k(\mathbf{x}, t) = -\frac{g}{\tau}[f_k(\mathbf{x}, t) - f^{(0)}(\mathbf{x}, t)] + J'_k(\mathbf{x}, t)\delta_t \,, \tag{1.34}$$

This equation reduces to the lattice-BGK Boltzmann equation for $b = 0$ and $g \equiv 1$.

Other mesoscopic models: dissipative particle dynamics

Originally introduced by Hoogerbrugge & Koelman in 1992 [48] as a discrete time algorithm, dissipative particle dynamics (DPD) was reinterpreted as the discrete approximation to an underlying continuous-time Langevin dynamics with momentum conservation by Español and Warren in order to guarantee the existence of a Gibbsian equilibrium state [49]. Further developments include the demonstration of detailed balance and an H-theorem for the continuous-time limit [50], an investigation of the equilibrium for discrete time steps [51], the proof of detailed balance and the existence of an H-theorem for interacting multicomponent fluids [52], and a procedure for deriving a coarse-grained DPD model from molecular dynamics [53]. A top-down DPD model has also been put forward by Pagonabarraga and Frenkel [54].

In its "traditional" version, the method evolves a set of point particles via Newtonian dynamics; since each particle represents a mesoscopic portion of fluid, dissipative and random forces are introduced in addition to Newtonian, pairwise additive and conservative forces. The dissipative forces model the viscous drag between the particles, whilst the random forces incorporate thermal effects and are the fingerprint that the particles are mesoscopic entities representing the underlying molecular realm. The DPD equations are the following stochastic differential equations for each particle i,

$$\dot{\mathbf{x}}_i = \mathbf{v}_i \,, \tag{1.35}$$

$$\dot{\mathbf{p}}_i = \sum_{j \neq i} \{\mathbf{F}^{\mathrm{C}}_{ij} + \mathbf{F}^{\mathrm{D}}_{ij} + \mathbf{F}^{\mathrm{R}}_{ij}\} \,, \tag{1.36}$$

where the forces, between particles i and j, all of equal mass, are

$$\mathbf{F}^{\mathrm{C}}_{ij} = -\frac{1}{m}\frac{\partial \phi}{\partial x_{ij}} \,, \tag{1.37}$$

$$\mathbf{F}^{\mathrm{D}}_{ij} = -\gamma \omega_{\mathrm{D}}(x_{ij})\{\mathbf{e}_{ij} \cdot \mathbf{v}_{ij}\}\mathbf{e}_{ij} \,, \tag{1.38}$$

$$\mathbf{F}^{\mathrm{R}}_{ij} = \sigma \omega_{\mathrm{R}}(x_{ij})\mathbf{e}_{ij}\zeta_{ij} \,. \tag{1.39}$$

Here, ϕ is a potential energy, $\mathbf{x}_{ij} \equiv \mathbf{x}_i - \mathbf{x}_j$ is the relative separation vector, $\mathbf{e}_{ij}$ is the unit vector in the direction of $\mathbf{x}_{ij}$ and x_{ij} is its modulus. The functions $\omega_{\mathrm{D}}(x_{ij})$ and $\omega_{\mathrm{R}}(x_{ij})$ are weighting functions which limit the action of the dissipative and random forces to a finite range, whereas the random variable ζ_{ij} is sampled from Gaussian white noise, i.e., such that $\langle \zeta_{ij} \rangle$ and $\langle \zeta_{ij} \zeta_{kl} \rangle = (\delta_{ik}\delta_{jl} + \delta_{il}\delta_{jk})\delta(t - t')$. These forces conserve linear and angular momentum, but not energy.

1.2.3 High-performance computing

From the early studies of fluid dynamics at the time of positivism, through the development of kinetic theory and the observation of Brownian motion, to the more recent use of techniques such as neutron scattering and transmission electron microtomography and the appeararance of discrete and multi-scale models, fluid research has had a long and rich history. Theoreticians have been presented with the increasingly difficult task of extending their models' validity to broader regimes or incorporating in them new experimentally observed phenomenology. Naturally, computer simulations started to play a growing importance in the testing and application of the models.

It would be redundant to recall the vertiginous progress of computer hardware miniaturisation and relevant performance increase during the past few decades. Computer simulations such as the first simulation of a liquid, carried out at Los Alamos in 1953 on MANIAC, one of the most powerful mainframe computers available at the time [55], can be performed nowadays on a laptop personal computer. This availability of computer power has enormously contributed to computer simulations becoming a methodological approach in itself to the study of nature, on an equal footing to analytical theory and experimentation.

Scientific computing interfaces analytical theory and experimentation in providing a tool to (a) solve the equations of analytical theory at scales and regimes comparable to the ones found in experiment, hence allowing for both prediction and feedback into theory, and (b) investigate the behaviour of the underlying mechanisms observed in experiment in order to predict laws. The term *in-silico experimentation* has been appropriately coined to describe the latter role of scientific computing. This role is becoming a complement and sometimes a substitute to analytical theory in explaining the physical world: in fact, the analytical approach breaks down when, due to technical difficulties, the ruling continuum equations cannot be solved analytically or numerically, let alone when the phenomenon under scrutiny cannot be represented in terms of continuum equations. This approach to the modelling of natural phenomena does not use continuum equations; they are rather replaced by discrete equations or *algorithms* which directly model the phenomenon under investigation. In this line of thought, recent and controversial interpretations dare to assert that spacetime is *ultimately* discrete and to extrapolate the application of the algorithmic

approach to all natural phenomena [56].

The advent of readily available computing power to the broad scientific community has made the computational approach operationally feasible. Such an availability has always been linked to the development of new, faster and more miniaturised hardware, and of efficient compilers tailored for such new architectures. The advance of the frontier of high-performance computing, at the renown current pace of doubling performance every two years, transmits the advantage of reducing costs down to existing, less powerful architectures.

The term *high-performance computing* (HPC) implies the use of the so-called massively parallel architectures. These are computers in which the number of processing elements (PEs or processes) can be counted in hundreds and thousands. Each processing element consists of one or more central processing units (CPUs or processors) accessing random access memory (RAM) which can be shared among all the PEs or local to each PE. Each CPU has a small RAM memory called *cache*, aimed at temporarily storing information being managed by the CPU, and its size and its *latency* (time taken by an operation to access the cache from the instant it is issued) are crucial, along with the latencies in accessing buses and RAM. Communication and data buses in these architectures are usually the among fastest the current technology can provide, allowing for the fast exchange of large amounts of information between the CPUs, the RAM and the input/output devices, also of the highest performance available.

As important as processing speed for the execution of scientific algorithms is the availability of compilers specific to the CPU architecture. The CPUs of HPC architectures usually differ from off-the-shelf, personal computers in the type of the instruction set. Personal computers are based on what is called a Complex Instruction Set Computer (CISC): the minimal set of machine-language instructions (*operons*) aimed at moving data between the registers and the Arithmetic-Logic Unit (ALU), and towards the buses, contains a small number of instructions, each representing a macro for smaller level operons. On the other hand, HPC machines are home to CPUs which are purpose-built with a different approach in mind: maximally simplify the complexity of the instruction set in what is called a Reduced Instruction Set Computer (RISC), and translate the burden of producing machine-level code compatible with the new, simpler operons from a high-level, user-friendly programming language entirely to the compiler. In addition, RISC processors incorporate *pipelining*: the execution of operations by the CPU is dictated by a pacemaker, the *clock*; CISC machines take four clock ticks to perform one operation, whereas on a RISC machine four consecutive operations are held in a queue so that one operation is flushed at each clock tick. RISC machines hence show higher performances than CISC machines for similar clock frequencies.

Machine performance in HPC is usually measured by the number of floating point op-

erations that can be executed per second of wallclock time (*flops*). Distinctively, the ALU performs integer arithmetic separately from floating point arithmetic, which is slower. Obviously, the number of flops a HPC machine can reach is associated to the particular code executing those floating point operations, usually a linear algebra package. Sometimes, mistakingly, comparisons of this number between machines are given without specifying the software employed for it.

Instead, high-performance computers are compared by weighing a series of parameters as a whole rather than individually, and ultimately, by benchmarking the software applications of interest on them. Among such parameters are: CPU architecture (chipset, clock frequency, cache size, latency, peak and sustained flops, processor interconnects), bus architecture (structure, latency), random access memory (size per PE, on distributed memory machines, or total size for shared-memory machines), hard-disk (latency, read/write speed), compilers (availability of flags for tailoring to machine-specific features, code bechmarks).

In Table 1.1 we show a list of HPC architectures and their most relevant characteristics, taken from the TOP500 list [57].

RANK	MANUFACTURER, COMPUTER, NO. PES	$R_{\max}$, R_{peak} (in Gflops)	INSTALLATION SITE, COUNTRY, YEAR
1	NEC, Earth Simulator, 5120	35860.0, 40960.0	Earth Simulator Center, Japan, 2002
7	Linux Networx, MCR Linux Cluster Xeon 2.4GHz-Quadrics, 2304	7634.0, 11060.0	Lawrence Livermore National Laboratory, USA, 2002
12	HP, AlphaServer SC ES45 1 GHz, 3016	4463.0, 6032.0	Pittsburgh Supercomputing Center, USA, 2001
15	HP, AlphaServer SC ES45 1 GHz, 2560	3980, 5120	Commisariat à l'Energie Atomique (CEA), France, 2001
16	IBM, pSeries 690 Turbo 1.3 GHz, 1280	3241.0, 6656.0	HPCx, UK, 2002
36	IBM, SP Power3 375 MHz 16 way, 1920	2106, 2880	Atomic Weapons Establishment, UK, 2002
210	Cray Inc., T3E-1200E, 812	671.0, 974.0	CSAR (U. Manchester), UK, 2000

Table 1.1: Some HPC architectures and their most relevant characteristics, as of May 2004, where the field COMPUTER specifies the chipset and its clock frequency, and performance is given by parameters $R_{\max}$ and R_{peak} [57]. Listed in rank 210 is one of the machines used to produce some of the results included in this thesis, now decommisioned.

High-performance computing hosts a range of working methodologies worth mentioning. From the elaboration of an algorithm for the model, the next step is its implementa-

tion in a high-level language, such as FORTRAN90, C or C++. Occasionally, more than one language is chosen in cases that only off-the-shelf libraries already implemented and optimised are available, or certain routines perform better, for one language and not the other. Care needs to be taken in checking for reduction of perfomance in inter-language calls.

The obvious advantage of parallel computing is the decoupling between compute-time and wall-clock time: many processes can concurrently tackle a (properly parallelised) single task and speed up the lengthy serial turn-around times. Hence, implementation demands a parallelisation strategy.

We shall deal here exclusively with the *Single Program Multiple Data* (SPMD) parallel paradigm: a *master* process farms out identical copies of the parallel program to *slave* processes for concurrent execution. The parallelised code contains directives placed at strategic points in the program flow which are executed depending on which PE the copy of the program is running on, i.e. on its *rank*. These directives consist of library calls for exchange of the data stored on the RAM assigned to each PE with other PEs.

Any parallelisation strategy aims at assigning a portion of the system to each PE, in a way such that inter-process communication is minimised since that is a pervasive factor in the reduction of code performance. In this department, there are several possibilities, highly dependent on the specifics of the system to be modelled: domain decomposition, toroidal, etc.

What parallelisation strategy to follow on a serial algorithm is determined by its structure. For example, an Ising model algorithm, which is a cellular automaton with nearest-neighbour, short-range interaction, updates the state of each lattice node at each time step of its evolution towards equilibrium only from its nearest neighbours; therefore, only information from nearest neighbouring cells in memory will needs to be exchanged. Parallel molecular dynamics algorithms, on the contrary, usually tag the atoms and logically group them in clusters, the elements of which need not be spatially close, in order to assign one PE for the computation of the evolution of each one of such clusters; also, interactions are long-ranged, implying that the structure of the inter-process communications can become complex and heavy. Indeed, molecular dynamics suites such as NAMD include a communications library at a higher level of abstraction than, e.g., MPI, for dealing with the complexity of intermolecular interactions [58].

The lattice-Boltzmann algorithm

Since the LB method originated as a coarse grained version of the lattice-gas method, many of the cellular automaton features of the latter are retained in the former [59]. One of them is *locality*, i.e., the state of a lattice site only depend on the state of its nearest neighbours and of itself at the previous time step. Not surprisingly, the adjective ‘embarrasingly

parallel' has been coined for the LB algorithm; clearly, however, more recent variants of it which include long-range interactions are discharged from the embarrassment. Locality leads to a parallelisation strategy which uses a cartesian topology for distributing the state of the lattice sites onto each process' memory, and communicates an amount of information between parallel processes which is much reduced with respect to computational fluid dynamics methods based on the solution of the Navier-Stokes equations. As a result, the algorithm can be optimised such that to sustain an optimal parallel efficiency up to a large number of processors.

Nonetheless the LB method shares features with lattice gases, it is also endowed with some of its own. In fact, the kind of variables needed to hold the state of the system differ between them: lattice gases use integers and lattice Boltzmann method employs floating point numbers. This leads to an important difference: the amount of memory required in both methods. For example, when space and velocity is discretised with a D3Q25 projected-FCHC lattice of N^3 sites, such as is the case in the LB method used in the papers reported in this dissertation, the number of bytes required to store the state of one fluid species in memory is $M \equiv 25bN^3/8$, where b is the number of bits needed to store the state variable per velocity link, i.e., a particle number for lattice gases and a probability density for LB methods. Since lattice-gases are usually designed so that the number of particles per velocity link and species is limited to one, $b = 1$ for them. For LB methods with double-precision arithmetics, $b = 32$ or 64, depending on the platform, which makes M between one and two orders of magnitude higher than for lattice gases. In practice, the lattice-gas update (collision) rule employs a search through a list holding all possible post-collisional states conserving, at least, mass and momentum, which adds an additional and important memory expense over LB methods. However, this expense does not scale with the lattice size, N, as M does, which makes LB methods more memory consuming than lattice gases for large enough lattices.

1.3 The research presented in this thesis

I begin my exposition with the published paper annexed on page 47, summarised on page 41. This aims to treat a paradigm phenomenon in complex fluids' dynamics known as spinodal decomposition employing a three-dimensional Shan-Chen lattice-Boltzmann model for binary fluids. For a number of symmetric mixtures, I study the segregation kinetics.

Once the capabilities and limitations of the lattice-Boltzmann method in modelling phase segregation have been put forth, I present its extension to modelling flow in ternary amphiphilic fluids (two binary immiscible fluids containing amphiphilic molecules) in the two papers included on pages 65 and 73. Therein I investigate the effect of the gradual

addition of amphiphile into a phase-segregating binary fluid, and report the finding, for the first time using a kinetic-theoretic method, of the gyroid cubic mesophase.

The dynamical properties of gyroid mesophases observed in the study just mentioned motivated the first part of a study of their rheology. Its results are included in the paper of page 95. In there, I report on three aspects of shear-induced transitions in mesophases: shear thinning, morphology transitions and stress transients.

The last paper covering the research reported in this dissertation, on page 107, is a study of the role of long-range interparticle interactions in the interfacial properties of a ternary amphiphilic fluid, using a two-dimensional lattice-gas model. We also briefly report on algorithm parallelisation. Long-range interactions are commonplace in amphiphilic self-assembly, and our aim is to lay a first stepping stone in lattice-gas modelling on its role in vesicle morphogenesis. The results found are of relevance to lattice-Boltzmann models in virtue of the similarity of how amphiphile is modelled in both methods.

Chapter 2

Summary of results

In this chapter I provide summaries of each of the papers included in this dissertation.

N. González-Segredo, M. Nekovee and P. V. Coveney, "Three-dimensional lattice-Boltzmann simulations of critical spinodal decomposition in binary immiscible fluids," Phys. Rev. E 67, 046304 (2003). (Annexed on p. 47.)

We use a modified Shan-Chen, noiseless lattice-BGK model for binary immiscible, incompressible, athermal fluids in three dimensions to simulate the coarsening of domains following a deep quench below the spinodal point from a symmetric and homogeneous mixture into a two-phase configuration. The model is derivable from a continuous-time Boltzmann-BGK equation in the presence of an intercomponent body force. We find the average domain size growing with time as t^{γ}, where γ increases in the range $0.545 \pm 0.014 < \gamma < 0.717 \pm 0.002$, consistent with a crossover between diffusive $t^{1/3}$ and hydrodynamic viscous, $t^{1.0}$, behaviour. We find good collapse onto a single scaling function, yet the domain growth exponents differ from others' works' for similar values of the unique characteristic length L_0 and time T_0 that can be constructed out of the fluid's parameters. This rebuts claims of universality for the dynamical scaling hypothesis. For $\mathrm{Re} = 2.7$ and small wavenumbers, q, we also find a $q^2 \leftrightarrow q^4$ crossover in the scaled structure function, which disappears when the dynamical scaling reasonably improves at later stages ($\mathrm{Re} = 37$). This excludes noise as the cause for a q^2 behaviour, as analytically derived from Yeung and proposed by Appert *et al.* and Love *et al.* on the basis of their lattice-gas simulations. We also observe exponential temporal growth of the structure function during the initial

stages of the dynamics and for wavenumbers less than a threshold value, in accordance with the diffusive Cahn-Hilliard Model B. However, this exponential growth is also present in regimes proscribed by that model. There is no evidence that regions of parameter space for which the scheme is numerically stable become unstable as the simulations proceed, in agreement with finite-difference relaxational models and in contradistinction with an unconditionally unstable lattice-BGK free-energy model previously reported. Those numerical instabilities that do arise in this model are the result of large intercomponent forces which turn the equilibrium distribution negative.

N. González-Segredo and P. V. Coveney, "Self-assembly of the gyroid cubic mesophase: lattice-Boltzmann simulations." Europhys. Lett. 65, 795 (2004). (Annexed on p. 65.)

We present the first simulations of the self-assembly kinetics of the gyroid cubic mesophase using a Boltzmann transport method. No macroscopic parameters are included in the model and three-dimensional hydrodynamics is emergent from the microscopic conservation laws. The self-assembly arise from local inter-particle interactions in an initially homogeneous, phase segregating binary fluid with dispersed amphiphile. The mixture evolves in discrete time according to the dynamics of a set of coupled Boltzmann-BGK equations on a lattice. We observe a transient microemulsion phase during self-assembly, the structure function peaks and direct-space imaging unequivocally identifying the gyroid at later times. For larger lattices, highly ordered subdomains are separated by grain boundaries. Relaxation towards the ordered equilibrium structure is very slow compared to the diffusive and microemulsion-assembling transients, the structure function oscillating in time due to a combination of Marangoni effects and long-time-scale defect dynamics.

N. González-Segredo and P. V. Coveney, "Coarsening dynamics of ternary amphiphilic fluids and the self-assembly of the gyroid and sponge mesophases: lattice-Boltzmann simulations." Phys. Rev. E, (in press, 2004). (Annexed on p. 73.)

By means of a three-dimensional amphiphilic lattice-Boltzmann model with short-range interactions for the description of ternary amphiphilic fluids, we study how the phase separation kinetics of a symmetric binary immiscible fluid is altered by the presence of the amphiphilic species. We find that a gradual increase in amphiphile concentration slows down domain growth, initially from algebraic, to logarithmic temporal dependence, and, at higher concentrations, from logarithmic to stretched-exponential form. In

growth-arrested stretched-exponential regimes, at late times we observe the self-assembly of sponge mesophases and gyroid liquid crystalline cubic mesophases, hence confirming that (a) amphiphile-amphiphile interactions need not be long-ranged in order for periodically modulated structures to arise in a dynamics of competing interactions, and (b) a chemically-specific model of the amphiphile is not required for the self-assembly of cubic mesophases, contradicting claims in the literature. We also observe a structural order-disorder transition between sponge and gyroid phases driven by amphiphile concentration alone or, independently, by the amphiphile-amphiphile and the amphiphile-binary fluid coupling parameters. For the growth-arrested mesophases, we also observe temporal oscillations in the structure function at all length scales; most of the wavenumbers show slow decay, and long-term stationarity or growth for the others. We ascribe this behaviour to a combination of complex amphiphile dynamics leading to Marangoni flows.

N. González-Segredo, Jens Harting and Peter V. Coveney, "Stress response and structural transitions in sheared gyroid and lamellar amphiphilic mesophases: lattice-Boltzmann simulations" (Preprint, Centre for Computational Science: London, 2004.) (Annexed on p. 95.)

We report on the stress response of the gyroid cubic mesophase to a steady Couette flow simulated by means of a bottom-up lattice-Boltzmann model for amphiphilic fluids and sliding periodic (Lees-Edwards) boundary conditions. We employ two gyroidal mesophases, the gyroid *per se* (above the sponge-gyroid transition, of high crystallinity) and the molten gyroids (within such a transition, of shorter-range order). These were allowed to self-assemble from a homogeneous mixture of two immiscible fluids with added amphiphile, the longer-range gyroid having 50% higher amphiphile concentration and inter-amphiphile coupling than the molten gyroid. We find that both mesophases exhibit shear thinning, more pronounced and at lower strain rates for the molten gyroid. We also find that, at late times after the onset of shear, the skeleton of the longer-range gyroid becomes a structure of interconnected irregular tubes and toroidal rings, mostly oriented along the velocity ramp imposed by the shear—in contradistinction with free-energy Langevin-diffusion studies finding a much simpler structure of disentangled tubes. We also compare the shear stress and deformation of lamellar mesophases with and without amphiphile in a steady Couette flow applied normally to the lamellae. We find that the presence of amphiphile allows (a) the shear stress at late times to be higher than in the case without amphiphile, and (b) the formation of rich patterns on the shear interface, characterised by alternating regions of high and low curvature.

N. González-Segredo and M. Foster, "pLRME2D: A parallel implementation of a two-dimensional hydrodynamic lattice-gas model with long-range interactions," Proceedings of the Sixth European SGI/Cray MPP Workshop, Manchester, UK (2000). (Annexed on p. 107 and available online,
cf. URL: http://mrccs.man.ac.uk/mpp-workshop6/proc/gonzalez.htm .)

Using a two-dimensional hydrodynamic lattice-gas model for the simulation of binary immiscible and ternary amphiphilic fluids, we investigate the effect of long-range interactions in the surface tension of a planar interface between two immiscible fluids of equal density with and without a layer of surfactant particles lying on it. This is the first stepping stone towards the simulation of the dynamics of fluid vesicles: the surface tension is one of the parameters of some continuum-mechanical descriptions [60] for vesicles, and long-range interactions are believed to be crucial in attaining stability. The parallel implementation of the lattice gas algorithm employs a new communication wrapper providing an object orientated approach to distributed memory programming of n-dimensional grid-based calculations. We find that the surface tension increases with the range of interactions of the immiscible fluid particles but not with that for the surfactant particles. We also find good scalability and minimal impact of the parallelisation strategy on the structure of the base serial code.

Chapter 3

Articles published and in press

Herewith I include copies of papers which have been published and/or accepted for publication in peer-reviewed journals and conference proceedings. These annexes give a detailed account of the research presented in this thesis, summarised in Chapter 2. They are:

- N. González-Segredo, M. Nekovee and P. V. Coveney, "Three-dimensional lattice-Boltzmann simulations of critical spinodal decomposition in binary immiscible fluids," Phys. Rev. E **67**, 046304 (2003). (Annexed on p. 47.)

- N. González-Segredo and P. V. Coveney, "Self-assembly of the gyroid cubic mesophase: lattice-Boltzmann simulations." Europhys. Lett. **65**, 795 (2004). (Annexed on p. 65.)

- N. González-Segredo and P. V. Coveney, "Coarsening dynamics of ternary amphiphilic fluids and the self-assembly of the gyroid and sponge mesophases: lattice-Boltzmann simulations." Phys. Rev. E, (in press, 2004). (Annexed on p. 73.)

PHYSICAL REVIEW E **67**, 046304 (2003)

Three-dimensional lattice-Boltzmann simulations of critical spinodal decomposition in binary immiscible fluids

Nélido González-Segredo*
Centre for Computational Science, Department of Chemistry, University College London, 20 Gordon Street, London WC1H 0AJ, United Kingdom

Maziar Nekovee†
Complexity Research Group, BT Laboratories, Martlesham Heath, Ipswich, Suffolk IP5 3RE, United Kingdom

Peter V. Coveney‡
Centre for Computational Science, Department of Chemistry, University College London, 20 Gordon Street, London WC1H 0AJ, United Kingdom

(Received 28 March 2002; revised manuscript received 28 August 2002; published 21 April 2003)

We use a modified Shan-Chen, noiseless lattice-BGK model for binary immiscible, incompressible, athermal fluids in three dimensions to simulate the coarsening of domains following a deep quench below the spinodal point from a symmetric and homogeneous mixture into a two-phase configuration. The model is derivable from a continuous-time Boltzmann-BGK equation in the presence of an intercomponent body force. We find the average domain size grows with time as t^{γ}, where γ increases in the range $0.545\pm0.014<\gamma<0.717\pm0.002$, consistent with a crossover between diffusive $t^{1/3}$ and hydrodynamic viscous, $t^{1.0}$, behavior. We find good collapse onto a single scaling function, yet the domain growth exponents differ from previous results for similar values of the unique characteristic length L_0 and time T_0 that can be constructed out of the fluid's parameters. This rebuts claims of universality for the dynamical scaling hypothesis. For Re=2.7 and small wave numbers q we also find a $q^2 \leftrightarrow q^4$ crossover in the scaled structure function, which disappears when the dynamical scaling reasonably improves at later stages (Re=37). This excludes noise as the cause for a q^2 behavior, as analytically derived from Yeung and proposed by Appert *et al.* and Love *et al.* on the basis of their lattice-gas simulations. We also observe exponential temporal growth of the structure function during the initial stages of the dynamics and for wave numbers less than a threshold value, in accordance with the diffusive Cahn-Hilliard Model *B*. However, this exponential growth is also present in regimes proscribed by that model. There is no evidence that regions of parameter space for which the scheme is numerically stable become unstable as the simulations proceed, in agreement with finite-difference relaxational models and in contradistinction with an unconditionally unstable lattice-BGK free-energy model previously reported. Those numerical instabilities that do arise in this model are the result of large intercomponent forces which turn the equilibrium distribution negative.

DOI: 10.1103/PhysRevE.67.046304 PACS number(s): 47.55.Kf, 47.11.+j, 83.10.Bb, 05.90.+m

I. INTRODUCTION

Homogeneous binary fluid mixtures segregate into two phases with different compositions when quenched into thermodynamically unstable regions of their phase diagram, a process also called spinodal decomposition. This is achieved by lowering the temperature well below the so called spinodal temperature. For incompressible, 50:50 mixtures, also called critical or symmetric mixtures, these phases form interconnected domains, which at late times produce a bicontinuous structure with sharp, well developed interfaces. For asymmetric mixtures (phases with different densities) there is a phase transition at early times from an interpenetrating "bicontinuous" structure to the so-called "droplet phase," which in turn undergoes subsequent coarsening via coalescence [1]. The composition of a binary immiscible fluid is one of the variables affecting its dynamics. Fields where spinodal decomposition is of industrial relevance comprise the metallurgical, oil, food, paints, and coatings industries. Polymer blends and gels immersed in a solvent are also potentially important applications, where phase separation occurs and needs to be controlled [2,3].

Spinodal decomposition has been extensively studied by experimental [4], analytical [5,6], and numerical [7–16] approaches. The fact that it entails a variety of mechanisms that can act concurrently and at different length and time scales has made it a testbed for complex fluid simulation methods. Among the latter are hydrodynamic lattice gases [17], the lattice Boltzmann equation [18], and dissipative particle dynamics [19].

Despite all the interest attracted by the subject, how the mechanisms responsible for domain separation act remains on unsettled grounds. In particular, the dynamics of the late time, true asymptotic growth is unclear. Also, the dynamical scale invariance hypothesis (to be explained later on in this

*Also at Grup de Física Estadística, Universitat Autònoma de Barcelona, 08193 Bellaterra, Barcelona, Spain. Email address: n.gonzalez-segredo@ucl.ac.uk
†Email address: maziar.nekovee@bt.com
‡Email address: p.v.coveney@ucl.ac.uk

paper), which is treated almost as canonical by analytical and numerical approaches to solving the continuum, local-thermodynamic Cahn-Hilliard equations, has been proven to fail experimentally at least under certain conditions [20].

Numerical studies on spinodal decomposition include methods at the *macroscopic scale*, based on the numerical solution of either the Navier-Stokes [21,22] or the Cahn-Hilliard equations [23,7,24], the *mesoscopic scale*, where lattice-Boltzmann (LB) methods [25,26], lattice gases [9,10], dissipative particle dynamics [27], and Ising [28] approaches are examples, and the *microscopic scale*, with classical molecular dynamics [14].

Fluid dynamical methods in the mesoscopic scale came to light as a way to grasp the relevant thermohydrodynamic behavior with as little computational effort as possible. This is achieved by evolving a microworld in which the usual vast number of molecular degrees of freedom and characterization have been drastically reduced, based on the fact that, far enough from critical points, a fluid's macrostate is largely insensitive to many of its microscopic properties. Some regard the Cahn-Hilliard equations to be within the mesoscopic scale. They derive from the van der Waals' formulation of quasilocal thermodynamics [29], extended by Cahn and Hilliard [23], and aim at solving a Langevin-like diffusion equation for the conserved order parameter. This equation involves a chemical potential derived from a phenomenological, Ginzburg-Landau expansion for the free energy, and leads to phase segregation if the temperature is below a critical value. The scheme commonly used for the study of phase segregation in immiscible fluids is termed Cahn-Hilliard *Model H* [30]; hydrodynamics is included by introducing mass currents, which couple the diffusion equation with the Navier-Stokes equation. Thermal effects are sometimes included in the dynamics by the addition of a noise term satisfying a fluctuation-dissipation theorem.

Cahn-Hilliard equations have been applied to model the segregation dynamics of deep and sudden thermal quenches of fluid mixtures. Such quenches are usually chosen to be sudden to avoid thermal noise effects and set up an initial condition that quickly leads to a state of steep domain walls and where diffusion is negligible compared with hydrodynamic effects, thus leaving the conditions that the dynamical scaling hypothesis requires. However, local equilibrium cannot be guaranteed for a mixture undergoing a sudden quench, which puts the existence of a free energy and the equilibrium states modeled by it on rather shaky grounds.

The lattice-Boltzmann method we use in this work is the Shan-Chen lattice-BGK scheme for binary immiscible and incompressible fluid flow [25]. The equilibrium state for each pure fluid is chosen to be a local isothermal Maxwellian, and Shan and Chen's contribution to the lattice-BGK scheme comes through the phase separation prescription. This is incorporated via intercomponent repulsive mean-field forces between fluid elements (meant to be at a mesoscopic scale) which alter the local equilibrium, rather than through a local equilibrium reproducing a chemical potential derived from a free-energy functional. The Shan-Chen method has been used by Martys and Douglas [31] to qualitatively simulate spinodal decomposition for critical and off-critical quenches in 3D (three dimensions). There have been recent quantitative studies in 2D using this method for critical spinodal decomposition [32,33]. An early study on critical 2D and 3D spinodal decomposition was put forward by Alexander, Chen and Grunau [34] using the lattice-Boltzmann method proposed by Gunstensen *et al.* [35].

Lattice-BGK methods based on a Ginzburg-Landau free-energy functional [26] achieve multiphase behavior by using two separate distribution functions: one for the mass density and one for the order parameter, this being defined as the difference between the phases' densities. Higher-order velocity moments of these distributions are imposed to coincide with thermomechanical quantities obtained from the free energy. The term "top-down" is used in the literature to address this type of approach, whereas we shall use "bottom-up" in the remainder to signify fully mesoscopic methods. Some criticisms of top-down approaches [36] include their frequent lack of Galilean invariance (although Inamuro [37] presented a model that does exhibit this property), and their phenomenological character. Studies of spinodal decomposition using these methods are described in the works of Wagner and Yeomans [12,38], Kendon *et al.* [11], and Cates *et al.* [39].

Numerical instabilities are a great cause for concern in lattice-Boltzmann methods, a study of which will be addressed for the lattice-BGK method we employ in this work. Their sources are two-fold: (a) the finite-difference, discrete-velocity scheme used to solve the BGK-Boltzmann equation prevents the existence of an H theorem, and (b) the approximations used for the equilibrium distribution do not guarantee its positivity, and hence that of the nonequilibrium distribution. Linear stability analyses have been applied to the lattice-BGK model by Sterling [40], and in more detail by Lallemand and Luo [41] comparing a lattice-BGK model to a generalized LB model with a different relaxation time for each physical flux. Qian, d'Humières, and Lallemand [42] gave conditions for the Mach number and the shear viscosity, such that the lattice-BGK scheme produces positive mass densities. New approaches to unconditionally stable lattice-Boltzmann models have recently appeared too [43–46]. They prove the existence of functionals satisfying an H theorem.

Our objective in this work is to present a bottom-up lattice-BGK method for the study of scaling laws in the spinodal decomposition of critical fluid mixtures in three dimensions. This method has certain advantages over lattice-BGK methods based on a free-energy functional, namely, a smaller number of free parameters to tune, Galilean invariance guaranteed, and a simpler equilibrium distribution. Moreover, it refuses to inject macroscopic information into the mesoscopic dynamics as the top-down methods do, on the grounds that for lattice-BGK methods there is no H theorem available that guarantees an unconditional approach to a given equilibrium. Indeed, in the context of general complex fluid applications, an expression for the free-energy itself may be unknown, and/or its validity be questioned for regimes far enough from local equilibrium, making a top down approach not even viable.

The remainder of the paper is structured as follows. In Sec. II we discuss the dynamical scaling hypothesis, which

asserts that after the quench all length scales in the mixture share the same growth law with time. The modified Shan-Chen model we use is explained in Sec. III; Sec. IV introduces the method we use to measure surface tension, while in Sec. V we describe the simulations performed and the growth laws and scaling functions drawn from them, which allow to test the validity of the dynamical scaling hypothesis. Finally, we present our conclusions in Sec. VII.

II. SPINODAL DECOMPOSITION

After domain walls have achieved their thinnest configuration via diffusion, the time evolution of the bicontinuous structure that is produced in the phase segregation process that symmetric mixtures undergo presents geometrical self-similarity to the initial stages of such a process when the structure is viewed at increasing magnification. This leads us to the *dynamical scaling hypothesis*, which states that at late times, when diffusive effects have died out, there is a unique characteristic length scale L which grows with time such that the geometrical structure of domains is (in a statistical sense) independent of time when lengths are scaled by L [47]. This amounts to saying that all length scales have the same time evolution. Such a characteristic length scale must be universal for all fluids with the same shear viscosity η, density ρ, and surface tension σ, provided that no mechanisms are involved in their late stage growth other than viscous dissipation, fluid inertia, and capillary forces, respectively. This is so because, as we shall see later on, only one length scale can be constructed out of the fluid's parameters η, ρ, and σ, these being the only ones present in a hydrodynamic description of the mixture via the Navier-Stokes equations.

The characteristic length scale is usually measured by looking at the first zero crossing of the equal-time pair-correlation function of the order parameter fluctuations [2],

$$C(\mathbf{r},T)\equiv\langle\phi'(\mathbf{x}+\mathbf{r},T)\phi'(\mathbf{x},T)\rangle, \tag{1}$$

where, on the lattice, $\langle\rangle\equiv\Sigma_{\mathbf{x}}\varsigma/V$, V is the spatial volume, ς is the volume of the lattice's unit cell (hence V/ς is the number of nodes in the lattice), T is the time parameter in time steps, $\mathbf{r}$ and $\mathbf{x}$ are spatial vectors, and $\phi'\equiv\phi-\langle\phi\rangle$ are the order parameter fluctuations, where $\phi(\mathbf{x})\equiv\rho^R(\mathbf{x})-\rho^B(\mathbf{x})$ is the order parameter for our binary fluid [say, a mixture of red (R) and blue (B) phases]. The units of $C(\mathbf{r},T)$ are squared mass density. In the remainder, "lattice units" will mean unity for the mass, length, and time units, respectively, in an arbitrary unit system. The Fourier transform of $C(\mathbf{r},T)$, called the structure function, is

$$S(\mathbf{k},T)=\frac{\varsigma}{V}|\phi'_{\mathbf{k}}(T)|^2. \tag{2}$$

The units for the structure function are the same as those for the correlation function, and $\phi'_{\mathbf{k}}$ is the Fourier transform of the fluctuations. Function (2) is volume normalized, and gives no power spectrum for infinite lengths, i.e.,

$$\frac{\varsigma'}{V'}\sum_{\hat{\mathbf{k}}}S(\mathbf{k},T)=1,\quad S(\mathbf{k}=\mathbf{0},T)=0,$$

where ς' is the unit cell volume in reciprocal space, and $V'=(2\pi/L)^3V/\varsigma=(2\pi)^3/\varsigma$ is the reciprocal space volume; in fact, $\varsigma'/V'=\varsigma/V$. Although Eqs. (1) and (2) are numerically equivalent, the intensity of x ray and neutron scattering is directly proportional to the structure function, which is hence easily measurable; it is thus this quantity that we prefer to use to measure the system's characteristic length scales.

We define the (time-dependent) characteristic size L of the domains as

$$L(T)\equiv\frac{2\pi}{k_1(T)}, \tag{3}$$

in lattice units, where $k_1(T)$ is the first moment (mean),

$$k_1(T)\equiv\frac{\sum_k kS(k,T)}{\sum_k S(k,T)}, \tag{4}$$

of the spherically averaged structure function $S(k,T)$, defined by

$$S(k,T)\equiv\frac{\sum_{\hat{\mathbf{k}}}S(\mathbf{k},T)}{\sum_{\hat{\mathbf{k}}}1}, \tag{5}$$

where $\hat{\mathbf{k}}$ indicates the set of wave vectors contained in a spherical shell of thickness one (in reciprocal-space lattice units) centered around $\mathbf{k}$, i.e., such that $n-\frac{1}{2}\leqslant(V^{1/3}/2\pi)k\leqslant n+\frac{1}{2}$, n being an integer. k is the modulus of $\mathbf{k}$ which is smaller than the Nyquist critical frequency $k_c=\pi$ to prevent aliasing. In the limit of short distances and large momenta, scaling arguments lead [47] to the relation

$$S(\mathbf{k},T)\sim\frac{1}{Lk^{D+1}} \tag{6}$$

valid for $kL\gg1$, also known as Porod's law, where D is the spatial dimension. Short distances here means $\xi\ll r\ll L$, where ξ is the interface thickness.

Other measures have also been used for the system's characteristic length scale, namely, the position of the structure function's maximum, and the structure function's second moment, k_2 [2]. We chose to use the first moment k_1 as it is the simplest quantity among the aforementioned. Appert *et al.* [48] found that the structure function's maximum's wave number provided a length evolving similarly, although in a noisier fashion, to that derived from the first moment.

Mathematically, the dynamical scaling hypothesis can be written as

$$C(\mathbf{r},T)=f(r/L), \tag{7}$$

or

$$S(\mathbf{k},T)=L^D g(kL), \tag{8}$$

where $L=L(T)$ is a function of time, and g is the Fourier transform of f, both of which are the same for any late time slice.

Using methods introduced by Kendon *et al.* [11], there are unique length and time units that can be defined from the fluid's density, shear viscosity, and surface tension, ρ, η, and σ, respectively, as follows:

$$L_0 \equiv \frac{\eta^2}{\rho\sigma}, \quad T_0 \equiv \frac{\eta^3}{\rho\sigma^2}. \tag{9}$$

We can think of these as a wavelength and a period associated with the system's fluctuations, respectively, although they do not necessarily have to refer to actual fluctuation averages. We can define the dimensionless variables

$$l \equiv L/L_0, \qquad t \equiv (T-T_{\text{int}})/T_0, \tag{10}$$

which serve to express the universal character of the dynamical scaling hypothesis. Parameter T_{int} is an offset that allows one to account for early time diffusional transients and lattice effects. Due to the finite resolution of the lattice the initial condition is not an infinitely fine-grained thorough mixture ($\phi=0$) but there is a non-negligible domain size measured at time $T=0$. We have then to specify a time origin prior to $T=0$, corresponding to a fictitious zero domain size.

For a critical binary immiscible mixture in three dimensions, scaling arguments applied to the terms of the Cahn-Hilliard Model-H equations show that Eq. (7) holds in the asymptotic limit [47], or, equivalently, that

$$l \propto t^{\gamma}, \tag{11}$$

where $\gamma=1$ and $\gamma=2/3$ for the cases when hydrodynamic viscosity and inertia dominate the dynamics, respectively. From the Cahn-Hilliard Model B, which is a Langevin diffusion equation without noise conserving the order parameter [30], an exponent of $\gamma=1/3$ is derived, identical to that obtained from the Lifshitz-Slyozov theory for the growth of a minority phase whose volume fraction is negligible, and is expected to appear at diffusive stages, before hydrodynamics kicks in. Scaling theories do not give any prediction for the crossovers' positions in time other than that they are "of order unity" [49].

Using a free-energy based, lattice-BGK method, Cates *et al.* [39] reached the viscous regime ($l \propto t$) for $L_0 \approx 5.9$ and $\text{Re}<0.1$, and the inertial regime ($l \propto t^{2/3}$) for $L_0 \approx 0.0003$ and $\text{Re}<350$. The Reynolds number is defined in this domain-coarsening context as

$$\text{Re} \equiv \frac{L}{\nu}\frac{\mathrm{d}L}{\mathrm{dT}} = l\dot{l}, \tag{12}$$

where ν is the kinematic viscosity of the fluid mixture, as defined in the following section, and $\dot{l}$ is the time derivative $\mathrm{d}l/\mathrm{d}t$.

There is also experimental [20] and 2D simulation [12] evidence of breakdown of scale invariance in symmetric binary immiscible quenches. In those experiments, the breakdown of scale invariance occurs [20] for symmetric binary mixtures in confined geometries under the influence of wetting, and a universality has been reported to hold. The process consists of a hydrodynamic coarsening occurring faster than mass diffusion, leaving the system with macroscopic domains whose concentrations are near to but not at the coexisting equilibrium ones. Metastability or instability of the domains then causes a secondary phase separation to kick in via diffusion. Scale invariance and self-similarity have also been recently found to break down for viscoelastic binary fluid mixtures [50]. Finally, there is simulation evidence of breakdown of scale invariance coming from free-energy based, lattice-BGK simulations in 2D. The rationale for this is the coexistence of competing mechanisms at all times in the mixture: diffusion, hydrodynamic modes, and surface tension, giving rise to length scales with different growth exponents [12].

III. OUR LATTICE-BOLTZMANN MODEL

Initially introduced as a coarse grained version of the lattice-gas automaton method for fluid flow simulation, the lattice-Boltzmann model can also be interpreted as a finite difference solver for the Bhatnagar-Gross-Krook (BGK) approximation to the Boltzmann transport equation [18]. From lattice gases it inherits a particulate, mesoscopic character, as their particles can be assimilated to any physical size which is negligible at a hydrodynamic scale; moreover, unlike lattice-gas automata, no fluctuations are present within the scheme [51]. From the simplicity of the Boltzmann-BGK collision term the LB method gains algorithmic efficiency in simulating fluid flow over solving the incompressible Navier-Stokes equations. When extended to multiphase flows, these features are especially valuable in looking at the complicated domain interfaces that arise in the coarsening of binary mixtures.

The method we use is a modification of the multicomponent, immiscible fluid LB scheme of Shan and Chen [25], which will be explained in detail in Sec. III B. The Shan-Chen LB model employs an expansion in Mach number of a Maxwellian equilibrium distribution. Phase-segregating interactions are introduced by means of a self-consistently generated mean-field force between particles. The inclusion of this force gives rise to a nonideal gas equation of state through the Navier-Stokes equation, which is reproduced via the usual multiscale Chapman-Enskog [52] or moment (Grad) [53] expansion of the distribution function. No thermohydrodynamic behavior is imposed on the equilibrium distribution, as aforementioned free-energy based, lattice-BGK methods do [26], partly because none of the lattice-Boltzmann implementations reported in the literature so far exhibit an H theorem ensuring the existence of an asymptote towards a prescribed equilibrium, and partly because a

purely mesoscopic, mean-field approach is preferred here. The coefficients of the equilibrium distribution expansion are determined by the conservation of mass and momentum, the property that Galilean invariance holds, and an isotropic pressure tensor.

In this work we employ a pseudo-four-dimensional lattice, which is the projection onto 3D of the D4Q24 face-centered hypercubic (FCHC), single-speed lattice, where the notation implies the spatial dimension (4) and the number of vectors linking a site to its nearest neighbors (24). The FCHC lattice guarantees isotropic behavior for the macroscopic momentum balance equation [17].

In the following sections we introduce our modified Shan-Chen model, first by looking at a noninteracting mixture of gases, and second including the mean-field force term that gives rise to a nonideal gas equation of state. Then, we modify the collision term such that the Shan-Chen scheme is consistent with that derived from a Boltzmann-BGK equation in the presence of a force.

A. Mixture of ideal gases

The finite-difference, finite-velocity fully-Lagrangian [40] scheme for the numerical solution of the multicomponent Boltzmann equation,

$$n_k^\alpha(\mathbf{x}+\mathbf{c}_k,t+1)-n_k^\alpha(\mathbf{x},t)=\Omega_k^\alpha, \tag{13}$$

governs the time evolution of the kth velocity's particle number density n_k^α for the fluid species α in a noninteracting mixture of gases. The lattice-BGK collision term is

$$\Omega_k^\alpha(\mathbf{x},t)\equiv-\frac{n_k^\alpha(\mathbf{x},t)-n_k^{\alpha(\mathrm{eq})}(\mathbf{x},t)}{\tau^\alpha}, \tag{14}$$

where the time increment and lattice spacing are both unity, $\mathbf{c}_k$ is one of the 24 discrete velocity vectors plus one null velocity, $\mathbf{x}$ is a point of the underlying Bravais lattice, and $\alpha=R,B$ [e.g., oil (R) or water (B)]. The parameter τ^α defines a single relaxation rate towards equilibrium for component α. The function $n_k^{\alpha(\mathrm{eq})}(\mathbf{x},t)$ is the discretisation of a third-order expansion in Mach number of a local Maxwellian [54],

$$n_k^{\alpha(\mathrm{eq})}(\mathbf{x},t)=\omega_k n^\alpha(\mathbf{x},t)\left[1+\frac{1}{c_s^2}\mathbf{c}_k\cdot\mathbf{u}+\frac{1}{2c_s^4}(\mathbf{c}_k\cdot\mathbf{u})^2-\frac{1}{2c_s^2}u^2+\frac{1}{6c_s^6}(\mathbf{c}_k\cdot\mathbf{u})^3-\frac{1}{2c_s^4}u^2(\mathbf{c}_k\cdot\mathbf{u})\right], \tag{15}$$

where ω_k are the coefficients resulting from the velocity space discretisation, and c_s is the speed of sound, both of which are determined by the choice of the lattice. For the projected-D4Q24 lattice we use, the speed of sound is $c_s=1/\sqrt{3}$, and $\omega_k=1/3$ for the speed $c_k=0$ and 1/36 for speeds $c_k=1,\sqrt{2}$ [42]. (The projection from 4D to 3D puts an additional speed into play, $\sqrt{2}$.) In Eq. (15), $\mathbf{u}$ is the macroscopic velocity of the mixture, through which the collision term couples the different velocities $\mathbf{c}_k$, and is a function of $\mathbf{x}$ and t. Also, $n^\alpha(\mathbf{x},t)$ is the local particle density for the αth component, defined as $\Sigma_k n_k^\alpha(\mathbf{x},t)$.

The judicious choice of the coefficients in the expansion of the equilibrium distribution (15) allows for mass and momentum to be conserved,

$$\sum_k \Omega_k^\alpha=0,\quad \sum_\alpha m_\alpha\sum_k \mathbf{c}_k\Omega_k^\alpha=0. \tag{16}$$

Momentum conservation requires the fluid's macroscopic velocity $\mathbf{u}$ to be defined in terms of the macroscopic velocity $\mathbf{u}^\alpha$ for component α,

$$n^\alpha(\mathbf{x},t)\mathbf{u}^\alpha\equiv\sum_k n_k^\alpha(\mathbf{x},t)\mathbf{c}_k, \tag{17}$$

as the solution of the three equations

$$\Xi(\mathbf{u})=\mathbf{v}, \tag{18}$$

where

$$\Xi_i(\mathbf{u})\equiv(2-3u^2)u_i+3u_i^3+3u_iu_{i+1}^2+3u_iu_{i+2}^2, \tag{19}$$

with the Cartesian index i ranging in the $i$mod3 set, and $\mathbf{v}$ being defined as the special average,

$$\mathbf{v}\equiv\sum_\alpha\frac{\rho^\alpha\mathbf{u}^\alpha}{\tau^\alpha}\Big/\sum_\alpha\frac{\rho^\alpha}{\tau^\alpha}. \tag{20}$$

Based on previous experience with lower orders, our choice of a third-order Taylor expansion in Mach number for the Maxwellian equilibrium distribution is an attempt to improve the approximation for velocities which, within the incompressibility limit, are large enough to make either the distribution function become negative or the error in the expansion too large.

B. Mixture of interacting, nonideal gases

In order to deal with nonideal gases, in particular, fluid mixtures whose volume elements interact among themselves, each fluid is forced to relax to a local equilibrium which is modified by the presence of its surrounding volume elements. The mean-field force density felt by phase α at site $\mathbf{x}$ and time t from its surroundings is defined as

$$\mathbf{F}^\alpha(\mathbf{x},t)\equiv-\psi^\alpha(\mathbf{x},t)\sum_{\bar\alpha}g_{\alpha\bar\alpha}\sum_{\mathbf{x}'}\psi^{\bar\alpha}(\mathbf{x}',t)(\mathbf{x}'-\mathbf{x}), \tag{21}$$

where $g_{\alpha\bar\alpha}$ (>0 for immiscible fluids) is a coupling matrix whose nondiagonal elements control interfacial tension, and ψ^α is the so-called *effective mass*, which serves as a functional parameter and can have a general form for modeling various types of fluids. For simplicity in our implementation, we have chosen $\psi^\alpha(\mathbf{x},t)\equiv n^\alpha(\mathbf{x},t)$ [32] and only allowed nearest-neighbor interactions, $\mathbf{x}'\equiv\mathbf{x}+\mathbf{c}_k$. Other choices for ψ have also been made [25].

Shan and Chen [25] incorporated the above force term in the collision substep of the LB dynamics by adding the increment

$$\Delta\mathbf{u}^{\alpha}\equiv\frac{\mathbf{F}^{\alpha}}{\rho^{\alpha}}\tau^{\alpha} \tag{22}$$

to the velocity $\mathbf{u}$ that enters the second-order expansion of the equilibrium distribution function. We perform the same procedure for our third-order expansion (15), obtaining additional terms

$$\begin{aligned} n_k^{\alpha(\mathrm{eq})}(\mathbf{u}+\Delta\mathbf{u}^{\alpha}) &= n_k^{\alpha(\mathrm{eq})}(\mathbf{u}) \\ &+\omega_k n^{\alpha}\left[\frac{\mathbf{c}_k-\mathbf{u}}{c_s^2}+\frac{(2\mathbf{c}_k\cdot\mathbf{u}-u^2)}{2c_s^4}\mathbf{c}_k\right]\cdot\mathbf{a}^{\alpha}\tau^{\alpha} \\ &+\frac{1}{2}\omega_k n^{\alpha}\left[\frac{\mathbf{a}^{\alpha}\cdot\mathbf{a}^{\alpha}}{c_s^2}-\frac{(\mathbf{c}_k\cdot\mathbf{a}^{\alpha})^2}{c_s^4}\right. \\ &\left.+\frac{(\mathbf{c}_k\cdot\mathbf{u})(\mathbf{c}_k\cdot\mathbf{a}^{\alpha})^2}{c_s^6}\right](\tau^{\alpha})^2 \\ &+\frac{1}{6c_s^6}\omega_k n^{\alpha}(\mathbf{c}_k\cdot\mathbf{a}^{\alpha}\tau^{\alpha})^3, \end{aligned} \tag{23}$$

where $\mathbf{a}^{\alpha}\equiv\mathbf{F}^{\alpha}/\rho^{\alpha}$.

Luo [36] and Martys, Shan, and Chen [55] expanded both the velocity space gradient in the BGK-Boltzmann equation force term,

$$\mathbf{a}\cdot\nabla_{\xi}n, \tag{24}$$

and the equilibrium distribution in Hermite polynomials in the lattice velocities. Then they rearranged the acceleration $\mathbf{a}$ such that it explicitly modifies the macroscopic velocity in the equilibrium distribution, leaving a term linear in $\mathbf{a}$. If only linear terms were to appear in Eq. (23), the Shan-Chen prescription for an interparticle force would then coincide with the way it is included in the continuum BGK-Boltzmann equation, as pointed out by Luo and Martys *et al.* To this end, following Nekovee *et al.* [32], we simply drop from Eq. (23) any term nonlinear in the acceleration $\mathbf{a}$. We thus obtain a modified Shan-Chen collision term, which is why our model is termed modified Shan-Chen. The modified Shan-Chen collision term is

$$\Omega_k'^{\alpha}\equiv\Omega_k^{\alpha}+\sum_{\bar{\alpha}}\sum_{l}\Lambda_{kl}^{\alpha\bar{\alpha}}n_l^{\bar{\alpha}}, \tag{25}$$

where

$$\Lambda_{kl}^{\alpha\bar{\alpha}}=\omega_k\left[\frac{1}{c_s^2}(\delta_{\alpha\bar{\alpha}}\mathbf{c}_k-\zeta_{\alpha\bar{\alpha}}\mathbf{c}_l)+\zeta_{\alpha\bar{\alpha}}\frac{\mathbf{c}_k\cdot\mathbf{c}_l}{c_s^4}\mathbf{c}_k\right]\cdot\mathbf{a}^{\alpha}\tau^{\alpha} \tag{26}$$

and

$$\zeta_{\alpha\bar{\alpha}}=\frac{n^{\alpha}}{n^{\bar{\alpha}}}\frac{\rho^{\bar{\alpha}}}{\tau^{\bar{\alpha}}}\Big/\sum_{\bar{\alpha}}\frac{\rho^{\bar{\alpha}}}{\tau^{\bar{\alpha}}}, \tag{27}$$

where we have made use of the condition Eq. (29) below. The second term arising in Eq. (25) accounts for interparticle interactions other than the binary collisions implicit in the Boltzmann collision term, Ω [56]. This includes a collision operator $\Lambda_{kl}^{\alpha\bar{\alpha}}$ resulting from mean-field interactions among different fluid components [32], which gives rise to phase separation for immiscible multicomponent systems.

The inclusion of a mean-field force in the Shan-Chen model leads to the breakdown of the local momentum conservation that holds for noninteracting ideal gases, cf. Sec. III A. However, the forces felt by neighboring portions of fluid follow an action-reaction mechanism that leads to global momentum conservation (i.e., over the whole lattice). This was numerically confirmed for our third-order-equilibrium, modified Shan-Chen model too.

It can be shown that the condition for momentum conservation in the absence of interactions, Eq. (18), leads to that needed when using a second-order expansion of the equilibrium distribution, namely

$$\mathbf{u}=\mathbf{v}, \tag{28}$$

only in the limit of creeping flows to second order, i.e.,

$$u^2\approx 0. \tag{29}$$

We therefore implemented the computation of the velocity according to Eq. (28) rather than Eq. (18). The condition Eq. (29) is satisfied, as global momentum would not be conserved otherwise. In addition, we confirmed in our simulations that the fluid velocity was kept under 28% of the speed of sound by 67% of the lattice nodes. This means squared Mach numbers under 0.08. This purports to show that the expansion to third order, implemented in this model to extend the parameter space for which the equilibrium distribution remains positive, for momentum conservation at least adds very little.

In our LB model, the kinematic viscosity of the mixture is given by

$$\nu=\frac{\eta}{\rho}=c_s^{-2}\left(\sum_{\alpha}x_{\alpha}\tau_{\alpha}-\frac{1}{2}\right), \tag{30}$$

where $c_s^{-2}=3$ for our lattice, τ_{α} is the relaxation time of the αth component and x_{α} is its mass concentration defined as ρ_{α}/ρ [25]. For a region of pure αth component

$$\nu=\frac{1}{3}\left(\tau-\frac{1}{2}\right), \tag{31}$$

which also holds for our case of a 50:50 mixture, for which

$$\sum_{\alpha} x_{\alpha}\tau^{\alpha}=\tau\sum_{\alpha} x_{\alpha}=\tau \tag{32}$$

since all relaxation times are the same.

IV. THE SURFACE TENSION

The surface tension σ arises as an emergent effect due to intercomponent interactions. It is calculated by measuring the components of the pressure tensor $\mathsf{P}=\{P_{ij}\}$ across a planar interface perpendicular to the z-axis through the formula

$$\sigma=\int_{-\infty}^{+\infty}[P_{zz}(z)-P_{xx}(z)]\mathrm{d}z, \tag{33}$$

where P_{ij} is the flux of the ith component of the momentum across a surface perpendicular to the jth cartesian axis. This pressure tensor, consistent with the force Eq. (21), is

$$\mathsf{P}(\mathbf{x})=\sum_{\alpha}\sum_{k}\rho_{k}^{\alpha}(\mathbf{x})\mathbf{c}_{k}\mathbf{c}_{k}+\frac{1}{4}\sum_{\alpha,\bar{\alpha}}g_{\alpha\bar{\alpha}}\sum_{\mathbf{x}'}[\psi^{\alpha}(\mathbf{x})\psi^{\bar{\alpha}}(\mathbf{x}')+\psi^{\bar{\alpha}}(\mathbf{x})\psi^{\alpha}(\mathbf{x}')](\mathbf{x}-\mathbf{x}')(\mathbf{x}-\mathbf{x}'), \tag{34}$$

with $\mathbf{x}'\equiv\mathbf{x}+\mathbf{c}_k$ in this study. This leads to the same expression for the scalar pressure as that in the momentum balance equation obtained by multiplying the LB equation (13) using the collision term Eq. (25) by $\mathbf{c}_k$ and summing over k. Here, $\rho_k^{\alpha}(\mathbf{x})$ is the mass density of species α with velocity $\mathbf{c}_k$ at the site $\mathbf{x}$. Equation (34) contains a *kinetic term* due to the free streaming of particles corresponding to an ideal gas contribution, plus a *potential* or *virial term* due to the momentum transfer among particles of equal and distinct color, through the interparticle force [52].

As previously noted, the surface tension in the modified Shan-Chen model is an emergent, hence not directly tunable quantity, in contradistinction to the situation with free-energy based lattice-Boltzmann models. It depends on the density ρ, the coupling g, and the relaxation time τ, and has to be determined by simulation. We computed its dependence on these parameters to be as follows:

$$\frac{\partial\sigma}{\partial\rho}>0,\quad \frac{\partial\sigma}{\partial g}>0,\quad \frac{\partial\sigma}{\partial\tau}<0. \tag{35}$$

This behavior is useful when steering through the parameter space in search of specific values of L_0 and T_0. Numerical results on the surface tension are reported in the following section.

V. SIMULATIONS

We restrict ourselves to critical (50:50) mixtures, which are the type of configurations leading to a spinodal decomposition process as opposed to nucleation. Experimentally, spinodal decomposition is characterized by long-wavelength, infinitesimal density perturbations which are unstable after the quench, hence favoring the segregation, whereas nucleation generally presents short wavelength, finite perturbations, and metastability is not uncommon. Nucleation is hence a more complex phenomenon which is usually considered after an initial study in spinodal decomposition has been performed.

TABLE I. Model parameters studied, including the surface tension $\sigma(\rho,\tau,g)$ measured for a planar interface on a $4\times4\times128$ lattice, and the characteristic length L_0 and time T_0 for each parameter set. The existence of the latter two is based on the validity of the dynamical scaling hypothesis, and that diffusive currents are negligible with respect to hydrodynamic currents and capillary forces.

Parameter set	ρ	τ	g	$\sigma(\rho,\tau,g)$	$L_0(\rho,\tau,g)$	$T_0(\rho,\tau,g)$
I	0.8	2.000	0.06	0.002 059	97.1	18 870
II	0.8	1.500	0.06	0.004 777	18.6	1038.8
III	0.8	1.000	0.06	0.010 292	2.16	28.0
IV	0.8	0.625	0.05	0.017 458	0.0796	0.152

We aim at reproducing the early time diffusive and later time viscous and inertial regimes predicted by carrying out scaling analyses on the Cahn-Hilliard Model-H equations [2,47]. Growth laws predicted for those are $l\propto t^{1/3}$, $l\propto t$, and $l\propto t^{2/3}$, respectively. Under the assumptions of the dynamical scaling hypothesis made in the introduction, those regimes are uniquely characterized by the length and time

$$L_0=\frac{\rho}{9\sigma(\rho,\tau,g)}\left(\tau-\frac{1}{2}\right)^2,\quad T_0=\frac{\rho^2}{27[\sigma(\rho,\tau,g)]^2}\left(\tau-\frac{1}{2}\right)^3, \tag{36}$$

obtained by inserting Eq. (31) into Eq. (9).

Having in mind keeping simulation time at a minimum, the values of ρ, τ, and g must be such as to allow the fluids to be immiscible and approach equilibrium quickly whilst ensuring numerical stability and positive shear viscosity. This amounts to keeping ρ as high as possible, τ close to 1/2, and g as large as allowed by the onset of numerical instabilities which set in when the forcing term is too large. A large g allows for the early time transient, dominated by diffusion, to be of short duration. Finally, seeking the diffusive regime means looking at very early times, which is attained for large values of T_0. Conversely, the hydrodynamic inertial behavior requires as small values of T_0 as possible.

In Table I we present the parameters selected in this study, along with the measured surface tension. We also include the length and time scales associated with them, which are used to compute dimensionless lengths and times in the model.

The initial condition used for all the simulations was a thorough mixture of the two phases, with randomly distributed fluctuations. To realize this, each velocity direction k at each lattice site was populated with one density $\rho_k^{\alpha}(\mathbf{x},t)\equiv m^{\alpha}n_k^{\alpha}(\mathbf{x},t)$ for each species $\alpha=R,B$ as a white-noise, pseudorandom floating point number between 0.0 and 0.8, where m^{α} are the particle masses, all set to unity. Note that the density ρ in Table I is defined as the lattice average

$$\rho\equiv\langle\rho^{\mathrm{R}}(\mathbf{x},t)+\rho^{\mathrm{B}}(\mathbf{x},t)\rangle, \tag{37}$$

where $\rho^{\alpha}(\mathbf{x},t)\equiv\Sigma_k\rho_k^{\alpha}(\mathbf{x},t)$, and due to the critical composition we use, amounts to the maximum value of either of the summands.

Lattice sizes used were 128^3 and then 256^3 to check for finite size effects. Simulations for 128^3 systems were run for 700 or 1400 time steps, and for 200 or 250 time steps for 256^3 systems, depending on the parameter set. Following prescription of Kendon *et al.* to keep finite size effects at bay [11], we neglected domain sizes larger than a quarter of the lattice side size. There is no reason *a priori* to choose this particular threshold. As we shall see, this allows the generation of a domain size range broad enough for data acquisition; furthermore, finite size effects were quantified by using the two aforementioned lattice sizes.

Surface tension was measured on $4\times4\times128$ and $16\times16\times128$ lattices, allowing plenty of room along the nonisotropic direction z for the fluid's physical quantitites to achieve values characteristic of the bulk before being affected by the second interface with periodic boundary conditions imposed. We found that the surface tension did not vary by more than 1% when the length along the z direction was doubled, which is the only direction where we would expect any variation as translational symmetry is broken.

To compute the average domain size, Eq. (3), we perform discrete Fourier transforms. The sampling theorem [57] warns us to ensure that our fluid mixture does not exhibit spatial frequencies larger than the Nyquist critical frequency f_c, defined as half the sampling frequency. This is not being the case, the power spectrum in the interval $[0,f_c]$ is altered by frequencies larger than f_c as a result of aliasing. Because the sampling frequency on the lattice is one, the maximum frequency any relevant quantity of our fluid mixture is allowed to have according to the sampling theorem is 1/2, i.e., of wavelength two. This means that any spatial variation is bound to happen between two contiguous lattice sites, which is something we already knew: the resolution of the lattice is finite and dictated by the lattice size. We used the FFT routine rlft3() for real, 3D data sets [57].

Calculation of the reduced time t requires an assessment of T_{int}. T_{int} serves to redefine the time such that the domains have zero size at the time origin, which is not the case in the actual simulations. Depending on the regime reached by the parameter set employed, domains may start to grow immediately after time step zero, completely avoiding the diffusive stage.

We assess T_{int} in the following way. We first compute the intersection with the abscissae of a linear fit interpolating all data starting after the initial purely diffusive transient is completed, that is, for which interfaces are thin enough and $L(T)$ just starts to grow. The intercept is used as an initial guess for a_1 in a Levenberg-Marquardt nonlinear least-squares fit of the form

$$y=a_0(x-a_1)^{a_2}. \tag{38}$$

Once T_{int} is computed, and the data sets are normalized by L_0 and T_0, hence becoming (t,l) data pairs, we perform fits to the function Eq. (38) to determine the growth exponent a_2. Initial guesses for the fitting coefficients are $a_0^0=1.0$, $a_1^0=0.1$, and $a_2^0=1.0$. The tolerance for these fits was set to 10^{-5}, this being defined as the unsigned increment of χ^2 between two consecutive iterations, divided by the number of degrees of freedom.

Uncertainties in parameters are also taken care of. Because standard errors $\{\Delta_k S\}$ are incurred in the structure function spherical averaging (5), these transmit down to L and l, and to t through the determination of T_{int}. In this study, however, errors in the abcissae are disregarded as they do not depend on time, and therefore represent equal weights for data points in the least-squares functional to minimize.

We performed the simulations using a number of processors ranging from 32 to 128 on a Cray T3E-1200E and on SGI Origin2000 and Origin3800 supercomputers. The code is an implementation in Fortran90 using the message passing interface (MPI) as parallelization protocol, and it shows scaling with the number of processors between 50% to 90% of linearity on the Cray T3E platform [58] up to 64 PEs, and better behavior on SGI Origin platforms. CPU times used up to run a 128^3 lattice for 1400 time steps, or a 256^3 lattice for 250 time steps, took up to 6 h per parallel process.

An important issue in dealing with the lattice sizes employed here is to have access to massive disk storage. For our largest lattices, 1.9 Gbytes of measurements were dumped onto disk at each measurement time step. A lattice of 256^3 sites run for 700 time steps, measuring every 25, requires 40 Gbytes to store the order parameter, the density fields for each phase, momenta, and checkpoint files, the latter being needed if we wish to restart the simulation at the point where it stops. To that we need to add some additional working space for converting the dumped binary data into machine-portable XDR format [59]. For this work we required 200 Gbytes on disk, plus tape storage to free up space when required. XDR files were visualized using the commercial package AVS [60].

It is worth noting that our results did not undergo a process of lattice size reduction, in the sense of averaging over nearest-neighboring sites in order to deal with limited computational resources, as was done in previous studies on 3D spinodal decomposition [49,61]. Hence, we benefitted from measuring and visualizing all data output from our simulations. Current limitations in computing resources prevented us from simulating lattices of 512^3 or 1024^3 sizes, which would otherwise be desirable in order to decrease the fluid's minimum Knudsen number, helpful in reaching the thermohydrodynamic limit as a multiscale Chapman-Enskog expansion procedure shows. However, this situation is bound to change soon with the advent of terascale computing capabilities (see http://www.RealityGrid.org).

A. Growth exponents

Figure 1 shows the average domain size in lattice units as obtained straight from the simulations, for all parameter sets (cf. Table I). Reynolds numbers achieved for each of these are Re=0.18, 0.49, 2.7, and 37. For parameter set I, we can see that after a transient during which there is a rapid mass convection to nearest neighbors, domain growth flattens out and starts growing at about $T=400$. We will look at this in

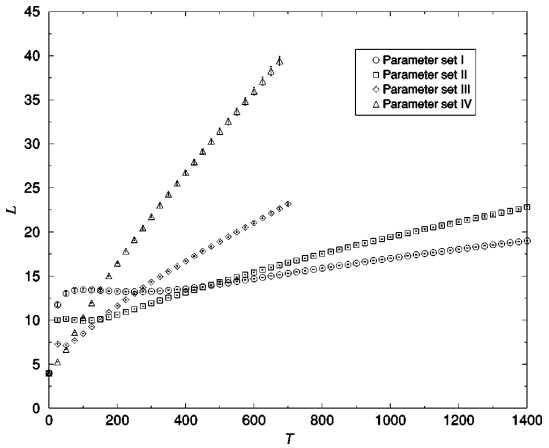

FIG. 1. Evolution of the average domain size for parameter sets I, II, III, and IV (cf. Table I) with the time step. Error bars are included and represent the uncertainty transmitted from the standard error of the structure function spherical average. Lattice size is 128^3. All quantities are reported in lattice units.

further detail; for now it can be seen that the breadth of the plateau decreases with the Reynolds number. Finally in Fig. 2 we show the same curves after rescaled to L_0 and T_0, in reduced units.

Fits to the model $y=a_0(x-a_1)^{a_2}$ for Fig. 2 are given in Table II, and they proved to be quite sensitive to the number of points fitted. Domain growth shows an increasing segregation speed, $t^{0.545}$, $t^{0.593}$, $t^{0.623}$, and $t^{0.717}$, with increasing Reynolds number. These data sets correspond to characteristic lengths and times in the ranges $0.0796<L_0<97.1$ and $0.152<T_0<18\,870$. These contain the values for which Kendon *et al.* [11] observed a viscous linear exponent, $L_0=5.9$ and $T_0=71$. This, therefore, invalidates the universality of

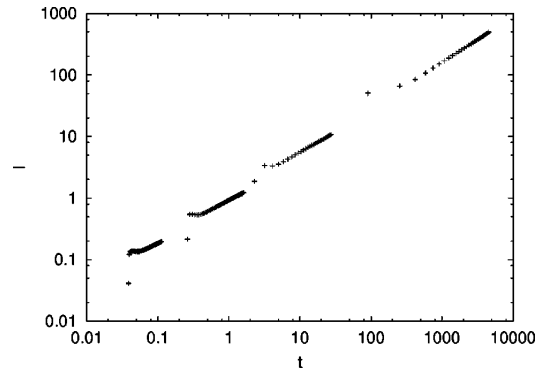

FIG. 2. Log-log plot of reduced length versus reduced time for the 128^3-lattice data sets. Error bars are included. The four data sets correspond to parameter sets I, II, III, and IV (cf. Table I), from left to right. Viewed from a grazing angle, one can see that a simple, algebraic interpolating curve is not truly obtainable here. The first few points of each set correspond to diffusive, zero-growth stages. The units on both axes are dimensionless.

the dynamical scaling hypothesis.

By looking at Fig. 2 from a grazing angle one can easily see that a simple, algebraic interpolating curve is not obtainable here. Kendon *et al.* [11,49] and Pagonabarraga, Wagner, and Cates [15,62] used a method to improve this curve. They left $T_{\rm int}$ as an adjustable fitting parameter such that there is a reasonable collapse onto a simple, single algebraic curve for all parameter sets simulated; from this they obtained a window of $T_{\rm int}$ in which collapse is reasonable. Then they checked whether the different values for $T_{\rm int}$ from each individual parameter set lay within such a window. Quoting Kendon *et al.* (cf. Sec. IX C in Ref. [49]), "although this [procedure] is capable of falsifying the scaling hypothesis [$\cdots$], its nonfalsification [$\cdots$] may not represent persuasive proof that the scaling is true." We adhere to this comment and prefer not to manipulate the data sets in such a way.

B. Structure function

For parameter set I (cf. Table I) we show in Fig. 3 a family of spherically-averaged structure functions versus wave numbers, corresponding to time steps 200, 400, 600, 800, 1000, 1200, and 1400, from right to left. Just as in scattering cross-section measurements [2], we observe the peaks to grow and approach small wave numbers as time evolves. In Figs. 4 and 5 we show the same family of curves using time steps as abscissas and wave numbers as parameters. Regions of linear growth with time on such a logarithmic scale indicate that a diffusive process is dominating the dynamics. In fact, an exponential time growth for the structure function shortly after the quench below the spinodal curve was predicted from the linearised Cahn-Hilliard Model-*B* equations without noise [2], which although incorporating order-parameter conservation, does not include hydrodynamics. This Cahn-Hilliard equation might be applicable to regimes in our fluid where hydrodynamic effects were unimportant, as in the initial stages. Assuming linear perturbations ϕ' to the order parameter, Cahn predicted that for fluctuations of small amplitude and long wavelength there is an instability of the form

$$S(k,t)=S(k,0)e^{-2\omega(k)t} \tag{39}$$

for $k<k_c$, where k_c depends on the diffusion constant. Here, t is the time, $\omega(k)<0$, and $S(k,t)\propto\langle|\phi'_{\mathbf{k}}(t)|^2\rangle$, the brackets denoting averaging in reciprocal space over a shell of radius k.

Exponential growth occurs in our simulations, as can be seen from Figs. 4 and 5 for about the first 350 time steps for most of the wave numbers, indicating its transient character. The plateau of Fig. 1, set I, lasts during the first 400 time steps, and we can see, Fig. 3, that up to 400 time steps the peak in the structure factor varies in height and very little in wave number, and is located at 0.491 (lattice units). This leads us to think that at these early stages the dynamics is mainly making walls thinner while average domain sizes barely change. In addition, visual inspection of the order parameter confirms the latter and suggests that hydrodynamic currents are weak, leaving diffusion as the mechanism leading the phase segregation process. When we check the

TABLE II. Levenberg-Marquardt nonlinear least-squares fits of l vs t data to model (38), for each parameter set attempted. The first line for each set belongs to 128^3 data, the second line to 256^3 data, the latter being unavailable for set I. Fitting parameters are given, plus the weighted sum of squared residuals (χ^2) divided by the fit's number of degrees of freedom. Weights are the inverses of squared uncertainties. Note that χ^2/ndf, also referred to as the variance of residuals, is expected to approach unity. Values larger than 1.0 may be due to an insufficient number of data points, data errors not normally distributed, or an incorrect model function. Values smaller than 1.0 may be the result of too large error bars, or too general a model function.

Parameter set	a_0	a_1	a_2	χ^2/ndf
I	0.644±0.014	-2×10^{-5}±0.002	0.545±0.014	0.46
II	0.924±0.004	6×10^{-6}±0.007	0.607±0.006	1.23
	0.922±0.003	-2×10^{-5}±0.007	0.593±0.007	0.48
III	1.248±0.031	−0.007±0.100	0.650±0.007	2.71
	1.362±0.010	-1×10^{-4}±0.03	0.623±0.002	0.68
IV	0.941±0.019	0.01±3.9	0.743±0.002	0.10
	1.139±0.017	−0.01±3.6	0.717±0.002	0.14

structure function temporal evolution, Figs. 4 and 5, for the curves at and around $k=0.491$, we see that up to exactly 400 time steps do they show exponential growth, as the Cahn-Hilliard Model B predicts for a diffusive scenario. Also, exponential growth does not hold for all wave numbers, but only for those smaller than about 0.7, in agreement with the existence of an upper cutoff for the validity of Eq. (39), predicted from Model B.

However, not all the wave numbers follow Model B's predictions, namely, that exponential growth is a transient and occurs up to a threshold wave number. In fact, exponential growth holds for all the time steps of the simulation for the larger length scales (wave numbers up to about 0.245), suggesting that diffusion never ceases to dominate their dynamics. Also, exponential growth is seen for very small domain sizes (wave numbers larger than 0.736) for time steps well advanced in the coarsening dynamics, after 600 time steps. These wave numbers are close to and above the expected Model-B upper cutoff for exponential growth, set by the change in slope from positive to negative in Fig. 5. These departures from Model B's predictions hold nonetheless for domain sizes far from the first moment of the structure factor, which is close to its peak and is our average domain size measure. It would be desirable in future works to investigate diffusional processes at $k<0.245$ for all of the simulation time, and $k>0.736$ at late times: according to the Cahn-

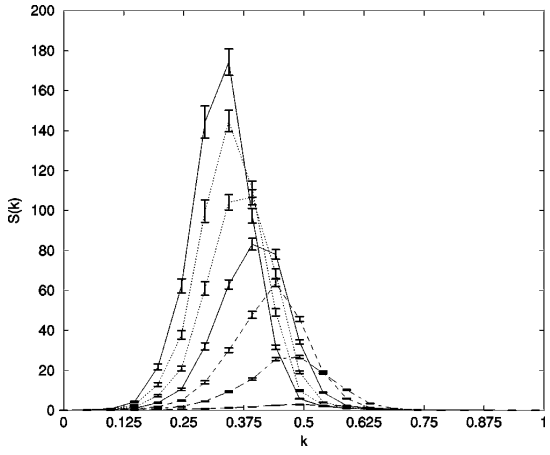

FIG. 3. Spherically averaged structure function versus wave number, for parameter set I (cf. Table I). 128^3 lattice. Error bars represent the standard error of the structure function spherical average. Time slices shown are time step 200, 400, 600, 800, 1000, 1200, and 1400 from right to left. All quantities are reported in lattice units.

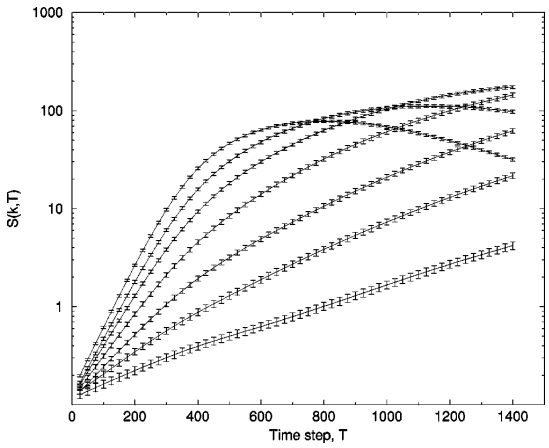

FIG. 4. Evolution of the spherically averaged structure function with the time step for parameter set I and a 128^3 lattice, on a logarithmic scale. When observed along the ordinate $T=200$, the curves correspond to wave numbers $k=0.147$, 0.196, 0.245, 0.295, 0.344, 0.393, and 0.442 from bottom to top, respectively. Error bars represent the standard error of the structure function spherical average. Regions of linear growth are those for which the exponential behavior Eq. (39) holds. For wave numbers up to 0.2 exponential and therefore diffusive behavior is seen for all the simulation time. For larger wave numbers (and hence smaller domain sizes) diffusion occurs as a transient. All quantities are reported in lattice units.

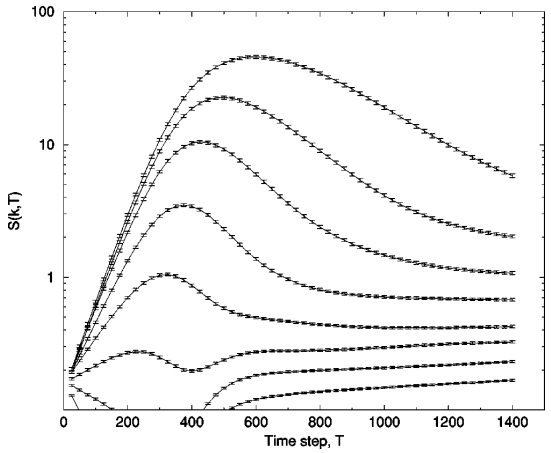

FIG. 5. Similar to Fig. 4, but the curves correspond to wave numbers k=0.491, 0.540, 0.589, 0.638, 0.687, 0.736, 0.785, and 0.834 from top to bottom, respectively. We can see that linear growth ceases to hold for wave numbers larger than about 0.736, in accordance with existence of an upper cutoff for the validity of Eq. (39). All quantities are reported in lattice units.

Hilliard linearized Model *B*, for these cases diffusion is negligible or forbidden, respectively.

Analogous behavior to Fig. 3 is exhibited for parameter sets II, III, and IV (cf. Table I) in Figs. 6, 7, and 8, respectively. For the last two time slices taken in Fig. 9, the peaks seem no longer to drift to the left, as a result of finite size effects (arrest of domain growth). Regarding regions of exponential growth with time, the three data sets confirm Eq. (39), with an upper bound for k.

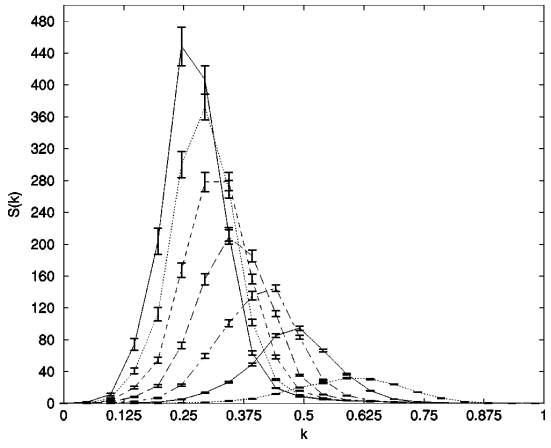

FIG. 6. Spherically averaged structure function versus wave number, for parameter set II (cf. Table I). 128^3 lattice. Error bars represent the standard error of the structure function spherical average. Time slices shown are time step 200, 400, 600, 800, 1000, 1200, and 1400 from right to left. All quantities are reported in lattice units.

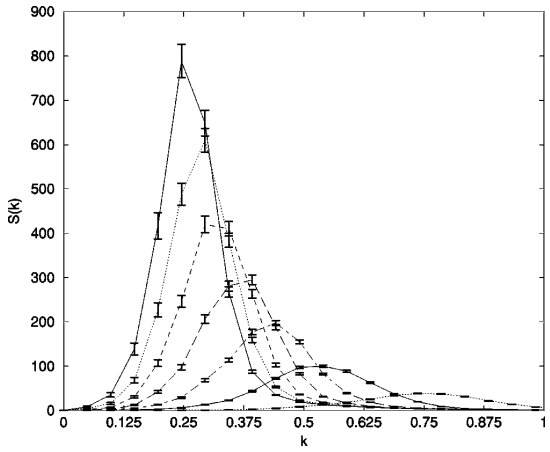

FIG. 7. Spherically averaged structure function for parameter set III (cf. Table I). 128^3 lattice. Error bars represent the standard error of the structure function spherical average. Time slices shown are time step 100, 200, 300, 400, 500, 600, and 700 from right to left. All quantities are reported in lattice units.

Figure 9 shows the collapse (matching) of the structure functions corresponding to parameter set III (cf. Table I), for a 128^3 lattice size and time steps from 450 to 700, when they are scaled by Eq. (8), the abscissas being rescaled by a factor of $(2\pi)^{-1}$, and the ordinates by the peak's maximum. Earlier times are represented in Fig. 8 by empty symbols, and later times by filled symbols. There is good collapse, and, therefore, scaling according to the scaling hypothesis, in the region from q=0.4 to about $q\approx 3$, where $q\equiv kL$ is dimensionless. The middle of the region $1<q<2$ follows a q^{-9} behavior, in accordance with Tomita's prediction of an exponent -6 or more negative [63].

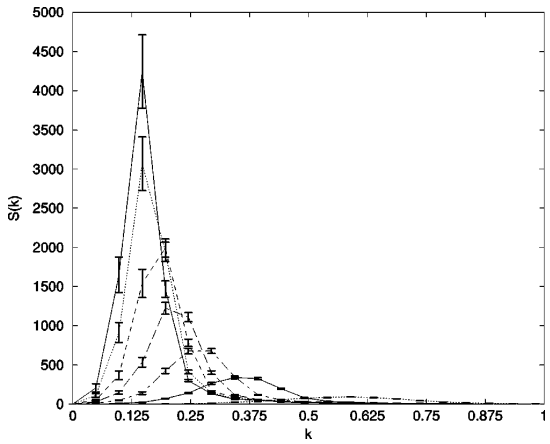

FIG. 8. Spherically averaged structure function versus wave number, for parameter set IV (cf. Table I). 128^3 lattice. Error bars represent the standard error of the structure function spherical average. Time steps shown are 100, 200, 300, 400, 500, 600, and 675, from right to left. All quantities are reported in lattice units.

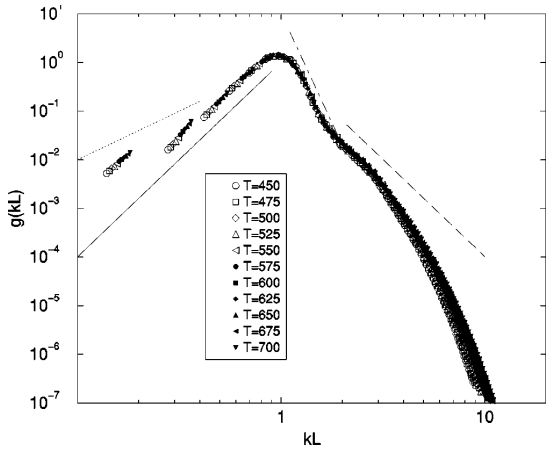

FIG. 9. Scaled spherically averaged structure function for parameter set III (cf. Table I), as defined by Eq. (8). Lattice size is 128^3. Time steps are as shown in the legend. Earlier times correspond to the empty symbols; later times to the filled symbols. Error bars are smaller than the size of the symbols. Straight lines serve as slope guides to the reader only, and represent power laws q^2, q^4, q^{-9}, and Porod's law q^{-4}, from left to right, respectively, with $q \equiv kL$. All quantities are reported in lattice units.

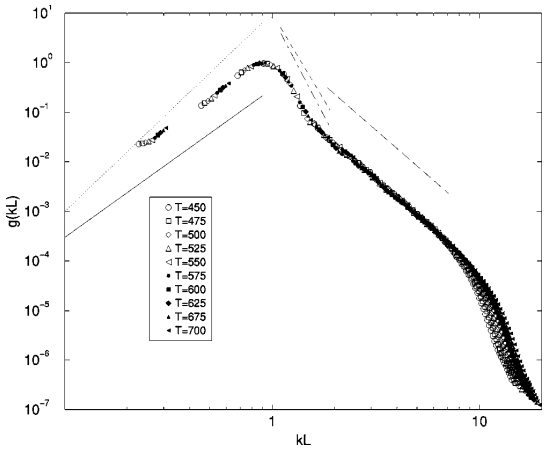

FIG. 10. Scaled spherically averaged structure function for parameter set IV (cf. Table I), as defined by Eq. (8). Lattice size is 128^3. Time steps shown are from 450 up to 675, every 25. Earlier times correspond to the innermost lines; later times to the outermost lines. Error bars are smaller than the size of the symbols, except for the two leftmost, detached data sets, for which they are slightly larger. Straight lines serve as slope guides to the reader only, and represent power laws q^3, q^4, q^{-8}, q^{-7}, and the fit to the large-q tail, $q^{-3.65}$, from left to right, respectively, with $q \equiv kL$. All quantities are reported in lattice units.

Close to $q \approx 3$ we observe the presence of a shoulder, as has been reported in experiments [64] and numerical simulations [48,65]. Most strikingly, the shape of our large-q tail is very reminiscent of that of Fig. 4 in Ref. [48] and that of Fig. 3 in Ref. [65]: (1) there is still a time dependence indicating that interfaces have not yet been fully resolved (we are probing the smallest scales, where diffusion still exists and ξ/L is not small enough); and (2) the tail decreases with an exponent which is in fact more negative than that of the Porod tail, Eq. (6), despite what these authors [48,65] claim.

For $q<0.4$, data points do not seem to collapse onto the same curve of those for $q>0.4$. This is similar to, but with more data than, the results of Koga and Kawasaki [65]. Our results show an exponent growing with time: the slope of a line (not shown) joining the first two empty circles ($T=450$) is 1.61, while the slope of a line (not shown) joining the last two filled downward triangles ($T=700$) is 2.12. This resembles the temporal growth cited by Appert *et al.* [48] on the results of Alexander, Chen, and Grunau [34]; nonetheless, we consider the amount of data in the latter insufficient to draw firm conclusions. Given that the points at $T=700$ are closer to the asymptotic regime, we take such a slope as our best approximation to the asymptotic regime.

In the small-q region, Yeung [66] predicted a q^4 behavior for the asymptotic limit ($L \to \infty$, or at late times). Additionally, at earlier stages, a term proportional to $L^{-2}q^2$ caused by thermal noise would also come into play. Now, the estimate of Appert *et al.* [48] applies well for our results: such a quadratic term is less dominant than the quartic one only for $q>0.4$, given that the largest value of $L(T)$ for which there are no finite size effects is also about 25. This happens to be the region where we find the $q^2 \leftrightarrow q^4$ crossover.

Figure 10 shows similar curves for parameter set IV (cf. Table I), where only time steps 450 to 675 are displayed and we have also normalized the curve such that the peak is located at (1,1). We have again neglected early time steps because of poor collapse. A fit to the tail in $2<q<10$ gives $q^{-3.65}$, close to being a Porod's law. It is when we probe the finest length scales, at $q \approx 10$ that it ceases to apply, due to lattice discretization effects.

The behavior at intermediate wave numbers is between q^{-8} and q^{-7}, again in agreement with Tomita's theory [63], and close to q^{-7} as computed using a dissipative particle dynamics method by Jury *et al.* [13] and a lattice-gas automaton by Love, Coveney, and Boghosian [9].

For small momenta (large domains) we found a behavior close to q^3, in agreement with the numerical results of Love, Coveney, and Boghosian [9] and in disagreement with Yeung's predictions [66].

The most notable difference between Figs. 9 and 10 is the behavior above $q \approx 1.5$. Figure 10 shows a neat Porod tail, which bends down dramatically for $q>10$, whereas Fig. 9 shows either a poor Porod tail in the region $3<q<5$, or a minute one in the region $1.5<q<3$. A condition assumed in the derivation of Porod's law [47] is that the sampling length r satisfies $\xi \ll r \ll L$, which in wave numbers means

$$1/L \ll k \ll 1/\xi. \tag{40}$$

By "eyeball" inspection of the system's order parameter we found that interface widths naturally shrink with an increasing number of time steps, going from about 5 or 6 lattice unit spacings at 200 time steps down to about 3 at 675 time steps,

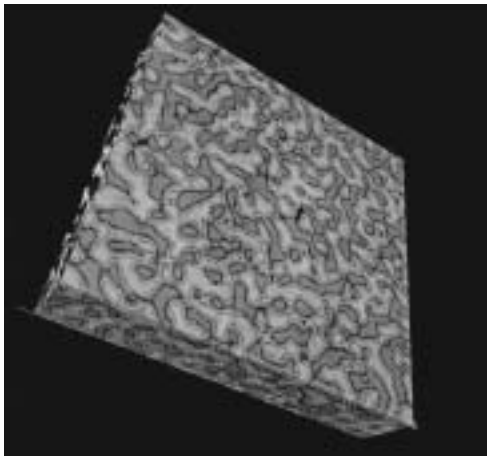

FIG. 11. Order parameter $(\rho^R-\rho^B)$ snapshot at time step 200 for parameter set IV (cf. Table I). We show a 256×256×40 slab of the lattice.

regardless of the data set, III or IV (cf. Table I). Simulations for a 256^3 lattice size revealed similar widths, and snapshots of the order parameter at 200 and 700 time steps are shown in Figs. 11 and 12. With these widths in mind, assuming domain sizes of a quarter of the lattice side length (the threshold imposed by our prescription for eliminating finite size effects), and a 128^3 lattice, condition (40) becomes

$$1 \ll q \ll 10, \tag{41}$$

which contains our large-q region. Despite this, we do not observe a Porod tail for data set III, or, as in data set IV, the tail obtained is only close to being a Porod tail. This is in agreement with the fact Eq. (40) is necessary but not sufficient for a Porod tail to hold.

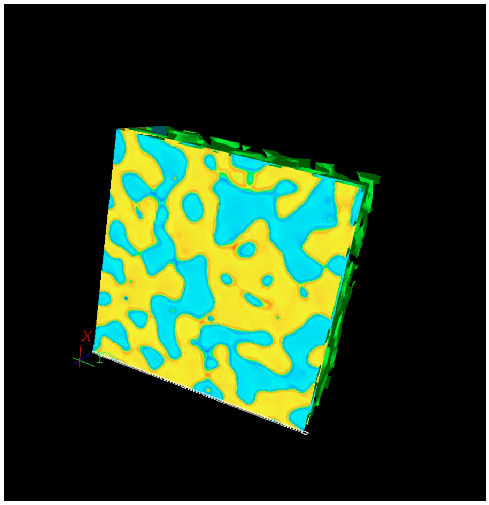

FIG. 12. Order parameter $(\rho^R-\rho^B)$ snapshot at time step 700 for parameter set IV (cf. Table I). We show a 256×256×64 slab of the lattice.

TABLE III. Model parameters leading to numerical instability, including the surface tension $\sigma(\rho,\tau,g)$ generated some time steps before the instability sets in, and the associated characteristic time. The lattice used was 4×4×128, and the instability sets in before 4000 ts.

ρ	τ	g	$\sigma(\rho,\tau,g)$	T_0
0.5	0.5625	0.06	0.0115	0.0169
0.5	0.5625	0.03	0.0052	0.0122
0.3	0.5625	0.10	0.0068	0.0174
0.3	0.5500	0.08	0.0061	0.0112

Finally, it is worth noting in Fig. 12 that the existence of nested domains and droplets much smaller than the average domain size.

VI. NUMERICAL STABILITY OF OUR LATTICE-BOLTZMANN ALGORITHM

As is well known, owing to the lack of an H theorem, an approach to equilibrium is not guaranteed in all lattice-Boltzmann models to date; recent theoretical developments to address and solve this have been made [43–46]. For single-phase lattice-Boltzmann models, equilibrium states are well defined in the collision term; if the automaton does relax to these, the pertinent macroscopic momentum (and sometimes energy) balance equations are reproduced in the low-Knudsen number limit. Interacting, multicomponent lattice-Boltzmann models exhibit the same situation in the bulk of pure fluid regions where intercomponent interactions are negligible. For regions where they are not, there is not even a well-established thermohydrodynamic theory which could provide equilibria to which the automaton could relax to, or with which to compare the stationary state to which it can evolve. Whether dealing with a single or multiphase system, lattice-BGK stationary regimes ought to be treated with caution and contrasted with experiment.

Numerical instabilities are the reflection of the lack of an H theorem, which is a direct consequence of space and time discretization on the BGK-Boltzmann equation and the freedom in the choice of the equilibrium distribution function [45,46]. These instabilities can be defined as follows. As is generally the case for a finite difference method with a single relaxation parameter, such as our lattice-BGK model for a zero phase-coupling constant [42], linear stability occurs within a finite interval of such a parameter. If multicomponent interactions are introduced, additional parameters may influence the stability: density, intercomponent coupling strength, and even composition. The mechanism is simple: certain choices of parameters can turn the lattice-BGK collision term positive (therefore increasing the mass density) for long enough to generate floating-point numbers larger than the largest the machine can deal with, hence causing an overflow signal. Numerical instabilities are defined in this work as the generation of such floating-point numbers. We con-

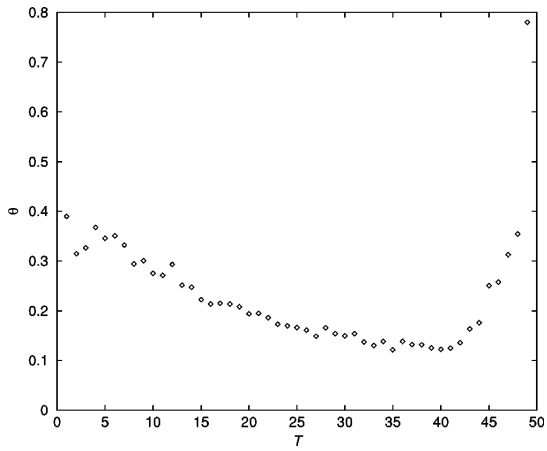

FIG. 13. Evolution of the collision term maximum absolute value, θ, Eq. (42), with the time step on a 32^3 lattice for parameters $\{\rho=0.3,\ g=0.06,\ \tau=0.5125\}$. All quantities are in lattice units.

sider it crucial to be able to map out regions in the model's parameter space leading to unstable configurations, and to report them alongside any lattice-BGK simulations.

Using the same initial conditions as explained in Sec. V, we found our algorithm to be unstable for regimes with the smallest length and time scales, L_0 and T_0, which coincide with those of the largest Mach numbers. In Table III we show some of the paramaters leading to numerical instability. The dependence of the surface tension on the model parameters, as given in Sec. IV, should be taken into consideration as a guide to steering through the parameter space. Note that all values of Δt included are larger than that for parameter set IV.

We then investigated the nature of our instabilities, as others have done. The group of Cates found troublesome numerical instabilities with their free-energy based, lattice-BGK model in 3D in regions in which quiescent binary portions of fluid go into a checkerboard state [61]. They reported that their model is unconditionally unstable [49]. Nonetheless, by improving the way gradients were treated numerically they were able to considerably reduce this unphysical behavior. For our model, we looked at the time evolution of the quantity

$$\theta(t)\equiv\max\{|\Omega_k'^{\alpha}(\mathbf{x},t)|\forall\,\mathbf{x}\forall\,k\forall\,\alpha\}, \qquad (42)$$

for parameters $\{\rho=0.3,\ g=0.06,\ \tau=0.5125\}$, where the collision term, $\Omega_k'^{\alpha}$, is defined in Eq. (25). We also monitored the maximum and average values of the fluid mixture's speed, $u_{\max}$ and $\bar{u}$, respectively, on the lattice. We show these quantities for a 32^3 lattice in Figs. 13–15. We see how θ reverses its decreasing trend in a few time steps; after that, it blows up at $T=52$ time steps. We only show data up to $T=49$, as $\theta(T=51)\approx 10^{111}$. $u_{\max}$ blows up in similar style: at $T=50$, $u_{\max}=7498$, and $\theta\approx 10^{21}$; at $T=51$, $u_{\max}$ has exceeded the maximum floating-point value that the computer can deal with, and overflow signals are generated. This indicates that at the time steps immediately prior to the onset of the instability the lattice gets more and more populated with increasing speeds until in two or three time steps they grow by ten or more orders of magnitude. That the population of lattice sites with rapidly increasing speeds over time is small compared to the lattice volume can be concluded from contrasting the time variation in the standard error (one sigma) of $\bar{u}$ to the time variation of $\bar{u}$, Fig. 15. The same parameter set run on a 128^3 lattice seems to make the instability set in much quicker, as it occurs during the first 10 time steps. As a final check, we ran a 128^3 lattice with parameter set I (cf. Table I) for 20000 time steps and found no instabilities. The time evolution of θ, u, and $\bar{u}$ is shown in Figs. 16–18, respectively. We conclude that the occurrence of instabilities only depends on the set of parameters used, regardless of the number of time steps simulated.

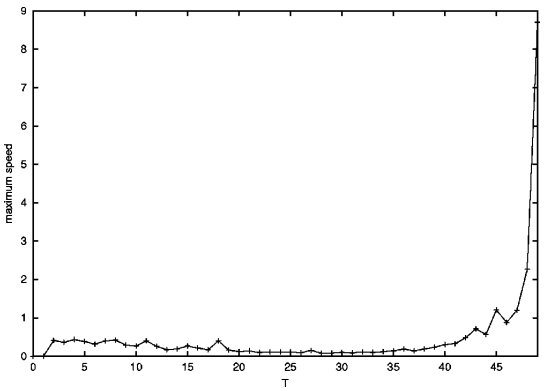

FIG. 14. Evolution of the maximum speed $u_{\max}$ with the time step on a 32^3 lattice for parameters $\{\rho=0.3,\ g=0.06,\ \tau=0.5125\}$. The interpolating curve serves as a guide to the eye only. All quantities are in lattice units.

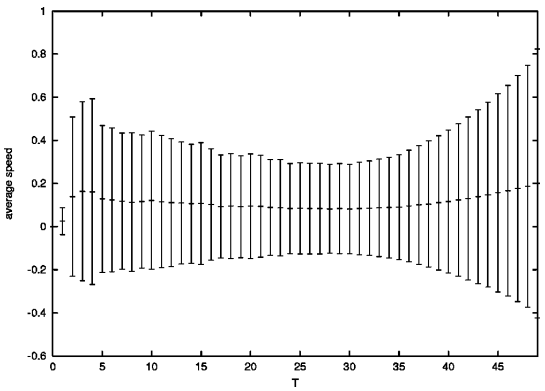

FIG. 15. Evolution of the speed average $\bar{u}$, with the time step on a 32^3 lattice for parameters $\{\rho=0.3,\ g=0.06,\ \tau=0.5125\}$. Error bars represent the standard error of the average (one sigma). All quantities are in lattice units.

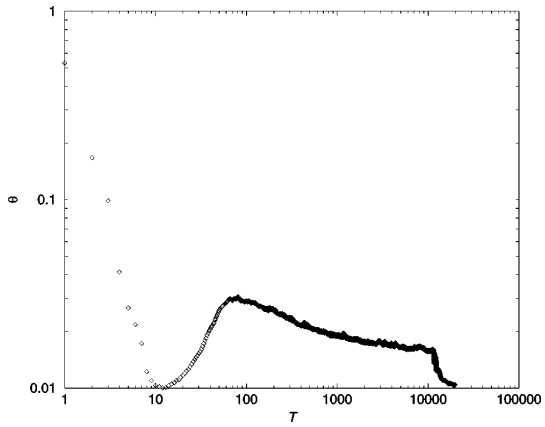

FIG. 16. Evolution of the collision term maximum absolute value, θ, Eq. (42), with the time step on a 128^3 lattice for parameter set I (cf. Table I). We can see a decreasing trend for most of the simulation, which accentuates after time step 10 000. The interpolating curve serves as a guide to the eye only. All quantities are in lattice units.

VII. CONCLUSIONS

We have presented a quantitative study of the phase separation dynamics in three dimensions for critical (50:50) fluid mixtures (spinodal decomposition) for a modified Shan-Chen lattice-BGK model of multicomponent, isothermal immiscible fluids.

We found that, after a brief diffusional transient in which interconnected regions of fluid species embedded into one another are formed, the average size of such regions grows with time as $l \propto t^{\gamma}$, where $\gamma \approx 2/3$. The trend is for the value to increase in the range $0.545 \pm 0.014 < \gamma < 0.717 \pm 0.002$ as the Reynolds number increases. This increase is consistent with a crossover from $l \propto t^{1/3}$ diffusive behavior to hydrodynamic viscous growth $l \propto t$ predicted by the Cahn-Hilliard

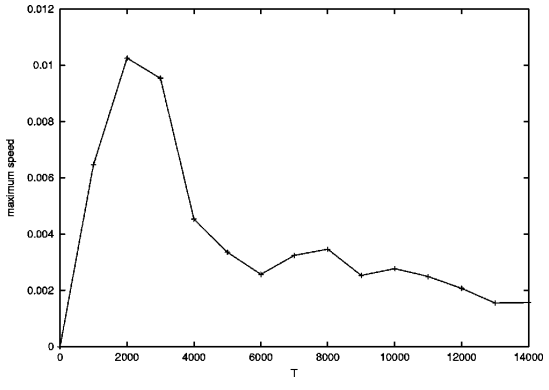

FIG. 17. Behavior of the maximum speed $u_{\max}$ with the time step for a 128^3 lattice with parameter set I (cf. Table I). It shows an overall decreasing trend. The interpolating curve serves as a guide to the eye only. All quantities are in lattice units.

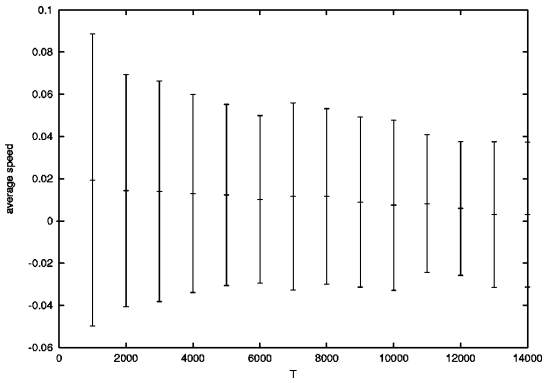

FIG. 18. Evolution of the speed average $\bar{u}$ with the time step on a 128^3 lattice for parameter set I (cf. Table I). We can see a decreasing trend of the average and its error. All quantities are in lattice units.

Model H. Owing to the significant amount of diffusion present at low Reynolds number, we do not consider our results to be indicative of a genuinely hydrodynamic inertial $t^{2/3}$ regime.

We observed exponential growth in the time dependence of the structure function for wave numbers up to a threshold value, in qualitative agreement with predictions from the linearized Cahn-Hilliard Model *B*. For small wave numbers, such an exponential growth is seen at all simulation times, whereas it is only an initial transient for larger wave numbers. These departures from Model *B* predictions are for wave numbers far from the one characterizing the average domain size. A natural continuation of this work would be to investigate the nature of diffusion currents for these cases.

We have found very good agreement with the dynamical scaling hypothesis in the form of a neat collapse of the structure function curves for Re=2.7 and Re=37 when they are appropriately scaled according to Eq. (8). This collapse holds roughly for the second half of the simulation time, as diffusional transients act during the first. By looking at order parameter snapshots we observed the formation of nested domains and smaller droplets for the largest Reynolds numbers achieved, as Wagner and Yeomans also found [12]. However, unlike them, in our case these are transients rather than a result of length scales growing at different speeds, as poor collapse of the scaling functions would then occur due to breakdown of scale invariance.

Yeung predicted a q^2 behavior at the small-q end of the spectrum as the result of thermal effects at preasymptotic stages [66]. Love, Coveney, and Boghosian [9] conjectured that a q^2 behavior, and a crossover to q^4, could be caused by (a) lattice-gas noise, or (b) a poor scaling collapse, and that their $t^{2/3}$ domain growth, instead of t, might be justified by the former. Appert *et al.* [48] ascribed the q^2 behavior and the crossover to not having reached the asymptotic limit, $L \to \infty$ (poor scaling collapse again). Our noiseless model reproduced the $q^2 \leftrightarrow q^4$ crossover at Re=2.7 and did not at Re=37, for which there is better scaling collapse, and also produced a 2/3 domain growth (crossover) exponent. All this

leads us to conclude that noise may not play as important a role as the lack of scaling collapse in explaining the $q^2 \leftrightarrow q^4$ crossover, and is definitely not a requirement for the reproduction of a 2/3 domain growth exponent. A q^2 behavior is the only one experimentally observed by Kubota *et al.* [64] for a mixture of isobutyric acid and water; they cite surface tension effects, measurement difficulties, multiple light scattering, and even specificity to the mixture's molecular weight as reasons for not seeing a q^4 behavior, and definitely discard thermal noise. Not surprisingly, in his prediction Yeung assumed a diffusive domain growth exponent of 1/3, which is rather seen in quenches of polymer mixtures and metal alloys.

In the case Re=37, the spectrum shows a q^3 behavior in the small-q limit, in disagreement with Yeung's prediction. In fact, his analysis is based on a Cahn-Hilliard model without hydrodynamics.

The numerical instabilities seen in our runs are caused by large speeds turning the equilibrium distribution negative for long enough to incur floating-point overflows. This happens for characteristic times (cf. Table I) below $T_0=0.0172$, and the population of lattice sites undergoing such a burst in the fluid's macroscopic speed is small compared to the lattice volume. We found no evidence that an initially stable regime becomes unstable at later times, as typically happens in relaxational models (such as is our model for $g_{a\bar{a}}=0$). This is in stark contrast with the findings of Kendon *et al.* [49] and Cates *et al.* [61] in their spinodal decomposition studies using a free-energy based, lattice-BGK model, who reported their algorithm to be unconditionally unstable.

A search for a crossover to growth laws other than $t^{2/3}$ at Reynolds numbers higher than Re=37 faces two major problems: (a) the triggering of numerical instabilities due to large interspecies coupling and smallness of relaxation time values; and (b) the approach to the compressible limit, whose macrodynamic behavior for pure phases cannot, by construction, be correctly described by our method. On the other hand, there is still scope to achieve Reynolds numbers smaller than Re=0.18 in search of the end of the crossover to $t^{1/3}$. Closeness to the miscibility threshold may make this endeavour difficult, as it is reached for characteristic times ca. $T_0=1.43\times10^8$.

Our results clearly challenge the claim that a domain growth linear with time is universal for all models of phase separating fluids sharing similar values of L_0 and T_0 since we obtained excellent collapse of scaled structure functions yet our domain growth exponents are in the crossover region between diffusive and hydrodynamic viscous regimes.

The properties of this binary immiscible fluid model are important for underpinning the more complex domain growth observable in ternary amphiphilic (oil/water/surfactant) fluids which we expect to report in forthcoming publications.

ACKNOWLEDGMENTS

This work was supported by EPSRC Grant Nos. GR/M56234 and RealityGrid GR/R67699, which provided access to Cray T3E-1200E, SGI Origin2000, and SGI Origin3800 supercomputers at Computer Services for Academic Research (CSAR), Manchester University, U.K., and by the Center for Computational Science, Boston University, through a collaborative project to access their several SGI Origin2000 platforms. We also thank the Higher Education Funding Council for England (HEFCE) for our on-site 16-node SGI Onyx2 graphical supercomputer. We wish to thank Dr. Hudong Chen and Dr. Peter J. Love for useful discussions, Mr. Jonathan Chin for implementing the parallel code, and Dr. Keir Novik for technical assistance. N.G.S. also wishes to thank Dr. Ignacio Pagonabarraga for useful discussions, and Professor David Jou, Professor José Casas-Vázquez, and Dr. Juan Camacho at the Universitat Autònoma de Barcelona, Spain, for their support.

[1] F. Perrot, P. Guenoun, T. Baumberger, D. Beysens, Y. Garrabos, and B. Le Neindre, Phys. Rev. Lett. **73**, 688 (1994).
[2] J.D. Gunton, M. San Miguel, and P.S. Sahni, in *Phase Transitions and Critical Phenomena*, edited by C. Domb and J. Lebowitz (Academic Press, New York, 1983), Vol. 8.
[3] A. Balazs, Curr. Opin. Colloid Interface Sci. **4**, 443 (2000).
[4] F. Perrot, D. Beysens, Y. Garrabos, T. Frölich, P. Guenoun, M. Bonetti, and P. Bravais, Phys. Rev. E **59**, 3079 (1999).
[5] M. Grant, M. San Miguel, J. Viñals, and J.D. Gunton, Phys. Rev. B **31**, 3027 (1985).
[6] F.J. Solis and M. Olvera de la Cruz, Phys. Rev. Lett. **84**, 3350 (2000).
[7] A. Chakrabarti, R. Toral, and J.D. Gunton, Phys. Rev. B **39**, 4386 (1989).
[8] O.T. Valls and J.E. Farrell, Phys. Rev. E **47**, R36 (1993).
[9] P.J. Love, P.V. Coveney, and B.M. Boghosian, Phys. Rev. E **64**, 021503 (2001).
[10] A.N. Emerton, P.V. Coveney, and B.M. Boghosian, Phys. Rev. E **55**, 708 (1997).
[11] V.M. Kendon, J.-C. Desplat, P. Bladon, and M.E. Cates, Phys. Rev. Lett. **83**, 576 (1999).
[12] A.J. Wagner and J.M. Yeomans, Phys. Rev. Lett. **80**, 1429 (1998).
[13] S. Jury, P. Bladon, S. Krishna, and M.E. Cates, Phys. Rev. E **59**, R2535 (1999).
[14] M. Laradji, S. Toxvaerd, and O.G. Mouritsen, Physica A **239**, 404 (1997).
[15] I. Pagonabarraga, A.J. Wagner, and M.E. Cates, J. Stat. Phys. **107**, 39 (2002).
[16] I. Pagonabarraga, J.-C. Desplat, A.J. Wagner, and M.E. Cates, New J. Phys. **3**, 9.1 (2001) (http://www.njp.org/).
[17] U. Frisch, D. d'Humières, B. Hasslacher, P. Lallemand, Y. Pomeau, and J.-P. Rivet, Complex Syst. **1**, 649 (1987); D.H. Rothman and J.M. Keller, J. Stat. Phys. **52**, 1119 (1988); G.D. Doolen, Physica D **47** (1991); C. Appert and S. Zaleski, Phys. Rev. Lett. **64**, 1 (1990).
[18] For a recent review see S. Chen and G.D. Doolen, Annu. Rev. Fluid Mech. **30**, 329 (1998).
[19] P.J. Hoogerbrugge and J.M.V.A. Koelman, Europhys. Lett. **19**, 155 (1992); E.G. Flekkøy and P.V. Coveney, Phys. Rev. Lett. **83**, 1775 (1999).

[20] H. Tanaka, Phys. Rev. Lett. **72**, 3690 (1994).
[21] G.K. Batchelor, *An Introduction to Fluid Dynamics* (Cambridge University Press, Cambridge, 1967).
[22] G. Tryggvason, B. Bunner, O. Ebrat, W. Tauber, *Computations of Multiphase Flows by a Finite Difference/Front Tracking Method. I Multi-Fluid Flows*, 29th Computational Fluid Dynamics Lecture Series 1998-03 (Von Karman Institute for Fluid Dynamics, Rhode-St.-Genèse, Belgium). (Available at http://www-personal.engin.umich.edu/~gretar)
[23] W. Cahn and J.E. Hilliard, J. Chem. Phys. **28**, 258 (1958).
[24] J.E. Farrell and O.T. Valls, Phys. Rev. B **40**, 7027 (1989).
[25] X. Shan and H. Chen, Phys. Rev. E **47**, 1815 (1993); **49**, 2941 (1994); H. Chen, B.M. Boghosian, P.V. Coveney, and M. Nekovee, Proc. R. Soc. London, Ser. A **456**, 1431 (2000).
[26] M.R. Swift, W.R. Osborn, and J.M. Yeomans, Phys. Rev. Lett. **75**, 830 (1995); M.R. Swift, E. Orlandini, W. Osborn, and J.M. Yeomans, Phys. Rev. E **54**, 5041 (1996).
[27] K.E. Novik and P.V. Coveney, Phys. Rev. E **61**, 435 (2000).
[28] P. Fratzl, O. Penrose, R. Weinkamer, and I. Žižak, Physica A **279**, 100 (2000).
[29] J.S. Rowlinson and B. Widom, in *Molecular Theory of Capillarity* (Clarendon Press, Oxford, 1982).
[30] An in-depth explanation of Model *B* and Model *H*, among others, can be found in P.C. Hohenberg, Rev. Mod. Phys. **49**, 435 (1977).
[31] N.S. Martys and J.F. Douglas, Phys. Rev. E **63**, 031205 (2001).
[32] M. Nekovee, P.V. Coveney, H. Chen, and B.M. Boghosian, Phys. Rev. E **62**, 8282 (2000).
[33] J. Chin and P.V. Coveney, Phys. Rev. E **66**, 016303 (2002).
[34] F.J. Alexander, S. Chen, and D.W. Grunau, Phys. Rev. B **48**, 634 (1993).
[35] A.K. Gunstensen, D.H. Rothman, S. Zaleski, and G. Zanetti, Phys. Rev. A **43**, 4320 (1991).
[36] L.-S. Luo, Phys. Rev. Lett. **81**, 1618 (1998).
[37] T. Inamuro, N. Konishi, and F. Ogino, Comput. Phys. Commun. **129**, 32 (2000).
[38] A.J. Wagner and J.M. Yeomans, Phys. Rev. E **59**, 4366 (1999).
[39] M.E. Cates, V.M. Kendon, P. Bladon, and J.-C. Desplat, Faraday Discuss R. Soc. Chem. **112**, 1 (1999) (also available at http://arXiv.org/abs/).
[40] J.D. Sterling and S. Chen, J. Comput. Phys. **123**, 196 (1996).
[41] P. Lallemand and L.-S. Luo, Phys. Rev. E **61**, 6546 (2000).
[42] Y.H. Qian, D. d'Humières, and P. Lallemand, Europhys. Lett. **17**, 479 (1992).
[43] I.V. Karlin, A. Ferrante, and H.C. Öttinger, Europhys. Lett. **47**, 182 (1999).
[44] H. Chen and C. Teixeira, Comput. Phys. Commun. **129**, 21 (2000).
[45] B.M. Boghosian, J. Yepez, P.V. Coveney, and A. Wagner, Proc. R. Soc. London, Ser. A **457**, 717 (2001).
[46] B.M. Boghosian, Peter J. Love, Peter V. Coveney, Iliya V. Karlin, Sauro Succi, and Jeffrey Yepez, e-print cond-mat/0211093.
[47] A.J. Bray, Adv. Phys. **43**, 357 (1994).
[48] C. Appert, J.F. Olson, D.H. Rothman, and S. Zaleski, J. Stat. Phys. **81**, 181 (1995).
[49] V.M. Kendon, M.E. Cates, I. Pagonabarraga, J.-C. Desplat, and P. Bladon, J. Fluid Mech. **440**, 147 (2001).
[50] T. Araki and H. Tanaka, Macromolecules **34**, 1953 (2001).
[51] In practice, some systems require a level of description that the lattice-Boltzmann mesoscopic dynamics cannot provide, and ensemble averaging over independent initial conditions is carried out. See, for example, G.D. Doolen, T. Clark, and E. Ben-Naim, in *Europhysics Conference Abstracts (Volume 25H) of the International Conference on Discrete Simulation of Fluid Dynamics, Institut d'Etudes Scientifiques de Cargèse, Corsica, 2001*, edited by J.P. Boon, P.V. Coveney, and S. Succi (European Physical Society, Mulhouse, France, 2002).
[52] J.H. Ferziger and H.G. Kaper, in *Mathematical Theory of Transport Processes in Gases* (North Holland, Amsterdam, 1972).
[53] N. González-Segredo, M.Phil. thesis, Universitat Autònoma de Barcelona, 1997; H. Grad, Commun. Pure Appl. Math. **2**, 331 (1949).
[54] X. He and L.-S. Luo, Phys. Rev. E **56**, 6811 (1997).
[55] N. Martys, X. Shan, and H. Chen, Phys. Rev. E **58**, 6855 (1998).
[56] The limit $N\to\infty$, $m\to 0$, $\lambda\to 0$, with both $N\lambda^2 \equiv (\text{mean free path})^{-1}$ and Nm fixed, where N stands for the number of particles, m is their mass, and λ is the range of the interparticle, hard-sphere potentials, was baptised "the Boltzmann-Grad limit" by O.E. Landford III. In addition, the density has to be sufficiently low so that only binary collisions need be considered (consequence of $\lambda\to 0$), and spatial gradients small enough such that collisions can be thought of as localised in space. The most rigorous proof that in this limit the *Stosszahlansatz*, and therefore the Boltzmann equation (without a body force term), is exact for at least short times was provided by Landford in 1981 [Physica A **106**, 70 (1981)], the system described being an ideal gas. In 1985 Reinhard Illner and Mario Pulvirenti extended the result to three dimensions [cf. C. Cercignani, R. Illner, and M. Pulvirenti, in *The Mathematical Theory of Dilute Gases*, Applied Mathematical Sciences Vol. 106 (Springer-Verlag, New York, 1994)]. See also http://www.ann.jussieu.fr/publications/1995/R95026_Perthame.ps.gz for a list of references on collision models in Boltzmann's theory.
[57] W.H. Press, S.A. Teukolsky, W.T. Vetterling, and B.P. Flannery, in *Numerical Recipes in C. The Art of Scientific Computing*, 2nd ed., software version 2.08 (Cambridge University Press, Cambridge, 1999).
[58] M. Nekovee, J. Chin, N. González-Segredo, and P.V. Coveney, in *Proceedings of the 4th UNAM Supercomputing Conference, Mexico, D.F., 2000*, edited by E. Ramos, G. Cisneros, R. Fernández-Flores, and A. Santillán-González (World Scientific, Singapore, 2001), p. 204.
[59] URL: http://www.faqs.org/rfcs/rfc1014.html; Unix manual pages (% man xdr).
[60] URL: http://www.avs.com
[61] M.E. Cates (private communication).
[62] I. Pagonabarraga (private communication).
[63] H. Tomita, Prog. Theor. Phys. **75**, 482 (1986).
[64] K. Kubota, N. Kuwahara, H. Eda, and M. Sakazume, Phys. Rev. A **45**, R3377 (1992).
[65] T. Koga and K. Kawasaki, Phys. Rev. A **44**, R817 (1991).
[66] C. Yeung, Phys. Rev. Lett. **61**, 1135 (1998).

EUROPHYSICS LETTERS 15 March 2004

Europhys. Lett., **65** (6), pp. 795–801 (2004)
DOI: 10.1209/epl/i2003-10129-8

Self-assembly of the gyroid cubic mesophase: Lattice-Boltzmann simulations

N. González-Segredo(*) and P. V. Coveney(**)

Centre for Computational Science, Department of Chemistry, University College London 20 Gordon Street, London WC1H 0AJ, UK

(received 7 October 2003; accepted in final form 23 January 2004)

PACS. 61.30.St – Lyotropic phases.
PACS. 61.20.Lc – Time-dependent properties; relaxation.

Abstract. – We present the first simulations of the self-assembly kinetics of the gyroid cubic mesophase using a Boltzmann transport method. No macroscopic parameters are included in the model and three-dimensional hydrodynamics is emergent from the microscopic conservation laws. The self-assembly arises from local inter-particle interactions in an initially homogeneous, phase-segregating binary fluid with dispersed amphiphile. The mixture evolves in discrete time according to the dynamics of a set of coupled Boltzmann-BGK equations on a lattice. We observe a transient microemulsion phase during self-assembly, the structure function peaks and direct-space imaging unequivocally identifying the gyroid at later times. For larger lattices, highly ordered subdomains are separated by grain boundaries. Relaxation towards the ordered equilibrium structure is very slow compared to the diffusive and microemulsion-assembling transients, the structure function oscillating in time due to a combination of Marangoni effects and long-time-scale defect dynamics.

Block copolymer melts or dispersions, and homopolymer-block copolymer blends are examples of systems that self-assemble into regular, liquid-crystalline structures when subjected to the appropriate temperature or pressure quenches [1–4]. These structures, called mesophases due to their features being intermediate between those of a solid and a liquid, are also found in fluid mixtures of a surfactant in a solvent, binary immiscible fluids containing a third, amphiphilic phase, and lipidic biological systems [1, 5]. They all form due to the competing attraction-repulsion mechanism between the species. The morphology of these mesophases is defined by the spatial loci where most of the amphiphile concentrates, forming multi- or mono-layer sheets of self-assembled amphiphile. Common equilibrium mesophases include lamellae, hexagonal columnar arrays, and the primitive "P", diamond "D" and gyroid "G" cubic phases [1, 2]. The sheets of these cubic phases are surfaces or *labyrinths* of zero mean curvature, the skeletons of which form double (inter-weaving), chirally symmetric bicontinuous cubic lattices which are 6-, 4- and 3-fold coordinated, respectively. The gyroid is the

(*) E-mail: n.gonzalez-segredo@ucl.ac.uk; also at the Departament de Física, Universitat Autònoma de Barcelona - 08193 Bellaterra, Spain.
(**) E-mail: p.v.coveney@ucl.ac.uk

phase which exhibits the least surface area per unit cell among those, and is ubiquitous in nature; we show in this paper that it can spontaneously self-assemble from a purely microscopic, kinetic-theoretical lattice model with hydrodynamic interactions.

Simulation approaches to the dynamics of mesophase formation have been hitherto based on Monte Carlo [6], Brownian dynamics [7], dissipative particle dynamics [7–9], Langevin diffusion equation [10,11] and molecular-dynamics methods [12]. In Langevin-diffusion methods, mass currents arise from chemical potential gradients, computed in turn from equilibrium free energies. Much of the published work is based on Ginzburg-Landau expansions for the latter, assuming that all surfactant is adsorbed as a continuum on the self-assembled sheets, incorporating white noise and excluding hydrodynamics [10]. More recently, extensions appeared including hydrodynamics and free energies explicitly calculated for the amphiphile, modelled as Gaussian bead-spring chains in a mean-field environment [11]. Dissipative particle dynamics (DPD) methods also model the amphiphile as bead-spring chains, yet the beads as well as the particles constituting the fluid species enter in the model as mesoscopic entities, undergoing 2-body interactions. In DPD, space is continuous and hydrodynamics is emergent from the mesodynamics. The presence of hydrodynamics is an important feature in modelling the nonequilibrium pathways of mesophase self-assembly and the possible metastable states they can lead to, but is absent in Monte Carlo [6] and Brownian dynamics [7] methods.

In this work we use a hydrodynamically correct lattice-Boltzmann model of amphiphilic fluids [13] to simulate the self-assembly of a liquid crystalline, double gyroid cubic phase from a randomly mixed initial binary immiscible fluid (say, of "oil" or "red", and "water" or "blue") with an amphiphilic species dispersed in it. The model [13] does not require the existence of a thermodynamic potential describing the local equilibria and a phase transition; rather, self-assembly arises as an emergent property of the microscopic interactions between the species. The dynamics is obtained by solving a set of coupled Boltzmann-BGK transport equations on a spatial lattice in discrete time steps with a discrete set of microscopic velocities; the scheme is known as the lattice-Boltzmann (LB) BGK method and has proved useful for single- and multi-phase flow modelling during the last decade [14]. At each time step, the probability density evolved by each LB equation is advected to nearest neighbours and modified by molecular collisions, which are local and conserve mass and momentum. A single time parameter controls relaxation in the collision term for all microscopic speeds, and in our model there is no stochastic noise present other than in the amphiphile dynamics. The mass density defines fluid elements on each lattice node which can be mapped onto experimental scales that are intermediate with respect to molecular and macroscopic lengths and times. Immiscible fluid behaviour is incorporated via scalar inter-particle forces of a mean-field form limited to nearest neighbours. The force enters in the hydrodynamics by modifying the local macroscopic velocity of the whole fluid and hence the local Maxwellian to which each species relaxes. For the correct lattice symmetry, and in the limits of low Mach and Knudsen numbers, the Navier-Stokes equations for incompressible flow hold in the bulk of each fluid phase. The model also leads to the growth exponents and dynamical self-similarity observed in binary immiscible spinodal decomposition experiments [15]. An amphiphile density is evolved by an additional coupled LB equation, and the bipolar, amphiphilic molecules are modelled as dipole vectors moving between the nodes of the lattice. Their orientations vary continuously and relax towards a Gibbsian canonical equilibrium which minimises the interaction energy between the local dipole and the mean fields generated by their nearest neighbours. The evolution of the surfactant density is also coupled to that of the other species [13].

The initial condition in our simulations is a random dispersion of surfactant in a random mixture of equal amounts of oil and water. The maximum values chosen for the (uniformly distributed) random densities were 0.70 for oil or water and 0.40, 0.60, $0.90 \equiv n^{(0)s}$ for the

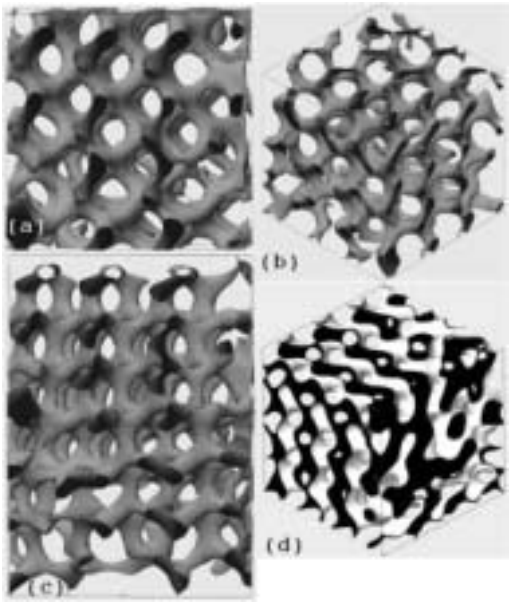

Fig. 1 – Isosurfaces of the order parameter $\phi(\boldsymbol{x})$ for a surfactant density of $n^{(0)s} = 0.60$ at time step $t = 15000$ in a highly ordered 33^3 subdomain of a 128^3 lattice. Panels (a), (b), and (c) display the $\phi = 0.40$, high-density isosurface viewed along the (100), $(1\,\overline{1}\,\overline{1})$ and (110) directions, respectively. Panel (d) shows the oil-water interface ($\phi = 0$) of the same lattice subdomain along the direction $(1\,\overline{1}\,\overline{1})$, where between three and four units cells fit laterally in the subdomain. Black and white have been used in panel (d) to distinguish one immiscible fluid phase from the other, and the scale for panels (a) and (c) varies from that for (b) and (d).

surfactant. These, as well as all magnitudes and parameters in the model, are in lattice units. All relaxation times were set to 1.0, the thermal noise parameter for dipolar relaxation was set to 10.0, and the parameters controlling the strength of the inter-species forces were set to $g_{\mathrm{br}} = 0.08$, $g_{\mathrm{bs}} = -0.006$ and $g_{\mathrm{br}} = -0.003$. We employed periodic boundary conditions on cubic lattices of 64^3, 128^3 and 256^3 nodes, the latter two initially being required to check that finite-size effects were absent. The choices made of densities and parameters were based on previous tests searching for regimes of oil-water immiscibility (*i.e.*, below the spinodal) for which, within the computing time and resources available, phase segregation was sufficiently fast, while flows were dominated by hydrodynamics and surface tension as opposed to diffusion.

We are interested in studying the nonequilibrium pathways that follow from the initial condition, for which we track the evolution of mass densities via direct-space imaging and analysis of the structure function. Defining a scalar order parameter, $\phi(\boldsymbol{x})$, at a particular time step as the oil density minus the water density, the oil-water structure function, $S(\boldsymbol{k})$, is the Fourier transform of the spatial auto-correlation function for the fluctuations of $\phi(\boldsymbol{x})$ around its lattice average, proportional to the intensities probed in scattering techniques widely used in the analysis of mesophase structure; the spherically averaged structure function, $S(k)$, is the average of $S(\boldsymbol{k})$ in a shell of radius $k \equiv |\boldsymbol{k}|$ and thickness one lattice unit, corresponding to the contribution of structures of size $L \equiv 2\pi/k$.

Figure 1 shows isosurfaces of the order parameter at time step $t = 15000$ in a 33^3 subdomain of a 128^3 lattice for an initial surfactant density flatly distributed up to $n^{(0)s} = 0.60$. We display three viewpoints of the isosurface $\phi = 0.40$ (in lattice units), corresponding to a water-in-oil, "rod-like" scenario where water is a minority phase and oil is in excess. Whereas on 64^3

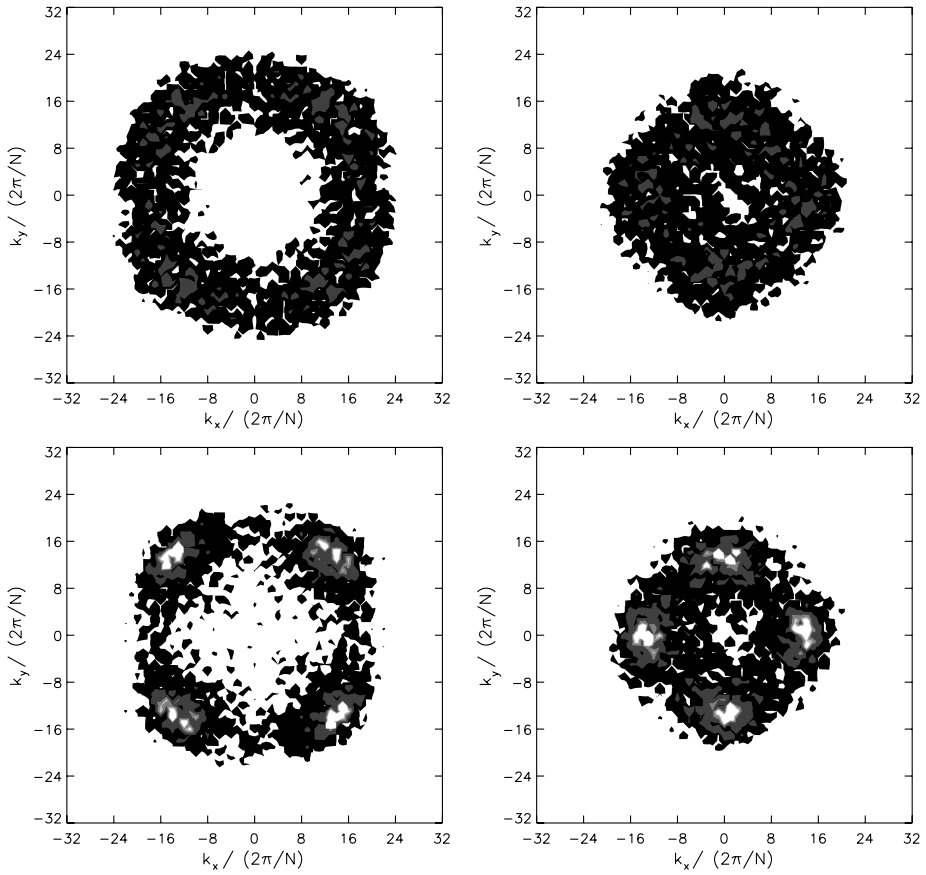

Fig. 2 – Temporal evolution of (k_x, k_y) slices of the structure function viewed along the (100) direction. The fluid is the same of fig. 1. Left and right columns show slices at $k_z/(2\pi/N) = 0, \pm 14$, respectively, where $N = 128$ is the lattice lateral size. Rows from top to bottom correspond to time steps $t = 500$ and 15000, respectively. Contours denote intensities $S = 1, 50$ and 100, where lighter shades denote higher intensities. The spherical shell structures in the top row indicate the presence of a sponge (microemulsion) phase, which becomes anisotropic at later times. In lattice units.

(or smaller) lattices the liquid crystalline structure uniformly pervades the simulation cell, on 128^3 (or larger) lattices there are some imperfections present, more prevalent as the lattice size is increased, resulting in liquid crystalline subdomains with slightly varying orientations between which exist domain boundaries —"defects".

The resemblance of the simulated structures in fig. 1 to transmission electron microtomography (EMT) images of the gyroid "G" cubic morphology is evident [4]: the morphology of $\pm\phi$, $\phi \neq 0$ (excess) isosurfaces is that of gyroid skeletons. The lattice resolution is insufficient to detect multiple peak fingerprints in plots of $S(k)$, as observed experimentally with SAXS techniques [3, 4]. However, its unaveraged counterpart (fig. 2) shows complete agreement of ratios of reciprocal vector moduli with those observed in diffraction patterns of the gyroid [4], which, in addition to visual (direct space) inspection of the unit cell, leads to unequivocal identification. EMT images and experimental self-assembly times of the gyroid phase allow us to broadly associate a length and time scale to our LB dynamics; *e.g.*, the systems in [4, 16] require resolutions to be 2.3 nm per LB-lattice unit and 10 μs up to 40 ms per LB time step.

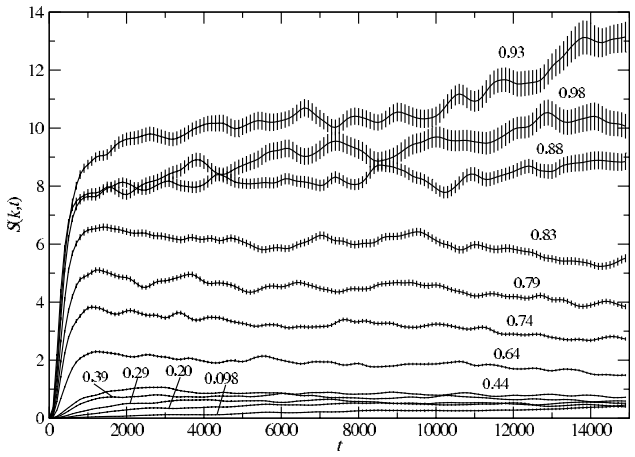

Fig. 3 – Temporal evolution of the spherically averaged structure function and its error (one-standard-deviation uncertainty in the average), for the wave numbers indicated next to each curve. The fluid is the same as in fig. 1. All quantities are in lattice units.

Values higher than $n^{(0)s} = 0.60$ also produce gyroid structures at late times, whereas there is gradual loss of long-range ordering for $0.40 < n^{(0)s} < 0.60$, leading to a molten gyroid phase. At $n^{(0)s} = 0.40$, the late-time structure becomes a *sponge* (microemulsion), isotropic and of short-range order, for which $S(\boldsymbol{k})$ is similar to that shown in fig. 2, top row. Although the observation of gyroid-related morphologies has earlier been claimed in Langevin-diffusion [11] and DPD [8] methods, the evidence was purely pictorial and not comprehensive —in fact, the structures more closely resemble molten gyroid states.

Figure 3 shows the time evolution of the spherically averaged structure function for the $n^{(0)s} = 0.60$ gyroid case and wave numbers corresponding to average domain sizes in $6.4 < L < 64$. Note three characteristic features of the curves: there are oscillations, decay (for $k < 0.83$ and $k > 1.1$, the latter not shown), and growth (for $0.88 < k < 1.0$ or $6.1 < L < 7.1$, close to the average domain size value). Modes of $k > 1.3$ ($L < 4.7$) decay fast enough ($S(k) < 0.1$ for $t \approx 1000$) that they do not contribute to the structure. The analogue curves for the $n^{(0)s} = 0.40$ case, leading to a sponge phase, exhibit similar oscillations, albeit of longer period. The fact that there are two types of temporal evolution, corresponding to increasing and decreasing modes, is a reflection of a phase segregation process still taking place. In the course of time, more domains accumulate in the $0.88 < k < 1.0$ range; we discard increasing interface steepness as another contributing factor to this, since oil/water diffusion is negligible in this regime.

Direct-space observation of the interface ($\phi = 0$) superimposed on surfactant density maps for a series of time slices allows us to ascribe the oscillations that mainly affect the growing modes to "self-sustained" Marangoni effects. These are caused by collective and inhomogeneous amphiphile adsorption and desorption to and from the (periodically modulated) interface, a region of high surfactant density. This permits us to set a time scale of between 100 and 500 time steps during which interfacial surfactant from regions of high density diffuses towards an adjacent interface (also with adsorbed surfactant), effectively forming a bridge between the two sheets. If the interfaces belong to boundary, inter-domain regions, where the global translational symmetry is broken, defects form, change shape and annihilate on the same time scale. Perusal of fig. 2 confirms that the smallest period of the oscillations is not dissimilar to such a time scale. The frequency spectrum of the time evolution of $S(k)$ gives a rich structure of peaks with a decaying envelope, higher-frequency modes becoming excited as the surfactant concentration increases.

Direct-space observation also shows an essential feature of the mesophase dynamics: each unit cell in the gyroid wanders in time about a fixed spatial position, whereas for the sponge the interface shows nonperiodic displacements. In other words, the temporal average of the displacement is zero for a gyroid's unit cell and nonzero for an interface element in the sponge phase. Displacements are small in the former: they are not larger than ca. 20% of the unit cell size and are in-phase with those of the unit cells belonging to the local, defect-delimited subdomain. We therefore expect the gyroid structure to be stable, *i.e.* the dynamics would relax to it for late times.

Temporal oscillations in the structure function of sponge phases have been reported previously by Gompper and Hennes via a stochastic Langevin diffusion equation method with hydrodynamics, based on a Ginzburg-Landau free energy [17]. This approach does not explicitly consider an order parameter for the amphiphile since it assumes that amphiphile relaxation is fast compared to that of the oil-water order parameter. The oscillations reported therein range from overdamped to underdamped depending on the wave number, and their frequency spectrum shows a single peak at finite frequency. This is in contradistinction to our finding of multiple-peak spectra, which we ascribe to the absence in that model of scalar or vector degrees of freedom for the amphiphile. In fact, Gompper and Hennes put forward a linearised Navier-Stokes model for Poiseuille flow wherein oscillations arise due to incompressibility competing with pressure gradients. Our LB method reproduces the same linearised, incompressible Navier-Stokes dynamics away from interfaces for the quiescent flows we observe, and, despite this, we obtain multiple-peak spectra. In addition, since stochastic sources are not present in the oil/water evolution, they cannot account for this spectral multiplicity. While it is true that randomness in the adsorbed surfactant directors may effectively reduce amphiphile adsorption strength, this effect is negligible compared to surfactant diffusion currents, facilitated by gradients of $\phi(\boldsymbol{x})$ from nearby interfaces.

Since the systems we simulate are dissipative and isolated (there is no mass or momentum exchange with external sources), oscillations are bound to die out at sufficiently late times. We observe interfacial widths to have reached their minimum (and hence interfacial tension its maximum) at about time step 1000, at which time the structure has a sponge-like morphology. Then the structure undergoes slow relaxation on a time scale which is $\mathcal{O}(10^4)$. We observe the pathway to equilibration to be a slow process dominated by currents created by surface tension and Marangoni effects acting on similar time scales. A free energy "leading the way" towards the equilibrium morphology might be less useful than a correct mesodynamics, and even bias the evolution; methods which are intrinsically mesoscopic *bottom-up* such as ours and DPD are better suited. From DPD simulations of copolymer melts [8], Groot and Madden found that melts of symmetric amphiphile led to lamellar phases, whereas a gyroid-like structure appeared only for asymmetric amphiphile as a transient phase precursor to a hexagonal columnar phase. Our results are in contradistinction to these: although our amphiphiles are symmetric, the gyroids we find are stable.

Finally, our reproduction of periodically modulated mesostructures rebuts claims that a necessary condition for their self-assembly is a disparity in the ranges of interaction of the competing morphogenic mechanisms, namely, short range *vs.* long range [18]. Unlike other mesoscopic approaches such as DPD, ours is strictly local, being based on nearest-neighbour interactions on a lattice.

The simulation of the gyroid cubic phase reported here highlights the richness of our model's parameter space. Our LB model represents a kinetically and hydrodynamically correct, bottom-up, mesoscale description of the generic behavior of amphiphilic fluids, which is also algorithmically simple and extremely computationally efficient on massively parallel platforms [19]. Natural extensions of this work include the search for regimes leading to equi-

librium mesophases of varied symmetries, the study of shear-induced symmetry transitions and the analysis of defect dynamics in large-scale simulations. Computational steering tools should prove invaluable in these respects [20].

* * *

Access to supercomputer resources was provided by the UK EPSRC under grants GR/M56234 and RealityGrid GR/R67699.

REFERENCES

[1] Seddon J. M. and Templer R. H., *Handbook of Biological Physics*, edited by Lipowsky R. and Sackmann E., Vol. **1** (Elsevier Science B. V., Amsterdam) 1995, p. 97.
[2] Klinowsky J., MacKay A. L. and Terrones H., *Philos. Trans. R. Soc. London, Ser. A*, **354** (1996) 1975.
[3] Laurer J. H., Hajduk D. A., Fung J. C., Sedat J. W., Smith S. D., Gruner S. M., Agard D. A. and Spontak R. J., *Macromolecules*, **30** (1997) 3938.
[4] Hajduk D. A., Harper P. E., Gruner S. M., Honeker C. C., Kim G. and Thomas E. L., *Macromolecules*, **27** (1994) 4063.
[5] Luzzati V., Vargas R., Mariani P., Gulik A. and Delacroix H. J., *Mol. Biol.*, **229** (1993) 540; Rummel G., Hardmeyer A., Widmer C., Chiu M. L., Nollert P., Locher K. P., Pedruzzi I., Landau E. M. and Rosenbusch J. P., *J. Struct. Biol.*, **121** (1998) 82.
[6] Dotera T. and Hatano A., *J. Chem. Phys.*, **105** (1996) 8413; Pakula T., Karatasos K., Anastasiadis S. H. and Fytas G., *Macromolecules*, **30** (1997) 8463.
[7] Groot R. D., Madden T. J. and Tildesley D. J., *J. Chem. Phys.*, **110** (1999) 9739.
[8] Groot R. D. and Madden T. J., *J. Chem. Phys.*, **108** (1998) 8713.
[9] Prinsen P., Warren P. B. and Michels M. A. J., *Phys. Rev. Lett.*, **89** (2002) 148302.
[10] Nonomura M. and Ohta T., *J. Phys. Condens. Matter*, **13** (2001) 9089; Imai M., Saeki A., Teramoto T., Kawaguchi A., Nakaya K., Kato T. and Ito K., *J. Chem. Phys.*, **115** (2001) 10525; Qi S. and Wang Z.-G., *Phys. Rev. E*, **55** (1997) 1682.
[11] Zvelindovky A. V., Sevink G. J. A. and Fraaije J. G. E. M., *Phys. Rev. E*, **62** (2000) R3063; van Vlimmeren B. A. C., Maurits N. M., Zvelindovsky A. V., Sevink G. J. A. and Fraaije J. G. E. M., *Macromolecules*, **32** (1999) 646.
[12] Marrink S.-J. and Tieleman D. P., *J. Am. Chem. Soc.*, **123** (2001) 12383.
[13] Chen H., Boghosian B. M., Coveney P. V. and Nekovee M., *Proc. R. Soc. London, Ser. A*, **456** (2000) 2043; Nekovee M., Coveney P. V., Chen H. and Boghosian B. M., *Phys. Rev. E*, **62** (2000) 8282.
[14] Succi S., *The Lattice-Boltzmann Equation—for Fluid Dynamics and Beyond* (Oxford University Press, Oxford) 2001.
[15] González-Segredo N., Nekovee M. and Coveney P. V., *Phys. Rev. E*, **67** (2003) 046304.
[16] Squires A. M., Templer R. H., Seddon J. M., Woenckhaus J., Winter R., Finet S. and Theyencheri N., *Langmuir*, **18** (2002) 7384.
[17] Gompper G. and Hennes M., *J. Phys. II*, **4** (1994) 1375.
[18] Seul M. and Andelman D., *Science*, **267** (1995) 476.
[19] Love P. J., Nekovee M., Coveney P. V., Chin J., González-Segredo N. and Martin J. M. R., *Comput. Phys. Commun.*, **153** (2003) 340.
[20] URL: `http://www.RealityGrid.org`; Chin J., Harting J., Jha S., Coveney P. V., Porter A. R. and Pickles S. M., *Contemp. Phys.*, **44** (2003) 417.

Coarsening dynamics of ternary amphiphilic fluids and the self-assembly of the gyroid and sponge mesophases: lattice-Boltzmann simulations

Nélido González-Segredo * and Peter V. Coveney †
Centre for Computational Science, Department of Chemistry, University College London, 20 Gordon Street, London WC1H 0AJ, UK
(Dated: March 29, 2004)

By means of a three-dimensional amphiphilic lattice-Boltzmann model with short-range interactions for the description of ternary amphiphilic fluids, we study how the phase separation kinetics of a symmetric binary immiscible fluid is altered by the presence of the amphiphilic species. We find that a gradual increase in amphiphile concentration slows down domain growth, initially from algebraic, to logarithmic temporal dependence, and, at higher concentrations, from logarithmic to stretched-exponential form. In growth-arrested stretched-exponential regimes, at late times we observe the self-assembly of sponge mesophases and gyroid liquid crystalline cubic mesophases, hence confirming that (a) amphiphile-amphiphile interactions need not be long-ranged in order for periodically modulated structures to arise in a dynamics of competing interactions, and (b) a chemically-specific model of the amphiphile is not required for the self-assembly of cubic mesophases, contradicting claims in the literature. We also observe a structural order-disorder transition between sponge and gyroid phases driven by amphiphile concentration alone or, independently, by the amphiphile-amphiphile and the amphiphile-binary fluid coupling parameters. For the growth-arrested mesophases, we also observe temporal oscillations in the structure function at all length scales; most of the wavenumbers show slow decay, and long-term stationarity or growth for the others. We ascribe this behaviour to a combination of complex amphiphile dynamics leading to Marangoni flows.

I. INTRODUCTION

The term *amphiphilic fluid* is broadly used to denote multiphase fluids in which at least one species is of a surfactant nature. A surfactant molecule (from *surf*ace *act*ive ag*ent*, which we shall also refer to as an amphiphile) contains a polar headgroup attached to a hydrocarbon tail which, dispersed in a binary immiscible fluid mixture, such as oil and water, is driven towards and adsorbed at the interface between the two fluids. The selective chemical affinity between each part of the surfactant molecule and the components of the binary mixture is the mechanism responsible for such a taxis [1]. Not only are amphiphilic fluids important in physical chemistry, structural biology, soft matter physics and materials science from a fundamental perspective, but their applications are also widespread. Detergents and mammalian respiration are two common examples in which surfactants are present. Living cell membranes are complex macromolecular assemblies comprised in large part of self-assembled phospholipids, of an amphiphilic nature [2]. Sponge mesophases are formed as a result of an amphiphile dispersion or melt at an appropriate composition, and enjoy numerous applications in medical research as well as the pharmaceutical, cosmetic, food, and agro- and petrochemical industries [3, 4]. Liquid-crystalline bicontinuous cubic mesophases of monoglycerides and the lipid extract from archaebacterium *Sulfolobus solfataricus* have been found at physiological conditions in cell organelles and physiological transient processes such as membrane budding, cell permeation and the digestion of fats [5]. Amphiphilic cubic mesophases can also be synthesised for important applications in membrane protein crystallisation, controlled drug release and biosensors [6, 7]. These phases are termed *mesophases* not only because their intrinsic internal length scales range between those characteristic of molecular and hydrodynamic (or macroscopic) realms, but also their mechanical properties are half-way between those found in a liquid and a solid [1, 2, 8].

Amphiphiles have the property of lowering the interfacial tension in a binary immiscible, say oil-water, fluid [8]. Given the bipolar nature of their molecular structure, amphiphile adsorption at the oil-water interface is a process which is energetically favoured relative to their entropically beneficial dispersion in the bulk. This effectively reduces the pressure tensor at the interface, making the immiscible species more alike. As more interfacial surface is created, so more amphiphile dispersed in the bulk can be accommodated at it.

The effect of adding surfactant above a critical concentration to an oil-water mixture undergoing phase separation is to slow down the demixing process, which, with the addition of sufficient amphiphile, can be totally arrested. Langevin, molecular dynamics and lattice gas simulations have shown that, as the concentration of dispersed surfactant increases, the temporal growth law of the average size of the immiscible oil-water domains, of the power-law form t^a in the surfactantless

*n.gonzalez-segredo@ucl.ac.uk. Also at Departament de Física, Universitat Autònoma de Barcelona, 08193 Bellaterra, Barcelona, Spain.
†p.v.coveney@ucl.ac.uk

case [9, 10], is seen to cross over to a slower, logarithmic growth of the form $(\ln t)^\theta$, where a and θ are fitting parameters and t is the time [11–13]. Emerton *et al.* showed that increasing the surfactant concentration even further leads to growth well described by the stretched exponential $A - B\exp(-Ct^D)$, where A, B, C and D are fitting parameters, including halted segregation at sufficiently late times [13]. Depending on temperature, pressure and fluid composition in such a stretched exponential regime, the amphiphile can self-assemble and force the oil-water mixture into a wealth of equilibrium structures. The self-assembling process is dictated by the competing attraction-repulsion mechanisms present among the species. Lamellae and hexagonally-packed cylinders are examples of these mesophases, also referred to as L_α and H, respectively, with continuous translational symmetry along one or two directions. Other examples are the sponge (L_3) mesophase and the micellar (Q^{223} or $Pm3n$, and Q^{227} or $Fd3m$), primitive ("P", Q^{229} or $Im3m$), diamond ("D", "F", Q^{224} or $Pn3m$) and gyroid ("G", Q^{230} or $Ia\bar{3}d$) cubic mesophases, all of which lack continuous translational symmetry [14]. Among all the aforementioned phases, only the sponge mesophase is devoid of long-range order and so cannot be classified as a liquid crystal: it is rather characterised by glassy features.

A sponge mesophase formed by the amphiphilic stabilisation of a phase-segregating binary fluid mixture is called a microemulsion. Since we shall be dealing with oil and water in equal proportions, we shall be concerned with bicontinuous microemulsions. A bicontinuous microemulsion is a structure consisting of two percolating, interpenetrating oil and water phases separated by a monolayer of surfactant molecules adsorbed at the interface. Oil and water are isotropically mixed, and ordering is short range. Sponge phases formed by the dispersion of amphiphile in a single phase solvent differ from microemulsions in that it is a surfactant bilayer which underlies the structure, and the regions it divides are occupied by the same fluid component. A gyroid phase is also a bicontinuous, interpenetrating structure; however, ordering is evidently long range, whence its classification as a liquid crystal. In the gyroid, the locus where most of the surfactant resides is a triply periodic minimal surface (TPMS) whose unit cell is of cubic symmetry. The surface has zero mean curvature, no two points on it are connected by a straight segment, and no reflexion symmetries are present. Isosurfaces of the gyroid phase for which oil and water are not at equal composition (minority phases) form mutually percolating, three-fold coordinated, regular lattices. Other examples of triply periodic surfaces of zero mean curvature arise in the P and D mesophases, the minority phase isosurfaces of which exhibit coordination numbers of six and four, respectively.

The purpose of the present paper is to report on a theoretical study of the segregation kinetics in ternary amphiphilic fluids and the self-assembly of the sponge and gyroid mesophases. By progressively adding surfactant to an initially homogeneous immiscible oil-water mixture on the way to achieving arrested domain growth, we shall give an account of how the segregation kinetics of the fluid domains is affected by the addition of surfactant, and study the features of the associated mesophases that are formed. The mesophases corresponding to such late time, arrested growth regimes are sponges which turn into gyroids as we increase the surfactant concentration. We shall also see that these phases exhibit temporal oscillations in the size of the oil-water domains, which we ascribe to Marangoni flows.

II. OVERVIEW OF MODELLING AND SIMULATION OF AMPHIPHILIC FLUID SELF-ASSEMBLY

Various methods have been used to date to model and simulate ternary amphiphilic mixtures and to study their phase segregation kinetics and the formation of microemulsions and liquid crystalline phases. We briefly review them in this section.

Kawakatsu *et al.* studied segregation kinetics employing a two dimensional hybrid model with thermal noise but without hydrodynamics, combining a continuum, Langevin diffusion equation for the oil-water dynamics and Newtonian dynamics with dissipation for bipolar particles modelling the surfactant [11]. They used a free energy in the form of a ϕ^4-Ginzburg-Landau expansion [15] plus terms modelling the surfactant-interface and surfactant-surfactant interactions. They found the average domain size of symmetric binary immiscible fluids with amphiphile to grow with time more slowly than $t^{1/3}$, the latter expected for binary alloys in two and three dimensions. Laradji *et al.*, instead of modelling the amphiphile as a particulate species, regarded it as a continuous density coupled to the oil-water order parameter in a ϕ^4-Ginzburg-Landau free energy [12]. In their work, they studied several cases of two-dimensional Langevin diffusion equations, one of which being the so-called Model D [16]. Model D incorporates noise, a conserved order parameter and surfactant density, but excludes hydrodynamics. Laradji *et al.* not only found logarithmic growth for the behaviour of the average domain size with time, but also observed a slowdown from it for higher surfactant concentrations and dynamical scaling for the structure function at intermediate times. Yao & Laradji, using a modified Lifshitz-Slyozov nucleation theory for continuum fields in two and three dimensions, studied how the Ostwald ripening dynamics of an asymmetric mixture of oil and water is altered by the presence of a surfactant species [17]. They found results similar to those of Laradji *et al.* [12].

The segregation kinetics of amphiphilic fluids have also been studied with fully particulate methods such as clas-

sical molecular dynamics and, more recently, hydrodynamic lattice gases. Using a minimalist molecular dynamics model in two dimensions, Laradji *et al.* [18] found a crossover scaling function similar to previous Langevin [11] and Lifshitz-Slyozov models [17], yet with a different algebraic exponent, and a slowing down from the algebraic growth laws for binary mixtures. Using two-dimensional hydrodynamic lattice gas models for symmetric [13] and asymmetric mixtures [19], the group of Coveney found that surfactant induces a crossover to a logarithmic slow growth, and, with sufficient surfactant, full arrest of domain growth which is well described by a stretched exponential function. The group found similar results with a three-dimensional hydrodynamic lattice gas model [20].

Particulate methods have also been used to tackle mesophase self-assembly. Using classical molecular dynamics methods, Marrink *et al.* simulated evolution of a surfactant bilayer, initially set up on the morphology of a "D" TPMS, to study both the surfactant packing structure and how close such a bilayer would remain to the TPMS after relaxation [6]. They, however, did not address self-assembly dynamics: time scales required for that are orders of magnitude above those reachable with atomistic techniques on present-day cutting-edge supercomputers. In dissipative particle dynamics (DPD) approaches, a Langevin dynamics with momentum conservation is solved to model ill-defined, mesoscopic dissipative particles interacting via repulsive, soft potentials; hydrodynamics is emergent and the amphiphile is represented by dissipative particles bound together by rods or springs [21–23]. The DPD simulations of Groot & Madden of copolymer melts [21] showed that melts of symmetric amphiphile led to lamellar phases, whereas a gyroid-like structure appeared only for asymmetric amphiphile as a transient phase, precursor to a hexagonally packed tubular phase. Nekovee & Coveney, using the lattice-Boltzmann model we employ in this work, were able to reproduce the "P" mesophase in a binary amphiphilic mixture of surfactant and solvent [24].

Many of the simulation studies on the formation kinetics of microemulsion and liquid crystalline mesophases have made use of stochastic Langevin diffusion methods, in which mass currents are driven by chemical potential gradients computed from free energies of the ubiquitous ϕ^4-Ginzburg-Landau expansion form. These models treat the amphiphile only implicitly through the functional dependence of the surface tension parameter with the amphiphile density [25–29]. In cases in which the amphiphile is a copolymer, however, the free energy is often derived from polymer models which aim at accounting for the amphiphile's molecular structure with a certain degree of specificity [30–32]. The validity of these Flory-Huggins type approaches rests on being able to derive the free energy from a microscopic model of the complex fluid mixture, which not only might entail considerable difficulty but does require the segregation to be a quasi-static, local equilibrium process. Under general far from equilibrium conditions, such as occurs in the sudden-quench scenario so often employed in the literature, equilibrium thermodynamic potentials are known not to adequately describe the process. Besides, free energy based methods also require surfactant adsorption and relaxation on the interface to be much faster than interface motion, a so-called *adiabatic approximation*. Free energy approaches are frequently represented as paradigms of thermodynamically consistent mesoscopic methods; some of them also pursue chemical specificity in elaborate empirical exercises amounting to little more than parameter fitting of polymer models. The philosophy behind them, nonetheless, is the use of macroscopic, local equilibrium information to specify a stochastic, and hence mesoscopic, non-equilibrium dynamics. None of these methods offers a dynamics satisfying detailed balance, let alone an H-theorem (Lyapunov function) guaranteeing irreversible evolution towards the equilibrium state described by the prescribed free energy. As a consequence, the 'thermodynamic consistency' of these methods remains on shaky grounds.

The fact that some free energy approaches [31, 32] focus on the specific molecular structure of the amphiphile raises the question of what use particulate methods, such as is the one we report in this paper, have in the simulation of amphiphilic fluid systems. Our method, by reducing the description of the amphiphilic molecule to its minimal possible expression—a point dipole, retains the minimum number of degrees of freedom necessary to model interfacial adsorption and micellisation, and, additionally, in a hydrodynamically consistent framework which does not require processes to be quasi-static. With these basic properties at our disposal, we want to fully exploit our model's capabilities to determine the non-equilibrium amphiphilic dynamics and the equilibrium fluid structures arising from it. The minimalistic bottom-up approach is in line with the fact that, far enough from criticality, distinct molecular structures and microscopic dynamics can produce similar macroscopic behaviour—this is universality emerging from microscopic complexity [33]. In addition, particulate methods are much more suitable than conventional continuum fluid dynamics methods [34] for the simulation of interface dynamics. Such dynamics is an emergent property of the underlying inter-particle interactions among the immiscible species; a set of continuum partial differential equations describing the locus of the interface is, rather, its macroscopic manifestation, and its solution a much more labourious endeavour. *A fortiori*, modelling surfactant adsorption and self-assembly in an explicit fashion via particulate methods provides a more realistic picture of the microscopics than doing so at the continuum, macroscopic limit described by free-energy approaches.

Lattice-Boltzmann (LB) methods were originally de-

veloped as a means of reducing the computational cost associated with lattice-gas automaton (LGA) algorithms [35]. LB methods evolve a single-particle distribution function via a discretised Boltzmann equation, usually in the linearised, relaxation-time (BGK) approximation. Such a single-particle distribution, at a particular time slice and spatial position on the lattice, is an average over the LGA velocity space for a statistically large number of different microscopic realisations (initial conditions). The fact that much of the phenomenology of binary immiscible and ternary amphiphilic fluids occurs for small spatio-temporal gradients permits us to take the mean-field (or molecular chaos) approximation, and the Boltzmann-Grad limit in which such an approximation holds, as heuristically appropriate for the modelling of their universal properties. Heuristics come into play in that tunable parameters are introduced in LB models in order to reproduce desired quantities of dense and/or complex fluids, such as surface tension, viscosity and thermal conductivity (for required values of Reynolds and Prandtl numbers), stress tensors (for required viscous or viscoelastic behaviour), and equations of state (for liquid-gas and phase segregating transitions). It is worth noting that the increasing popularity of LB methods in recent years is primarily based on pragmatic considerations associated with their simplicity and algorithmic efficiency.

This paper presents the first quantitative account of amphiphilic phase segregation dynamics using a three-dimensional model based on the Boltzmann transport equation. It describes the spontaneous self-assembly of the gyroid liquid crystalline cubic mesophase and an order-disorder transition between the latter and the sponge mesophase, of glassy features. The remainder of the paper is structured as follows. In Section III we describe the model. In Section IV we look at how the segregation kinetics of the fluid domains is affected by the addition of surfactant. Section V studies the temporal oscillations of the average domain size and the structure function, which are only observed for segregation-halted regimes. In Section VI we characterise the morphology of the mesophases corresponding to those regimes via direct- and Fourier-space imaging, and identify the sponge↔gyroid structural transition. Finally, we provide conclusions in Section VII.

III. A LATTICE-BOLTZMANN MODEL FOR TERNARY AMPHIPHILIC FLUIDS

The amphiphilic lattice-Boltzmann model we employ in this paper is derived from that originally proposed by Chen *et al.* [36, 37]. The method can be regarded as a fully mesoscopic, bottom-up approach, which does not require the existence of a thermodynamic potential describing phase transitions. In fact, the method is athermal in the sense that, for algorithmic efficiency reasons, the microdynamics is devised *ex professo* to conserve velocity moments of the distribution function only up to first-order; this simplification is valid wherever thermal fluctuations are negligible, e.g. away from criticality. This is, for example, the case of deep quenches into the spinodal region of the fluid's phase diagram, which is our case in this paper. As opposed to top-down LB methods, based on the imposition of a free energy functional [38, 39], the global dynamics arise as an emergent property of the interactions between mesoscopic levels of description, in agreement with a complexity paradigm [33]. Oil-water segregation is achieved via inter-species forces which modify the fluid's macroscopic velocity. The dynamics in the bulk of each binary immiscible species (e.g. oil and water) can be derived from a Boltzmann equation with a forcing term. An amphiphilic molecule is modelled as a continuously orientable massive point dipole subjected to thermal noise and relaxing towards an equilibrium that minimises its interaction energy with mean fields generated by its nearest neighbours on the lattice. The densities of surfactant, oil and water evolve via coupled lattice-BGK equations. This is a mean-field approach which exhibits Galilean invariance and reproduces correct hydrodynamics. We have also shown, in a previous paper which serves as a reference benchmark for this study [9], that the model reproduces the dynamical scaling hypothesis during the phase segregation experienced by binary immiscible (oil-water) fluids. Its algorithmic simplicity allows it to achieve extremely high performance on massively parallel computers [40], and substantially reduces the domain of numerical instability present in free-energy-based LB methods [9]. Because an H-theorem is lacking in essentially all multiphase lattice-Boltzmann models hitherto proposed [41], we consider it artificial to try to enforce a prescribed thermodynamic equilibrium in these schemes; a method which is algorithmically simpler, fully mesoscopic, mean-field and bottom-up is of greater fundamental interest.

A. Binary immiscible fluids

The core of our model is a lattice-BGK equation governing the evolution of the mass density distribution $m^\alpha n_k^\alpha(\mathbf{x},t)$ of component α in an interacting fluid mixture at position $\mathbf{x}$, instant t, and for discrete molecular velocity $\mathbf{c}_k$, on a regular lattice and in discrete time. Here, m^α is the particle mass which we set to unity for convenience, and the single-particle distribution $n_k^\alpha(\mathbf{x},t)$ obeys the lattice-BGK relaxation-streaming mechanism:

$$n_k^\alpha(\mathbf{x}+\mathbf{c}_k,t+1)-n_k^\alpha(\mathbf{x},t)=\Omega_k^\alpha\,, \qquad (1)$$

where the collision term has two contributions accounting for the kinetics of non-interacting (ideal) plus interacting

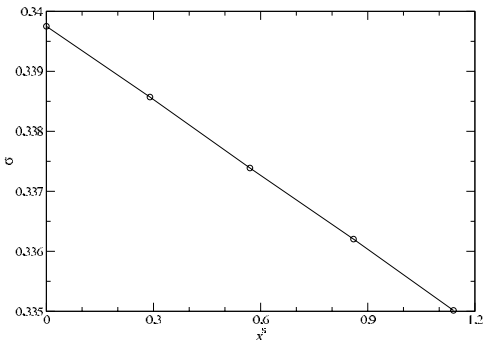

FIG. 1: Surface tension dependence on the surfactant concentration (mass fraction, *cf.* Table I) as measured at a planar interface making use of Eq. (15). A lattice of size $4 \times 4 \times 128$ was allowed to evolve up to time step 25000, and pressure tensor components were measured every 1000 time steps. The surface tension tends to grow with time and reaches a horizontal asymptote; at that time step the surface tension only differs in 16% from that at the previous measurement. Interpolation serves as a reference to the eye. Coupling constants used were $g_{\rm br} = 0.08$, $g_{\rm bs} = -0.006$, and $g_{\rm ss} = -0.003$. Oil and water densities used were $n^{(0)\rm R} = n^{(0)\rm B} = 0.7$. All quantities are reported in lattice units.

(non-ideal) multicomponent species, respectively:

$$\Omega_k^\alpha(\mathbf{x},t) \equiv \Omega_k^{(0)\alpha}(\mathbf{x},t) + \sum_{\bar\alpha}\sum_l \Lambda_{kl}^{\alpha\bar\alpha} n_l^{\bar\alpha}\,. \qquad (2)$$

the sums extending over all available species and directions, and

$$\Omega_k^{(0)\alpha}(\mathbf{x},t) \equiv -\frac{n_k^\alpha(\mathbf{x},t) - n_k^{\alpha(\rm eq)}(\mathbf{x},t)}{\tau^\alpha}\,. \qquad (3)$$

Here, the time increment and lattice spacing are both unity, $\mathbf{x}$ is a node of such a lattice, $\alpha = \mathrm{r}, \mathrm{b}$ (e.g. oil (r) or water (b)), and $\mathbf{c}_k$ is one of the 24 ($\equiv N_{\rm vec}$) discrete velocity vectors plus one null velocity of the projected face centred hypercubic D4Q25 lattice we use to guarantee isotropy in the macroscopic equations that the model reproduces for a bulk, single phase fluid [42]. The parameter τ^α defines a single relaxation rate towards equilibrium for component α, $\Lambda_{kl}^{\alpha\bar\alpha}$ can be regarded as a matrix element of a cross-collision operator Λ which is a function of both τ^α and the acceleration $\mathbf{a}^\alpha$, the latter being experienced by a fluid element due to its neighbours, as will be defined later. The function $n_k^{\alpha(\rm eq)}(\mathbf{x},t)$ in Eq. (3) is the discretisation of a third-order expansion in Mach number of a local Maxwellian [9], representing the local equilibrium state of the αth component,

$$n_k^{\alpha(\rm eq)}(\mathbf{x},t) = \omega_k\, n^\alpha(\mathbf{x},t)\Big[1 + \frac{1}{c_s^2}\mathbf{c}_k\cdot\mathbf{u} + \frac{1}{2c_s^4}(\mathbf{c}_k\cdot\mathbf{u})^2 - \frac{1}{2c_s^2}u^2 + \frac{1}{6c_s^6}(\mathbf{c}_k\cdot\mathbf{u})^3 - \frac{1}{2c_s^4}u^2(\mathbf{c}_k\cdot\mathbf{u})\Big] \qquad (4)$$

where ω_k are the coefficients resulting from the velocity space discretisation, and c_s is the speed of sound, both of which are determined by the choice of the lattice. For the projected D4Q25 lattice we use, the speed of sound is $c_s = 1/\sqrt{3}$, $\omega_k = 1/3$ for the speed $c_k = 0$, and $1/36$ for speeds $c_k = 1$ and $\sqrt{2}$. In Eq. (4), $\mathbf{u} = \mathbf{u}(\mathbf{x},t)$ is the macroscopic velocity of the mixture, through which the collision term couples the different molecular velocities $\mathbf{c}_k$. This is because $\mathbf{u}$ is a function of the components' macroscopic velocities, defined as $n^\alpha(\mathbf{x},t)\,\mathbf{u}^\alpha \equiv \sum_k n_k^\alpha(\mathbf{x},t)\,\mathbf{c}_k$.

A judicious choice of the coefficients in the expansion of the equilibrium distribution Eq. (4) allows for mass and momentum to be (non-locally) conserved for the non-interacting, ideal gas mixture case, i.e.

$$\sum_k \Omega_k^{(0)\alpha} = 0\,, \qquad \sum_\alpha m_\alpha \sum_k \mathbf{c}_k \Omega_k^{(0)\alpha} = 0\,. \qquad (5)$$

It can be shown that in the limit of creeping flows to second order, i.e. $u^2 \approx 0$, the expression for the fluid mixture's macroscopic velocity $\mathbf{u}$ required for momentum conservation in the absence of interactions, as a function of $\mathbf{u}^\alpha$, simplifies to that obtained for a second-order expansion of the equilibrium distribution, namely $\mathbf{u} \equiv \sum_\alpha \frac{\rho^\alpha \mathbf{u}^\alpha}{\tau^\alpha} / \sum_\alpha \frac{\rho^\alpha}{\tau^\alpha}$, which we have incorporated in our implementation.

The form of the collision term (2) derives from adding an increment $\Delta\mathbf{u}^\alpha$ to the fluid mixture's macroscopic velocity $\mathbf{u}$ which enters in the equilibrium distribution (4), i.e. $\Omega_k^\alpha(\mathbf{u}) \equiv \Omega_k^{(0)\alpha}(\mathbf{u} + \Delta\mathbf{u}^\alpha)$ where $\Delta\mathbf{u}^\alpha \equiv \mathbf{a}^\alpha\tau^\alpha$ and $\mathbf{a}^\alpha \equiv \mathbf{F}^\alpha/\rho^\alpha$. Here

$$\mathbf{F}^{\alpha,\rm c}(\mathbf{x},t) \equiv -\psi^\alpha(\mathbf{x},t)\sum_{\bar\alpha} g_{\alpha\bar\alpha}\sum_{\mathbf{x}'}\psi^{\bar\alpha}(\mathbf{x}',t)(\mathbf{x}'-\mathbf{x}) \qquad (6)$$

is the mean-field force density felt by phase α at site $\mathbf{x}$ and time t due to its surroundings; $g_{\alpha\bar\alpha}$ is a coupling matrix controlling the interfacial tension between the fluid species, interface adsorption/desorption properties of the surfactant molecules, and the surfactant-surfactant interaction; ψ^α is an *effective mass* which serves as a functional parameter and can have a variety of forms for modelling various types of fluids. We only allow nearest-neighbour interactions, $\mathbf{x}' \equiv \mathbf{x} + \mathbf{c}_k$, and choose $\psi^\alpha(\mathbf{x},t) \equiv 1 - \exp\Big[-n^\alpha(\mathbf{x},t)\Big]$, where $n^\alpha \equiv \sum_k n_k^\alpha$. This choice for ψ has also been made by Shan and Chen to model liquid-gas phase transitions [43] although, as we shall see, our motivation here is different.

B. Amphiphilic fluids

The incorporation of a third, amphiphilic species not only requires the inclusion of an extra variable ("s") for the superscript denoting the species in Eq. (1), but also a modification of the cross-collision operator Λ since amphiphiles interact with fluid elements and between themselves. In addition, the physics of amphiphilic molecules,

namely, self-assembly and adsorption to immiscible fluid interfaces, cannot be modelled without introducing a new type of body force: in Subsection III A ordinary bulk fluid species are thought of as point-like particles given that their interactions depend on their relative distances alone. For surfactant molecules, however, their orientations are important too [36], and a dipole is the simplest configuration to mimic their essential character. In short, we must extend the scalar lattice-BGK model hitherto described into a vector model.

Each surfactant molecule is represented by an average dipole vector $\mathbf{d}(\mathbf{x},t)$ at each site and time step, whose orientation is allowed to vary continuously. The average is taken over nearest neighbours before advection, according to the propagation equation

$$n^{\mathrm{s}}(\mathbf{x},t+1)\mathbf{d}(\mathbf{x},t+1)=\sum_k \tilde{n}^{\mathrm{s}}_k(\mathbf{x}-\mathbf{c}_k,t)\tilde{\mathbf{d}}(\mathbf{x}-\mathbf{c}_k,t)\,, \tag{7}$$

where the tildes denote post-collisional values, as defined by Eq. (1) for the $\Lambda\equiv 0$ ($g_{\alpha\bar{\alpha}}\equiv 0$) case if we replace the leftmost summand with $\tilde{n}^{\alpha}_k(\mathbf{x},t)$. For the sake of simplicity and computational efficiency, the model does not assign microscopic velocities $\mathbf{c}_k$ to single dipole vectors but to site-averaged surfactant densities instead, as can be seen, for example on the right hand side of Eq. (7).

Dipole relaxation is governed by the BGK process

$$\tilde{\mathbf{d}}(\mathbf{x},t)=\mathbf{d}(\mathbf{x},t)-\frac{1}{\tau^{\mathrm{s}}}\Big[\mathbf{d}(\mathbf{x},t)-\mathbf{d}^{\mathrm{eq}}(\mathbf{x},t)\Big]\,, \tag{8}$$

where τ^{s} is a new parameter controlling the relaxation towards the local equilibrium $\mathbf{d}^{\mathrm{eq}}(\mathbf{x},t)$, which is understood as the average orientation with respect to the Gibbs measure, i.e.

$$\mathbf{d}^{\mathrm{eq}}(\mathbf{x},t)\equiv d_0\,\frac{\int \mathrm{d}^2\Omega\;\mathrm{e}^{-\beta H_{\hat{\Omega}}(\mathbf{x},t)}\hat{\Omega}}{\int \mathrm{d}^2\Omega\;\mathrm{e}^{-\beta H_{\hat{\Omega}}(\mathbf{x},t)}}\,, \tag{9}$$

where $\mathrm{d}^2\Omega$ is an element of solid angle whose director is the unit vector $\hat{\Omega}$ representing the dipole orientation, and β is an inverse temperature-like parameter. The modulus of the distribution (9) ranges between 0 and the scale value d_0, chosen to be unity for convenience. That, along with $\tau^{\mathrm{s}}\geq 1$, guarantee the magnitude of the dipole vector to be less than d_0 at all times. Equation (9) favours surfactant orientations which minimise the *energy* $H_{\hat{\Omega}}\equiv -\hat{\Omega}\cdot\mathbf{h}(\mathbf{x},t)$, where $\mathbf{h}(\mathbf{x},t)$ is the sum of the mean fields created by surrounding bulk fluid and surfactant, namely

$$\mathbf{h}^{\mathrm{c}}(\mathbf{x},t)\;\equiv\;\sum_\alpha q_\alpha\sum_k n^\alpha(\mathbf{x}+\mathbf{c}_k,t)\mathbf{c}_k\,, \tag{10}$$

$$\mathbf{h}^{\mathrm{s}}(\mathbf{x},t)\equiv\;\sum_k\Big[n^{\mathrm{s}}_k(\mathbf{x},t)\mathbf{d}(\mathbf{x},t)+\sum_{l\neq 0} n^{\mathrm{s}}(\mathbf{x}+\mathbf{c}_l,t)\theta_l\cdot\mathbf{d}(\mathbf{x}+\mathbf{c}_l,t)\Big]\,. \tag{11}$$

allowing for nearest-neighbour interactions only. The first equation is a discrete approximation to the colour gradient for the immiscible species, where $q_\alpha=0,\pm 1$ is the colour charge of species α. The second equation is a dipole vector density, where summation over k performs local dipole averaging, summation over l includes all nearest neighbour contributions, and the second-rank tensor $\theta_l\equiv\mathbf{I}-D\mathbf{c}_l\mathbf{c}_l/c^2$, where c is the modulus of $\mathbf{c}_l$ and D is the spatial dimension, picks up desired orientations from nearest-neighbour dipoles. Finally, Eq. (9) can be integrated analytically in three dimensions to give $\mathbf{d}^{\mathrm{eq}}=d_0\Big[\coth(\beta h)-\frac{1}{\beta h}\Big]\hat{\mathbf{h}}$, where h is the magnitude of $\mathbf{h}$ and $\hat{\mathbf{h}}$ its unit vector.

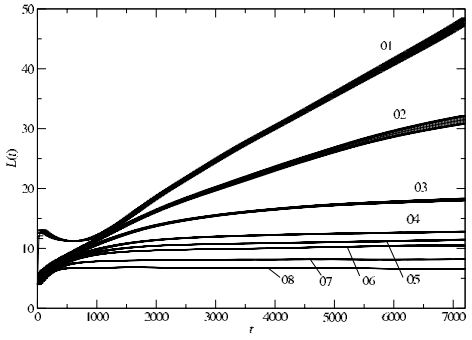

FIG. 2: Temporal evolution of the average fluid-fluid domain size for surfactant concentrations 0.0, 0.15, 0.22, 0.30, 0.35, 0.40, 0.60 and 0.90 for curves from top to bottom and corresponding to simulation runs 01, 02, 03, 04, 05, 06, 07 and 08, respectively (*cf.* Table I). Measurements have been taken every 25 time steps, and the plots include error bars, which represent the uncertainty (one standard error) transmitted from the standard error of the structure function spherical average. We used a lattice of size 128^3 for simulation run 01 and 64^3 for the remaining curves, since finite size effects start to creep in for domain sizes larger than $L\approx 30$. All quantities are reported in lattice units. Note that the surfactant-containing fluids lack the zero-growth, linear transient found for simulation run 01 [11].

The new interactions that modify the interspecies collision operator Λ are the force on an immiscible fluid element from other fluid elements and amphiphiles, $\mathbf{F}^\alpha\equiv g_{\mathrm{br}}\mathbf{F}^{\alpha,\mathrm{c}}+g_{\mathrm{bs}}\mathbf{F}^{\alpha,\mathrm{s}}$, where $\mathbf{F}^{\alpha,\mathrm{c}}$ is that in Eq. (6), and the force on an amphiphilic molecule from neighbouring fluid elements and amphiphiles, $\mathbf{F}^{\mathrm{s}}\equiv g_{\mathrm{bs}}\mathbf{F}^{\mathrm{s,c}}+g_{\mathrm{ss}}\mathbf{F}^{\mathrm{s,s}}$. In these expressions, g_{br}, g_{bs} and g_{ss} are coupling scalar parameters, and the analytical expressions for each force

term, derived in [36], are

$$\mathbf{F}^{\alpha,\mathrm{s}} \equiv -2g_{\alpha\mathrm{s}}\psi^{\alpha}(\mathbf{x},t)\sum_{k\neq 0}\tilde{\mathbf{d}}(\mathbf{x}+\mathbf{c}_l,t)\theta_l\cdot\psi^{\mathrm{s}}(\mathbf{x}+\mathbf{c}_l,t) \tag{12}$$

$$\mathbf{F}^{\mathrm{s},\mathrm{c}} \equiv 2\psi^{\mathrm{s}}(\mathbf{x},t)\tilde{\mathbf{d}}(\mathbf{x}+\mathbf{c}_l,t)\cdot\sum_{\alpha}g_{\alpha\mathrm{s}}\sum_{k\neq 0}\theta_k\psi^{\alpha}(\mathbf{x}+\mathbf{c}_k,t) \tag{13}$$

$$\mathbf{F}^{\mathrm{s},\mathrm{s}} \equiv -\frac{4D}{c^2}g_{\mathrm{ss}}\psi^{\mathrm{s}}(\mathbf{x},t)\sum_{k}\Big\{\tilde{\mathbf{d}}(\mathbf{x}+\mathbf{c}_k,t)\cdot\theta_k\cdot\tilde{\mathbf{d}}(\mathbf{x},t)\mathbf{c}_k + \Big[\tilde{\mathbf{d}}(\mathbf{x}+\mathbf{c}_k,t)\tilde{\mathbf{d}}(\mathbf{x},t)+\tilde{\mathbf{d}}(\mathbf{x},t)\tilde{\mathbf{d}}(\mathbf{x}+\mathbf{c}_k,t)\Big]\cdot\mathbf{c}_k\Big\}\times \psi^{\mathrm{s}}(\mathbf{x}+\mathbf{c}_k,t)\,. \tag{14}$$

Equations (12), (13), and (14) were derived considering only nearest-neighbour interactions, modelling each dipole as a dumbell of oppositely colour-charged particles displaced $\pm\mathbf{d}/2$ from the dipole's centre of mass location $\mathbf{x}$, and carrying out Taylor expansions of the force (6) to leading order in $\mathbf{d}$ about $\mathbf{x}$ as well as those at the neighbouring sites [36]. Also, Eq. (13) is the reaction to force (12), and Taylor expansions in the ratio of $|\mathbf{c}_k|$ to the length scale that the colour gradient sets can be used to further simplify the expressions. Finally, additional coupling parameters $g_{\alpha\mathrm{s}}$ have been introduced, where g_{ss} should be chosen negative to model attraction between two amphiphile heads or tails, and repulsion between a head and a tail.

C. Selection of the parameters for the simulations

The model is implemented as a parallel code in Fortran90 making use of the Message Passing Interface parallel paradigm [44] and spatial domain decomposition, and incorporating wrap-around, periodical boundary conditions. It was executed on 16 to 64 processors on SGI Origin2000 and Origin3800 parallel platforms. The form $\psi \equiv 1-\exp[-n(\mathbf{x},t)]$ for the effective mass in the force in Eq. (6) was heuristically chosen so as to broaden the region of numerical stability in parameter space: numerical instabilities can arise as the result of high values of forces and speeds, and are more likely to occur in our model when surfactant interactions are included than for binary immiscible fluids [9, 45].

Preliminary studies allowed us to determine the values of the model's various parameters for which an initially thorough mixture of two immiscible fluid phases plus a dispersed amphiphilic species produced a segregated mixture with arrested domain growth [45]. Those values were the surfactant thermal parameter $\beta = 10.0$, all particle masses and relaxation times set to 1.0, and coupling constants $g_{\mathrm{br}} = 0.08$, $g_{\mathrm{bs}} = -0.006$, and $g_{\mathrm{ss}} = -0.003$. (Masses, m^{α}, enter in the description through $\rho^{\alpha}(\mathbf{x},t) \equiv \sum_k m^{\alpha}n_k^{\alpha}(\mathbf{x},t)$.) We simulated the behaviour of a ternary mixture by varying the coupling constants around the values mentioned above, and for initial surfactant particle densities ranging in the interval $0.00 \leq n^{(0)\mathrm{s}} \leq 0.90$. The lattice sites and directions were initially populated with flatly distributed mass densities, $0 \leq \rho_k^{\alpha}(\mathbf{x},0) \leq m^{\alpha}n^{(0)\alpha}/N_{\mathrm{vec}}$, where $n^{(0)\alpha}$ is the particle density of phase α, and k numbers each of the $N_{\mathrm{vec}} = 24$

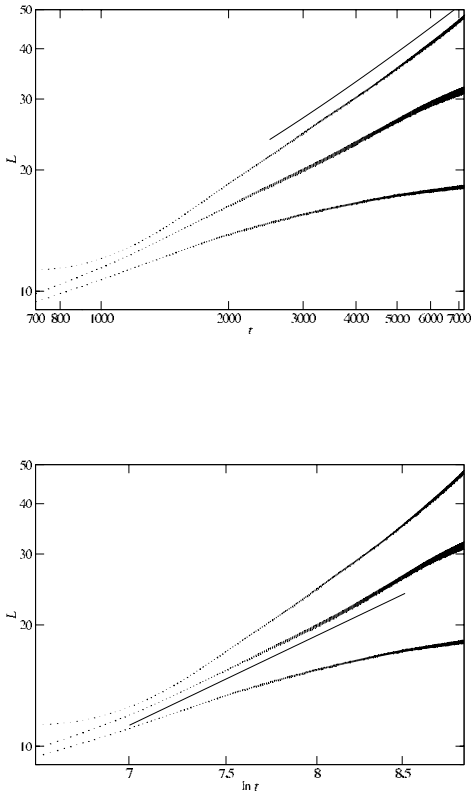

FIG. 3: Panel (a) shows the time evolution of the average domain size for simulation runs 01, 02 and 03, see Fig. 2. The log-log scale helps to visually detect behaviours following Eq. (18)—in this case, that of the uppermost curve. The straight line above it serves as a guide to the eye only and its slope is given by c_1 in Table II. Panel (b) shows the evolution of the average domain size with the logarithm of the time step for simulation runs 01, 02 and 03, on a log-log scale. This is useful to discriminate growth between that of Eq. (18) and Eq. (19); see Table II for the fitting parameters. The straight solid line shown indicates a good fit to Eq. (19) for $t > 1100$ ($\ln t \approx 7$). For $t < 1100$, the curve is better fit by Eq. (18), albeit still quite poorly. Measurements have been taken every 25 time steps, and the plot includes error bars representing the uncertainty (one standard deviation) of the spherical averaged structure function. We use a 128^3 lattice for simulation run 01 and a 64^3 lattice for the remainder. All quantities are reported in lattice units.

velocity vectors. In addition, we used periodic boundary conditions in all three dimensions. We determined that setting $n^{(0)\alpha} > 0.6$ for both species guaranteed immiscibility. In all the simulations we present here we set oil:water mass fractions to 1:1, specifically at $n^{(0)\alpha} = 0.7$ for $\alpha = \mathrm{r}, \mathrm{b}$.

It is experimentally known that the addition of amphiphile into an immiscible fluid mixture reduces the interfacial tension, as has also been reported for various lattice gas models in two and three dimensions [13, 20]. To confirm that our model reproduces this important property, we ran simulations on a $4 \times 4 \times 128$ lattice of a planar interface with surfactant adsorbed onto it and whose initial density was varied between simulation runs. The surface tension was calculated with the line integral along the normal to the interface [46]

$$\sigma = \int_{-\infty}^{+\infty} \Big[P_{zz}(z) - P_{xx}(z) \Big] \mathrm{d}z \,, \tag{15}$$

where, for the pressure tensor $\mathsf{P} \equiv \{P_{ij}\}$, we used the expression [9]

$$\begin{aligned} \mathsf{P}(\mathbf{x}) \;=\; & \sum_{\alpha} \sum_{k} \rho_k^{\alpha}(\mathbf{x}) \mathbf{c}_k \mathbf{c}_k \\ & + \frac{1}{4} \sum_{\alpha,\bar{\alpha}} g_{\alpha\bar{\alpha}} \sum_{\mathbf{x}'} \Big[\psi^{\alpha}(\mathbf{x}) \psi^{\bar{\alpha}}(\mathbf{x}') + \psi^{\bar{\alpha}}(\mathbf{x}) \psi^{\alpha}(\mathbf{x}') \Big] \times \\ & (\mathbf{x} - \mathbf{x}')(\mathbf{x} - \mathbf{x}') \,. \end{aligned} \tag{16}$$

We restrict ourselves in this study to nearest-neighbour interactions, $\mathbf{x}' \equiv \mathbf{x} + \mathbf{c}_k$, and transversal symmetry allows the second summand within the integrand in Eq. (15), which in general is $\frac{1}{2}(P_{xx}+P_{yy})$, to be simplified as shown. Equation (16) contains a kinetic (first) term, the momentum flux, due to the free streaming of particles corresponding to an ideal gas contribution, plus a potential or virial (second) term due to the inter-particle momentum transfer derived from the force (6) [47, 48].

Figure 1 shows the surface tension σ plotted against initial surfactant density, and details on parameters and densities used are included in the caption. Notice that in the regime the binary fluid is in, and for the values of surfactant density we use, the surface tension decreases linearly with surfactant concentration. It is entirely possible that there may be departures from linearity were we to increase the surfactant concentration beyond that shown in Fig. 1 because of interfacial saturation with surfactant, as observed in two and three-dimensional lattice-gas studies [13, 20].

IV. DOMAIN GROWTH KINETICS

We ran simulations starting with a homogeneous mixture of oil and water particles mixture to which surfactant was randomly added across on the lattice. Lattice sizes employed were 64^3 and 128^3 to assess finite size effects. Each lattice site was populated with a density uniformly distributed in the range zero up to the values summarised in Table I.

simulation run	01	02	03	04	05	06	07	08
$n^{(0)\mathrm{s}}$	0.0	0.15	0.22	0.30	0.35	0.40	0.60	0.90
x^{s}	0.0	0.21	0.31	0.43	0.50	0.57	0.86	1.3

TABLE I: Surfactant densities employed in the study of the algebraic-to-logarithmic and logarithmic-to-stretched exponential transitions. The mass fraction, x^{s}, is the ratio of $n^{(0)\mathrm{s}}$ to $n^{(0)\mathrm{b}} = n^{(0)\mathrm{r}} = 0.7$, and the rest of the parameters used were $g_{\mathrm{br}} = 0.08$, $g_{\mathrm{bs}} = -0.006$, $g_{\mathrm{ss}} = -0.003$, masses and relaxation times set to 1.0, and $\beta = 10.0$. The lattice used was sized 64^3 for all simulation runs except 01, for which it was 128^3 in order to avoid finite size effects entering at about $L \approx 25$.

The average size of the oil-water domains is a natural measure of the degree of segregation within the mixture. We define it as the inverse first moment of the spherically averaged oil-water structure function, $L(t) \equiv 2\pi/k_1(t)$, where $k_1(t) \equiv \sum_k k S(k,t) / \sum_k S(k,t)$. The spherically averaged oil-water structure function, $S(k,t)$, is $\sum_{\hat{\mathbf{k}}} S(\mathbf{k},t) / \sum_{\hat{\mathbf{k}}} 1$, where the $S(\mathbf{k},t)$ is the oil-water structure function,

$$S(\mathbf{k},t) \equiv \frac{\varsigma}{V} \Big| \phi'_{\mathbf{k}}(t) \Big|^2 \,, \tag{17}$$

and $\sum_{\hat{\mathbf{k}}}$ denotes summation over the set of wavevectors contained in the spherical shell $n - \frac{1}{2} \leq \frac{V^{1/3}}{2\pi} k \leq n + \frac{1}{2}$, for integer n. Equation (17) is the Fourier transform of the spatial auto-correlation function for the oil-water order parameter $\phi \equiv \rho^{\mathrm{r}} - \rho^{\mathrm{b}}$, where V is the lattice volume, ς the volume of the lattice unit cell, and $\phi'_{\mathbf{k}}(t)$ is the Fourier transform of the fluctuations of the order parameter, ϕ. Our choice of the structure function, rather than alternative measures of domain size such as the auto-correlation function, was made on the basis that it is directly proportional to X-ray or neutron scattering intensities, hence facilitating direct comparison with empirical data [49].

In Fig. 2 we plot the temporal evolution of the average domain size L for the surfactant concentrations of Table I. The amount of surfactant needed to slow down the kinetics of the binary immiscible oil-water mixture (simulation run 01) is seen to be relatively low. We now need to find the growth laws that best fit these data. Previous simulation studies, for 1:1 oil-water fluid mixtures with or without surfactant [9, 13, 20, 37], have found algebraic, logarithmically slow and stretched exponential behaviours, as follows

$$a_1 (t - b_1)^{c_1} \,, \tag{18}$$

$$a_2 (\ln t)^{c_2} \,, \tag{19}$$

$$a_3 - b_3 \exp\Big[-c_3 (t - d_3)^{e_3} \Big] \,, \tag{20}$$

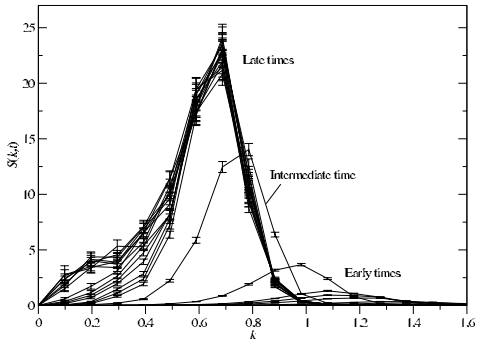

FIG. 4: Spherically averaged structure functions for the oil-water order parameter simulation run 06 (*cf.* Table III). According to how close to asymptotic behaviour the distribution of domain sizes appears to be, we have classified simulation times for this simulation run in three groups: early times (time steps 25, 50, 75, 125, 150, 175, and 300 in the plot), intermediate times (time steps roughly from 800 to 1700), and late times (time steps 1800, 2300, 2800, 3300, 3800, 4300, 4800, 6000, 10000, 14000, 18000, 22000, 26000, and 30000 in the plot). Error bars represent the standard error of the shell average. Lattice size is 64^3. All quantities are reported in lattice units.

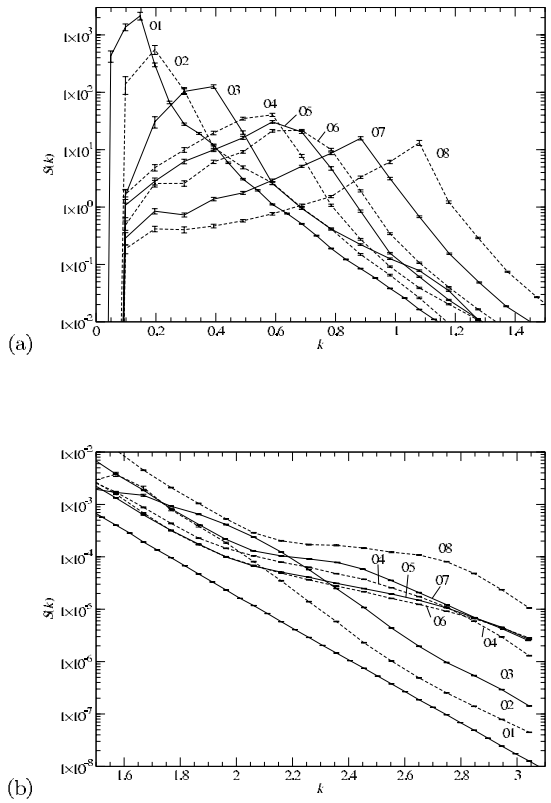

FIG. 5: Log-linear plots of the spherically averaged structure functions at time step 7200 for increasing surfactant concentrations indicated by the numerical labelling on each curve, corresponding to simulation runs 01, 02, 03, 04, 05, 06, 07 and 08, respectively, *cf.* Table I. For large wavelengths, panel (a), we can see how the peaks move to higher wavenumbers, decrease in height, and broaden. Note that for short wavelengths, panel (b), the only straight tail is for curve $n^{(0)s} = 0.0$, whose slope is -4.46×10^{-4}. Error bars represent one standard error of the shell average $S(k)$. Lattice size is 128^3 for simulation run 01 and 64^3 for the others. All quantities are reported in lattice units.

to be those characterising the temporal growth of the average domain size, $L(t)$, of an oil-water mixture without surfactant, Eq. (18) [9], and when surfactant is added above a minimum threshold concentration, Eq. (19), and at a sufficiently high amphiphile concentration, Eq. (20), the latter being a regime for which arrested growth is reached at late times. The coefficients a_i and b_i ($i = 1, 2, 3$) are fitting parameters. While we shall take these functional forms as suggested choices, we would also like to find out how closely they in fact fit our data.

Linearity in the (t, L) data cloud on a log-log plot would permit us to ascertain whether or not the data follow Eq. (18), regardless of the zero-time offset value b_1 since this is a horizontal displacement. To find out which data may be better fit by Eq. (19), we would require $(\log t, L)$ pairs of data in a search for linearity on a log-log plot. This method, however, is not likely to be of much help given the small difference between plots of the logarithm of a data series and plots of the logarithm of such logarithmic data, as we shall see. We therefore prefer to adopt the criterion of considering candidates for the model of Eq. (18) from the log-log linearity method, while resorting to both visual inspection and a search for a reduced chi-squared statistic (χ^2/ndf) close to 1.0 in order to identify a slower growth such as that of Eq. (19) (ndf is the number of degrees of freedom). Finally, Eq. (20) possesses a distinctive horizontal asymptote which best fits data whose domain growth at late times is fully arrested.

From the linearity of curves in Fig. 3 we can infer that simulation runs 01 and 02 (Table I) are good candidates for the growth model of Eq. (18). Figure 3, however, leads to the same conclusion, as expected given the small difference between these two plots. We then resort to looking at the χ^2/ndf statistic in assessing how well Eqs. (18) and (19) fit simulation runs 01, 02 and 03, see Table II. The binary immiscible fluid simulation run 01, with no surfactant present, exhibits an exponent consistent with the system being in a crossover between the known diffusive ($t^{1/3}$) and viscous hydrodynamic ($t^{1.0}$) regimes, already reported for binary immiscible fluids

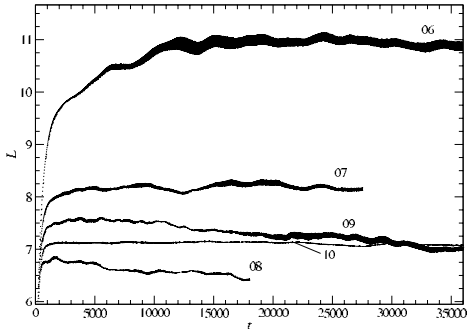

FIG. 6: Temporal evolution of the average domain size for simulation runs 06, 07, 09, 10, and 08, as seen from top to bottom at $t = 10000$ (*cf.* Table III). Measurements have been taken every 25 time steps; error bars are included and represent the uncertainty ("one sigma") transmitted from the standard error of the spherically averaged structure function. *Caveat lector*: an oscillation in the average domain size is genuinely representative of oscillations in the domain sizes only if error bars are smaller than the oscillation amplitude. Lattice size is 64^3. All quantities are reported in lattice units.

simulated with the lattice-BGK model we employ in this paper [9]. Simulation run 02 has the peculiarity that Eq. (18) holds (poorly) only during an initial transient, and Eq. (19) takes over to give a very good fit at later times, $t > 1100$. This transient is due to the time required by the surfactant to adsorb onto the interface and affect the binary immiscible interfacial dynamics. Finally, simulation run 03 is best fit by Eq. (19), although the high χ^2/ndf value indicates that the data contain more detail than the model does. In addition, from Fig. 3b, this mixture segregates at a slower speed than that given by Eq. (19), yet it does not reach total arrest, at least up to 7200 time steps. Rather, total arrest is seen at higher surfactant concentrations, as in runs 06 and 07 (see Fig. 6). We conclude that simulation run 03 represents a fluid which is in a transition regime between the logarithmic and the stretched exponential behaviours. A similar behaviour was previously observed by others using lattice-gas methods in two [13] and three-dimensions [20], and lattice-Boltzmann methods in two dimensions [37]. Emerton *et al.*, using a two-dimensional lattice-gas model, reported the divergence of the coefficients of Eq. (20) in an attempt to fit data for which total growth arrest had not been achieved [13]. The fits to our data, which include error bars, also produced the same divergences. Their fluid mixtures as well as ours, we conclude, were, rather, in a transitional regime well described by a growth law slower than Eq. (19) which still allowed for domain growth. It is, however, possible that growth arrest could be achieved at later times; this pre-arrest regime would then be a long-lived transient.

simulation run	c_1	χ^2/ndf	c_2	χ^2/ndf
01	0.896 ± 0.007	0.18	—	—
02	0.644 ± 0.004	7.5	3.850 ± 0.010	0.92
03	—	—	2.649 ± 0.022	39

TABLE II: Fits of the average domain size growth with time to the models of Eqs. (18) and (19) for simulation runs corresponding to surfactant mass fractions 0.0, 0.21 and 0.31, from top to bottom, respectively, as detailed in Table I. Lattice sizes used were 128^3 for simulation run 01 and 64^3 for the rest. Poor fits are indicated as blank fields. Simulation run 02 shows two behaviours in its temporal evolution, Eq. (18) for $t < 1100$ and Eq. (19) for $t > 1100$. Note the very good value of the χ^2/ndf statistic for the latter. The poor value of the statistic for simulation run 03 indicates that Eq. (19) is insufficient and a more detailed model is required, albeit not Eq. (20).

We now look at wavenumbers of the spherically averaged structure function, $S(k)$, other than the first moment, already provided by $L(t)$. Figure 4 shows the spherically averaged structure function for simulation run 06 at several time steps. The temporal evolution of the curves

resembles the segregation kinetics for binary immiscible fluid mixtures, except that domain growth arrest for late times makes them tend to superimpose. Note that a hump appears at these times, indicating the formation of structures, statistically weak, of size close to half the lattice side length. Inspection of ϕ(x) snapshots suggests the spurious presence of elongated domains of such sizes which are extended rather than folded. At the late times we examined, these elongations tend to vanish or fold. Still in Fig. 4, it is worth noting that for all length scales above a threshold (about $k < 0.9$), curve superposition is not sharp. This is a consequence of the fact that for the fluid composition of simulation run 06, and those of higher surfactant concentrations, there are small temporal oscillations in $S(k)$. All these mixtures have in common that they have achieved total growth arrest—in fact, $L(t)$ decreases in time for simulation run 08, as we shall see later on and discuss in more detail. Oscillations in the structure function and a hump at low wavenumbers have been reported previously in a hydrodynamic Langevin model of sponge phase dynamics, using field-theoretic methods [28]. However, this approach did not consider the amphiphile concentration explicitly but, rather, embedded it into a Ginzburg-Landau free energy through the surface tension, in a scenario where amphiphile relaxation is assumed to be fast compared to that of the oil-water order parameter.

In Figs. 5a and 5b we show the spherically averaged structure function at time step 7200 of the mixtures in Table I, for the larger and smaller length scales, respectively.

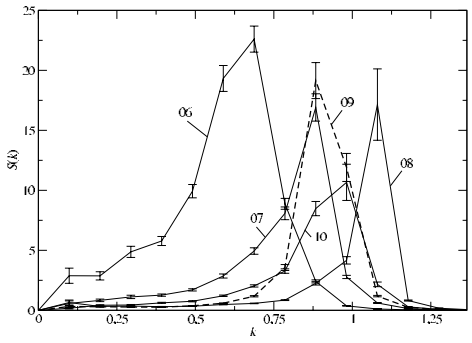

FIG. 7: Structure functions at late time step 17000 for simulation runs 06, 07, 09, 10 and 08 (*cf.* Table III). Error bars represent the standard error of the shell average $S(k)$. Lattice size is 64^3. All quantities are reported in lattice units.

As the initial density of surfactant is increased in a series of replica initially homogeneous water-oil-surfactant fluid mixtures, as indicated by Table I, it is expected that the oil-water structure function peaks will move to higher wavenumbers, decrease in intensity, and broaden [4, 8, 50]. This is indeed what we observe in Fig. 5a. Note that at smaller length scales, Fig. 5b, the exponential decay of the structure function that occurs for simulation run 01 does not hold for the ternary amphiphilic mixtures. This can be explained by the contribution of small micellar structures that form in the bulk of each immiscible phase, more likely to take place for mixtures of higher surfactant concentration. Indeed, in Fig. 5b, the latter exhibit the most manifest deviations.

V. SELF-SUSTAINED OSCILLATIONS

Arrest of domain growth occurs for high surfactant density only, *cf.* Fig. 2, as expected. Further inspection, however, shows that not only are there small temporal oscillations of the average domain size, as we mentioned at the end of the last section, but also that they do not die out during the simulation window. Similarly to what was previously reported using a bottom-up lattice-Boltzmann method in two dimensions akin to the one employed here [37], the amplitude of the oscillations is very small compared to the average domain size, and smaller than previous lattice-gas simulations in two and three dimensions [13, 20]. The fact that, in lattice-gas methods, these oscillations persist after ensemble averaging is consistent with their occurrence in lattice-Boltzmann approaches, since the latter are effectively ensemble-averaged versions of the former. Since the systems we simulate are dissipative and isolated (there is no mass or momentum exchange with external sources), oscillations, however, are expected to die out at sufficiently late times.

Motivated by the observation of oscillating average domain sizes, we performed additional simulation runs in order to check the role of the coupling constants $g_{\rm ss}$ and $g_{\rm bs}$ in the reproduction of such oscillations, our hypothesis being that both an increased surfactant-surfactant interaction and an increased tendency for surfactant to adsorb on the interface might be expected to have an influence on their frequency and amplitude. In Table III we summarise the parameters used in the new simulation runs (09 and 10) along with those of previous 'oscillating fluid mixtures.'

simulation run	$n^{(\rm O)s}$	$x^{\rm s}$	$g_{\rm ss}$	$g_{\rm bs}$
06	0.40	0.57	-0.0030	-0.006
07	0.60	0.86	-0.0030	-0.006
08	0.90	1.3	-0.0030	-0.006
09	0.60	0.86	-0.0045	-0.006
10	0.60	0.86	-0.0030	-0.009

TABLE III: Parameters employed in studying domain size oscillations, whose onset occurs for surfactant mass fractions $x^{\rm s} \geq 0.57$; the remaining parameters of the model are stated in the caption of Table I, also for the additional runs 09 and 10. In lattice units.

Figure 6 shows the temporal oscillations in the average domain size for the mixtures of Table III, and Fig. 7 shows their structure functions at time step 17000. All these mixtures exhibit domain growth arrest; interestingly, Fig. 6 shows that the average domain size shrinks in time for some of them (mixtures 08 and 09). In addition, we uncover the role that the coupling constants $g_{\rm ss}$ and $g_{\rm bs}$ have in the oscillations: whilst increasing $|g_{\rm ss}|$ seems to enhance their frequency, an increase in $|g_{\rm bs}|$ drastically dampens them and reduces their amplitude. However damped the oscillations of simulation run 10 may seem, zooming into smaller scales reveals the existence of minute oscillations (less than 0.10 lattice sites in amplitude), which is not the case for simulation runs 01 through to 05. (Note that the length scales reported in Fig. 6 are lattice averages; an amplitude being less than one lattice site hence remains physically meaningful.) Oscillations are, therefore, the signature of all growth-halted regimes.

The structure function plots of Fig. 7 provide further insight into the role of coupling constants $g_{\rm ss}$ and $g_{\rm bs}$ in the oscillation dynamics. Note that mixture 08 produces a peak of intensity similar to that of mixture 07, a feature already seen at much earlier times (see Fig. 5a). This peak height similarity could have been ascribed to a transient, such as turned out to be the case for the difference in peak intensities between mixtures 06 and 07; however, it persisted in time. Mixture 09 also shows a peak intensity similar to that of mixture 07. Peak inten-

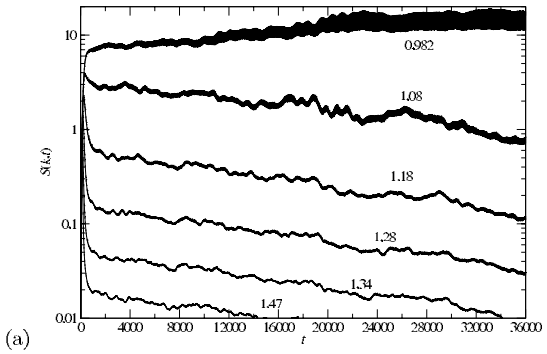

(a)

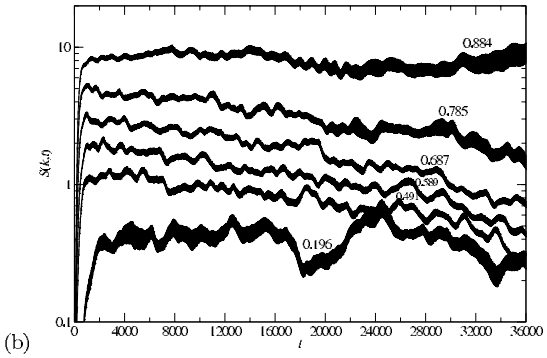

(b)

FIG. 8: Temporal dependence of the structure function for simulation run 09, *cf.* Table III. Panels (a) and (b) show the short and long wavelengths, respectively. Measurements have been taken every 25 time steps; error bars have been included. Lattice size is 64^3. All quantities are reported in lattice units.

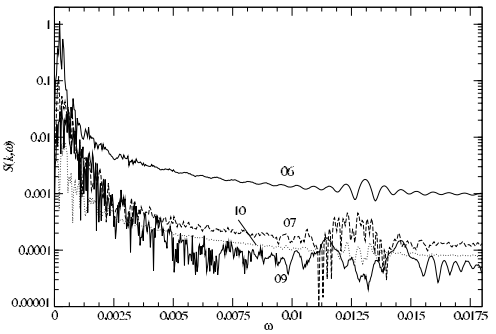

(a)

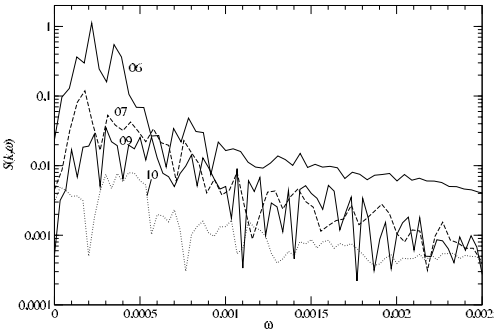

(b)

FIG. 9: Frequency power spectra of the structure function for simulation runs 06, 07, 09 and 10 (*cf.* Table III) at wavenumber 0.589. Panel (b) is a blowup of panel (a) for long periods of oscillation. Error bars were neither considered for the Fourier analysis nor plotted here. All quantities are reported in lattice units, and ω is the inverse period.

sities bear a direct relation to the steepness of oil-water domain walls and, hence, to their surface tension. The fact that increasing the surfactant concentration (in mixture 08 compared to mixture 07) does not reduce the surface tension denotes that the interface is close to its saturation limit with respect to surfactant adsorption. If enough surfactant is dispersed in the bulk, a process of diffusion towards and adsorption onto the interface could continue to occur, much slower compared to the initial adsorption leading to growth arrest, which could explain the slow domain size reduction. In the cases of simulation runs 08 and 09, close to interface saturation, surfactant concentration in the bulk is high. An amphiphilic mixture being close to the saturation limit implies that the value of its surface tension is the lowest among all amphiphilic mixtures sharing the same composition, relaxation times and coupling constants $g_{\alpha\bar{\alpha}}$. Surface tension may be further reduced only by allowing more surfactant molecules onto the interface, which can be done by increasing $|g_{\rm bs}|$. This is exactly what we observe in Fig. 7 for fluid composition 10.

As we saw in Fig. 4, small oscillations in the average domain size indicate that the structure function varies in time back and forth between distributions of sizes which are close to each other. The first moment of such distributions, as studied in Fig. 6, may not be representative of the dynamics at other length scales, as we shall see immediately. In Fig. 8 we show the temporal evolution of $S(k)$ for mixture 09 for a range of wavelengths. Note three characteristic features of the $S(k)$ curves: they all oscillate, decrease for $k < 0.785$ and $k > 1.08$, and increase or remain stationary in the long time average for $k \approx 0.884$ and $k \approx 0.982$. This behaviour corresponds to the sharpening of the distribution $S(k)$ with time. Modes with $k > 1.28$ ($L < 4.91$) decay fast enough ($S(k) < 0.1$

for $t \approx 1000$) for them to be negligible in terms of their contribution to the fluid mesostructure. Other decreasing modes take much longer ($t > 30000$) to vanish.

Our study of the oscillations would be incomplete without looking at frequency power spectra. The time series we analyse correspond to $S(k = 0.589)$ of fluids 06, 07, 09 and 10; this choice is made on the basis that this wavenumber apprehends characteristic features of each data set. From each time series we subtracted its longest waves (i.e. its envelope), computed as the average $\frac{1}{\lambda}\sum_{t'} S(k,t')$, λ being a lag large enough so as to decouple high-frequency from low-frequency waves ($\lambda = 5000$ time steps), the sum extending over the interval $t - \lambda/2 \leq t' \leq t - \lambda/2$. The Fourier transform of the resulting time series we take as the definition of $S(k,\omega)$, *cf.* Fig. 9. Note therein two high peaks for simulation run 06, and a collection of weak peaks (which we define as those whose heights are less than 5% the height of the largest peak) occuring for higher frequencies. An increase in surfactant density (simulation run 07) causes the number of excited high-frequency modes to grow slightly, yet they also decrease in intensity. Simulation run 09, which differs from mixture 07 in having an increased $|g_{ss}|$, very clearly exhibits a substantial increment in the number of excited high-frequency modes. Finally, the spectrum for mixture 10 corroborates the quenching effect on fluctuations caused by increasing $|g_{bs}|$.

The term Marangoni instability describes a convective flow caused wherever an inhomogeneous temperature or mass distribution locally alters the interfacial tension [51]. By visualising the oil-water interface for mixtures 06 to 10 we observed that the density of adsorbed surfactant is not evenly distributed on it; hence the conditions are set for the appearance of Marangoni instabilities. Figure 10 displays the late time evolution of a subdomain of a fluid of the same composition as simulation run 09 but simulated on a larger (128^3) lattice. We display the surfactant density on a slice through the mid-plane of the subdomain, along with the locus of the oil-water interface depicted as an isosurface cropped close to the plane. Surfactant inhomogeneities on the interface are evident from these images, as well as the existence of a slow, creeping flow. Distinctive features include the regularity of the order parameter (which we shall study in detail shortly), the existence of high surfactant density necks bridging adjacent portions of the interface, and local regions where regularity is absent, reminiscent of the defects in crystalline materials, which possess their own larger-scale dynamics.

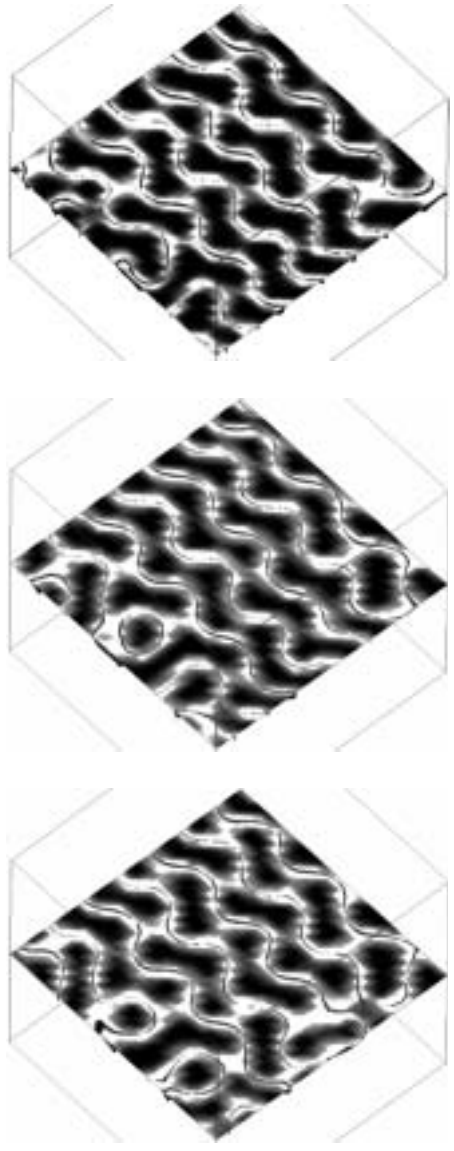

FIG. 10: Slices of the surfactant density in 33^3 subsets of a 128^3 lattice, for composition 09 (*cf.* Table I). Panels (a), (b) and (c) are snapshots at $t = 14000$, 14600 and 15000 time steps, respectively, which are times for which the structure is close to equilibration. We only show regions where surfactant density is the highest ($0.31 \leq \rho^s \leq 0.35$), in grey and white, where lighter shading denotes a higher value. We can see that the surfactant mainly concentrates around the oil-water interface ($\phi(\mathbf{x}) = 0$), whose intersection with the slice is depicted as open undulating or closed lines. Also, there are ordered, crystalline regions along with smaller regions lacking long-range order and evolving in time. Finally, ρ^s is non-uniform on the interface (as regions with lighter shading show), favouring the formation of "surfactant bridges" between adjacent portions of the interface; this leads to Marangoni effects which account for the observed oscillatory behaviour. All quantities are in lattice units.

VI. THE SPONGE AND GYROID MESOPHASES

It is known that, in an initially homogeneous 1:1 oil-water mixture, the arrest of phase segregation experienced through the addition of sufficient amphiphile can

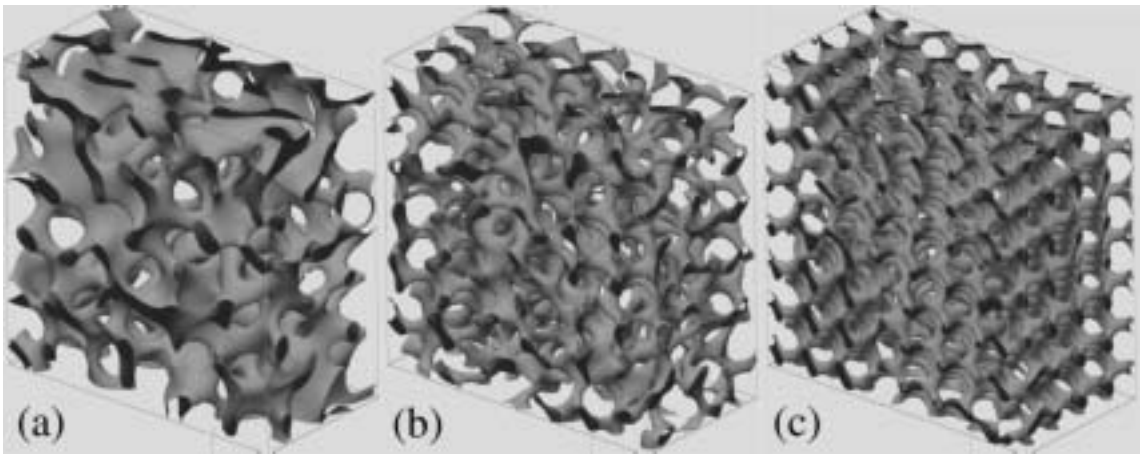

FIG. 11: Equilibrium minority-phase order parameter isosurfaces $\phi(\mathbf{x}) = 0.37$ (in lattice units), taken at time step $t = 30000$, at which $-0.69 \leq \phi \leq 0.68$ over the whole lattice. Snapshot (a) corresponds to simulation run 06, snapshot (b) to simulation run 07, and snapshot (c) to simulation run 08, *cf.* Table I. Shown are $16 \leq z \leq 48$ slabs of a 64^3 lattice. Note that increasing surfactant concentration leads to an increased ordering in the mesostructure: simulation run 06 exhibits sponge-like features, whereas simulation run 08 is a liquid crystalline cubic gyroid mesophase. Snapshot (b) is a crossover state in this lyotropic transition—a "molten gyroid".

lead to the formation of a thermodynamically stable bicontinuous sponge phase [11, 13, 20]. In Fig. 11 we show the late time morphologies for fluid compositions 06, 07 and 08. They are displayed as the $\phi(\mathbf{x}) = 0.37$ isosurface, corresponding to a water-in-oil, "rod-like" scenario, where water is a minority phase and oil is in excess (the order parameter ranges as $-0.69 \leq \phi \leq 0.68$ over the lattice at that time slice). The structure suggested by minority-phase isosurfaces and the structure of the interface ($\phi(\mathbf{x}) = 0$) for fluid composition 06 resembles that of a microemulsion, for which structural disorder is the predominant feature. Fluid composition 08, by contrast, shows an evident resemblance to minority-phase images seen in transmission electron microtomography of the gyroid "G" cubic phase [52]. The morphology is an interweaving, chirally symmetric, three-fold coordinated, bicontinuous lattice. Fluid mixture 07 seems to be a crossover, *conatus* structure, sharing a substantial amount of disorder with the presence of three-fold coordinated "unit cells"; the latter can be seen as vestigial in fluid system 06. Fluid systems 09 and 10 show that this sponge↔gyroid structural order-disorder transition not only occurs via an increase in surfactant concentration (a lyotropic transition), but in the interaction strength between surfactant with itself and with the interface. We leave for further work a systematic investigation of the $\{n^{(0)s}, g_{bs}, g_{ss}, g_{br}\}$ parameter space in mapping out the equilibrium mesostructures' phase diagram. In this endeavour, recently developed *compusteering* tools [53, 54] may prove valuable in optimising expensive simulation time: they allow the user to postprocess and visualise the compute job's output at run-time with negligible turnaround times, and eventually temporarily stop execution in order to modify simulation parameters which are fed back into the algorithm on immediate restart.

Finite size effects can play an important role in the stabilisation of fluidic structures like these, given that we are using periodic boundary conditions. With this in mind, and using the same parameters as for mixture 09, we computed the wavenumber-averaged difference $\langle \Delta_{N,N'} S \rangle$ for each time step of evolution of the spherically averaged structure function $S(k)$ between lattices of sizes N^3 and N'^3, where $N, N' = 64, 128, 256$. Note that the lattice size is increased eight and sixty-four times from the original 64^3 size. Finite size effects would be present if $\langle \Delta_{N,N'} S \rangle$ were larger than the error derived from the differences and the averages. Nonetheless we found $\langle \Delta_{N,N'} S \rangle$ to be larger than the error (27% larger on average for $N = 128$ and $N' = 256$), the fact that it strongly decreased with N (i.e. $\langle \Delta_{128,256} S \rangle \approx 0.38 \langle \Delta_{64,128} S \rangle$) provides the confidence necessary to assert that finite size effects are not significant in the $N = 128$ simulations we are about to report. Moreover, as we shall see immediately, since the structures corresponding to a 64^3 lattice exhibit the same morphologies as do the 128^3 and 256^3 cases, the qualitative features of the former are the same as those for the asymptotic limit $N \to \infty$. This also extends to the oscillation of the structure function: the equivalent of Fig. 8 for the 128^3 and 256^3 cases (not shown) exhibits similar features, albeit including more wavenumbers for which $S(k)$ grows.

Figure 12 displays three viewpoints of the isosurface $\phi = 0.40$ for the same composition of fluid mixture 09 as simulated on a 128^3 lattice. We show the restriction to a

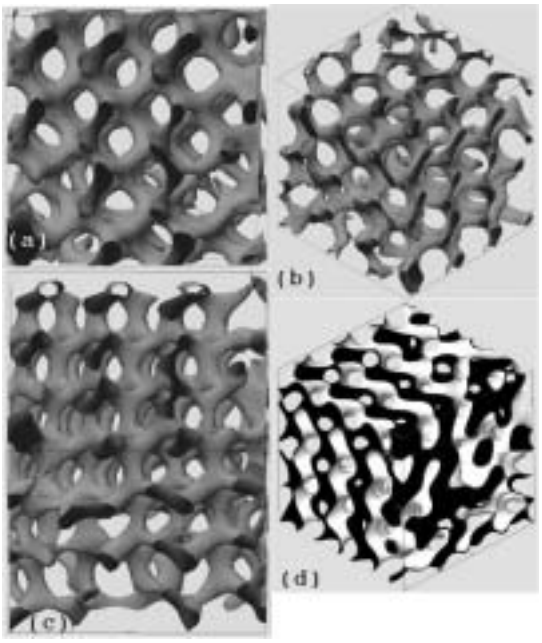

FIG. 12: Isosurfaces of the order parameter at time step $t = 15000$ in a highly ordered 33^3 subdomain on a 128^3 lattice for fluid composition 09. Panels (a), (b) and (c) display the $\phi(\mathbf{x}) = 0.40$ (in lattice units) minority phase isosurface viewed as axonometric projections along the $(1\,0\,0)$, $(1\,\bar{1}\,\bar{1})$ and $(1\,1\,0)$ directions, respectively. Panel (d) shows the interface of the same lattice subdomain along direction $(1\,\bar{1}\,\bar{1})$, where black and white have been used to distinguish one immiscible fluid phase from the other.

33^3 subdomain, all at time step $t = 15000$, together with the oil-water interface. Whereas on 64^3 (or smaller) lattices the liquid crystalline structure uniformly pervades the simulation cell, on 128^3 (and larger) lattices there are some imperfections present resulting in ordered subdomains with slightly varying orientations between which there exist domain boundaries. These boundaries can be considered as defects in the structure, the presence of which is a characteristic feature of liquid crystals. A time scale for the dynamics of some of these defects for our simulated gyroids (simulation run 09) can be roughly estimated from Fig. 10: we observe for that particular slice that the topological genus of the interface changes in an interval ranging between 500 and 1000 time steps. State-of-the-art visualisation proved key in the analysis of results, and virtual reality technologies can enhance its usefulness by increasing interactivity with the data [54].

Small-angle x-ray scattering (SAXS) techniques have been widely used in the determination of the nanostructure of fluid mesophases [14, 52, 55, 56]. SAXS spectra, or their numerically computed versions [57], give peak patterns for these mesophases that are used as fingerprints in determining unknown structures. However, the lattice resolution of our simulations is insufficient to detect multiple peak fingerprints in plots of the spherically averaged structure function. Instead, its unaveraged counterpart, $S(\mathbf{x})$, shows complete agreement of ratios of reciprocal vector moduli with those observed in diffraction patterns of the gyroid, as we display in Fig. 13 for fluid composition 09 [55]. In addition, visual inspection of the unit cell of the oil-water interface unequivocally identifies it with that of the gyroid. The size of such a unit cell as seen in optical textures allows us to associate a length scale to the lattice for a particular experimental realisation. For the system reported by Hajduk *et al.* [55], the lattice would need to be 291 nm in side length with a resolution of 2.3 nm per lattice unit.

Although previous simulation papers on amphiphilic mixtures using free-energy based Langevin diffusion equations have reported the reproduction of structures resembling the gyroid [31, 32], none of them have studied its features or dynamics, or incontestably demonstrated its gyroid morphology. Furthermore, in one of these articles we observe that the fluid mesostructure is not stationary [31], whereas by eyeballing the whole simulation cell in another [32] one becomes aware that the structure has a morphology which is reminiscent of the molten gyroid we describe here.

In our simulations we observe that, at late times, the gyroid is much closer to stationarity than the sponge mesophase: for equal time slices in their evolution, temporal changes of the mesostructure over a period of 1000 time steps are considerable for the sponge (e.g. simulation run 06) whereas for the gyroid (e.g. simulation run 09) they appear as slight interfacial rearrangements and undulations, reminiscent of breathing modes, keeping the variation in the position of each unit cell small compared to the lattice size N. This late-time (ca. 30000 time steps) structural dynamics is characterised in our simulations by the fact that the topological genus is (statistically) preserved for the gyroid; for the sponge, it is not. This can be understood as structural stabilisation by rigidity in the gyroid, and a flowing, glassy dynamics for the sponge. Such a distinctive behaviour for the sponge may have a bearing on its density fluctuations and render them different to those occurring in a topology-conserving dynamics. It is therefore not surprising that (a) we found the oscillation modes for the sponge (simulation run 06) to be at least one order of magnitude more intense than those for the different gyroids we simulated (simulation runs 08, 09 and 10, *cf.* Fig. 9), and (b) recent experimental studies, using dynamic light scattering and various relaxation methods [58], do not report on fluctuations for the gyroid [59], whereas they do for the sponge mesophase.

It is accepted wisdom [60], and a working hypothesis in many simulation studies [25, 61, 62], that periodically modulated phases may arise in fluid mixtures whenever a

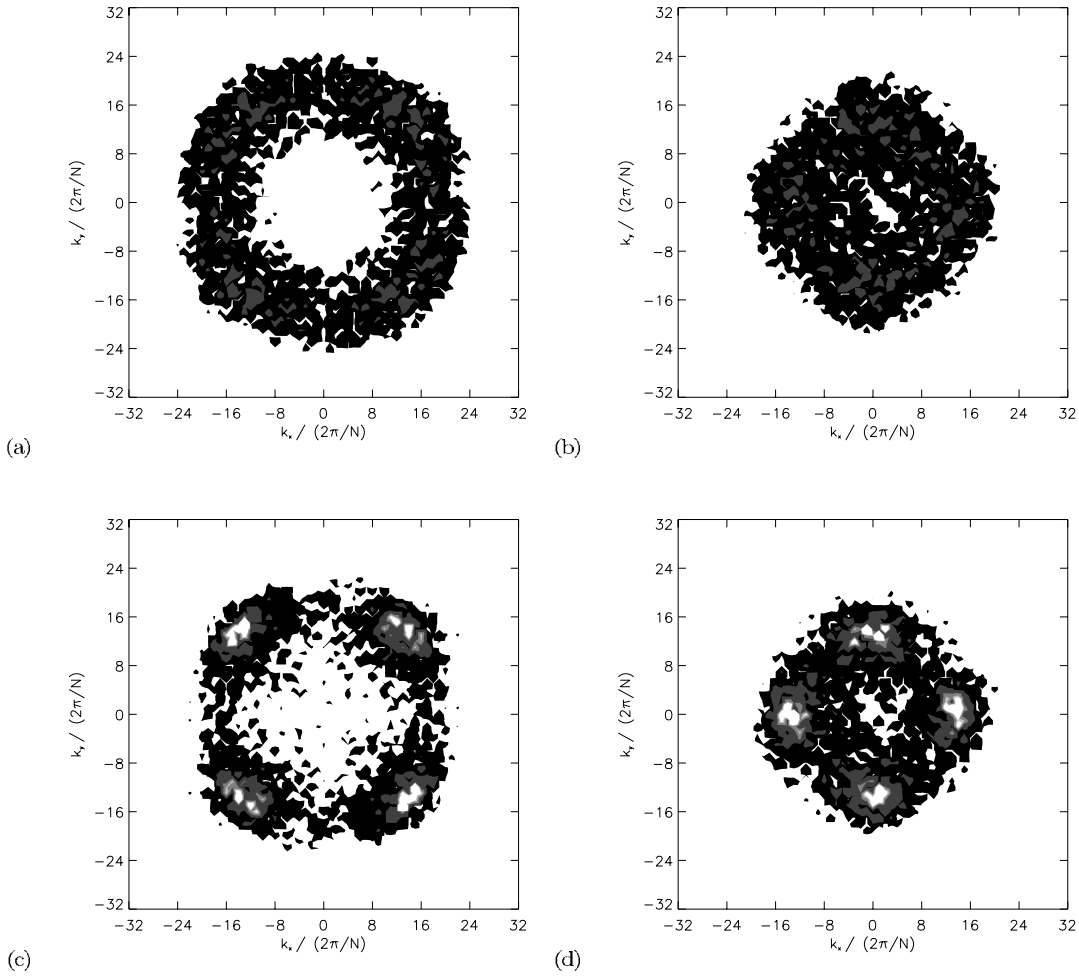

FIG. 13: Temporal evolution of (k_x, k_y) slices of the structure function $S(\mathbf{k})$ for fluid composition 09, viewed along the $(\bar{1}00)$ direction. Panels (a) and (b) show slices at time step $t = 500$, where $k_z/(2\pi/N) = 0$ for (a) and $k_z/(2\pi/N) = \pm 14$ for (b). Similarly, panels (c) and (d) are slices at time step $t = 15000$ for $k_z/(2\pi/N) = 0, \pm 14$, respectively; $N = 128$ is the lateral lattice size. Shading denote intensities $S = 1, 50$ and 100, where lighter greys up to white mean higher intensities. The spherical shell structure in (a) and (b) indicates the presence of a sponge (microemulsion) phase, which becomes anisotropic at later times, (c) and (d). The superposition of slices (c) and (d), namely, the ratio of peaks' positions of $\sum_{k_z} S(\mathbf{k})$, are in full agreement with SAXS experimental data for the gyroid mesophase. All quantities are in lattice units.

repulsive long-range interaction competes with an attractive short-range one for a configuration that minimises the interfacial Hamiltonian, possibly also in the presence of a thermal, entropic contribution. Little is said about whether non-locality is not only a sufficient but also a necessary condition, or whether the non-locality of the relevant model needs to be imposed *ab initio* or is rather an effective emergent feature picked up by the order-parameter autocorrelation function. The LB model we employ in this paper only incorporates local interactions in its mesodynamics; this feature allows its algorithm to be easily parallelised and achieve exceptionally good performance [40]. Nonetheless, we have demonstrated that the model is able to simulate liquid crystalline, cubic mesophases, such as the gyroid in binary immiscible fluid mixtures with an amphiphile, and the primitive "P" in binary, amphiphile-solvent mixtures [24], whose density-density correlations are markedly non-local, and in the formation of which hydrodynamic interactions play a vital role. Non-locality, in our case, is an emergent property

of a local model.

It is worthwhile pointing out that Prinsen *et al.* [23], using a DPD model and basing their claims on Monte Carlo studies of equilibrium cubic phases by Larson [63], suggested that cubic phases could be engineered to appear if their bead-rod model were elaborated beyond dimers. If fact, Groot & Madden's (inconclusive) finding of a gyroid-like structure with a DPD model for bead-spring chain copolymers [21] might be considered to support such an assertion. Part of the importance of our simulations, as well as those of Nekovee & Coveney [24], is to refute such conjectures, by demonstrating that cubic mesophases arise in very simple, minimalist, athermal and hydrodynamically-correct fluid models, with a locally-interacting vector order parameter and reproducing universal behaviour.

VII. SUMMARY AND CONCLUSIONS

Our simulations furnish the first quantitative account of phase segregation kinetics and mesophase self-assembly in amphiphilic fluids with a three-dimensional model based on the Boltzmann transport equation. The method is hydrodynamically correct, athermal, and models the amphiphilic species as bipolar, point-like particles experiencing short-range interactions with mean fields created by the surrounding binary immiscible ("oil-water") and amphiphilic medium.

We studied the phase segregation pathway in a homogeneous oil-water-surfactant mixture at composition $1:1:x$, respectively, where $0 \leq x \leq 1.3$ is the surfactant-to-water (or to oil) mass fraction. We observed segregation slowdown in the average size of oil-water domains with increasing x, and the reproduction of known crossovers, namely, from algebraic to logarithmic to stretched exponential functions. This confirms the usefulness of our method in apprehending the fundamental phenomenology of amphiphilic fluid mixtures; the presence of transients in these crossovers is gratifying given their experimental observation. In order to rule out an increase in total density as x is increased as a factor contributing to the slowdown along with the reduction in surface tension, future work should investigate domain growth at constant total density.

The stretched exponential functional form occurring at domain growth arrested regimes can be ascribed to the accumulation of a large number of relaxation modes associated with surfactant dynamics onto and at the oil-water interfaces [19]. The late-time structure at these regimes are (a) disordered non-stationary sponge mesophases if the initial amphiphile concentration is lower than a threshold region or (b) well-defined liquid-crystalline cubic gyroid mesophases of pinned domain sizes with defects if this initial concentration is higher than such a threshold. We also found thresholds in the surfactant coupling strengths, $|g_{ss}|$ and $|g_{bs}|$, for a sponge-to-gyroid transition. In the transition region we observed a crossover structure sharing the structural features of both the gyroid and sponge. We also found that, for the number of time steps simulated, both sponge and gyroid exhibit undamped oscillations at all length scales. For some length scales, the temporal trend of their Fourier amplitudes is to slowly die out; for others, it increases.

We found that extremely slow domain growth can be mistaken for genuine arrested growth if attention is not paid to minute length scales. Truly segregation-halted regimes exhibit oscillations in average domain size, which can be seen at sufficiently late times. These oscillations are caused partly by Marangoni flows generated by inhomogeneities in the surfactant adsorbed on the oil-water interface, and partly by a surfactant dynamics dictated by competing mechanisms, namely, surfactant attraction towards the interface and surfactant-surfactant interactions. Because our model does not presuppose that all the surfactant is adsorbed on the interface, as Langevin approaches based on the adiabatic approximation do [25, 28, 60], surfactant-surfactant interactions are not limited to repulsion. Hence, in regimes of large surfactant concentration, and especially in those for which regions of the (oil-water) interface can be sufficiently close to each other, surfactant is not constrained to dwell on the interface; rather, it is reasonable to propose the existence of an adsorption-desorption dynamics driving surfactant towards and away from it. Our results showing that (a) an increase in $|g_{\rm ss}|$ excites higher frequencies, (b) an increase in $|g_{\rm bs}|$ dampens most frequencies, and (c) there appear surfactant currents bridging adjacent interfacial regions, confirm this proposal.

Our method is not only the first lattice-Boltzmann model to deal with segregation kinetics in three-dimensional amphiphilic fluid mixtures, but the first complex fluid model to unequivocally reproduce the gyroid cubic mesophase, using a high level of abstraction in modelling the amphiphile. The truly mesoscopic, particulate nature of the surfactant in this model accounts for the complex, dynamical behaviour observed, even in a noiseless scenario like ours. It is not surprising that Ginzburg-Landau-based Langevin models which treat surfactant implicitly through a scalar parameter modifying the free energy are only able to exhibit oscillations which decay rapidly in time and whose frequency spectrum has but one peak. Our simulations of liquid crystalline mesophases prove that, contrary to what has been previously claimed [60–62], surfactant-surfactant interactions need not be long ranged in order for periodically modulated, long-range ordered structures to self-assemble. In addition, our findings rebut the suggestion [23] that cubic mesophases can be simulated only when the amphiphile is modelled with a high degree of molecular specificity.

The simulation of the sponge and gyroid phases, and their complex oscillatory dynamics, confirms the richness

of our model's parameter space. Our lattice-Boltzmann model provides a kinetically and hydrodynamically correct, bottom-up, mesoscale description of the generic behaviour of amphiphilic fluids, which is also extremely computationally efficient on massively parallel platforms. Future extensions of this work include the search for regimes leading to equilibrium mesophases of more varied symmetries, the study of shear-induced symmetry transitions, and large scale studies of defect dynamics in liquid crystalline phases. In fact, the TeraGyroid project, a successful Grid-based transatlantic endeavour employing more than 6000 processors and 17 teraflops at six supercomputing facilities [64], has its scientific *raison d'être* based on the results we report in this paper. TeraGyroid proves the value of computational steering tools [53] in mapping new parameter space regions of our model.

VIII. ACKNOWLEDGMENTS

This work was supported by the UK EPSRC under grants GR/M56234 and RealityGrid GR/R67699 which provided access to SGI Origin2000 and SGI Origin3800 supercomputers at Computer Services for Academic Research (CSAR), Manchester Computing Consortium, UK. We also thank the Higher Education Funding Council for England (HEFCE) for our on-site 16-node SGI Onyx2 graphical supercomputer. We thank Dr Rafael Delgado Buscalioni for enlightening discussions and Dr Keir Novik for technical assistance. NGS also wishes to thank Prof David Jou, Prof José Casas-Vázquez and Dr Juan Camacho at the Universitat Autònoma de Barcelona, Spain, for their support.

[1] W. M. Gelbart, D. Roux, and A. Ben-Shaul, *Modern ideas and problems in amphiphilic science.* (Springer, Berlin, 1993).
[2] D. Chapman and M. N. Jones, *Micelles, Monolayers, and Biomembranes.* (Wiley, John & Sons, 1994).
[3] P. Kumar and K. L. Mittal (eds), *Handbook of Microemulsion Science and Technology.* (Marcel Dekker, New York, 1999).
[4] G. Gompper and M. Schick, "Microscopic models of microemulsions." In *Handbook of microemulsion science and technology.* P. Kumar & K. L. Mittal (eds) (Marcel Dekker, New York, 1999.)
[5] P. Mariani, V. Luzzati and H. Delacroix, J. Mol. Biol. **204**, 165 (1988).
[6] S.-J. Marrink and D. P. Tieleman, J. Am. Chem. Soc. **123**, 12383 (2001).
[7] V. Luzzati, R. Vargas, P. Mariani, A. Gulik, and H. Delacroix, J. Mol. Biol **229**, 540 (1993).
[8] G. Gompper and M. Schick, "Self-assembling amphiphilic systems." In *Phase Transitions and Critical Phenomena.* C. Domb and J. Lebowitz (eds), Vol. 16, pages 1-176 (Academic Press, London, 1994).
[9] N. González-Segredo, M. Nekovee, and P. V. Coveney, Phys. Rev. E **67**, 046304 (2003).
[10] A. J. Bray, Adv. Phys. **43**, 357-459 (1994).
[11] T. Kawakatsu, K. Kawasaki, M. Furusaka, H. Okabayashi, and T. Kanaya, J. Chem. Phys. **99**, 8200 (1993).
[12] M. Laradji, H. Guo, M. Grant, and M. Zuckermann, J. Phys. A **24**, L629 (1991); M. Laradji, H. Guo, M. Grant, and M. Zuckermann, J. Phys.: Cond. Matt. **4**, 6715 (1992).
[13] A. N. Emerton, P. V. Coveney, and B. M. Boghosian, Phys. Rev. E **55**, 708 (1997).
[14] J. M. Seddon and R. H. Templer, in *Handbook of Biological Physics.* R. Lipowsky and E. Sackmann (eds) (Elsevier Science B. V., London, 1995.) Vol. 1, pp97-153.
[15] P. C. Hohenberg and B. I. Halperin, Rev. Mod. Phys. **49**, 435 (1977).
[16] B. I. Halperin, P. C. Hohenberg, and S. K. Ma, Phys. Rev. B. **10**, 139 (1974).
[17] J. H. Yao and M. Laradji, Phys. Rev. E **47**, 2695 (1993).
[18] M. Laradji, O. G. Mouritsen, S. Toxvaerd, and J. Zuckermann, Phys. Rev. E **50**, 1243 (1994).
[19] F. W. J. Weig, P. V. Coveney, and B. M. Boghosian, Phys. Rev. E **56**, 6877 (1997).
[20] P. J. Love, P. V. Coveney, and B. M. Boghosian, Phys. Rev. E **64**, 021503 (2001).
[21] R. D. Groot and T. J. Madden, J. Chem. Phys. **108**, 8713 (1998).
[22] R. D. Groot, T. J. Madden, and D. J. Tildesley, J. Chem. Phys. **110**, 9739 (1999).
[23] P. Prinsen, P. B. Warren, and M. A. J. Michels, Phys. Rev. Lett. **89**, 148302 (2002).
[24] M. Nekovee and P. V. Coveney, J. Am. Chem. Soc. **123**, 12380 (2001).
[25] M. Nonomura and T. Ohta, J. Phys.: Condens. Matt. **13**, 9089 (2001).
[26] M. Imai, A. Saeki, T. Teramoto, A. Kawaguchi, K. Nakaya, T. Kato, and K. Ito, J. Chem. Phys. **115**, 10525 (2001).
[27] S. Qi and Z.-G. Wang, Phys. Rev. E. **55**, 1682 (1997).
[28] G. Gompper and M. Hennes, J. Phys. II France **4**, 1375 (1994).
[29] G. Gompper and J. Goos, Phys. Rev. E. **50**, 1325 (1994).
[30] T. Ohta and K. Kawasaki, Macromolecules **19**, 2621 (1986).
[31] A. V. Zvelindovsky, G. J. A. Sevink, and J. G. E. M. Fraaije, Phys. Rev. E. **62**, R3063 (2000).
[32] B. A. C. van Vlimmeren, N. M. Maurits, A. V. Zvelindovsky, G. J. A. Sevink, and J. G. E. M. Fraaije, Macromolecules **32**, 646 (1999).
[33] P. V. Coveney, Phil. Trans. R. Soc. Lond. A **361**, 1057 (2003).
[34] D. Gueyffier, J. Lie, A. Nadim, R. Scardovelli, and S. Zaleski, J. Comput. Phys. **152**, 423 (1999).
[35] S. Succi, *The lattice-Boltzmann equation–for fluid dynamics and beyond.* (Oxford University Press, Oxford, 2001.)
[36] H. Chen, B. M. Boghosian, P. V. Coveney, and M.

Nekovee, Proc. Roy. Soc. Lond. A **456**, 2043 (2000).
[37] M. Nekovee, P. V. Coveney, H. Chen, and B. M. Boghosian, Phys. Rev. E **62**, 8282 (2000).
[38] A. Lamura and G. Gonnella, Int. J. Mod. Phys. C **22**, 1469 (1998); A. Lamura, G. Gonnella, and J. M. Yeomans, Europhys. Lett. **45**, 314 (1999).
[39] O. Theissen, G. Gompper, and D. M. Kroll, Europhys. Lett. **22**, 419 (1998); O. Theissen and G. Gompper, Eur. Physical J. B **43**, 91 (1999).
[40] The scaling with the number of processing elements (PE) for our LB model's implementation is close to linearity and superlinear on more than 64 PEs on Cray T3E-1200E and SGI Origin 3800 supercomputers, respectively; *cf.* P. J. Love, M. Nekovee, P. V. Coveney, J. Chin, N. González-Segredo, and J. M. R. Martin, Comp. Phys. Commun. **153**, 340-358 (2003).
[41] No entropic LB scheme for immiscible fluid mixtures has been reported to date. See I. V. Karlin, A. Ferrante, and H. C. Öttinger, Europhys. Lett. **47**, 182 (1999); H. Chen and C. Teixeira, Comp. Phys. Comm. **129**, 21 (2000); B. M. Boghosian, J. Yepez, P. V. Coveney, and A. Wagner, Proc. Roy. Soc. Lond. A **457**, 717 (2001); B. M. Boghosian, P. J. Love, P. V. Coveney, I. V. Karlin, S. Succi, and J. Yepez, Phys. Rev. E **68**, 025103(R) (2003).
[42] U. Frisch, D. d'Humières, B. Hasslacher, P. Lallemand, Y. Pomeau, and J.-P. Rivet, Complex Systems **1**, 649 (1987).
[43] X. Shan and H. Chen, Phys. Rev. E **47**, 1815 (1993); X. Shan and H. Chen, Phys. Rev. E **49**, 2941 (1994).
[44] URL: `http://www.mpi.org/` .
[45] I. Murray, *Lattice Boltzmann study of amphiphilic fluids.* Centre for Computational Science Internal Report, Department of Chemistry, Queen Mary, University of London, October 2001.
[46] J. S. Rowlinson and B. Widom, *The molecular theory of capillarity.* (Clarendon Press, Oxford, 1982.)
[47] J. H. Ferziger and H. G. Kaper, *Mathematical theory of transport processes in gases* (North Holland, Amsterdam, 1972).
[48] M. P. Allen and D. J. Tildesley, *Computer simulations of liquids.* (Clarendon Press, Oxford, 1990.)
[49] J. D. Gunton, M. San Miguel, and P. S. Sahni, in *Phase Transitions and Critical Phenomena.* C. Domb & J. Lebowitz (eds), Vol. 8. (Academic Press, New York, 1983).
[50] G. Gompper, "Bulk and interfacial properties of amphiphilic systems: A Ginzburg-Landau approach." In *Structure and dynamics of strongly interacting colloids and supramolecular aggregates in solution.* S.-H. Chen, J. S. Huang, & P. Tartaglia (eds) (Kluwer Academic Publishers, Dordrecht, 1992).
[51] V. I. Kovalchuk, H. Kamusewitz, D. Vollhardt, and N. M. Kovalchuk, Phys. Rev. E **60**, 2029 (1999).
[52] J. H. Laurer, D. A. Hajduk, J. C. Fung, J. W, Sedat, S. D. Smith, S. M. Gruner, D. A. Agard, and R. J. Spontak, Macromolecules **30**, 3938 (1997).
[53] J. Chin, J. Harting, S. Jha, P. V. Coveney, A. R. Porter, and S. M. Pickles, Contemp. Phys. **44**, 417 (2003).
[54] URL: `http://www.RealityGrid.org` .
[55] D. A. Hajduk, P. E. Harper, S. M. Gruner, C. C. Honeker, G. Kim, and E. L. Thomas, Macromolecules **27**, 4063 (1994).
[56] J. Klinowsky, A. L. MacKay, and H. Terrones, Phil. Trans. R. Soc. Lond. A **354**, 1975 (1996).
[57] P. Garstecki and R. Hołyst, J. Chem. Phys. **115**, 1095 (2001).
[58] B. Schwarz, G. Mönch, G. Ilgenfritz, and R. Strey, Langmuir **16**, 8643 (2000).
[59] A. M. Squires, R. H. Templer, J. M. Seddon, J. Woenckhaus, R. Winter, S. Finet, and N. Theyencheri, Langmuir **18**, 7384 (2002).
[60] M. Seul and D. Andelman, Science **267**, 476 (1995).
[61] C. Sagui and R. C. Desai, Phys. Rev. Lett. **71**, 3995 (1993); C. Sagui and R. C. Desai, Phys. Rev. E **49**, 2225 (1994); C. Sagui and R. C. Desai, Phys. Rev. E **52**, 2807 (1995).
[62] C. Roland and R. C. Desai, Phys. Rev. B **42**, 6658 (1990).
[63] R. G. Larson, J. Phys. II France **6**, 1441 (1996).
[64] See, e.g., *TeraGyroid: Grid-based lattice-Boltzmann simulations of defect dynamics in amphiphilic liquid crystals*, demonstration at the SuperComputing2003 conference, Phoenix (Arizona, USA), 15th–21st November 2003, URLs: `http://www.sc-conference.org/sc2003/` , `http://www.RealityGrid.org/news.html` .

Chapter 4

Other articles

This chapter contains two articles: one preprint of imminent submission by this thesis' submission date, and one paper in the proceedings of an international conference, as follows:

- N. González-Segredo, Jens Harting and Peter V. Coveney, "Stress response and structural transitions in sheared gyroid and lamellar amphiphilic mesophases: lattice-Boltzmann simulations" (Preprint, Centre for Computational Science: London, 2004.) (Cf. p. 95.)

- N. González-Segredo and M. Foster, "pLRME2D: A parallel implementation of a two-dimensional hydrodynamic lattice-gas model with long-range interactions," Proceedings of the Sixth European SGI/Cray MPP Workshop, Manchester, UK (2000). (Cf. p. 107 and available online:
URL: http://mrccs.man.ac.uk/mpp-workshop6/proc/gonzalez.htm .)

. . .

Stress response and structural transitions in gyroid and lamellar amphiphilic mesophases: lattice-Boltzmann simulations

Nélido González-Segredo,* Jens Harting,† and Peter V. Coveney‡
Centre for Computational Science, Department of Chemistry,
University College London, 20 Gordon Street, London WC1H 0AJ, United Kingdom
(Dated: October 12, 2004)

We report on the stress response of the gyroid cubic mesophase to a steady Couette flow simulated by means of a bottom-up lattice-Boltzmann model for amphiphilic fluids and sliding periodic (Lees-Edwards) boundary conditions. We employ two gyroidal mesophases, the gyroid *per se* (above the sponge-gyroid transition, of high crystallinity) and the molten gyroids (within such a transition, of shorter-range order). These were allowed to self-assemble from a homogeneous mixture of two immiscible fluids with added amphiphile, the longer-range gyroid having 50% higher amphiphile concentration and inter-amphiphile coupling than the molten gyroid. We find that both mesophases exhibit shear-thinning, more pronounced and at lower strain rates for the molten gyroid. We also find that, at late times after the onset of shear, the skeleton of the longer-range gyroid becomes a structure of interconnected irregular tubes and toroidal rings, mostly oriented along the velocity ramp imposed by the shear—in contradistinction with free-energy Langevin-diffusion studies finding a much simpler structure of disentangled tubes. We also compare the shear stress and deformation of lamellar mesophases with and without amphiphile in a steady Couette flow applied normally to the lamellae. We find that the presence of amphiphile allows (a) the shear stress at late times to be higher than in the case without amphiphile, and (b) the formation of rich patterns on the shear interface, characterised by alternating regions of high and low curvature.

I. INTRODUCTION

The study of the response to shear in amphiphilic mesophases has been the subject of attention for numerical modellers only in recent years. The interest in the subject is sustained not only by the wide range of applications in materials science and chemical engineering, but also by the need to gain a fundamental understanding of the universal laws ruling the self-assembly processes and competing mechanisms present.

The research has been mainly focused on the structural changes induced by steady and oscillatory shear, near and far from critical points, on block copolymer systems [1–5]. The morphologies studied have been cubic micellar, lamellar and hexagonally-packed tubular mesophases; more complex structures such as bicontinuous morphologies, and, in particular, mesophases of cubic symmetry have been looked at in lesser, insufficient detail [3].

The purpose of this paper is to report on the rheology of amphiphilic mesophases simulated with a bottom-up kinetic-theoretic model for fluid flow. The numerical studies measuring the stress response to shear have been hitherto concentrated on two opposite ends of complex fluid research: in phase-segregating binary immiscible fluids [6], and in polymeric [7] and glassy systems [8]. Since our model is genuinely particulate in the sense that no hypothesis of desirable macroscopic behaviour is imposed on the microdynamics, we consistently adhere to a complexity paradigm [9, 10]. In addition, since our model describes the amphiphilic molecule with the minimal possible amount of information—a dipole—the rheology to report is expected to cover features, in a broad range of amphiphilic systems, which are independent of the molecular structure.

This paper is structured as follows. In the next section we briefly introduce the model and describe the boundary conditions allowing the imposition of shear on the mesophases. In Section III we report our measurements of shear stress in long-range and molten gyroids as a function of time after the onset of shear, and study their shear-thinning non-Newtonian behaviour. We also report, in direct and Fourier space, on the plastic deformation of the longer-range gyroid into a tubular-like mesophase as the strain increases, and show how the stress decays as the steady shear is abruptly ceased. In section IV we reveal how the presence of amphiphile induces the formation of rich interfacial patterns in lamellar mesophases and allows the stress to reach higher values than in lamellar mesophases without amphiphile. Finally, we provide some conclusions in Section V.

*Email: nelido@amolf.nl; now at the FOM Institute for Atomic and Molecular Physics (AMOLF), P. O. Box 41883, 1009 DB Amsterdam, The Netherlands. Also at the Department of Physics, Universitat Autònoma de Barcelona, 08193 Bellaterra, Spain.
†Email: j.harting@ica1.uni-stuttgart.de; now at the Institut für Computerphysik, Pfaffenwaldring 27, D-70569 Stuttgart, Germany.
‡Email: p.v.coveney@ucl.ac.uk

II. THE MODEL AND THE LEES-EDWARDS BOUNDARY CONDITIONS

We employed an existing bottom-up lattice-Boltzmann (LB) model for amphiphilic fluids [10, 11], extended to simulate shear flow by means of Lees-Edwards boundary conditions [12]. The model is in turn based on an extension made to the bottom-up Shan-Chen LBGK model for immiscible fluids to model amphiphilic fluids, and utilises 25 microscopic velocities, of speeds 0, 1 and $\sqrt{2}$, in three dimensions (D3Q25 lattice) [13, 14]. The model reproduces the Navier-Stokes (NS) equation in the bulk of each immiscible fluid phase ("oil" and "water" hereafter) for large enough lattices [15], and it exhibits correct growth kinetics for the average size of the immiscible domains in the absence [16] and presence [11] of a third amphiphilic (surfactant-like) species. In addition, the model simulates the nonequilibrium self-assembly and relaxation dynamics of sponge and gyroid mesophases [10, 11]. It endows gyroids with rigidity, arising from their crystalline ordering, which gradually fades away as the amphiphile density is reduced, since a lyotropic transition causes the correlation length to decrease towards that of the sponges through a molten-gyroid state. This idea is central to the work we present herewith: we shall see that the mesophase's crystalline ordering enhances its stress response; indeed, we find shear-thinning to occur at higher strain rates for gyroids than for sponges.

The Lees-Edwards boundary conditions (LEBC) were originally proposed by Lees and Edwards in the context of molecular dynamics simulations [12]. They showed that these boundary conditions gave rise to a desired linear, wedged velocity profile whilst avoiding the troublesome spatial inhomogeneities arising when solid walls were used to induce the shear flow [17]. A particular realisation of the LEBC on the cartesian simulation box $[0, N_\mathrm{x}] \times [0, N_\mathrm{y}] \times [0, N_\mathrm{z}]$ is established by letting the periodic images, for which $N_\mathrm{x} < x \leq 2N_\mathrm{x}$ and $-N_\mathrm{x} \leq x \leq 0$, move parallel to unit vectors $\pm\mathbf{e}_\mathrm{z}$, respectively, both with speed U. The LEBC are expressed as a Galilean transformation from the unprimed to the primed position (x, y, z) and velocity $(\xi_\mathrm{x}, \xi_\mathrm{y}, \xi_\mathrm{z})$ co-ordinates of a particle, as follows

$$
\begin{aligned}
x' &\equiv x \bmod N_\mathrm{x} \\
y' &\equiv y \bmod N_\mathrm{y} \\
z' &\equiv \begin{cases} (z + \Delta_\mathrm{z}) \bmod N_\mathrm{z} & , x > N_\mathrm{x}, \\ z \bmod N_\mathrm{z} & , 0 \leq x \leq N_\mathrm{x}, \\ (z - \Delta_\mathrm{z}) \bmod N_\mathrm{z} & , x < 0, \end{cases} \qquad (1) \\
\xi'_\mathrm{x} &\equiv \xi_\mathrm{x} \\
\xi'_\mathrm{y} &\equiv \xi_\mathrm{y} \\
\xi'_\mathrm{z} &\equiv \begin{cases} \xi_\mathrm{z} + U & , x > N_\mathrm{x}, \\ \xi_\mathrm{z} & , 0 \leq x \leq N_\mathrm{x}, \\ \xi_\mathrm{z} - U & , x < 0, \end{cases} \qquad (2)
\end{aligned}
$$

where $\Delta_\mathrm{z} \equiv U\Delta t$ is the image's shift at time Δt after starting shearing.

An implementation of the LEBC on a lattice differs from that of molecular dynamics in that the shift Δ_z is not in general a multiple of the lattice unit, as Wagner and Pagonabarraga have pointed out [17], and hence an interpolation scheme is needed. We use a parallel implementation of the LEBC in three dimensions which includes this interpolation scheme to move mass densities with velocity $\mathbf{c}_k$ for each (fluid and amphiphilic) species α, $n_k^\alpha(\mathbf{x})$, and amphiphile dipoles, $\mathbf{d}(\mathbf{x})$. The spatial displacement follows Eqs. (1); the velocity shift, however, is not enforced by replacing the discrete microscopic speeds $\mathbf{c}_k \cdot \hat{\mathbf{z}}$ for the continuum velocity component ξ_z in Eqs. (2), where $k = 1, \ldots, 25$, since the velocities $\mathbf{c}_k$ are constant vectors. Instead, this is enforced by modifying the macroscopic fluid velocity contained in the truncated local Maxwellian, towards which the BGK scheme makes the density relax, in the same fashion that immiscibility is enforced [11, 16]. This procedure guarantees that all accelerations in the fluid are ruled by the same BGK process, controllable via the shape of the distribution function and the relaxation time parameter.

Our LEBC implementation is embedded into an efficient parallel LB algorithm [18] which allows us to employ large lattices and hence reach the small Knudsen number limit where (a) regions away from interfaces satisfy the incompressible NS equation in the limit of low Mach numbers (Ma) [16], and (b) observables vary by less than 10% when the lateral lattice dimension is doubled. González-Segredo and Coveney previously found that the lattice size guaranteeing condition (b) is 128^3 for the parameters generating the mesophases investigated here [10, 11].

III. SHEARING GYROID MESOPHASES

We sheared two gyroidal mesophases differing in the density of amphiphile dispersed and the value of the inter-amphiphile interaction coupling parameter. Each of these structures was allowed to self-assemble from a thorough, homogeneous mixture of oil and water with an third added amphiphilic species. They have been appropriately characterised by probing direct and Fourier-space late-time snapshots of the density order parameter $\phi \equiv \rho^\mathrm{oil} - \rho^\mathrm{water}$; more precisely, they correspond to gyroid (cf. Fig. 1) and molten gyroid mesophases, as previously reported by González-Segredo and Coveney [10, 11].

The common parameters used for both gyroids were oil and water densities flatly distributed in the range $0 < n^{(0)\mathrm{b}} = n^{(0)\mathrm{r}} < 0.7$, coupling strengths $g_\mathrm{br} = 0.08$, $g_\mathrm{bs} = -0.006$, relaxation times $\tau^\mathrm{b} = \tau^\mathrm{r} = \tau^\mathrm{s} = \tau^\mathrm{d} = 1$, and, for the amphiphile's dipoles, $\beta = 10$ and $d_0 = 1$.

Their differing parameters were surfactant densities flatly distributed in the ranges $0 < n^{(0)\mathrm{s}} < 0.9$ (gyroid) and $0 < n^{(0)\mathrm{s}} < 0.6$ (molten gyroid), with coupling strengths $g_\mathrm{ss} = -0.0045$ (gyroid) and $g_\mathrm{ss} = -0.003$

(molten gyroid). These parameters for the gyroid are 50% higher than those for the molten gyroid.

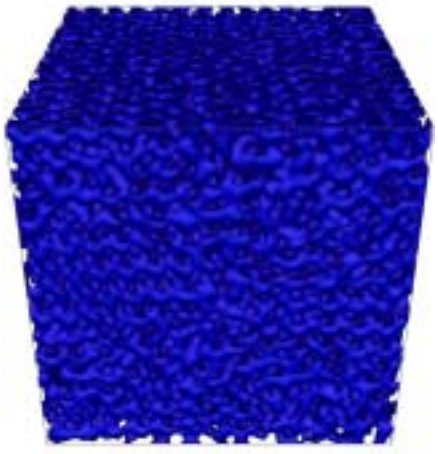

FIG. 1: High-density volume rendering of one of the two immiscible fluids in the gyroid mesophase employed, before the application of shear. This configuration, on a 128^3 lattice, is reached after 15 000 time steps of self-assembly from an initial homogeneous mixture of "oil", "water" and amphiphile, with the amphiphile density being flatly distributed across the lattice in the range $0 \leq n^{(0)s} \leq 0.9$ and an inter-amphiphile coupling parameter of $g_{ss} = -0.0045$. The regions visible to the reader are those for which the density order parameter is $\phi \equiv \rho^{oil} - \rho^{water} \geq 0.36$ (oil), whilst over the whole fluid $-0.79 \leq \phi \leq 0.79$; the regions for which $\phi \leq -0.36$ (water, not shown) display a similar structure which is complementary (interweaving) to the one shown here.

While the gyroid relaxes to a highly crystalline structure [19], the molten gyroid shows both shorter-range order and stronger temporal oscillations than the former [11]. In order to allow for the latter to relax sufficiently, we took the structure at time step 32 500 as initial condition for the shear; regarding the gyroid, the time slice chosen was time step 15 000. For practical reasons, we generated the molten gyroid by upscaling a mesophase of the same parameters and similar features, previously self-assembled on a 64^3 lattice [11], onto a 128^3 lattice. Upscaling consisted in replicating identical copies of the system—the periodic boundary conditions used to generate the former guarantee that the density field is smooth across the replica boundaries. Upscaling produces a mesophase with an added, undesirable long-wavelength periodicity of half the lattice size, whose gyroidal unit cell sizes in general do not match those of a molten-gyroid allowed to self-assemble on a 128^3 lattice. However, we observed that this mesophase takes less than 1 000 time steps to relax to a structure in which the long wavelength periodicity has disappeared [19]. Since this relaxation occurs during a short transient period, we took the upscaled, unrelaxed structure as an initial condition for our shearing study.

It is worth noting that we did not require an elongated aspect ratio for the lattices along the direction parallel to the translation of the shearing walls since spatial density fluctuations were much smaller than the lattice size. This is not the case when shearing phase segregating fluids without a growth-arresting species, such as an amphiphile, as was recently reported by Harting, Venturoli and Coveney with this LB model using lattices of up to $128 : 128 : 512$ sizes and aspect ratio [20].

A. Stress response and transients

Shear thinning occurs when the shear viscosity drops as the strain rate increases. For structured fluids such as the ones we used here, the dynamic shear viscosity, η, is not expected to be a constant of the strain rate $\dot{\gamma} \equiv \frac{1}{2}(\partial_x u_z + \partial_z u_x)$, as is assumed in Newton's law of viscosity,

$$P_{xz} = -2\eta\,\dot{\gamma}\,, \qquad \eta \neq \eta(\dot{\gamma}) \tag{3}$$

where P_{xz} is one off-diagonal component of the pressure or stress tensor. Throughout this paper we work with the steady shear described in Section II, i.e., the shear is generated by the two image cells of the LB lattice located along the x-axis moving in opposite directions. As a consequence, $\partial_x u_z$ becomes the only non-vanishing component of the velocity gradient, also true for the P_{xz} component of the stress tensor (and P_{zx}, since the physical requirement that the vorticity, $W \equiv \frac{1}{2}(\partial_x u_z - \partial_z u_x)$, remains bounded above requires the stress tensor to be symmetric).

As done previously by González-Segredo, Nekovee and Coveney to compute diagonal components of the pressure tensor [10, 11, 16], we measured P_{xz} from its definition as the sum of a kinetic term plus a virial mean-field term accounting for interactions giving rise to non-ideal gas behaviour, namely,

$$\begin{aligned} \mathsf{P}(\mathbf{x}) \;\equiv\; & \sum_{\alpha}\sum_{k} \rho_k^{\alpha}(\mathbf{x})(\mathbf{c}_k - \mathbf{u}(\mathbf{x}))(\mathbf{c}_k - \mathbf{u}(\mathbf{x})) \\ & + \;\frac{1}{4}\sum_{\alpha,\bar{\alpha}} g_{\alpha\bar{\alpha}} \sum_{\mathbf{x}'} \left[\psi^{\alpha}(\mathbf{x})\psi^{\bar{\alpha}}(\mathbf{x}') + \psi^{\bar{\alpha}}(\mathbf{x})\psi^{\alpha}(\mathbf{x}')\right] \times \\ & (\mathbf{x}-\mathbf{x}')(\mathbf{x}-\mathbf{x}')\,, \end{aligned} \tag{4}$$

where ψ has the form $\psi \equiv 1 - \exp[-n(\mathbf{x})]$, saturating at high density values in order to avoid unbounded inter-particle forces whilst reproducing a meaningful equation of state [11]. In addition, since the interaction matrix $\{g_{\alpha\bar{\alpha}}\}$ is symmetric with all diagonal elements identically zero, and only nearest neighbour interactions are being considered, the virial term reduces to

$$\frac{1}{2}\sum_{\alpha\neq\bar{\alpha}} g_{\alpha\bar{\alpha}} \sum_{k} \psi^{\alpha}(\mathbf{x})\psi^{\bar{\alpha}}(\mathbf{x}+\mathbf{c}_k)\mathbf{c}_k\mathbf{c}_k\,. \tag{5}$$

Since in the incompressible limit our LB model reproduces the NS equation away from interfaces [13, 15], or,

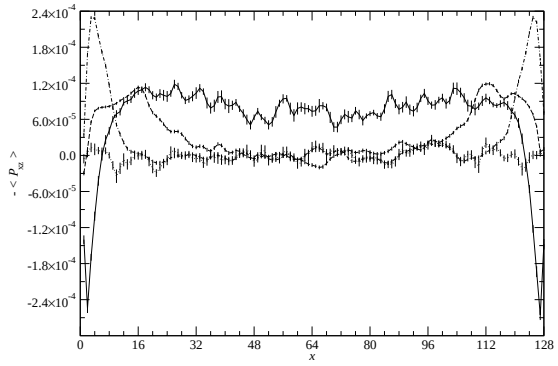

FIG. 2: Shear stress response of a gyroid mesophase along the direction of the velocity gradient. As initial condition, we have taken a gyroid on a $N_{\rm x}N_{\rm y}N_{\rm z} = 128^3$ cubic lattice at time step $t = 15\,000$ of self-assembly [10, 11]. The Lees-Edwards walls move with speed $U = 0.10$ (Ma $= 0.17$). For each x coordinate, the original field has been averaged on the plane $[1, N_{\rm y}] \times [16, N_{\rm z} - 16]$, where the excluded interval on the z-axis account for wrapped-round densities. Standard errors of the averages are about 6×10^{-8} throughout, and are not shown. Each line represents the response at Δt time steps after the start of steady shear: $\Delta t = 0$ (dotted line), $\Delta t = 100$ (dash-dotted), $\Delta t = 800$ (dashed) and $\Delta t = 9\,000$ (solid), where the last is ca. the time at which the core (i.e., the plane $x = 64$) fully responds. From the figure we can see that momentum transfer decreases as it reaches the core from the walls. Also, note that the stress inverts its sign at late times adjacent to the boundaries, $|x - x_0| \leq 2$ ($x_0 = 0$, 128). All quantities reported are in lattice units.

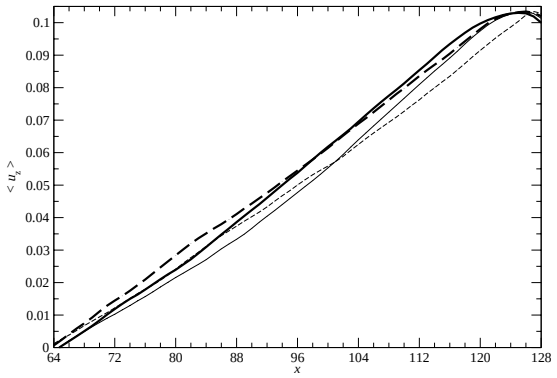

FIG. 3: Spatially averaged velocity component $u_{\rm z}$ for the molten gyroid and the gyroid mesophases sheared with $U = 0.10$, at late times and over the $x \geq 64$ half of the system. The dashed thin and thick curves correspond to the molten gyroid at time steps $\Delta t = 9\,000$ and $13\,000$, respectively. The solid thin and thick curves correspond to the gyroid at time steps $\Delta t = 9\,000$ and $13\,000$, respectively. The average is over the same two-dimensional domain as described in Fig. 2, for each x, and its standard error is shown as negligible error bars. Note that the velocity shows a maximum located from 2 to 4 sites away from the boundary, unlike a simple fluid which would display it exactly at the boundary. The value of this maximum coincides with the actual velocity at which the BGK relaxation process of our LB model is forcing the fluid to move, which needs not coincide with the input parameter $U = 0.10$. Note that the inversion in the sign of the stress that we reported in Fig. 2 occurs precisely for $|x - x_0| \leq 2$, $x_0 = 0$, 128 and at (late) times close and after $\Delta t = 9\,000$. The behaviour at the other boundary region is similar and symmetric to that displayed here. All quantities reported are in lattice units.

equivalently, for $g_{\alpha\bar{\alpha}} \equiv 0$, the source term for momentum balance is given by $\nabla \cdot \left(p\mathsf{I} - 2\eta(\nabla \mathbf{u})^{\rm s} \right)$ with $\nabla \cdot \mathbf{u} = 0$, where I is the unit second-rank tensor and s denotes the same symmetrisation done for $\dot{\gamma}$ above. The dissipative term is the contribution to stress from shearing a single phase fluid, which coincides with Newton's law, Eq. (3), since in this model $\eta = \rho c_{\rm s}^2(\tau - 1/2)$ is a constant, where $c_{\rm s} = 3^{-1/2}$ is the speed of sound in our LB model and τ is the (oil or water) relaxation time parameter. We hence set out to study the response to shear modelled by the off-diagonal components of the virial term, whose diagonal entries are already known to give rise to a correct interfacial tension [10, 11, 16].

In order to probe the function $\eta = \eta(\dot{\gamma})$ for the gyroid and molten gyroid mesophases, we measured $P_{\rm xz}$ for a number of different applied shear rates. The chosen values for U were such that fluid speeds remained within the incompressibility limit, i.e., small compared to the speed of sound for the model, $c_{\rm s} = 3^{-1/2} \approx 0.58$. Values chosen were $U = 0.05, 0.10, 0.15, 0.20$, corresponding to Mach numbers Ma $= 0.086, 0.17, 0.26, 0.34$, respectively. Part of the merit of meso- and microscopic numerical simulation rests in their ability to measure quantities with finer resolution than is possible with many experimental techniques. In fact, all observables we report in this paper are spatial averages, at least on $x =$ const. planes where a simple fluid under the same shear would show translational symmetry for the velocity field, i.e., perpendicular to the velocity gradient.

Figure 2 shows how the (averaged) stress varies across the system for the sheared gyroid. Several curves therein allow us to depict the time evolution of momentum making its way to the core (i.e., the plane $x = 64$) of the gyroid as the strain grows. Distinctively, the profiles have spatial fluctuations, which is a result of the presence of the gyroid's convoluted structure whose (internal) interfacial tension modifies the momentum transport expected for a simple fluid. The $u_{\rm z}$ component of the velocity field, averaged in the same way as stated for $\langle -P_{\rm xz} \rangle$ in the caption of Fig. 2, is however not inhomogeneous but follows a transient similar to that expected for a simple fluid—we observe the setting up of a steady, smooth and wedge-shaped profile, except at the borders, see Fig. 3, which also includes the behaviour of the averaged velocity profile for the molten gyroid at late times.

Remaining with the gyroid, we show in Fig. 4 the temporal evolution of the stress displayed in Fig. 2; the values plotted are averages of the latter on the $8 \leq x \leq N_{\rm x} - 8 = 120$ interval, which amounts to averaging over the whole lattice except thin slabs adjacent to the boundaries. In addition to Fig. 2, we include higher and lower shear velocities, namely $U = 0.05$, 0.15, 0.20. Were the strain

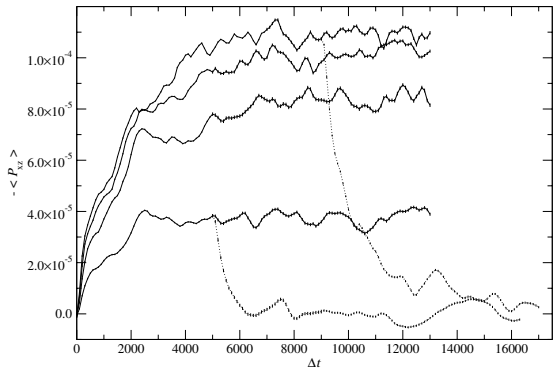

FIG. 4: Temporal evolution of the average shear stress of the gyroid for different values of steady shear. The initial condition is the same mentioned in Fig. 2. The curves, as seen, e.g., at $\Delta t = 4000$ from bottom to top, correspond to Lees-Edwards walls moving with speeds $U = 0.05, 0.10, 0.15, 0.20$ (shear rates $S/10^{-3} = 0.39, 0.78, 1.17, 1.56$), respectively. The dotted curves are the responses after a sudden termination of shear; they are also referred to as the system's relaxation functions for the relevant shear speeds. The average here is in the three-dimensional domain $[8, N_{\rm x} - 8] \times [1, N_{\rm y}] \times [16, N_{\rm z} - 16]$, where $N_{\rm x} = N_{\rm y} = N_{\rm z} = 128$ and error bars are the standard error of the average. All quantities reported are in lattice units.

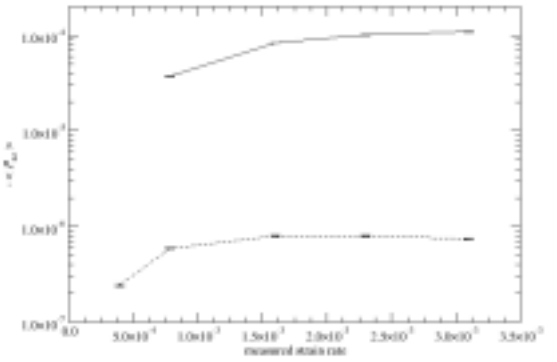

FIG. 5: Both the gyroid (solid line) and the molten gyroid (dashed) mesophases exhibit shear thinning. Shown is the stress averaged over the interval $24\,000 \leq t \leq 28\,000$. From the figure it is clear that the gyroid manifests greater stiffness than the molten gyroid and its (effective) viscosity drops for higher strain rates. All quantities reported are in lattice units.

rate at which the gyroid deforms coincident with the applied shear rate, this curve would itself confirm shear thinning to be occurring and would be the first indication of shear thinning reported by means of a bottom-up kinetic-theoretic model for fluid flow. In fact, while the increments in applied shear rate between these curves are kept constant, the increments in the (absolute) values of the stress at late times do not remain so but decrease. In Fig. 5 we show the stress averaged over time steps 24 000 to 28 000, plotted against the true strain rate, where the latter was measured from the linear velocity profile generated at $\Delta t \geq 9\,000$ ($t \geq 24\,000$), as displayed in Fig. 3. Figure 5 clearly shows shear thinning: the slope, i.e., the effective viscosity $\eta^{\rm eff} \equiv \partial P_{\rm xz}/\partial\dot{\gamma}$, decreases with the strain rate.

Figure 5 also contains the analogous curve for the molten gyroid, which shows shear thinning for the latter at lower strain rates than those at which the gyroid does, and at of higher intensity, i.e.

$$\frac{\partial\eta^{\rm eff}}{\partial\dot{\gamma}}\Big|_{\rm molten} < \frac{\partial\eta^{\rm eff}}{\partial\dot{\gamma}}\Big|_{\rm gyroid} < 0\,. \qquad (6)$$

B. Morphological transitions

Figure 6 shows the configuration of the gyroid in the $40 \leq y \leq 52$ slab of the $128 : 128 : 128$ lattice, before and at late times after applying a shear of $U = 0.20$. The volume rendering graphics method employed [21] makes regions where $\phi \geq 0.37$ opaque to the (normally incident) lighting rays; since $-0.79 \leq \phi \leq 0.79$ over the whole system, these regions are the high-density locus of one of the species (say, oil). Before shear, the structure contains highly ordered subvolumes of gyroid symmetry and diagonal length from about 32 to 64 lattice sites, cf. Fig. 6(a). The gyroid is hence depicted as a regular tubular structure making up two three-fold coordinated, interweaving chiral lattices. Since the size of the unit cell for the LB parameters employed is approximately 5 to 6 lattice sites, the depth (y-dimension) of the slabs shown in Fig. 6 is of about two gyroid unit cells. As can be seen in Fig. 6(a), the interfaces between these gyroid subvolumes are defective regions where long-range order and symmetry drastically reduce [10, 11]. Two features characterising them is the spatial variation in coordination number and chirality, seen by the presence of elongated tubules and toroidal rings, cf. figure 7.

At late times after the start of shear, $\Delta t = 21\,000$, the structure has lost any resemblance with the initial gyroid, except for the persistence of the toroidal rings, see Fig. 6(c). Also, the structure at these times is essentially the same as that at time steps between $\Delta t = 3\,000$ and $\Delta t = 5\,000$—it is a nonequilibrium steady state at least for the previous 16 000 time steps, a time longer than that required for the initial configuration to self-assemble from a homogeneous mixture of oil, water and amphiphile. The structure at $\Delta t = 21\,000$ consists of a non-crystalline network of mostly the same elements characterising the defective regions before shear, i.e. elongated tubules, with a tendency to align along the $(1, 0, 1)$ direction (characterising the velocity profile), and toroidal, ring-like structures. This description is independent of the subvolume of the lattice visualised.

We also looked into the structure of the sheared molten

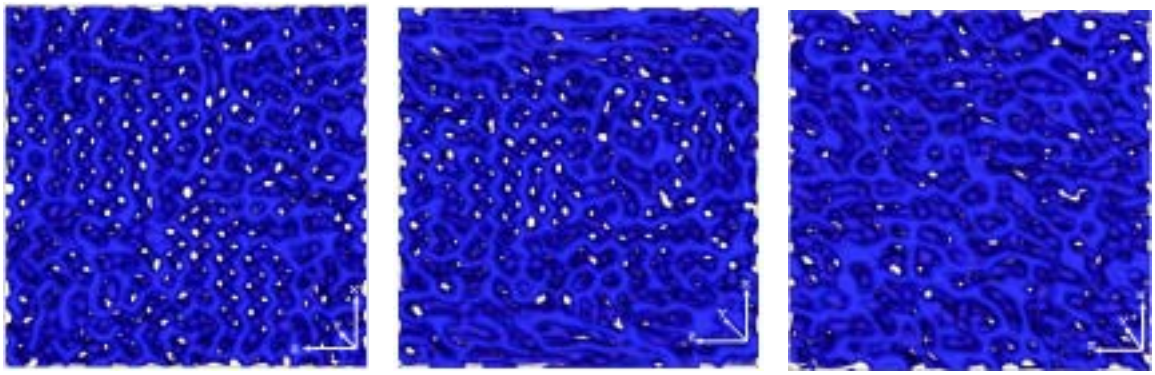

(a) $\Delta t = 0$ (b) $\Delta t = 1\,000$ (c) $\Delta t = 21\,000$

FIG. 6: High-density regions of one species (say, oil) in the gyroid mesophase, before shearing, Fig. (a), and at an early (Fig. (b)) and late time slice (Fig. (c)) after the onset of shear. The shear speed is $U = 0.20$. The complementary immiscible fluid (water) fills the voids with a similar, inter-weaving structure. The system is on a $128 \times 128 \times 128$ lattice, and all figures show the subvolume $40 \leq y \leq 52$ and the reference system in use (the y-axis enters the reader's plane). The initial configuration is a gyroid at 15 000 time steps of self-assembly. These images are volume renderings of the density order parameter, $\phi \equiv \rho^{\text{oil}} - \rho^{\text{water}}$; the regions visible to the reader are those for which $\phi \geq 0.36$ whilst over the entire fluid $-0.79 \leq \phi \leq 0.79$. All quantities reported are in lattice units.

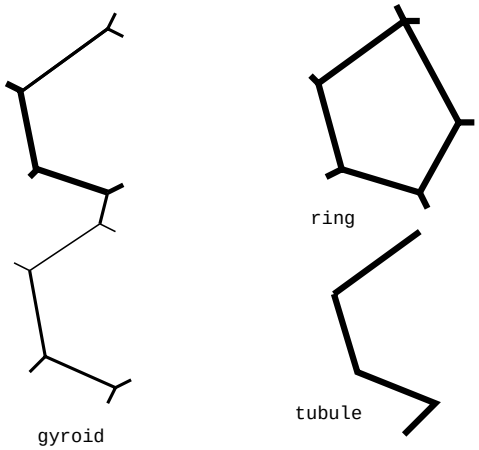

FIG. 7: Schematic representation of the skeleton (locus of highest density) of the gyroid mesophase we employ, and two of its structural features before and at late times after the onset of steady shear. The thickness provides a sense of perspective, and represents how close each segment is to the reader; note that the figures on the right are planar. The skeleton denoted by 'gyroid' depicts a portion of one of the two chiral lattices making up the long-range order regions of the gyroid before shear, cf. Fig. 6a—the coordination number is three at each node. In the regions of the gyroid containing defects, as well as in most of the sheared mesophase at late times, the coordination number can be reduced to two, describing a 'tubule'. We also show the skeleton of the 'ring' structure ubiquitous in the sheared gyroid at late times, also present in smaller proportion as a defect in the mesophase before the onset of shear. At lower values of density, this ring appears as toroidal.

gyroid at late times. In contradistinction to the gyroid's state at high strain, showing tubules of shape similar to that included in Fig. 7 and at an angle with the $x = \text{const.}$ planes, the highly strained molten gyroid display tubes which are more stretched and placed along the $\hat{\mathbf{z}}$ direction. The toroidal rings, also present for the molten gyroid before shear, represent a much smaller volume fraction for the sheared molten gyroid than for the sheared gyroid.

Figure 8 shows the summed structure function $\sum_{k_y} S(\mathbf{k})$, or scattering pattern, for the sheared gyroid mesophase, where $S(\mathbf{k}, t)$ is the structure function, computed according to [11, 16]

$$S(\mathbf{k}, t) \equiv \frac{\varsigma}{V} \left| \phi'_{\mathbf{k}}(t) \right|^2 . \tag{7}$$

Here, $\mathbf{k}$ is the discrete wavevector, V is the lattice volume, ς is the volume of the D3Q25 lattice unit cell, and $\phi'_{\mathbf{k}}(t)$ is the Fourier transform of the fluctuations of ϕ. $S(\mathbf{k}, t)$ is the Fourier transform of the autocorrelation function for the order parameter,

$$C_{\phi\phi}(\mathbf{r}, t) \equiv \langle \phi((\mathbf{x}, t)) \phi(\mathbf{x} + \mathbf{r}, t) \rangle \tag{8}$$

where $\mathbf{r}$ is a vector lag and the brackets indicate average over the spatial coordinate $\mathbf{x}$. Figures 8(a), (b) and (d) are the yz 'scattering patterns' of the structures in Fig. 6, produced by summing up the structure function along the x direction; these patterns represent characteristic stages in the plastic deformation of the gyroid. At $\Delta t = 1\,000$ (not shown), the maximum intensity is reduced to 29% of its value at $\Delta t = 0$, while there appear horizontal 'smeared out filaments' of very weak intensity, intrinsically related to the shearing process, as we shall conclude

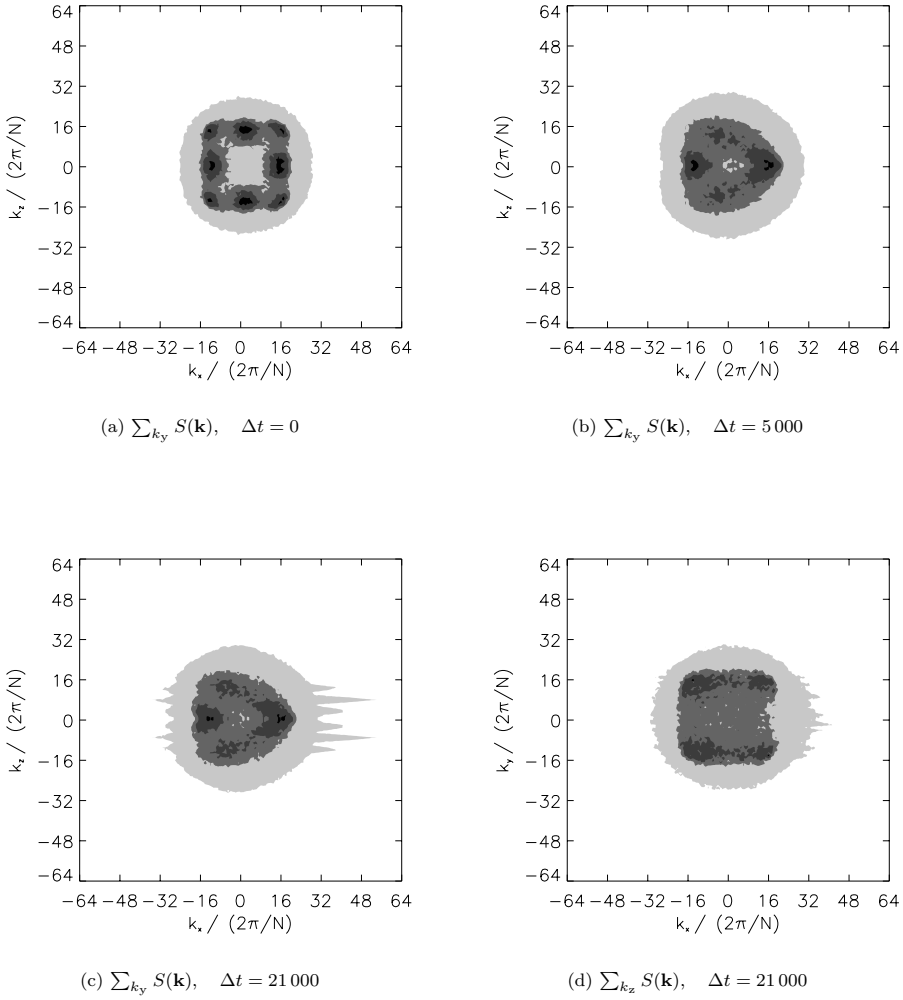

(a) $\sum_{k_y} S(\mathbf{k})$, $\Delta t = 0$

(b) $\sum_{k_y} S(\mathbf{k})$, $\Delta t = 5\,000$

(c) $\sum_{k_y} S(\mathbf{k})$, $\Delta t = 21\,000$

(d) $\sum_{k_z} S(\mathbf{k})$, $\Delta t = 21\,000$

FIG. 8: Projected structure function ('scattering pattern') as a function of the time step for the sheared gyroid, as calculated using Eq. (7). Shear velocity is $U = 0.20$. Figures (a), (b) and (c) are scattering patterns before shear and at intermediate and late times after the onset of shear, respectively, while, for completeness, Fig. (d) details the side view of the structure function corresponding to Fig. (c). The initial condition for shearing was a gyroid on a 128^3 lattice at 15 000 time steps of self-assembling. Time steps after the start of shear for these snapshots are indicated below each. Darkness in the greyscale grows with the scattering intensity—filled isocurves correspond to values $S = 1, 80, 200, 700$. The spikes are shear-dependent features; see Fig. 9 and text for discussion. All quantities reported are in lattice units, and $N \equiv N_x = N_z$.

from Fig. 9. At $\Delta t = 5\,000$ a clear *cardioid* shape has developed, which persists for the rest of the simulation; this confirms our observation that the system reaches a steady state at time step 5 000; in addition, there is no trace of gyroidal patterns along the x-direction.

In order to investigate the origin of the cardioid shape, we computed the scattering pattern for a 'synthetic gyroid',

$$G(\mathbf{x}) \equiv \sin qx \cos qy + \sin qy \cos(qz - \delta(\mathbf{x})) + \sin(qz - \delta(\mathbf{x})) \cos qx \,. \quad (9)$$

where $\delta(\mathbf{x}) = (x - N_x/2)\delta_{\max}$ is a spatially-varying dephase used to obtain a linear strain on the morphology (its maximum value, $\delta_{\max}$, is reached at the lattice boundaries), and $q = $ const. is a wavenumber controlling the size of the surface's unit cell. It is known that $G(\mathbf{x}) = 0$ for

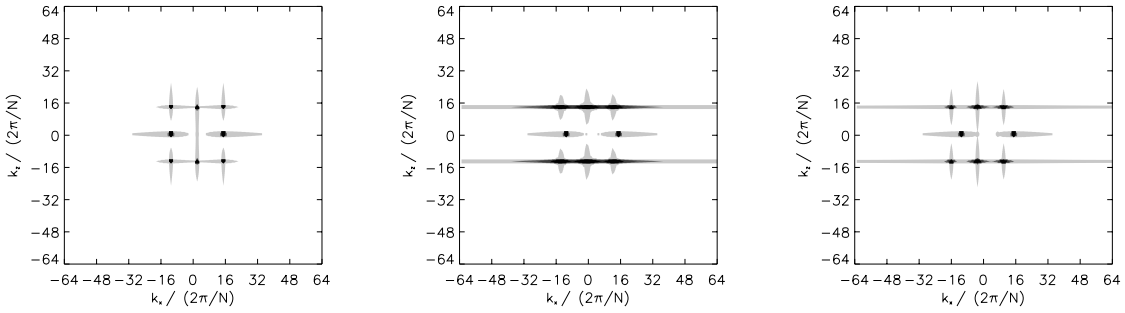

(a) $\delta_{\max} = 0$ (b) $\delta_{\max} = 8$ (c) $\delta_{\max} = 16$

FIG. 9: Structure function of the 'synthetic gyroid', as calculated using Eq. 7 on the field $G(\mathbf{x})$, cf. Eq. 9. Parameter $\delta_{\max}$ is the maximum value of the dephase $\delta(\mathbf{x}) = (x - N_x/2)\delta_{\max}$, which serves to mimic a uniform strain across the structure. The case $\delta_{\max} = 0$ [lattice sites] gives an approximation to the Schoen G (or 'ideal gyroid') structure. Darkness in the greyscale grows with the scattering intensity, and the filled isocurves shown correspond to $S = 1, 80, 200, 700$. For nonzero k_x, the strain appears to shift the pattern leftwards and smear the peaks, while leaving the zero k_x intact. The smearing not in direct relation to the strain—panel (b) shows more smearing than panel (c)—explains the spikes shown in Fig. 8. The 'cardioid' shape reported in Fig. 8 originates from the combination of the structure undergoing a structural transition (losing its $k_z \neq 0$, $k_x \neq 0$ peaks) whilst being sheared with a velocity profile of positive slope (cf. Fig. 3, which orients the 'atria' leftwards). All quantities reported are in lattice units, and $N \equiv N_x = N_z$.

$\delta_{\max} \equiv 0$ is a good approximation to the Schoen "G" triply periodic minimal surface of $Ia\bar{3}d$ cubic symmetry [22]. Figure 9 shows the scattering patterns for the unstrained morphology and for dephases $\delta_{\max} = 8$, 16.

Comparing the structure function maps, Figs. 8 and 9, at the same value of the strain rate might prove useful. For the ideal gyroid, strain is controlled by the number of unit cells that the dephase causes the structure to shift at the lattice boundary, following a linear profile as we approach the other boundary through a zero at the lattice core. For the amphiphilic gyroid, however, the strain does not follow a linear profile at early times; instead, the strain at time t would need be computed from the integral $\frac{1}{N_x}\int_0^t \int_0^{N_x} \mathrm{d}t'\mathrm{d}x\, \partial_x u_z(\mathbf{x}, \mathbf{t}')$, where t' is the time parameter. For the purposes of this paper, however, this analysis would be superfluous; in fact, Fig. 9 already provides us with enough information to understand the origin of the cardioid shape. For all panels, (a), (b) and (c) therein, the position of the peaks at $k_x = 0$ ($k_z/(2\pi/N) \approx -14$, 15, where $N = 128$) are invariant under the strain (dephase); not so with the peaks at $k_x \neq 0$, which shift leftwards. (The shift would be rightwards were $\partial_x u_z < 0$.) The shape of the maps in Figs. 8(c) and 8(d) is that of a transformed scattering pattern shifted leftwards. This transformation occurs early, between $\Delta t = 0$ and $\Delta t = 3\,000$, and is characterised by two strong ($S \geq 700$) peaks similar to those of the gyroid at $k_x = 0$, and two weaker ($200 \leq S < 700$) peaks at $k_z = 0$.

IV. SHEARING THE LAMELLAR MESOPHASE: DEPENDENCE ON THE AMPHIPHILE DENSITY

In the last section we reported on the gyroid displaying lower shear stress than the molten gyroid. Since the structural transition between these two mesophases can be driven by the density of amphiphile and/or the inter-amphiphile coupling parameter, as González-Segredo and Coveney reported [11], our aim in this section is to elucidate the role of the amphiphile density alone on the stress response to shear; we choose the lamellar mesophase as the subject of the study, since it has the simplest possible internal interface.

The initial configuration employed was a cubic 128^3 lattice with 16 lamellae, stacked perpendicularly to unit vector $\hat{\mathbf{z}}$. The lamellae were of alternating, oil-water compositions, separated by a thin monolayer of amphiphile. The thickness of the immiscible and amphiphilic lamellae were 7 and 1 lattice sites, respectively. We populated each lattice site with a value of density which kept constant over the region corresponding to a same species; each microscopic velocity is assigned the same fraction of this value. We gave amphiphilic regions the densities $n^{(0)\mathrm{s}} = 0$, 0.80, 0.95, and oil and water regions the densities $n^{(0)\mathrm{r}} = n^{(0)\mathrm{b}} = 0.7$. Shear was applied perpendicularly to the lamellae via with the same LEBC's presented in the last section, with speed $U = 0.10$.

Before shearing, the case without amphiphile of the lamellar initial condition just described is, *a priori*, a metastable state in our LB model. In fact, the structure

has a stationary morphology since short-range oil-water forces and the absence of fluctuations maintain immiscibility while keeping the interface's shape; however, a large enough perturbation in ϕ can make these forces drive the interface to a radically different shape. Moreover, shear will work against the interfacial tension by reducing the interface steepness (i.e., $|\nabla\phi|$), which will lead to miscibility ($phi \equiv 0$) for high enough strain rates. Despite these arguments, we observed stability for the sheared lamellar mesophase without amphiphile, as we report next.

Figure 10 shows the stress as measured in the same fashion carried out in the last section (see Fig. 4), for several amphiphile densities. The behaviour observed is diverse. For zero amphiphile concentration (solid curve), the stress reaches a peak at early times before it proceeds to a second, lower maximum at late times, going through a trough at intermediate times due to the fact that $|\nabla\phi|$ experiences a transient decrease.

The high-density regions for one of the immiscible species (say, oil) is shown in Fig. 11(a) at late times, $\Delta t = 8\,000$; for the lamellar morphology, these are representative of the shape of the oil-water interface. Away from the boundaries ($x = 0$, 128), there is a large surface area of interface with zero curvature, where we define the curvature as $H \equiv \partial^2_{zz} x_\phi(z)$, $x_\phi(z)$ being the curve resulting from projecting of the $\phi = 0.18$ surface onto the xz plane. Curiously, we observe two changes of curvature passing through an inflexion point as we follow the curve $x_\phi(z)$ around $x = 64$ for $y =$ const.—we would have expected the steady, late-time configuration for the sheared lamellar mesophase to minimise the interfacial area showing non-zero concavity. We can associate a curvature energy density (per unit of interfacial area) to H^2, following Helfrich's definition of the rigidity modulus [23].

The stress curve corresponding to $n^{(0)\mathrm{s}} = 0.80$, cf. Fig. 10 shows the absence of a trough, as it occurs for the $n^{(0)\mathrm{s}} = 0$ case, despite the fact that interfacial tension is drastically reduced by the presence of the amphiphile. In addition, the stress grows with time to higher values than those achieved by the $n^{(0)\mathrm{s}} = 0$ case at late times. The late time order-parameter configuration is displayed in Fig. 11(b), showing a rich interfacial pattern. Using the same arguments of the last paragraph, this structure could be characterised by a higher curvature energy, $\int_I \mathrm{d}\sigma\, H^2$, where σ is a measure on the oil-water interface, I, and H is now defined as the inverse radius of curvature, parameterised on the arclength, s. Figure 11(b) shows similar regions of high curvature at an equal distance from the shearing walls, where $u_\mathrm{z} =$ const., which we shall call *nodal* planes. Also note that the interface, as approximately depicted by the boundary of the $\phi \geq 0.22$ volume, joins the lattice boundary at an angle close to 90 degrees.

The stress curve for the $n^{(0)\mathrm{s}} = 0.95$ case shows a dramatically different situation for the first 5 000 time steps: the presence of a trough, deeper than that present for the $n^{(0)\mathrm{s}} = 0$ density. After that, there appears a shoot-off whereby the stress rapidly grows and equals the late time value achieved in the $n^{(0)\mathrm{s}} = 0.80$ case. However, the order-parameter displays a configuration analogous to the $n^{(0)\mathrm{s}} = 0.80$ case, cf. Fig. 11(c). By looking at the amphiphile density field, $\rho^\mathrm{s}(\mathbf{x})$, for the case $n^{(0)\mathrm{s}} = 0.95$, we observed that the high curvature regions arise close to the boundaries first ($\Delta t < 1000$), and then rapidly move away from them as the strain progresses.

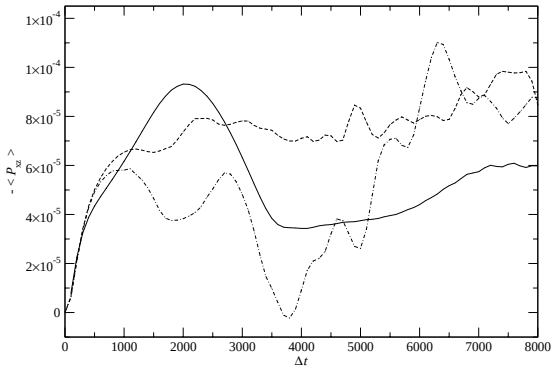

FIG. 10: Temporal evolution of the average shear stress response of a lamellar mesophase at a shear speed of $U = 0.10$, for different amphiphile densities. The solid, dashed, and dash-dotted curves correspond, respectively, to $n^{(0)\mathrm{s}} = 0$, 0.80, 0.95. The average is computed over the three-dimensional domain $[8, N_\mathrm{x} - 8] \times [1, N_\mathrm{y}] \times [16, N_\mathrm{z} - 16]$, where $N_\mathrm{x} = N_\mathrm{y} = N_\mathrm{z} = 128$ and error bars are not included since they are negligible. All quantities reported are in lattice units.

V. CONCLUSIONS

In this paper we reported on the shear stress response of two gyroidal cubic amphiphilic mesophases previously self-assembled using the same bottom-up LB model we employ here, namely, the gyroid *per se*, which shows high crystallinity at late self-assembly times, and the molten gyroid, endowed with shorter-range order and located within the sponge-gyroid lyotropic structural transition [11]. Shear was imposed via sliding periodic (Lees-Edwards) boundary conditions, and we investigated the system's response to several values of the strain rate. In addition, in order to investigate the dependence of the shear stress on the amphiphile density, we also sheared a lamellar mesophase, of a much simpler morphology than the gyroidal mesophases.

We found that the gyroidal mesophases exhibit shear thinning, more pronounced and at lower strain rates for the molten gyroid than the gyroid. In other words, momentum is transported more easily across the mesophase from the shearing walls for the mesophase containing more amphiphile, of longer-range ordering.

We also found a shear-induced transition from an ini-

(a) $n^{(0)s} = 0$ (b) $n^{(0)s} = 0.80$ (c) $n^{(0)s} = 0.95$

FIG. 11: Slabs $0 \leq y \leq 8$ of the order parameter ϕ for the lamellar mesophases with different amounts of amphiphile density, $n^{(0)s}$, at time step $\Delta t = 8\,000$ after the onset of a shear of velocity $U = 0.10$. (The coordinate system is the same of Fig. 6.) In panel (a), the regions opaque to incident (volume rendering) light are those for which $\phi \geq 0.18$, where $|\phi| \leq 0.36$ across the system. In panel (b), the opaque regions are those for which $\phi \geq 0.22$, where $|\phi| \leq 0.45$ across the system. In panel (c), the opaque regions are those for which $\phi \geq 0.24$, where $|\phi| \leq 0.48$ across the system. It is worth noting that the surfactantless case, (a), exhibits a curved interface. The amphiphilic cases, (b) and (c), display the formation of irregularities in the interface and nodal planes, as a result of the inter-amphiphile interaction. All configurations have translational symmetry along the y-axis. All quantities reported are in lattice units.

tial gyroid morphology to a mesophase at large strain characterised by the coexisting elongated tubules and toroidal, ring-like structures. This mesophase is in contrast with one found by Zvelindovsky et al. with free-energy Langevin-diffusion methods by shearing a bicontinuous structure reminiscent of a molten gyroid [3]. The structure they found is of a shorter-range ordering than that of the molten gyroid employed for the study reported in this paper, and the high-strain structure consists of coexisting lamellae and hexagonally packed tubes elongated along the direction of the imposed shear velocity. Our shear molten gyroid also shows enlongated tubes along this direction, but the structure is far more complicated than that found by Zvelindovsky et al. in that it exhibits remnant toroidal rings and 'hard shoulders' reminiscent to gyroidal skeletons, and hexagonal packing and coexisting lamellae are absent.

The shear performs a plastic deformation which effectively breaks the gyroidal skeleton's links which interpose an (oil-water) interface whose normal, $\mathbf{n}$, is parallel or antiparallel to the flow, $\mathbf{u}$. In other words, by shearing we apply a (mixing) force which is not only in competition with the oil-water force, generating immiscibility, but also with the inter-amphiphile force. Our hypothesis here is that adsorbed dipoles sitting on interfacial regions with an angle $\theta \equiv \angle(\mathbf{u}, \mathbf{n})$ in the range $0 < \theta < 180$ degrees require more work from the shear forces to draw them away from the interface than those regions placed normally to the flow, since the (shear-induced) mixing reduces as $\cos\theta$. In particular, when $\theta = 0$, the inter-amphiphile force can sustain considerably long interfaces—shear induces a preferential direction along which the long-range order present before shearing is not reduced. These arguments explain not only the formation of the elongated tubules but also their reconnection (increase in coordination number). In fact, the toroidal, ring-like structures are not only vestigial gyroid defects which have survived the gradient $\nabla\mathbf{u}$, but also born anew resulting from reconnections.

Applying shear to a lamellar mesophase, we found that the presence of amphiphile on the oil-water interface of the mesophase causes the interface to fold into a wealth of structures with a (discrete) translational symmetry on planes equidistant to the shearing walls and along the direction of the shear velocity. In other words, the inter-amphiphile force couples the adsorbed amphiphilic dipoles so that the interface locally increases its curvature energy density. It is worth investigating whether this local increase is due to the amphiphile being incapable of sustaining interfacial regions of low curvature under shear, i.e., whether shear induces a 'breaking' mechanism. Regarding the shear stress, our amphiphile-containing lamellae responded with higher stress at late times than those without. This contrasts with the results found for the gyroidal mesophases, and leads us to conclude that it is the gyroid's cubic morphology that allows this structure to be stiffer.

VI. ACKNOWLEDGMENTS

We thank Dr. Rafael Delgado-Buscalioni for enlightening discussions, and acknowledge Iain Murray, Elena

Breitmoser and Jonathan Chin for their involvement in algorithm implementation and optimisation within the RealityGrid and TeraGyroid projects. This work was supported by the UK EPSRC under grant RealityGrid GR/R67699 which also provided access to a 512-processor SGI Origin3800 platform at Computer Services for Academic Research (CSAR), Manchester Computing, UK. We also thank the Higher Educat England (HEFCE) for our on-s graphical supercomputer. NGS Prof David Jou, Prof José Casa Camacho at the Universitat A Spain, for their support.

[1] A. V. M. Zvelindovsky, B. A. C. van Vlimmeren, G. J. A. Sevink, N. M. Maurits, and J. G. E. M. Fraaije, J. Chem. Phys. **109**, 8751 (1998).
[2] A. V. M. Zvelindovsky, G. J. A. Sevink, B. A. C. van Vlimmeren, N. M. Maurits, and J. G. E. M. Fraaije, Phys. Rev. E **57**, R4879 (1998).
[3] A. V. M. Zvelindovsky, G. J. A. Sevink, and J. G. E. M. Fraaije, Phys. Rev. E **62**, R3063 (2000).
[4] A. N. Morozov, A. V. M. Zvelindovsky, and J. G. E. M. Fraaije, Phys. Rev. E **64**, 051 803 (2001).
[5] A. N. Morozov and J. G. E. M. Fraaije, Phys. Rev. E **65**, 031 803 (2002).
[6] A. Xu, G. Gonella, and A. Lamura, Phys. Rev. E **67**, 056 105 (2003).
[7] R. D. Groot and W. G. M. Agterof, Macromolecules **28**, 6284 (1995).
[8] P. Sollich, Phys. Rev. E **58**, 738 (1998).
[9] P. V. Coveney, Phil. Trans. R. Soc. Lond. A **361**, 1057 (2003).
[10] N. González-Segredo and P. V. Coveney, Europhys. Lett. **65**, 795 (2004).
[11] N. González-Segredo and P. V. Coveney, Phys. Rev. E, (in press, 2004).
[12] A. W. Lees and S. F. Edwards, J. Phys. C **5**, 1921 (1972).
[13] H. Chen, B. M. Boghosian, P. V. Coveney, and M. Nekovee, Proc. R. Soc. London A **456**, 2043 (2000).
[14] An example of the use of the D3Q25 lattice in lattice-gas methods is: P. J. Love, P. V. Coveney, and B. M. Boghosian, Phys. Rev. E **64**, 021503 (2001).
[15] S. Succi, "The lattice-Boltzmann equation–for fluid dynamics and beyond." (Oxford University Press, Oxford, 2001.)
[16] N. González-Segredo, M. Nek Phys. Rev. E **67**, 046304 (2003
[17] A. J. Wagner and I. Pagonaba 521 (2002).
[18] P. J. Love, M. Nekovee, P. González-Segredo, and J. M. Commun. **153**(3), 340 (2003).
[19] This has been corroborated b TeraGyroid project [11], aime employ in this paper to study phiphilic gyroids on large (simulation times (up to 10 see URLs: http://www.sc-co http://www.RealityGrid.org/n
[20] J. Harting, M. Venturoli and P grid-enabled lattice-Boltzmann fluid flow in porous media and ings of the 12th International C Simulation of Fluid Dynamics J. P. Boon and P. V. Coveney. R. Soc. London Series A, Augu
[21] For an explanation of volu W. Schroeder, K. Martin, B. tion Toolkit: An Object Orient ics." Kitware Inc., ISBN 1930 URL: http://public.kitware.co
[22] M. Wohlgemuth, N. Yufa, J. H Macromolecules **34**, 6083 (200
[23] R. Lipowsky, Nature **349**, 475

pLRME2D: A parallel implementation of a two-dimensional hydrodynamic lattice gas model with long-range interactions

Nélido González-Segredo *[1] and Martyn Foster †[2]

[1] *Centre for Computational Science, Queen Mary & Westfield College, University of London, Mile End Road, London E1 4NS, UK*
[2] *Manchester Research Centre for Computational Sciences, Manchester Computing, University of Manchester, Oxford Road, Manchester M13 9PL, UK*

Using a two-dimensional hydrodynamic lattice-gas model for the simulation of binary immiscible and ternary amphiphilic fluids, we investigate the effect of long-range interactions in the surface tension of a planar interface between two immiscible fluids of equal density with and without a layer of surfactant particles lying on it. This is the first stepping stone towards the simulation of the dynamics of fluid vesicles: the surface tension is one of the parameters of some continuum-mechanical descriptions [5] for vesicles, and long-range interactions are believed to be crucial in attaining stability. The parallel implementation of the lattice gas algorithm employs a new communication wrapper providing an object orientated approach to distributed memory programming of n-dimensional grid-based calculations. We find that the surface tension increases with the range of interactions of the immiscible fluid particles but not with that for the surfactant particles. We also find good scalability and minimal impact of the parallelisation strategy on the structure of the base serial code.

I. INTRODUCTION

A wide range of fluids found in nature and in industrial processes are in the form of immiscible mixtures. Oil and water are archetypical examples of such systems, important in the food and petroleum industries, although polymeric and colloidal solutions are also common cases.

The addition of amphiphilic (also called surfactant) chemicals in a fluid or in an immiscible mixture gives rise to the self-assembling of complex morphologies of great interest in physical chemistry, biology and chemical engineering [1]. The mechanism for their formation relies in the polar nature of the surfactant molecules, with an ionic head attached to a hydrocarbon tail. In immiscible mixtures, opposite parts are attracted to different phases, thereby favouring their absorption at, and causing the formation of, binary immiscible interfaces [2]. When dispersed in single fluids, either organic or ionic, they aggregate such that the part of the molecule which is insoluble in the medium is shielded from it.

Examples of these self-assembled, fluidic structures are spherical and wormlike micelles, lamellar and sponge phases, microemulsions, and bicontinuous tubular structures, and are also termed lyotropic liquid crystals [3]. Their properties have produced a wealth of applications: the very low surface tension in amphiphilic microemulsions has led to the use of surfactants as detergents; the viscoelasticity of wormlike micelles is a desirable property for food products and paints; spherical micelles can be used as carriers in drug transport and delivery by the pharmaceutical industry.

The aim of this work is to lay down a first stepping stone in the modelling of amphiphilic membranes with a mesoscopic technique such as the *lattice gas automaton* [2]. We are interested in simulating vesicles, which are the backbone of many biological structures, such as cell membranes. They are made up of closed bilayer sheets of phospholipids,of an amphiphilic nature.

A hydrodynamic lattice gas automaton for amphiphilic and immiscible fluids is a class of cellular automata. Our model, based on the Boghosian-Coveney-Emerton (BCE) model [2], consists in a regular lattice of the required symmetry which is populated with particles of different species with discrete velocities, colliding and advecting in discrete timesteps, and satisfying local conservation of mass and momentum. The collision operator is nondeterministic in that local, postcollisional states are sampled from a distribution which enforces phase separation of immiscible fluid species. In the macroscopic, spatial averaging limit, the Navier-Stokes equations for incompressible, viscous, low Mach number (*creeping*) flows are recovered for each single phase. The added feature to the BCE model is the incorporation of long range interactions.

Long-range interactions were introduced into cellular automata to model phenomena in which inhomogeneities may become more stable than homogeneous phases [8–10].

In the macroscopic modelling of vesicles, many continuum mechanical models have appeared [4], initially motivated by the study of the sickle red blood cell shape [5]. They all introduce the vesicle's surface tension, bending elasticity and osmotic pressure as key parameters of their model determining the vesicle's equilibrium shapes.

Our novel approach is to propose a fluid model, entirely based on mesoscopic particle interactions, which

*n.gonzalez-segredo@qmw.ac.uk. Also at Departament de Física, Universitat Autònoma de Barcelona, 08193 Bellaterra, Barcelona, Spain.
†Email: martyn.foster@man.ac.uk. Telephone number: +44 (0)161 275 6821

could not only mimic the shape of surfactant vesicles at late times (equilibrium) but be able to reproduce their dynamic, nonequilibrium behaviour [6]. There have already appeared other mesoscopic approaches to the problem [7], yet injecting macroscopic information about the interface back down to the underlying transport dynamics. Length scale-wise, our aim is to follow a *down-to-top-only* approach.

Because surface tension and bending rigidity arise as a result of spatial correlations of the fluid's molecules, it seems plausible that in our model they can be a function of the range of the particle interactions. In this work we focus our attention on the surface tension alone.

In section II the lattice-gas model itself is explained. We deal with a binary system (two-dimensional, planar interface) comprising two immiscible phases which, for simplicity, we will refer to as water and oil, and a ternary system when adding a third, surfactant phase. Finally a method for measuring its surface tension is outlined.

In section III we present details on the parallel implementation of the algorithm. We use a set of wrapper functions acting as a general-purpose interface to MPI directives. Section IV contains the results of our simulations, and in section V we conclude and propose a natural continuation to this work.

II. AN AMPHIPHILIC IMMISCIBLE LATTICE GAS WITH LONG RANGE INTERACTIONS

The lattice-gas model we use is an extension of the nearest-neighbour-interaction model used by Boghosian, Coveney and Emerton (BCE) [2], which in turn is a generalisation of the immiscible lattice gas of Rothman and Keller [11], with the inclusion of surfactant particles. Before tackling the extension to long-range interactions on the Boghosian-Coveney-Emerton model, we will give as follows a detailed description of it.

The BCE automaton is a two-dimensional triangular lattice containing up to seven particles per node. The choice of a triangular lattice guarantees isotropic behaviour in the macroscopic limit leading to the correct Navier-Stokes equations for incompressible, single-phase fluids. The particle velocities may take on any of the six unit vectors $\mathbf{c}_i$ $(i = 1, ..., 6)$ that the geometry permits, or a null vector $\mathbf{c}_0$ representing a particle at rest. To allow for different fluid types to be modelled, they assign *colour* to the particles. In this way, the state of the 2D model at site $\mathbf{x}$ and time t is completely specified by the occupation numbers $n_i^\alpha(\mathbf{x}, t)$ for particles of colour α and velocity $\mathbf{c}_i/\Delta t$. These occupation numbers can be either zero or one, and there can be at most one particle of either species per direction. The latter is a form of exclusion principle that, while restricting the application of the model to systems with low density gradients, constitutes a major assumption necessary for algorithm simplicity and speed of execution.

To consider the amphiphilic species, the surfactant particles are modelled as *colour-dipole vectors* $\sigma_i(\mathbf{x}, t)$, their occupation numbers being denoted as $n_i^S(\mathbf{x}, t)$.

The evolution of this lattice gas occurs in two substeps. In the *propagation* substep the particles at a site $\mathbf{x}$ hop to neighbouring sites along the directions corresponding to their velocity vectors. In the *collision* substep, the newly arrived particles change their velocities such that the mass of each species and the total momentum at the site ('total' meaning summed over all the species) is conserved. The *outgoing state* allowed by the conservation laws can be degenerate, and so each possible outgoing state is numbered and assigned a probability value. Then, the outgoing state is sampled according to these probabilities. If there are two states with equal probability, they are randomly chosen.

The probability values referred to in the last paragraph depend on the interaction of site $\mathbf{x}'$ with its neighbouring site $\mathbf{y}$, which in turn depends on the states of $\mathbf{x}'$ and $\mathbf{y}$. We say that we incorporate *long-range interactions* in our model when we consider not only the nearest neighbours but sites further away from $\mathbf{x}'$ to compute these probability values.

The probability values have the form of Boltzmann weights

$$e^{-\beta \Delta H}, \tag{1}$$

where β is an inverse "thermal noise" parameter and ΔH has the form of an electrostatic *interaction Hamiltonian*,

$$\begin{aligned} \Delta H &= \alpha \Delta H_{cc} + \mu \Delta H_{cd} + \epsilon \Delta H_{dc} + \zeta \Delta H_{dd} \\ &= \alpha \mathbf{J} \cdot \mathbf{E} \Delta t + \mu \mathbf{J} \cdot \mathbf{P} \Delta t \\ &+ \epsilon \Big(\sigma' \cdot \mathbf{E} + \mathcal{J} : \mathcal{E} \Delta t \Big) \\ &+ \zeta \Big(\sigma' \cdot \mathbf{P} + \mathcal{J} : \mathcal{P} \Delta t \Big) \end{aligned} \tag{2}$$

and represents the work carried out by the outgoing particles, when they hop to neighbouring lattice sites, against the field produced by the neighbouring particles. Subscript c stands for "colour", and d for "dipole", and α, μ, ϵ, and ζ are coupling parameters. ΔH_{cc} represents the work performed by a colour charge in the colour field produced by fixed surrounding colour charges, and corresponds to the relative immiscibility of oil and water; ΔH_{cd} is the work performed by a moving colour charge in the dipolar field created by surrounding fixed surfactant particles, and models the tendency of surrounding surfactant to bend around oil or water droplets, and hence favours micelle formation; ΔH_{dc} is the work carried out by an outgoing dipole when moving in a colour field produced by surrounding fixed colour charges, and corresponds to the propensity of surfactant dipoles to align across oil-water interfaces; and ΔH_{dd} is the dipole-dipole interaction. Here, Δt is the time step, and

· and : denote contraction of one and two tensor indices, respectively. Following an electrostatic analogy, we have defined the *colour flux* of an outgoing state at an arbitrary site $\mathbf{x}$ and time t as

$$\mathbf{J}(\mathbf{x},t) \equiv \sum_i^6 \frac{\mathbf{c}_i}{\Delta t} q_i'(\mathbf{x},t), \tag{3}$$

where the prime denotes that the charge is computed on an outgoing state. The *colour field* has been defined as

$$\mathbf{E}(\mathbf{x},t) \equiv \sum_{\mathbf{y}\in\mathcal{L}} f_1(y)\mathbf{y}q(\mathbf{x}+\mathbf{y},t), \tag{4}$$

where $f_1(y)$ is a derivative of the potential shape function $f(y)$

$$f_l(y) \equiv \left(-\frac{1}{y}\frac{d}{dy}\right)^l f(y) \tag{5}$$

where $l = 0, 1, ...,$ and $f(y)$ is analogous to the electric potential in electrostatics: it conveys the idea of shape and type of the interaction, i.e., how it decays with distance and whether a test particle would be attracted or repelled by a particle of alike colour generating the field. In addition, $\mathbf{y}$ is a displacement vector from site $\mathbf{x}$, y its module, $\mathcal{L}$ is the lattice, and $q(\mathbf{x},t)$ is the *colour charge* of the relevant site at time t. The latter is defined as the sum over all the directions of the *colour charge per direction*

$$q_i(\mathbf{x},t) = n_i^R(\mathbf{x},t) - n_i^B(\mathbf{x},t), \tag{6}$$

where R stands for a *red* particle and B for a *blue* particle. Note that $q_i(\mathbf{x},t)$ is positive when it is only a red particle that moves along i and negative for a blue particle.

We have also defined the *dipolar-field vector*

$$\mathbf{P}(\mathbf{x},t) \equiv -\sum_{\mathbf{y}\in\mathcal{L}} \Big[f_2(y)\mathbf{y}\mathbf{y} - f_1(y)\mathsf{I}\Big]\cdot\sigma'(\mathbf{x}+\mathbf{y},t), \tag{7}$$

where σ' is the sum of the outgoing colour dipole vector σ_i over all the directions i, and I is the rank-two unit tensor. The *dipolar-flux tensor* is

$$\mathcal{J}(\mathbf{x},t) \equiv \sum_i^6 \frac{\mathbf{c}_i}{\Delta t}\sigma'(\mathbf{x}+\mathbf{y},t), \tag{8}$$

the *colour-field gradient tensor* is

$$\mathcal{E}(\mathbf{x},t) \equiv \sum_{\mathbf{y}\in\mathcal{L}} \Big[f_2(y)\mathbf{y}\mathbf{y} - f_1(y)\mathsf{I}\Big]q(\mathbf{x}+\mathbf{y},t), \tag{9}$$

and the *dipolar-field gradient tensor* is defined as

$$\mathcal{P}(\mathbf{x},t) \equiv -\sum_{\mathbf{y}\in\mathcal{L}} \Big[f_3(y)\mathbf{y}\mathbf{y}\mathbf{y} - f_2(y)\mathbf{y}\cdot\Omega\Big]\cdot\sigma'(\mathbf{x}+\mathbf{y},t), \tag{10}$$

where Ω is the completely symmetric and isotropic fourth-rank tensor.

It is worth mentioning that the prescription for immiscibility (phase separation) is contained in the sampling process of the collision substep. In fact, it is most likely to obtain outgoing states with the highest probability values, which according to (1) correspond to the lowest values for ΔH. Thus, the velocity configurations that leave $\mathbf{J}$ and $\mathbf{E}$ antiparallel are the ones with the highest chance of being chosen by the sampling. As a result of these vectors being antiparallel, particles move towards regions of particles of like colour, and hence phase separation is induced.

Long-range interactions come into play in this scheme if we allow the sum in (4) to range over not just the nearest neighbours to $\mathbf{x}$ (i.e., $y = 1$) but a few layers of sites further away or even the whole lattice. The extension carried out in this work consists in using 3, 4, 5, 6, 7 and 8 layers of nearest neighbours, cases that we will refer to in the sequel as *LR3*, *LR4*, *LR5*, and so on, the nearest-neighbour case being denoted by *SR*.

As to what form for $f_l(y)$ in (4) and (7) was used, we chose one that is constant within the interaction range and whose value is that at nearest neighbouring sites, i.e., such that

$$f_l(y) \equiv \begin{cases} f_l(1) & \text{if } y \le \text{interaction range} \\ 0 & \text{otherwise} \end{cases} \tag{11}$$

We have used $f(y) = -1/y$ as a suitable general function. (The negative sign allows inducing cohesion in immiscible mixtures.) This particularisation leaves (4) and (7) as

$$\mathbf{E}(\mathbf{x},t) \equiv \sum_{\mathbf{y}\in\mathcal{L}} r(y)\hat{\mathbf{y}}q(\mathbf{x}+\mathbf{y},t), \tag{12}$$

$$\mathbf{P}(\mathbf{x},t) \equiv -\sum_{\mathbf{y}\in\mathcal{L}} r(y)\Big[\frac{3}{2}\hat{\mathbf{y}}\hat{\mathbf{y}} - \mathsf{I}\Big]\cdot\sigma'(\mathbf{x}+\mathbf{y},t), \tag{13}$$

where $\hat{\mathbf{y}}$ is the unit vector $\mathbf{y}/y$, I is the rank-two unit tensor, and $r(y)$ is a step function that controls the extent of the interactions, namely

$$r(y) = \begin{cases} -1 & \text{if } y \le \text{interaction range} \\ 0 & \text{otherwise} \end{cases} \tag{14}$$

This choice of the interaction potential allows us to focus our attention on the effect of varying the number of neighbours as a parameter, without the additional complications associated with a decaying function of distance.

The factor 3/2 in (13) is a choice necessary to guarantee that the dipole-dipole interaction work has well-defined minima, i.e., such that there are a finite number of angles towards which the dipoles tend to tilt and that they show the correct self-assembly behaviour: Aligning in parallel, head to head and tail to tail. When using the factor 2 instead of 3/2, as would directly follow from (5), those minima turn out to be a continuum of values.

Incrementing the number of neighbours to sum over in (4) is always done at the expense of increasing the computing time needed compared to what the nearest-neighbour case requires. However, to get round this problem, our code exploits to great advantage the fact that both (12) and (13) have the form of a *convolution*. For two arbitrary scalar functions f and g defined over a subset Ω of the integers, the convolution can be defined as

$$f * g = \sum_{\tau \in \Omega} f_\tau \, g_{t-\tau}. \tag{15}$$

If we generalise this to one-dimensional real functions over the lattice $\mathcal{L} \subset \mathbf{Z}^2$ and replace g by q and f by $f(y)\mathbf{y}$, we realise that the cartesian components of $\mathbf{E}$ are

$$E_1 = f(y)y_1 * q, \qquad E_2 = f(y)y_2 * q, \tag{16}$$

where the subscripts 1 and 2 denote x and y components, respectively. The benefit of expressing the colour and dipolar fields in this way comes about because the convolution of two functions is the inverse Fourier transform of the product of the functions' Fourier transforms,

$$f * g = \mathcal{F}^{-1}\Big[(\mathcal{F}f)\,(\mathcal{F}g)\Big]. \tag{17}$$

Because the Fourier transforms are computed over the whole lattice regardless the range of the interactions, there is no increase in computational expense when increasing this range. Moreover, Fourier transforms can be calculated very efficiently using Fast-Fourier-Transform (FFT) algorithms.

For computer implementation, we need to store our triangular lattice in memory arrays, whose unit cells are squares and not hexagons. That is, we have to transform the lattice into a square one. We do so by moving every even row in the triangular lattice by half the lattice constant along the negative x direction (ie., to the left). In order to keep the particles moving in the same way as they do in a triangular lattice, particles are not allowed to move along all the diagonals: those lying on an even row cannot move along any diagonal towards the left, and particles on an odd row cannot move along any diagonal towards the right. These *selection rules* ensure that we have the behaviour of a triangular lattice, and therefore that our model leads macroscopically to isotropic behaviour [12].

A. Surface tension of a planar interface

The surface tension σ of a planar interface between two immiscible fluids [13] is given by

$$\sigma = \int_{-\infty}^{+\infty} [P_N(x) - P_P(x)]dx, \tag{18}$$

where the interface is perpendicular to the x axis, and $P_N(x)$ and $P_P(x)$ are projections of the pressure tensor along the direction normal and parallel to the interface, $P_{xx}(x)$ and $P_{yy}(x)$, respectively.

Interactions	σ $(nx = 64)$	σ $(nx = 128)$	σ $(nx = 256)$
SR	0.340 ± 0.006	0.341 ± 0.013	0.339 ± 0.025
LR3	0.403 ± 0.007	0.401 ± 0.013	0.409 ± 0.025
LR4	0.413 ± 0.007	0.412 ± 0.013	0.412 ± 0.025
LR5	0.398 ± 0.007	0.401 ± 0.013	0.413 ± 0.025
LR6	0.396 ± 0.006	0.473 ± 0.013	0.592 ± 0.025
LR7	0.424 ± 0.006	0.511 ± 0.013	0.639 ± 0.025
LR8	0.516 ± 0.006	0.823 ± 0.013	1.358 ± 0.025

TABLE I: Surface tension of a planar interface as the oil-water interaction range increases, for three different lattice sizes.

The definition of the pressure tensor in our 6-velocity lattice gas is

$$P_{\alpha\beta} = \sum_{i=0}^{6} c_{i\alpha}c_{i\beta}N_i, \tag{19}$$

where $c_{i\alpha}$ is the $\alpha-$component of the velocity vector along the direction i, and N_i is defined as the number of particles on direction i at the relevant site and averaged over an ensemble of systems prepared with different initial conditions, but subjected to the same external constraints (*ensemble averaging*). According to this, the components we are interested in become

$$\begin{aligned} P_N(x) &= \sum_i c_{ix}^2 N_i = N_0 + N_3 + \frac{1}{4}(N_1 + N_2 + N_4 + N_5), \\ P_P(x) &= \sum_i c_{iy}^2 N_i = \frac{3}{4}(N_1 + N_2 + N_4 + N_5), \end{aligned} \tag{20}$$

where N_i is the number of particles in the direction i of the site under consideration and c_{ix} and c_{iy} are the x and y components of the (unit) velocity vector along that direction. It is vital that we state here how we label directions in our automaton,

$$\mathbf{c}_i = (\cos 2\pi i/6, \sin 2\pi i/6), \qquad i = 0, ..., 5, \tag{21}$$

where direction $i = 6$ denotes the rest particle, with zero velocity.

In kinetic theory the pressure tensor is expressed as the average of $m\mathbf{cc}$ over the molecular velocities,

with m the particle mass and $\mathbf{c}$ the molecular velocity relative to the macroscopic velocity,

$$P_{\alpha\beta} = \int mc_\alpha c_\beta f \, d\mathbf{v}, \tag{22}$$

where f is the velocity distribution function. For lattice gases the pressure tensor is given by (19), in which the ensemble averaging performs the velocity averaging and the fact that the elements of the ensemble are uncorrelated with each other guarantees that the velocity domain is uniformly sampled. In this paper averaging over lattice velocities is carried out by ensemble and time averaging over states which are approximately stationary. Ensemble averaging is done over independent runs, which guarantees uncorrelated realisations of lattice velocities; time averaging, on the other hand, is performed for every single time step of the simulation, and hence there is correlation of velocities at least for the few measurements adjacent in time to every single time step. In future work we could calculate the *time correlation neighbourhood* inside of which averaging would be pointless in terms of a rigorous calculation of N_i, and therefore measure outside it.

Moreover, a vertical interface exhibits translational symmetry along the y axis and therefore we also average over the y coordinate for fixed x, as these sites have to have uncorrelated pressure due to the translational symmetry. According to this, we compute (18) as

$$\sigma = \left\langle \frac{1}{2n_y} \sum_{i_x=0}^{n_x-1} f(i_x) \sum_{i_y=0}^{n_y-1} [P_N(i_x, i_y) - P_P(i_x, i_y)] \right\rangle, \tag{23}$$

where the brackets denote time averaging, i_x and i_y are the x and y coordinates on our lattice, n_x and n_y are the width and height of the lattice respectively, and $f(i_x)$ is a factor coming from the integration method. We used an integration method of the same order of Simpson's rule, for which

$$f = \begin{cases} 3/8 & \text{if } i_x = 0 \text{ or } n_x - 1 \\ 7/6 & \text{if } i_x = 1 \text{ or } n_x - 2 \\ 23/24 & \text{if } i_x = 2 \text{ or } n_x - 3 \\ 1 & \text{elsewhere.} \end{cases}$$

Dividing by $2n_y$ in (23) comes from vertical averaging and the fact that, as we use periodic boundary conditions both on the vertical and horizontal directions, there are actually two interfaces contributing to the surface tension, at $i_x = n_x/2$ and at $i_x = 0$. As we will mention later, we work with $n_x = 64$ and $n_y = 512$.

Interactions	σ $(nx = 64)$
SR	0.2692 ± 0.0069
LR3	0.2708 ± 0.0069
LR8	0.2708 ± 0.0069

TABLE II: Surface tension of a planar interface with surfactant, as the range of the potential for the surfactant particles absorbed at the interface increases.

In practice the interface is not flat but has irregularities that can make sites of equal x coordinate lie at different distances from the interface. As the pressure profile theoretically depends on that distance, vertical averaging over an irregular interface would give rise to a statistical error (increased dispersion around the mean) in addition to that coming from the noise of our automaton.

There is an added difficulty apart from averaging: the configuration of the system for the initial time step has to be such that the total linear momentum is zero, at least along the direction perpendicular to the interface. When this is not the case, the interface moves aside with constant speed, making time-averaging difficult. In other words, a non-zero initial momentum does not allow the system to achieve stationary configurations. To achieve stationarity, it was enough for us to remove around 80% of the initial momentum of the automaton before letting it evolve in time. Cohesion keeps the interface in place, which otherwise would drift due to residual momentum in the lattice.

An important caveat to be considered is that enough amount of surfactant has to be added to the interface for it to reflect a reduction in surface tension. Due to for a surfact particle sitting at the interface is energetically favoured, that reduction only occurs if the interface length has to be increased to accommodate all the surfactant particles present. Let N_I be the number of sites of the interface, N_S the number of sites with the added surfactant, and ρ_s the reduced density of surfactant. Then the condition for increase of interface length is

$$7\rho_s N_S > 7N_I \tag{24}$$

For the planar interface, $N_S = \theta n_y$, where θ is the thickness of the surfactant layer, and $N_I = n_y$. Then Eq.(24) reduces to

$$\rho_s > 1/\theta \tag{25}$$

Hence, for example, for a surfactant layer of 1.2, reduced densities smaller than 0.83 will not produce a reduction in surface tension.

III. PARALLEL IMPLEMENTATION

The development of the algorithms to encompass parallel environments was driven by the desire to study problems too large for workstation class machines both in memory and computation time. An underlying aim in the development of a parallel version was to produce a code-base in which the parallelization had minimal impact on the structure and layout

of the original code. This enables a more seamless transition to high performance machines and maintains accessibility for those inexperienced in HPC development who can take a toolkit approach to building applications for high end machines.

The parallelization of the code, a two dimensional regular triangular problem is naively simplistic. A number of lattices of varying data types are decomposed over processors in regular fashion. Initial examination of problem types demonstrate this to be the correct approach, however the longer term usage of the code is unlikely to reflect this, as there is no inherent load balancing of the algorithm.

The communications API developed allows the development of more sophisticated approaches to domain decomposition without requiring alteration to the scientific portions of the code, as well as providing abstraction of communication primitives to facilitate optimisation on a per platform basis.

The approach taken was to develop an object orientated abstraction of domain decomposed data structures as well as wrappers around the lowest level primitives. In this picture the primary objects relating to the lattice gas simulation are the decomposition, which may be regarded as a layout of processors, and the grid (a regular domain decomposed array). The grid object inherits properties of the decomposition (including its dimensionality and distribution) and any number of different decompositions and data distributions are supported dynamically within the same application. The code is implemented as a state machine written in ANSI c with context switches between grids allowing parameterless calls to common operations such as halo exchange, file I/O or mathematical transformations from a supporting library. Portability to Irix, Linux, and the Cray T3E has been demonstrated.

The initial implementation has been written in MPI with an MPI_Type_vector used as the default type for synchronous boundary exchange operations providing seamless access to "nearest neighbour" data. The dominant fraction of computation time (around 50 %) is spent in complex-complex Fourier transform routines as can be seen in Figure 1. This routine is a management wrapper and is currently layered upon FFTW [14]. At the current time this sustains around 80MFlops per processor including data rearrangement and communications overheads. This proves significantly faster than the "computation only" Numerical Recipes original algorithm and is found to be accurate in forward-reverse tests to around 15 significant figures. Scalability of the FFT to small numbers of processors is illustrated in Figure 2.

Current and future development of the communications interface include the development of a high performance IO layer based on MPI/IO and ffio on Cray T3E systems, abstraction to provide dynamic visualization and computational steering (initially based on COVICE [15]), and an automatic profiling and tuning layer.

IV. SIMULATIONS

A. Oil-water system

We performed three sets of measurements. In the first, we simulated the evolution of the planar interface for 10000 time steps for all of the interaction potentials, with 8 independent runs for each. The pressure measurements were taken every 10 time steps, discarding the first 1000 time steps for the averaging on the assumption that any transient behaviour would die out at the end of this interval. The system size was 512 sites in height and 64 sites in width, which were the values that best fit to our requirements for a small computational demand and a large number of samples for averaging, all leading to an error in the surface tension smaller than 10%. We assumed that $n_x = 64$ was a value large enough to avoid interference between interfaces (i.e., the transfer of momentum from one to another), which would have the effect of distorting their required flatness.

In the second set we repeated the simulations, but doubled the size of the system to $n_x = 128$, and in the third set to $n_x = 256$. Our aim was to check for finite-size effects, and reduce the standard error of the average.

For $n_x = 64$ we present the profile for the integrand in (18) and interaction potentials *SR*, *LR4* and *LR8* in Figs. 3, 4 and 5, respectively. Error bars are all smaller than the plotting symbols and were computed by propagating the standard errors

$$\pm s/\sqrt{N} \tag{26}$$

originating from vertical averaging through further averages, i.e., over time and runs. These errors cover 66% of the averaging sample, where s is the standard deviation of the distribution of pressure measurements and N is the number of measurements. We see that the height of the peaks at the two interfaces (located at the lattice centre and borders) tends to grow from *SR* to *LR4*; from that interaction range onwards up to *LR8* the height decreases and the width broadens. As for our interest, we are only concerned about the area under the profile, and this increases as we move up to longer ranges.

In Fig. 6 we plot the dependence of the surface tension with the interaction range, for the three sets of measurements. The error bars are the difference between the integral of $y_i + \epsilon_i$ and of $y_i - \epsilon_i$, where y_i symbolically denotes the integrand in (18), discretised by the integration method, and ϵ_i its respective error. For $n_x = 64$ we see an increase in surface tension as we go from *SR* to *LR4*, and from *LR5* to *LR8*, but a drop-off of 3.9% in *LR5* with respect to *LR4*. For $n_x = 128$ there is a similar decrease from *LR3* to *LR4*, but for *LR5* it shows an increase. Finally, for $n_x = 256$ we get an increasing behaviour for all the interaction ranges. It is expected the latter to be more reliable a result than for narrower lattices as finite size effects are less important. The data plotted in Fig.6 is summarised

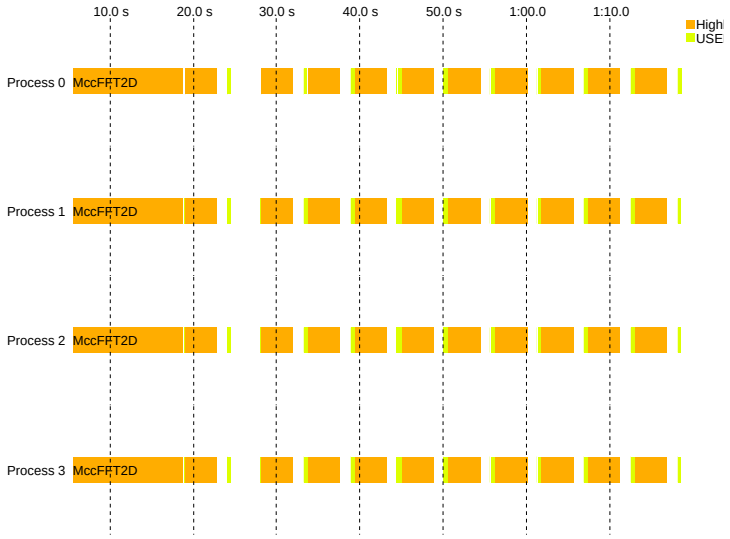

FIG. 1: Time line for a four processor run of the simulation. Dark grey regions are spent in FFTW, light grey represents propagation of states and associated boundary exchange.

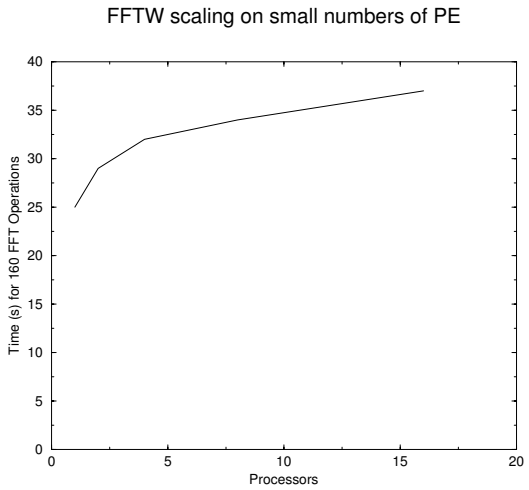

FIG. 2: Time spent in FFTW wrapper per processor on varied size processor array at fixed size per processor of 256^2.

in Table I.

Finally we mention that, in the simulation of the planar interface, the differences in code execution times when using different long-range potentials were 0.4% at most.

B. Oil-water-surfactant system

We make now use of a lattice of the same size, 64×512, and working with reduced densities of 0.5, we put now a layer of surfactant particles of thickness 2.4 lattice sites at the interface, following the reasoning leading to Eq.(25). In order to check for the reduction in surface tension when adding surfactant to the

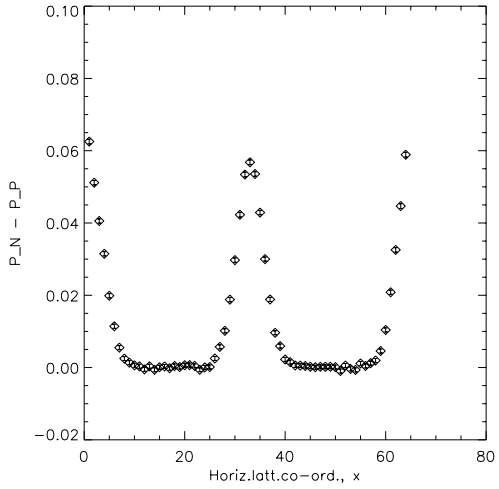

FIG. 3: Pressure profile $P_N - P_P$ for a vertical planar interface using nearest neighbour colour-colour interactions. The interface is located around $x = 32$ and at one end (periodic boundary conditions are used). As the title intends to indicate, this profile is the result of ensemble averaging over 6 runs and time averaging from time steps 1500 to 10000, taking measurements every 10 time steps, in addition to vertical averaging over the 512 sites the lattice has in height. The surface tension calculated is 0.364 ± 0.036 (9.9% error).

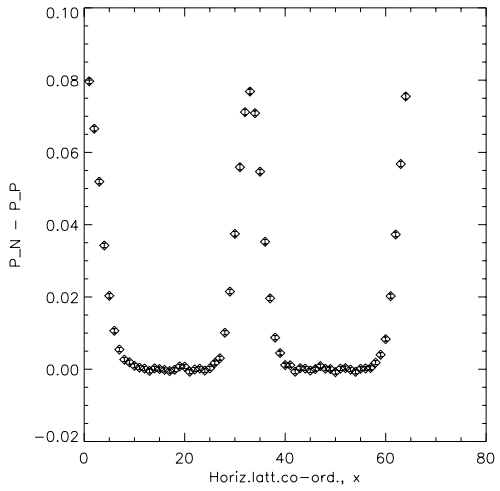

FIG. 4: Pressure profile $P_N - P_P$ for a vertical planar interface. Using *LR4* colour-colour interactions. Same averaging as before. The surface tension calculated is 0.436 ± 0.037 (8.5% error).

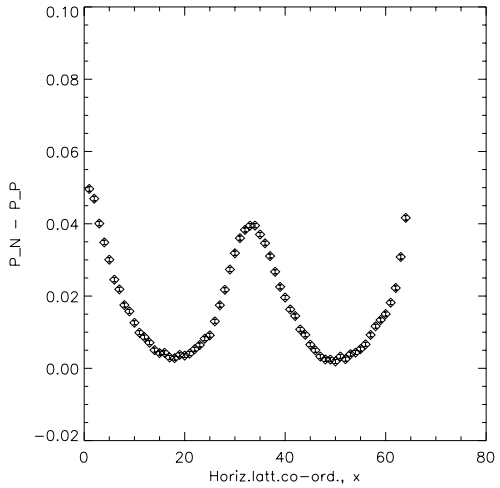

FIG. 5: Pressure profile $P_N - P_P$ for a vertical planar interface. Using *LR8* colour-colour interactions. Same averaging as before. The surface tension calculated is 0.436 ± 0.037 (8.5% error).

interface, we also simulated a planar interface with density 0.5 and no surfactant layer on it.

We carried out three runs: We used a surfactant particle interaction potenttial of ranges SR, LR3 and LR8. The results are summarised in Table II. There is no dependence of the surface tension with the range of the dipolar potentials.

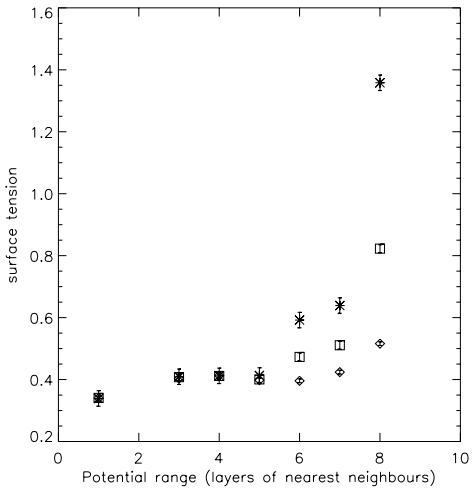

FIG. 6: Surface tension of the planar interface as a function of the colour-colour interaction range. The diamonds correspond to nx=64, 15000 time steps, 8 independent runs each, measuring at all the time steps after the first 1000. The squares correspond to doubling the lattice width (nx=128), other parameters remaining the same. And the stars to doubling again the lattice width (nx=256), same parameters.

V. DISCUSSION AND CONCLUSIONS

The principal result of this study is that our mesoscopic, long-range lattice-gas model can control the surface tension of the interface between two immiscible fluids depending on how many layers of neighbours are included when computing the colour field (12). In addition, the range of the dipole interaction potential (cf. 13) does not affect the surface tension.

If we could increase the lattice size as we please for an immiscible mixture, there should be no other limitation for us to compute an ever increasing surface tension as we increase the range of the oil-water interactions.

The fact that the surface tension is independent of the range of the dipole potential gives us insight on the capability of our lattice gas in the study of surfactant structures in a single fluid phase: we will not be able to control the surface tension in that case.

We show in Fig.6 how the surface tension for the planar interface exhibits a strong dependence with the size of the system: It increased for a larger lattice. We expect the surface tension to achieve asymptotic limits for large enough lattices.

The model is implemented using an object based approach to domain decomposed data structures that allows platform specific implementation of methods forming an efficient toolkit-like approach to parallel programming. Core computation is layered on FFTW which is found to provide portability and good perfor-

mance on the Cray T3E over a range of problem sizes.

Finally, a natural continuation of this work would be the reproduction of the bending rigidity in closed membranes. We foresee the increase of the range of dipole potentials having an influence on this coefficient, as some kind of long range order is enforced among surfactant particles lying at the interface.

VI. ACKNOWLEDGMENTS

The parallel C code used in this work was developed upon a serial version by Brian Gregor, Physics Department, Boston University, USA. N.G.S. wishes to thank Prof Peter V Coveney and Dr Keir Novik (Centre for Computational Science, Queen Mary & Westfield College, University of London, UK) for their support.

[1] Gelbart W M, D Roux, A Ben-Shaul (eds.): "Modern ideas and problems in amphiphilic science." Springer, Berlin, 1993.

[2] Boghosian B M, P V Coveney and A N Emerton: "A lattice-gas model of microemulsions." *Proc R Soc Lond A* **452** 1221-1250 (1996).

[3] Hamley I W: "Introduction to soft matter: polymers, colloids, amphiphiles and liquid crystals." Wiley, Chichester (UK), 2000.

[4] Deuling H J and W Helfrich: "The curvature elasticity of fluid membranes: A catalogue of vesicle shapes." *Journal de Physique* **37** 1335 (1976).

[5] Canham P B: "The Minimum Energy of Bending as a Possible Explanation of the Biconcave Shape of the Human Red Blood Cell." *J Theor Biol* **26** 61 (1970).

[6] Rosso R, A Sonnet, E G Virga: "Evolution of vesicles subject to adhesion." *Proc Roy Soc Lond A* **456** 1523 (2000).

[7] Stelitano D, D Rothman: "Fluctuations of elastic interfaces in fluids: Theory and simulation." *LANL arXiv:cond-mat/0006232* (14 Jun 2000).

[8] Boon J P, C Bodenstein and D Hanon: "Class of Cellular Automata for the formation of surface aggregates." *Int J Mod Phys C* **9**(8) 1559 (1998).

[9] Ebihara K, T Watanabe and H Kaburaki: "Surface of dense phase in Lattice-Gas fluid with long-range interaction." *Int J Mod Phys C* **9**(8) 1417 (1998).

[10] Appert C and S Zaleski: "Lattice Gas with a Liquid-Gas Transition." *Phys Rev Lett* **64**(1) 1 (1990).

[11] Rothman D H and J M Keller: "Immiscible Cellular-Automaton Fluids." *J Stat Phys* **52** 1119 (1988).

[12] Frisch U, B Hasslacher, Y Pomeau: "Lattice-gas automata for the Navier-Stokes equation." *Phys. Rev. Lett.* **56** 1505 (1986).

[13] Adler C, D d'Humières and D H Rothman: "Surface tension and interface fluctuations in immiscible lattice gases." *J Phys I France* **4** 29 (1994).

[14] http://www.fftw.org/

[15] http://www.hlrs.de/structure/organisation/vis/covise/

Chapter 5

Conclusions and future work

In this thesis I have presented investigations on the ability of two lattice methods to model the behaviour of binary immiscible and ternary amphiphilic fluids: a three-dimensional kinetic-theoretic lattice-Boltzmann (LB) model and a two-dimensional lattice-gas (LG) model. In this last section I give general conclusions on the work done, and suggest possible paths for its continuation.

The renowned ability of the LB and LG methods we used to model simple fluid flows rests in the principle of similarity of fluid mechanics, and its intrinsic algorithmic structure renders them ideal for high computational efficiency. In fact, two fluids with quite different microscopic structures can have the same macroscopic behaviour because the form of the macroscopic equations ruling it is entirely governed by the microscopic conservation laws and symmetries—this allows us to employ a simplified, algorithmically efficient microworld instead of retaining the full molecular dynamics. The fact that the lattice-Boltzmann model we used is in fact a local cellular automata of a simple update rule allows its algorithm to be readily deployed on massively parallel computers, and, hence, the low Knudsen number limit—effectively, the limit of large enough lattices—in which the model is designed to reproduce the Navier-Stokes equations can, in actuality, also be achieved in simulations. As regards the lattice-gas model with long-range interactions that we used, since its collision rule can be expressed as a convolution of fields on the lattice, use of Fourier transforms makes the algorithmic efficiency of its implementation independent of the range of the interactions. Tackling the large lattice limit can thus be achieved with an efficient Fourier-transform algorithm.

In these methods, the macroscopic properties are emergent from, rather than imposed on, the microscopic dynamics. In particular, interfacial tension between immiscible fluids arises as the result of the appropriate collision rules, giving rise to an interface which does not require to be explicitly computed, contrary to what occurs in methods solving the

Navier-Stokes equations. As my **first conclusion** to lay down, our bottom-up LB simulations on interfacial behaviour show the demixing of 1:1 fluid mixtures well below the spinodal (i.e., away from criticality) to follow domain-growth algebraic exponents compatible with predictions from continuum theories, which in turn reproduce experimental observations. Furthermore, the interface kinetics reproduces the dynamic scaling hypothesis, whereby the time evolution of the segregating bicontinuous morphology for times $t > t_0$ can be expressed, in the statistical sense, as a spatial scaling ('zoom-in') law on the morphology at $t = t_0$; in other words, the fluid demixes with a speed of growth common to all domains. In addition, our simulations allow to rebut previous claims in the literature that all fluid models showing dynamical scaling and sharing the same unique length and timescales will show similar domain-growth algebraic exponents.

Correct kinetics for the interface between two immiscible fluids is not the only macroscopic property sought after for these lattice methods for fluid dynamics. We also looked at phenomenology for which there is no satisfactory macroscopic, continuum theory: amphiphilic adsorption and self-assembly. In fact, the behaviour of amphiphilic molecules is adequately described *ab initio*, using particulate methods—continuum approaches are valid only in the 'adiabatic' limit. My **second conclusion**: LB simulations show that the amphiphilic molecules, modelled as point dipoles interacting with themselves and the immiscible species via coupled BGK equations and mean-field forces with nearest neighbours, behave as experimentally observed for ternary amphiphilic fluid mixtures, i.e., adsorption onto the interface, reduction of interfacial tension, slowdown of growth kinetics, and arrest of domain growth and formation of a microemulsion (sponge) mesophase. We also find, for the first time using a kinetic-theoretic model, **third conclusion**, a lyotropic transition between the sponge mesophase and the gyroid liquid-crystalline cubic mesophase as the amphiphile concentration and inter-amphiphile coupling is varied, going through a molten-gyroid mesophase. As a **fourth conclusion**, the gyroid mesophase found shows slowly decaying oscillations in the size of its unit cells caused by Marangoni flows, and coincident with the existence of structural defects which slowly annihilate, that is to say, relax to the crystalline structure surrounding them.

Long-range interactions are commonplace in nature, and the hydrophobicity and chemical affinity driving phase segregation are nothing but effective long-range electrostatic forces between species. Increasing the range of the LB inter-particle interactions further than nearest neighbours can have dramatic effects on the behaviour of the interfacial tension, and hence, on the growth exponents, scaling behaviour and amphiphile self-assembly just referred to. A first approach to the problem, and considering the difficulty in laying out an efficient long-range LB algorithm, has been my use of a LG model for ternary amphiphilic fluids, in which performance is not affected by increasing the range of the interactions. My **fifth conclusion** states that our LG simulations show that the interfa-

cial tension of an interface between two immiscible fluids with amphiphile adsorbed on it grows with the range of the inter-molecular interaction between these two fluids, and not with the range of the interaction between the amphiphilic molecules.

Last, our study of amphiphilic mesophases would go incomplete without an investigation, albeit introductory, of their dynamic response to shear. My **sixth conclusion** reads: the gyroid amphiphilic cubic mesophase shows shear thinning, less pronounced than that exhibited by the molten gyroid mesophase. At late times after the onset of shear on the gyroid, **seventh conclusion**, we find a complex steady nonequilibrium mesophase consisting of toroidal rings and elongated tubules; in the sheared molten gyroid, the number of toroidal rings is lower and the number of elongated tubules higher and more aligned with the flow than in the gyroid, at late times and for the same value of shear.

Suggestions of a number of ways that the research presented in this dissertation can be continued are duly here. As regard the LB method, there is an ongoing line of investigation at the Centre for Computational Science (University College London, UK) aimed at continuing the rheological studies of gyroid mesophases which took off from the work I presented here. The research can be aimed at (a) computing the gyroid's memory function guiding the response to a sudden interruption of steady shear, and find out its dependence with the model parameters; (b) investigate the viscoelastic response of the gyroid mesophase to small-amplitude oscillatory shear by plotting one component of the complex elastic shear modulus against the other (Cole-Cole plots), i.e., by looking at the interdependence between the loss and storage elastic moduli; and (c), investigate hysteretic behaviour in the dynamical response of gyroids to large-amplitude and high-frequency oscillatory shear, by looking at stress *versus* strain plots.

Regarding the LG model we employed, the research presented herewith is the first stepping stone towards investigating the role of long-range interations in providing mechanical stability to ternary amphiphilic droplets. Using the same (two-dimensional) LG model, I started tests to compute the Canham-Helfrich stiffness coefficient (or rigidity modulus) by fitting the (excess) pressure, p, of "oil-in-water" droplets containing a monolayer of amphiphilic molecules adsorbed on the interface to their inverse radius of curvature, H. Minimisation of the Canham-Helfrich energy as a functional of the interface's curvature gives a cubic polynomial dependence between the two, $p = \gamma H - \kappa H^3$, where γ is the interfacial tension and κ is the stiffness coefficient. Fits to this law showed that an insufficient number of points being sampled and/or their error bars (standard errors from ensemble averaging) being large produce large uncertainty in the value of κ. Ways forward could be: (a) to substantially increase the number of points sampled (i.e., larger lattices are needed in order to include more droplet radii) and the number of initial conditions (and their pathways) over which to ensemble average; or (b), change the method to compute κ, e.g., from the functional (line integral) dependence of κ on a stress tensor difference, similar to

the one used in this thesis to compute the interfacial tension on a planar interface.

I have already pointed out in the introduction that our LB research on gyroids was employed by TeraGyroid, a UK-USA project on the developement and application of computational grids for distributed high-performance computing, as its scientific motivation [5, 6, 7]. During the production runs, headquartered at the SuperComputing 2003 conference, Phoenix (AZ, USA), in November 2003, grid technologies developed within it allowed researchers to concurrently use up to ca. 6000 processors distributed among platforms in the UK and the USA. The simulations were aimed at self-assembling gyroid mesophases on lattices up to 1024^3 lattice sites and simulation times of up to one million time steps, the data of which are still being analysed. The unique opportunity provided by the project and its academic partners allowed researchers to simulate the whole temporal pathway of defect relaxation that we probed only in its initial stages, as reported in this thesis, and to reach sufficient spatial resolution (in terms of number of gyroid unit cells) in order to study the spatial distribution of defective regions. Needless to say, the information provided by our simulations, as presented in this thesis, as well as those of the TeraGyroid project, can be of straightforward interest for materials scientists: simulation length scales mapped onto experimental ones could supply direct-space relevant information to experimentalists on defect dynamics, who, more often than not, are constrained by the limitations in time-resolving the nanoscopic unsteady dynamics in question.

Bibliography

[1] J.-P. Hansen and I. R. McDonald, "Theory of simple liquids." (London: Academic Press, 1990.)

[2] J. P. Boon and S. Yip, "Molecular hydrodynamics." (New York: Dover, 1991.)

[3] J. O. Hirschfelder, C. F. Curtiss and R. B. Bird, "Molecular theory of gases and liquids." (New York: Wiley, 1964.)

[4] P.-G. de Gennes: "Scaling concepts in polymer physics." (Ithaca, NY: Cornell University Press, 1979.)

[5] Cf. "TeraGyroid: Grid-based lattice-Boltzmann simulations of defect dynamics in amphiphilic liquid crystals," demonstration at the SuperComputing2003 conference, Phoenix (Arizona, U. S. A.), November 2003; see also URL: http://www.realitygrid.org/teragyroid-index.html .

[6] S. M. Pickles, R. J. Blake, B. M. Boghosian, J. M. Brooke, J. Chin, P. E. L. Clarke, P. V. Coveney, N. González-Segredo, R. Haines, J. Harting, M. Harvey, M. A. S. Jones, M. McKeown, R. L. Pinning, A. R. Porter, K. Roy, M. Riding, "The TeraGyroid Experiment." Workshop on Case Studies on Grid Applications, Proceedings of the Global Grid Forum GGF10 Conference, Berlin, 2004. (Available online, cf. URL: http://www.zib.de/ggf/apps/meetings/ggf10.html .)

[7] J. Harting, M. J. Harvey, J. Chin and P. V. Coveney, "Detection and tracking of defects in liquid crystals." (Submitted for publication, 2004.)

[8] I. W. Hamley, "Introduction to soft matter." (Chichester, UK: Wiley, 2000.)

[9] W. M. Gelbart, D. Roux, and A. Ben-Shaul, "Modern ideas and problems in amphiphilic science." (Berlin: Springer, 1993.)

[10] G. Gompper and M. Schick, In *Phase Transitions and Critical Phenomena.* C. Domb and J. Lebowitz (eds), Vol. 16, pp. 1–176 (London: Academic Press, 1994).

[11] D. Chapman and M. N. Jones, "Micelles, Monolayers, and Biomembranes." (Chichester: Wiley, 1994).

[12] P. Kumar and K. L. Mittal (eds), "Handbook of Microemulsion Science and Technology." (New York: Marcel Dekker, 1999).

[13] G. Gompper and M. Schick, In *Handbook of microemulsion science and technology.* P. Kumar & K. L. Mittal (eds) (New York: Marcel Dekker, 1999.)

[14] S.-J. Marrink and D. P. Tieleman, J. Am. Chem. Soc. **123**, 12383 (2001).

[15] V. Luzzati, R. Vargas, P. Mariani, A. Gulik, and H. Delacroix, J. Mol. Biol **229**, 540 (1993).

[16] J. M. Seddon and R. H. Templer, in *Handbook of Biological Physics.* R. Lipowsky and E. Sackmann (eds) (Elsevier Science B. V., London, 1995.) Vol. 1, pp. 97–153.

[17] L. D. Landau and E. M. Lifshitz, "Fluid mechanics." (London: Pergamon Press, 1959.); G. K. Batchelor, "An introduction to fluid dynamics." (Cambridge : Cambridge University Press, 1967.)

[18] G. K. Batchelor, "An introduction to fluid dynamics." (Cambridge: Cambridge University Press, 1967).

[19] D. Gueyffier, J. Lie, A. Nadim, R. Scardovelli, and S. Zaleski, J. Comput. Phys. **152**, 423 (1999).

[20] O. A. Ladyzhenskaia, "The mathematical theory of viscous incompressible flow." (New York: Gordon & Breach, 1969.)

[21] G. Tryggvason, B. Bunner, O. Ebrat, W. Tauber, in *Computations of Multiphase Flows by a Finite Difference/Front Tracking Method. I Multi-Fluid Flows*, 29th Computational Fluid Dynamics Lecture Series 1998–03 (Von Karman Institute for Fluid Dynamics) (Cf. URL: http://www-personal.engin.umich.edu/˜gretar .)

[22] S. Harris: "An Introduction to the Theory of the Boltzmann Equation." (New York: Holt, Rinehart & Winston, 1971.)

[23] J. H. Ferziger and H. G. Kaper, "Mathematical theory of tranport processes in gases." (Amsterdam: North-Holland, 1972.)

[24] The limit $N \to \infty$, $m \to 0$, $\lambda \to 0$, with both $N\lambda^2 \equiv$ (mean free path)$^{-1}$ and Nm fixed, where N stands for the number of particles, m is their mass, and λ is the range of the interparticle, hard-sphere potentials, was baptised 'the Boltzmann-Grad limit'

by O. E. Landford III. In addition, the density has to be sufficiently low so that only binary collisions need be considered (consequence of $\lambda \to 0$), and spatial gradients small enough such that collisions can be thought of as localised in space. The most rigorous proof that in this limit the *Stosszahlansatz*, and therefore the Boltzmann equation (without a body force term), is exact for at least short times was provided by Landford in 1981 (Physica A **106**, 70 (1981)), the system described being an ideal gas. In 1985 Reinhard Illner and Mario Pulvirenti extended the result to three dimensions (*cf.* C. Cercignani, R. Illner and M. Pulvirenti, in *The mathematical theory of dilute gases*, Applied Mathematical Sciences **106** (New York: Springer-Verlag, 1994)). See also http://www.ann.jussieu.fr/publications/1995/R95026_Perthame.ps.gz for a list of references on collision models in Boltzmann's theory.

[25] M. Bonitz, "Quantum Kinetic Theory." (Stuttgart: Teubner Verlag, 1998. ISBN 3-519-00238-8.)

[26] H. Grad, Comm. Pure Appl. Math. **2**, 331 (1949).

[27] D. Jou, J. Casas-Vázquez and G. Lebon, "Extended Irreversible Thermodynamics." (Berlin: Springer, 1996.)

[28] I. Prigogine, "Introduction to thermodynamics of irreversible processes." (New York: Interscience, 1967.)

[29] R. M. Velasco and L. S. García-Colín, J. Non-Equilib. Thermodyn. **20**, 1 (1995).

[30] N. González-Segredo, *Treball de recerca* (MPhil Thesis), Physics Department, Universitat Autònoma de Barcelona, September 1997.

[31] R. Balescu, "Equilibrium and non-equilibrium statistical mechanics." (New York: Wiley, 1975.)

[32] U. Frisch, D. d'Humières, B. Hasslacher, P. Lallemand, Y. Pomeau, and J.-P. Rivet, Complex Systems **1**, 649 (1987).

[33] S. Bastea, R. Esposito, J. L. Lebowitz and R. Marra, J. Stat. Phys. **101**, 1087 (2000).

[34] J. S. Rowlinson and B. Widom, in *Molecular theory of capillarity* (Clarendon Press, Oxford, 1982).

[35] T. Ohta and K. Kawasaki, Macromolecules **19**, 2621 (1986).

[36] J.-L. Barrat and J.-P. Hansen, "Basic concepts for simple and complex liquids." (Cambridge: Cambridge University Press, 2003.)

[37] See, for example, the renormalisation group procedure applied to the Becker-Döring description of self-reproducing micelles, in: P. V. Coveney, Phil. Trans. R. Soc. Lond. A **361**, 1057 (2003).

[38] W. Cahn and J. E. Hilliard, J. Chem. Phys. **28**, 258 (1958).

[39] An in-depth explanation of Model B and Model H, among others, can be found in: P. C. Hohenberg, Rev. Mod. Phys. **49**, 435 (1977).

[40] U. Frisch, B. Hasslacher and Y. Pomeau, Phys. Rev. Lett. **56** 1505 (1986).

[41] S. Wolfram, J. Stat. Phys. **45**, 471 (1986).

[42] J. von Neumann, "Theory of self-reproducing automata." (Champaign, IL: University of Illinois Press, 1966.)

[43] U. Frisch, B. Hasslacher, Y. Pomeau, Phys. Rev. Lett. **56**, 1505 (1986).

[44] M. Hénon, Complex Systems **1**, 475 (1997).

[45] L.-S. Luo, Phys. Rev. Lett. **81**, 1618 (1998).

[46] S. Succi, "The lattice-Boltzmann equation for fluid dynamics and beyond." (Oxford: Oxford University Press, 2001.)

[47] X. He and L.-S. Luo, Phys. Rev. E **56**, 6811 (1997).

[48] P. J. Hoogerbrugge and J. M. V. A. Koelman, Europhys. Lett. **19**, 155 (1992).

[49] P. Español and P. Warren, Europhys. Lett. **30**, 191 (1995).

[50] C. A. Marsh, G. Backx and M. H. Ernst, Phys. Rev. E **56**, 1676 (1997).

[51] C. A. Marsh and J. M. Yeomans, Europhys. Lett. **38**, 411 (1997).

[52] P. V. Coveney and P. Español, J. Phys. A: Math. and General **30**, 779 (1997); C. A. Marsh and P. V. Coveney, J. Phys. A: Maths and General **31**, 6561 (1998).

[53] E. G. Flekkøy and P. V. Coveney, Phys. Rev. Lett. **83**, 1775 (1999).

[54] I. Pagonabarraga and D. Frenkel, J. Chem. Phys. **115**, 5015 (2001).

[55] N. Metropolis, A. W. Rosenbluth, M. N. Rosenbluth, A. H. Teller and E. Teller, J. Chem. Phys. *21*, 1087 (1953).

[56] S. Wolfram: "A new kind of science." (Champaign, IL: Wolfram Media, 2002.)

[57] URL: http://www.top500.org/ .

[58] URL: http://www.ks.uiuc.edu/Research/namd/ .

[59] P. J. Love, M. Nekovee, P. V. Coveney, J. Chin, N. González-Segredo, and J. M. R. Martin, Comp. Phys. Commun. **153**(3), 340–358 (2003).

[60] P. B. Canham, J. Theor. Biol. **26**, 61 (1970).